NOVEL III-NITRIDE GROWTH BY ULTRAVIOLET RADIATION ASSISTED METAL ORGANIC MOLECULAR BEAM EPITAXY

A Dissertation
Presented to
The Academic Faculty

By

David C. Pritchett

In Partial Fulfillment
Of the Requirements for the Degree
Doctor of Philosophy in Electrical and Computer Engineering

Georgia Institute of Technology

May 2009

NOVEL III-NITRIDE GROWTH BY ULTRAVIOLET RADIATION ASSISTED METAL ORGANIC MOLECULAR BEAM EPITAXY

Dr. W. Alan Doolittle
School of Electrical and Computer Engineering
Georgia Institute of Technology

Dr. A. Bruno Frazier
School of Electrical and Computer Engineering
Georgia Institute of Technology

Dr. Ian T. Ferguson
School of Electrical and Computer Engineering
Georgia Institute of Technology

Dr. Gabriel A. Rincón-Mora
School of Electrical and Computer Engineering
Georgia Institute of Technology

Dr. W. Brent Carter
School of Materials Science and Engineering
Georgia Institute of Technology

Date Approved: February 2009

To my dear family – Amanda, John, Mama, and Daddy

ACKNOWLEDGEMENTS

I thank the following individuals for their contributions that made this work possible:

Amanda Jackson, John C. Pritchett, Tsai-Yueh (Becky) Chu Pritchett, and Franklin R. Pritchett

Dr. W. Alan Doolittle and Mrs. Charlotte Crawley

Walter Henderson, Dr. Shawn D. Burnham, Elaissa Trybus, and Alexander Carver

Daniel Billingsley, Dr. Stuart Bowden, Dr. Gon Namkoong, Kyoung-Keun Lee, W. Laws Calley III, Brian Smith, and Michael Moseley

Linda Newton, Louis Boulanger, and Lorand Csiszar

Dr. A. Bruno Frazier, Dr. Ian T. Ferguson, Dr. Gabriel A. Rincón-Mora, and Dr. W. Brent Carter

Dr. Donald Silversmith, Dr. Gerald Witt, and Dr. Todd Steiner
United States Air Force Office of Scientific Research
This work was funded under the
"Non-Equilibrium, Wide Application Epitaxial Patterning by Intelligent Control"
multidisciplinary university research initiative.

Richard Graham, Mark Krikorian, Jay Hightower, Pete Graham, Jim Krutak, Jeff Bradley, Andres Giles, Andrew Gomez, and Richard Fullerton
ILC (presently Datapath)

TABLE OF CONTENTS

LIST OF TABLES

LIST OF FIGURES

LIST OF NOMENCLATURE

2D	two-dimensional
2DEG	2D electron gas
3D	three-dimensional
3DE	3D Epitaxy
λ	wavelength
κ	thermal conductivity
μ_n	electron mobility
μ_p	hole mobility
σ	absorption cross section
σ_{RMS}	RMS surface roughness
[C]	carbon concentration
C_{Ga}	gallium substitution by carbon
c-GaN	cubic GaN
C_I	interstitial carbon
C_N	nitrogen substitution by carbon
Cp_2Mg	bis-cyclopentadienyl magnesium, magnesocene, $Mg(C_5H_5)_2$
C-V	capacitance-voltage
CW	continuous-wave
DEGa	diethylgallium
DIET	desorption induced by electronic transitions
DMD	digital micromirror device
DMEAA	dimethylethylamine alane, $AlH_3N(CH_3)_2(C_2H_5)$
DMEGa	dimethylethylgallium
E_c	conduction band, lowest unoccupied molecular orbital
E_g	bandgap
E_v	valence band, highest occupied molecular orbital
EQE	external quantum efficiency, η_{ext}
f_{max}	maximum oscillation frequency
f_T	current gain cutoff frequency
FIB	focused ion beam
FISH	free idle substrate heater
FWHM	full width half maximum
GR	growth rate
[H]	hydrogen concentration
HBT	heterostructure bipolar transistor
HEMT	high electron mobility transistor

HR	highly resistive
I_F	forward current
IR	infrared
LD	laser diode
LED	light emitting diode
LEEBI	low-energy electron beam irradiation
LN_2	liquid nitrogen
J_{Cp2Mg}	Cp_2Mg flux
$J_{eff,N}$	effective N flux
$J_{eff,Ga}$	effective Ga flux
J_{DMEAA}	DMEAA flux
J_{III}	total Group III flux ($J_{TEGa} + J_{TMIn} + J_{TEAl\ or\ DMEAA}$)
J_{NH3}	NH_3 flux
J_{TEAl}	TEAl flux
J_{TEGa}	TEGa flux
J_{TMIn}	TMIn flux
LRI	laser reflectance interferometry
MBE	molecular beam epitaxy
m/e	mass-to-charge ratio
MEGa	monoethylgallium
[Mg]	magnesium concentration
Mg_{Ga}	gallium substitution by magnesium
ML	monolayer
MMEGa	monomethylethylgallium
MOCVD	metal organic chemical vapor deposition
MOMBE	metal organic molecular beam epitaxy
MOVPE	metal organic vapor phase epitaxy
MQW	multiple quantum well
n	electron concentration or refractive index
N/MEMS	nano-/micro- electromechanical systems
[O]	oxygen concentration
O_N	nitrogen substitution by oxygen
p	hole concentration
P_b	base pressure
P_{ch}	chamber pressure
PCVS	pressure controlled vapor source
PEC	photo-electrochemical
PL	photoluminescence
PID	proportional-integral-derivative
P_{out}	output power
R	reflectance, reflectivity

RC	rocking curve
RF	radio frequency
RGA	residual gas analyzer/analysis
RHEED	reflection high energy electron diffraction
RMS	root-mean-square
SI	semi-insulating
Si_{Ga}	gallium substitution by silicon
SIMS	secondary ion mass spectroscopy
SSG	surface selective growth
TC	thermocouple
TEAl	triethylaluminum, $Al(C_2H_5)_3$
TEGa	triethylgallium, $Ga(C_2H_5)_3$
TMGa	trimethylgallium, $Ga(CH_3)_3$
TMIn	trimethylindium, $In(CH_3)_3$
T_s	substrate temperature
UHV	ultra high vacuum
UID	unintentionally doped
UV	ultraviolet
V_{Ga}	gallium vacancy
V_N	nitrogen vacancy
VP	vapor pressure
x	mole fraction
XRD	x-ray diffraction
YL	yellow luminescence

SUMMARY

While modern epitaxial methods enable precise, monolayer (ML) control of the thin film deposition process, the complexity of certain device structures is ultimately limited by the capability and cost of the fabrication process. The objective of this work is to develop a pathway toward three-dimensional epitaxy (3DE) – the ability to intentionally and dynamically pattern regions of a film during the deposition process – in order to enable novel device concepts unbound by the traditional device fabrication paradigm. This work pioneers UV-assisted metal organic molecular beam epitaxy (MOMBE) as a particularly selective epitaxy technique to create a pathway toward 3DE of a crucial and topical material system – the III-Nitrides.

A novel UV-assisted MOMBE system is developed enabling intense UV irradiation of films during growth. High quality, heavily (unintentionally) carbon-doped GaN is successfully grown by NH_3-based MOMBE and for the first time InGaN, AlGaN, and magnesium-doped GaN are demonstrated by NH_3-based MOMBE. Intense UV irradiation of films during NH_3-based MOMBE significantly enhances photo-desorption of species during the growth process, subsequently affecting the resultant InGaN alloy composition, carbon dopant concentration, or magnesium dopant concentration. A digital micromirror device is introduced to pattern incident UV radiation during InGaN growth, demonstrating that the effects of photoexcitation during MOMBE which have been proposed, discovered, and identified by this thesis indeed can be leveraged to deposit an InGaN film that is compositionally patterned within the growth plane. The results

demonstrate that the new approach presented herein is possible for the 3DE of III-Nitrides if additional challenges in practical implementation can be overcome.

CHAPTER 1: INTRODUCTION

Modern epitaxy enables precise monolayer (ML) control of both thin film composition and doping with abrupt (2D) interfaces in the growth direction. However, modern epitaxy lacks the ability to control composition and doping *within* the growth plane (lateral inhomogeneity), requiring expensive lithography, etching, and regrowth sequences for device fabrication. 3D Epitaxy (3DE) – the ability to intentionally and dynamically pattern regions of a depositing film – could usher in a new era of device design no longer bound by the traditional device fabrication paradigm. Metal organic molecular beam epitaxy (MOMBE) is a thin film deposition technology which is particularly sensitive to surface reaction chemistry; as such, MOMBE is a promising candidate for the photo-assisted manipulation of growth processes enabling 3DE. Moreover, the III-Nitrides are a modern and prevailing semiconductor family providing a diverse feature set for best leveraging the capabilities of 3DE. However, photo-assisted MOMBE for the growth of III-Nitrides has yet to be reported independent of the work contained herein.

1.1 3D Epitaxy – 3DE

The 3DE concept is a dramatic extension to the capability of 2D epitaxy – ***3DE enables the ability to dynamically pattern the composition or doping within each***

epitaxial layer. Fig. 1.1 shows a simple four layer structure typical of modern epitaxy. The colors represent arbitrary differences in material composition or doping (*e.g.* associated material properties such as bandgap, refractive index, carrier concentration, etc.). In this example, the interfaces are abrupt, but the dimensions can be considered arbitrary. Each layer of Fig. 1.1 is homogenous, as illustrated by the lack of color variation *within* each layer. In contrast, Fig. 1.2 is an example of a potential four layer structure enabled by 3DE. The individual layers are shown in Fig. 1.3. ***Variations in material properties within the growth plane and during epitaxy are possible, enabling the creation of 3D structures during growth.*** Such a structure enabled by 3DE is not possible using traditional fabrication techniques (including substrate pre-pattering) in tandem with modern epitaxy or specialized epitaxial techniques such as surface selective growth (SSG) [1] – or only under cost prohibitive circumstances.

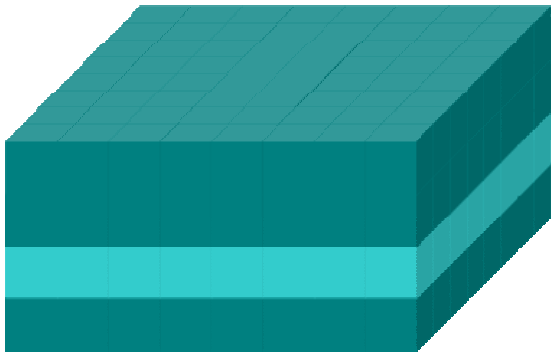

Fig. 1.1. Four layer epitaxial structure possible with modern epitaxy, a 2D process.

Fig. 1.2. Four layer epitaxial structure enabled by 3DE.

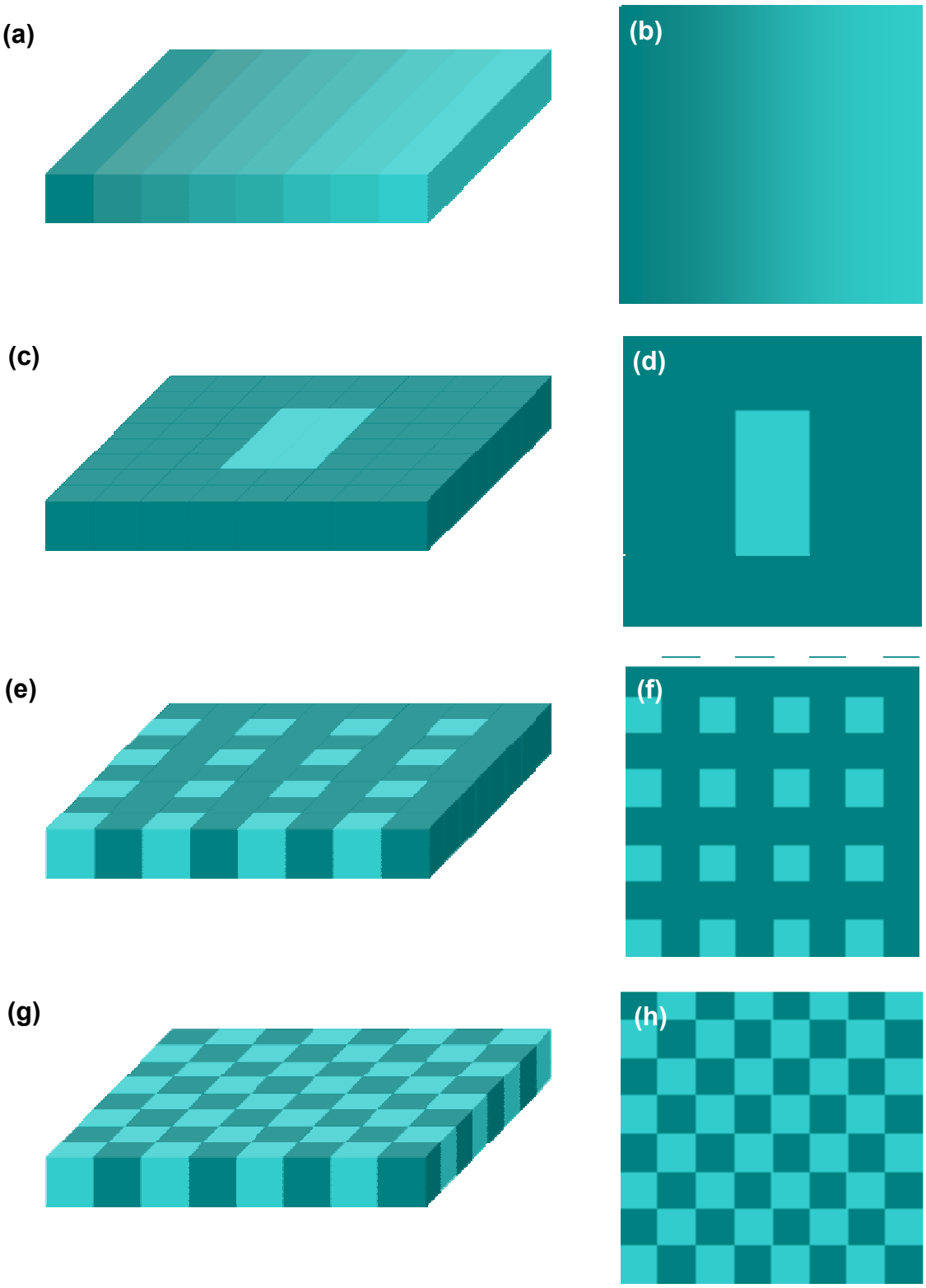

Fig. 1.3. Individual layers (a), (c), (e), and (g) of the basic four layer structure of Fig. 1.1. Corresponding growth plane (2D) composition or doping variations (color variations) are shown in (b), (d), (f), and (h).

1.2 MOMBE

III-Nitride films are most commonly deposited using molecular beam epitaxy (MBE) or metal organic chemical vapor deposition (MOCVD). In MBE, (Fig. 1.4(a)), elemental Group III sources are thermally evaporated from an effusion cell and impinge on a heated substrate in the presence of a Group V flux [2]. Active N is typically produced by plasma induced dissociation of N_2; however, thermal dissociation of NH_3 (referred to as gas source or reactive MBE) has received attention [3]. An ultra high vacuum (UHV) ensures source delivery is collision-free and in the form of molecular beams (Fig. 1.4(b)). This fundamental MBE characteristic facilitates high quality, high purity layers with abrupt interfaces. Moreover, the UHV enables *in situ* characterization tools including reflection high energy electron diffraction (RHEED) and residual gas analysis (RGA) which can provide significant insight into the growth process. However, the MBE environment does have specific limitations. First, flux control is limited by the speed that effusion cells are able to attain the necessary temperature for a required flux. Hence, in order to obtain both a stable flux and a range of fluxes, multiple effusion cells for individual elements are typically necessary in MBE. Also, as the elemental sources and the effusion cells are in UHV, replacement of the sources requires opening the UHV to atmosphere – resulting in significant downtime to restore the UHV. Lastly, the scale-up potential of MBE is limited by the large source-to-substrate distances necessary for large area deposition.

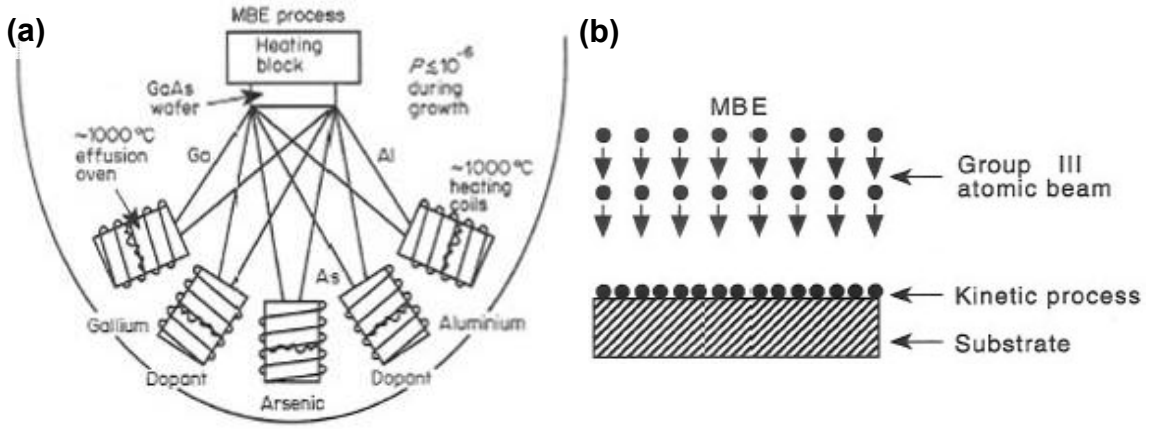

Fig. 1.4. Schematic description of (a) an arsenide MBE growth chamber and (b) MBE growth kinetics [4].

Alternatively, MOCVD [5,6] (Fig. 1.5(a)) – also referred to as metal organic vapor phase epitaxy (MOVPE) – employs vapor sources. Atomic elements arrive on a heated substrate as their partially dissociated gasses undergo further dissociation while diffusing through a stagnant boundary layer (Fig. 1.5(b)). Growth is relatively fast and is generally limited by mass transport. The vapor sources enable a reproducible flux control with reasonably fast transient response. The reactor pressure is usually ≥ 1 Torr, requiring the metal organic Group III sources to be carried, typically by H_2 or N_2. NH_3 is typically used as the source of N, yet hydrazine (N_2H_4) [7], hydrogen azide (HN_3) [8] and N_2-plasma [9,10] have been employed. The lack of UHV and ease of controlling vapor sources drastically reduces maintenance and operating costs but the consumable costs of the metal organics, ammonia, and H_2 is significantly (4-50*x*) higher than MBE. Additionally, the growth chemistry is significantly more complex than MBE – gas phase and surface reactions between NH_3, carrier gasses, and metal organics may yield adducts or byproducts which can significantly affect growth rate (GR), uniformity, and alloy composition [11-13].

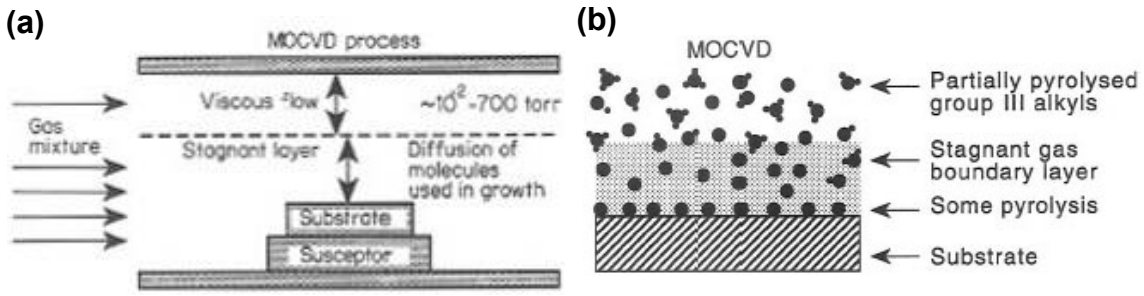

Fig. 1.5. Schematic description of (a) a MOCVD growth chamber and (b) MOCVD growth kinetics [4].

MOMBE (Fig. 1.6(a)) combines the molecular beam nature of MBE (UHV) for ML abruptness and *in situ* analysis with the speed, convenience, and scale-up potential of vapor sources (MOCVD), while drastically reducing the quantity (cost) of toxic and expensive precursors used by MOCVD. MOMBE was initially investigated in 1981 for GaAs [14], and its sensitive growth mechanism was quickly leveraged for surface selective growth (SSG) by using SiO_2 to mask no-growth regions [15,16] (Fig. 1.7). In MOMBE, epitaxy occurs as impinging Group III and V molecular beams are pyrolized on a heated substrate. ***The sensitive growth mechanism of MOMBE originates from the vacuum environment which minimizes gas-phase interactions (low gas density), resulting in surface-pyrolysis-dependent growth (i.e. no stagnant boundary layer exists in MOMBE, Fig. 1.6(b)). Hence, surface-catalyzed reactions, molecular decomposition pathways, and subsequent byproduct surface interactions are critical in the growth process. Likewise, the dependence on surface-catalyzed dissociation means growth is strongly dependent on substrate temperature (T_s). Consequently, growth is complicated as the kinetics of adatom adsorption and desorption are also determined by T_s.***

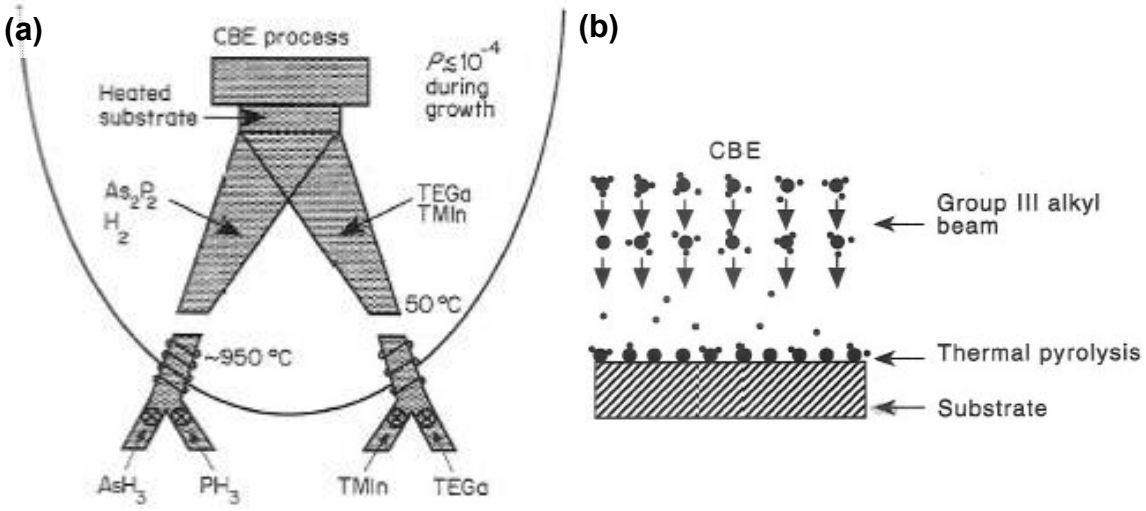

Fig. 1.6. Schematic description of (a) an arsenide/phosphide MOMBE growth chamber and (b) MOMBE growth kinetics [4].

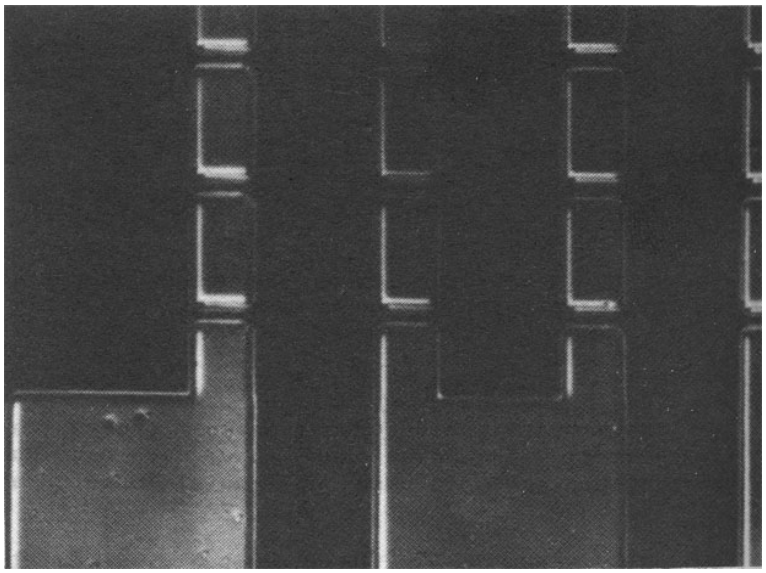

Fig. 1.7. Optical micrograph of GaAs deposited by selective epitaxy through small squares of a SiO_2 mask [15].

The most comprehensive studies of the sensitive MOMBE growth mechanism consider the arsenides [17-20], which can be used herein as a base model to understand the chemistry of the present nitride system. In the MOMBE growth of GaAs, triethylgallium (TEGa, $Ga(C_2H_5)_3$) is the most common precursor due to a reduced C incorporation [21] when compared to more strongly bound alkyl derivatives, such as trimethylgallium (TMGa – $Ga(CH_3)_3$) [22]. For GaAs, the availability of active As results in growth limited by TEGa dissociation, given by reaction (1.1).

$$Ga(C_2H_5)_{3\,(g)} \rightarrow Ga_{\,(ads)} \tag{1.1}$$

The chemisorption of Ga is possible after a series of sensitive, substrate temperature (T_s) dependent surface reactions, including adsorption, dissociation, diffusion, and desorption. If TEGa is adsorbed and dissociates, diethylgallium (DEGa, $Ga(C_2H_5)_2$) is formed via reaction (1.2), which may subsequently desorb as a result of weak adsorption.

$$Ga(C_2H_5)_{3\,(ads)} \rightarrow Ga(C_2H_5)_{2\,(ads)} + C_2H_{5\,(ads)} \tag{1.2}$$

However, DEGa may dissociate into monoethylgallium (MEGa, $Ga(C_2H_5)$) via reaction (1.3).

$$Ga(C_2H_5)_{2\,(ads)} \rightarrow GaC_2H_{5\,(ads)} + C_2H_{5\,(ads)} \tag{1.3}$$

At each step, TEGa, DEGa, MEGa, or free ethyl species may evolve ethylene (C_2H_4, also referred to as ethene) via β-hydride elimination (Fig. 1.8), as in reaction (1.4) for the case of a free ethyl.

$$C_2H_{5\,(ads)} \rightarrow C_2H_{4\,(g)} + H_{\,(ads)} \qquad (1.4)$$

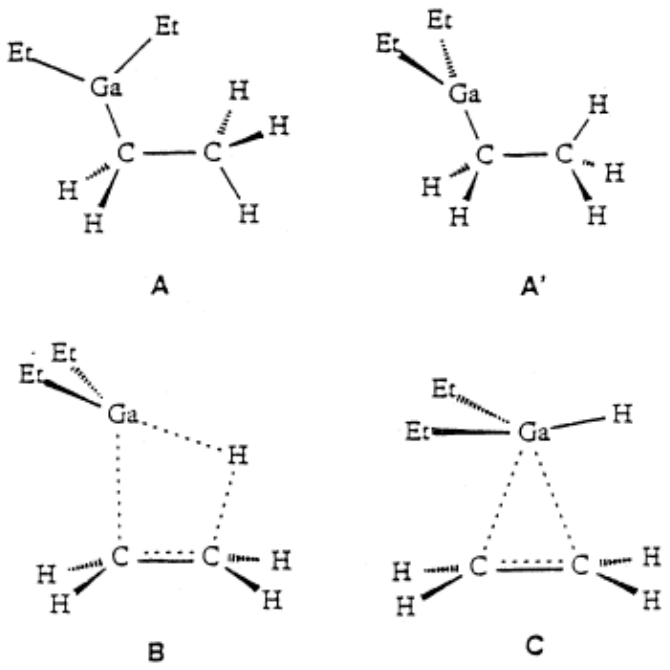

Fig. 1.8. β-hydride elimination process for TEGa [23].

Despite the possible formation of stable species (*e.g.* ethylene, methane, etc.), the step-wise dissociation of reactions (1.2) and (1.3) may result in significant atomic site-blocking by an alkyl surface population. Increasing T_s to enhance the desorption of site blocking species similarly increases DEGa desorption, reducing the effective surface Ga ($J_{eff,Ga}$) and consequently reducing the GR under Ga-limited growth conditions [18,24]. For the growth of ternaries, mixed alkyl species and mixed cations further complicate the growth process. For example, surface coverage by Al during AlGaAs growth has been shown to suppress DEGa and ethylene desorption, while In has demonstrated the opposite effect during InGaAs growth [25]. As shown in Fig. 1.9(a), increasing In coverage reduces the required T_s for DEGa desorption, and effectively increases DEGa

desorption for a given T_s. Similarly, Fig. 1.9(b) shows that increasing In coverage enhances surface liberation of ethylene species, promoting InGaAs growth at lower T_s by uncovering surface sites.

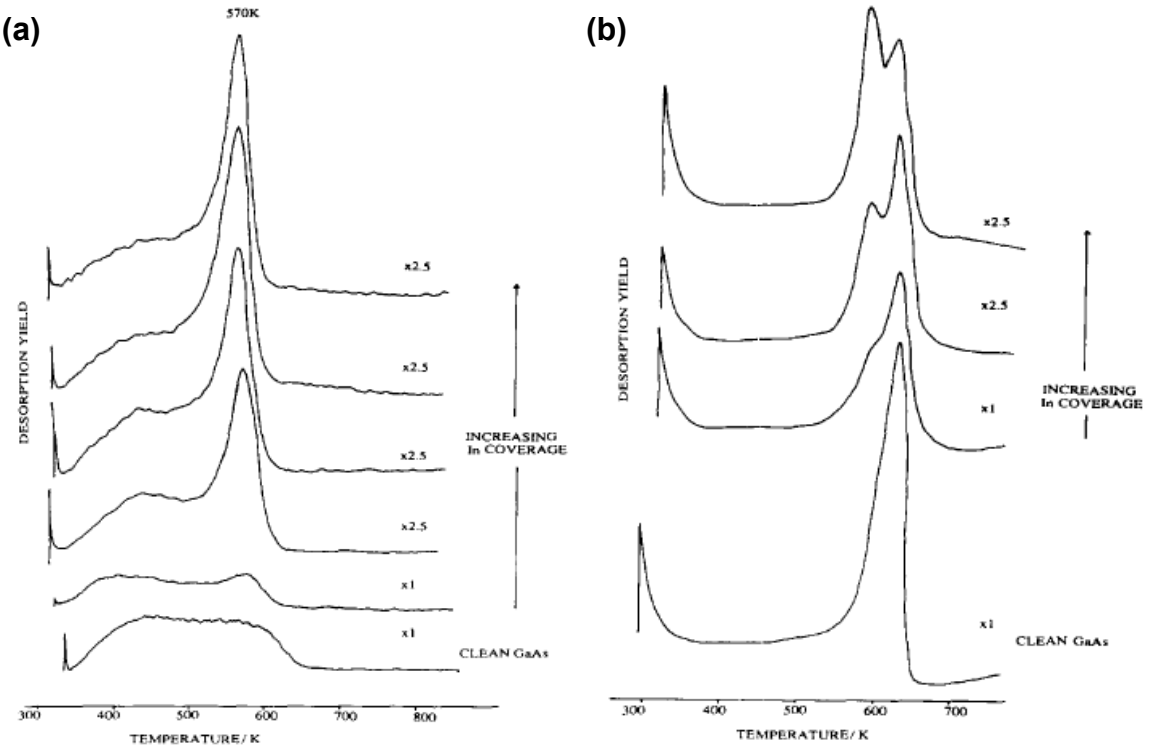

Fig. 1.9. Thermal desorption spectra of (a) DEGa and (b) ethylene with increasing In coverage [25].

Alternatively, dissociating species (*i.e.* TEGa, DEGa, MEGa, or free alkyl) may adsorb and become buried in the growing film. In the case of methyl species on the GaAs surface, the step-wise loss of hydrogen from the methyl center competes with methyl desorption [26]. As hydrogen loss occurs, increasingly strong surface-bonded methylene (CH_2) and CH species result in irreversible C incorporation in the absence of hydrogenation. For ethyl and isopropyl species, cleavage of the α-β bond (bond between metal bonded carbon and subsequent carbon) results in the analogous case, which may

compete with β-hydride elimination and effectively increase the carbon concentration in the film [4]. Such high C incorporation features of MOMBE have produced GaAs with *p*-type doping levels up to 5×10^{20} cm^{-3} ([C] ~ hole concentration) [27] that have been utilized in high performance heterojunction bipolar transistors (HBTs) [28].

The sensitive surface catalyzed reactions which govern the MOMBE growth process present unique opportunities over MBE or MOCVD to achieve selective epitaxy [4] without the use of static masks, but through means such as localized energy transfer via direct photo-desorption [29,30]. However, despite the conceptual versatility of MOMBE compared to MOCVD and MBE, the demonstrated SSG capability of MOMBE for arsenide [31], phosphide [31], and antimonide [32] based structures, and the possibility for novel photo-induced manipulation of the MOMBE growth process, the growth of III-Nitrides by NH_3-based MOMBE has received little attention. This middle ground between MOCVD and MBE is virtually unexplored for the growth of III-Nitrides with only a handful of reports regarding GaN by NH_3-based MOMBE in the literature [33-38] and no known reports of InGaN, AlGaN or intentionally doped GaN by NH_3-based MOMBE available before the work of this thesis.

1.3 The III-Nitride system

GaN is a wide bandgap semiconductor, exhibiting a direct 3.44 eV transition at 300 K for the wurtzite polytype. A less common zincblende structure exists, exhibiting a

0.2 eV narrower bandgap. III-Nitride alloys span a bandgap (E_g) range of ~0.65 to 6.13 eV corresponding to pure InN and AlN respectively. This bandgap relationship can be expressed as a composition-weighted average of binaries A and B given in (1.5), where x represents the fraction of binary B and b represents the bowing parameter accounting for the non-linear bandgap interpolation [39].

$$E_g = (1-x)E_{g,A} + xE_{g,B} - x(1-x)b \quad (1.5)$$

Assuming bowing of 1.43 [40] and 1.33 eV [41] yields bandgap expressions (1.6) and (1.7) for InGaN and AlGaN respectively.

$$E_g(In_xGa_{1-x}N) = 3.44 - 4.17x + 1.43x^2 \quad (1.6)$$

$$E_g(Al_xGa_{1-x}N) = 3.44 + 1.36x + 1.33x^2 \quad (1.7)$$

The exceptional direct bandgap range from ~0.65 to 6.13 eV allows only a single material system to realize efficient emitters and detectors from the near IR to UV spectral range (Fig. 1.10). High quality InGaN/GaN multiple quantum well (MQW) blue (λ = 460 nm) LEDs have been demonstrated with external quantum efficiency (EQE, η_{ext}) of 47% (P_{out} = 25.5 mW at I_F = 20 mA and 3.1 V). Short wavelength UV LEDs have been demonstrated utilizing AlGaN/GaN MQWs – examples include emission at λ = 321 nm (P_{out} = 0.2 mW at I_F = 20 mA and 4.1 V) [42] and λ = 265 nm (I_F = 50 mA and 10 V, $Al_{0.49}Ga_{0.51}N/Al_{0.58}Ga_{0.42}N$ MQW) [43]. AlN UV LEDs have demonstrated emission as short as λ = 210 nm (P_{out} = 0.02 μW at I_F = 40 mA, η_{ext} ~10^{-6}% *vs.* ~10% for commercial visible LEDs) [44]. Violet (λ = 405 nm) InGaN/GaN MQW laser diodes (LDs) are also commercially available with P_{out} = 30 mW and an estimated lifetime of 15,000 h at 60°C [45]. LDs emitting as short as λ ~ 343 nm has been reported [42]. As a

result, III-Nitride based visible LEDs are being utilized in robust traffic signals, full-color displays, and white lighting. III-Nitride based UV LEDs and LDs are being utilized in high-density optical storage systems, biological agent detection, communications, and water purification.

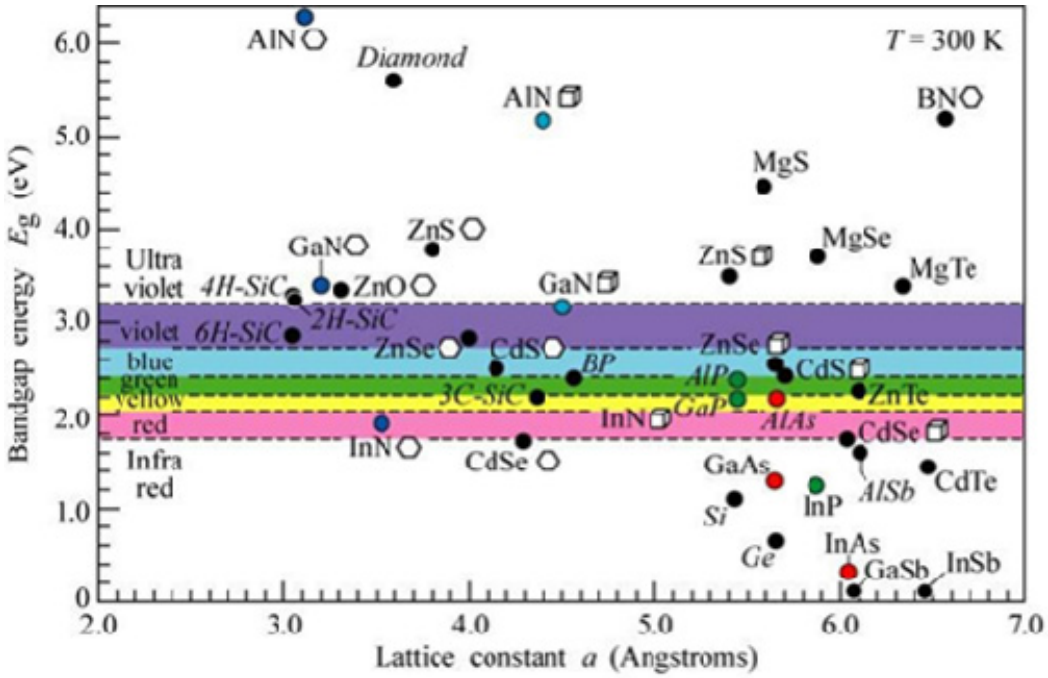

Fig. 1.10. Energy bandgap with corresponding spectral range vs. lattice constant of wurtzite III-Nitrides and common semiconductors (300 K) [46]. The bandgap of InN is shown as previously accepted 1.9 eV, but it has been reported recently as ~0.65 eV [47].

Wurtzite III-Nitrides have a polar axis, such that the bonds in the [0001] direction are all faced by N in one direction and the cation (*i.e.* Ga, Al, or In) in the opposite direction. In the Ga-face/Ga-polar structure, bonds along the [0001] direction are from Ga to N (Fig. 1.11). This results in an internal electric field in the [0001] direction and spontaneous polarization in the opposite direction. Conversely, the $[000\bar{1}]$ direction is the N-face/N-polar structure, with c-axis bonds from N to Ga. The polarity is

independent of the surface termination, and the polarity can drastically affect bulk and surface properties [48,49]. The effects of the macroscopic (spontaneous and piezoelectric) polarization field on the band edges from Stark and Franz-Keldysh effects significantly affects III-Nitride optical properties including effective bandgap, recombination probability of electron hole pairs, and electron or hole interface accumulation [50].

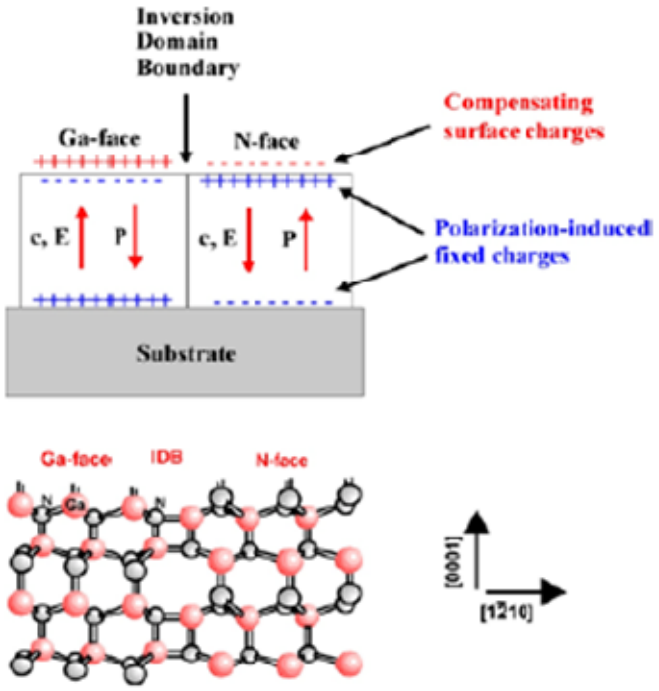

Fig. 1.11. Macroscopic polarization **P**, corresponding electric field **E**, and induced terminating interface charges for Ga- and N-face GaN [51].

Table 1.1 summarizes some attractive properties of III-Nitrides compared to traditional Si and GaAs semiconductors. ***A one-order greater breakdown electric field compared to Si and GaAs, low intrinsic carrier concentration, and good thermal conductivity is desirable for high power and high temperature (harsh environment) electronics [52]. The strong macroscopic polarization is a decade greater than***

conventional semiconductors and can easily generate a 2×10^{13} cm^{-2} sheet carrier density in an AlGaN/GaN two-dimensional electron gas (2DEG) [53] (Fig. 1.12). AlGaN/GaN HEMTs have demonstrated one-order greater power density and higher efficiency over existing Si and GaAs based technologies. Thus, GaN-based devices can be 10 times smaller for the same output power [54]. Continuous wave (CW) power density up to 32.2 W/mm at 4 GHz has been demonstrated [55]. Furthermore, good transport properties of GaN – including a saturated electron velocity up to double that of Si and GaAs – are useful for high frequency electronics. AlGaN/GaN HEMTs with current gain cutoff frequency (f_T) of 81 GHz and maximum oscillation frequency (f_{max}) of 187 GHz have been demonstrated [56].

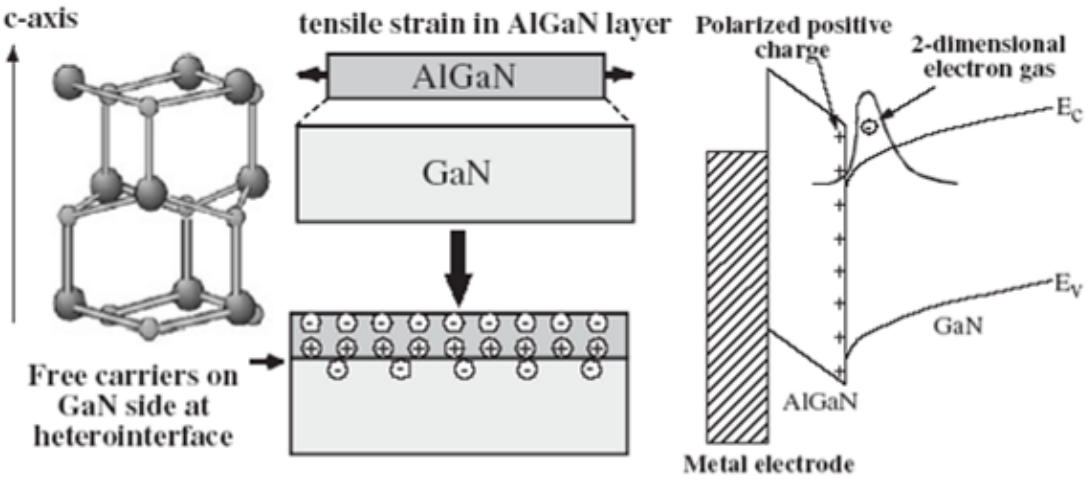

Fig. 1.12. AlGaN/GaN heterostructure and band diagram. Free carriers accumulate at the interface due to the piezoelectric effect [57].

Table 1.1. Properties of wurtzite InN, GaN, and AlN and traditional semiconductors Si and GaAs [47,58-62].

Parameter	InN	GaN	AlN	GaAs	Si
bandgap, E_g(300 K) (eV)	0.65	3.44	6.13	1.424	1.124
lattice parameter, a/c (300 K) (Å)	3.537 5.704	3.190 5.189	3.111 4.979	5.654	5.431
intrinsic carriers, n_i (300 K) (cm^{-3})	1×10^{13}	1.9×10^{-10}	1×10^{-31}	2.1×10^{6}	1×10^{10}
electron mobility, μ_n ($cm^2/V\cdot s$)	3000	1200	1100	≤ 9000	≤ 1450
hole mobility, μ_p ($cm^2/V\cdot s$)	39	10	14	≤ 400	≤ 505
saturated electron drift velocity, v_{sat} ($\times10^7$ cm/s)	2.5	2.5	1.8	2.0	1.0
thermal conductivity, κ (W/cm·K)	0.45	1.3	3.19	0.455	1.56
breakdown electric field, E_c (MV/cm)	1	3.3	11.7	0.4	0.3
dielectric constant, ε	9.6	9.5	8.7	12.8	11.9
refractive index, n	2.56	2.29	2.2	3.255	3.42

1.4 III-Nitride growth challenges

GaN has been most studied of the III-Nitrides, with the first powders synthesized in 1932 by reacting metallic Ga with NH_3 at 900-1000°C [63]. The lack of a substrate necessitates heteroepitaxy, typically on sapphire (Al_2O_3) because of high thermal stability and similar expansion coefficient [64] despite a large 16% lattice mismatch. The highly mismatch system results in a 10^7 - 10^{11} cm^{-2} dislocation density (versus 10^3 - 10^4 cm^{-2} for GaAs while Si is essentially dislocation free) which can reduce radiative recombination

efficiency with extended defects and increased piezoelectric polarization. In 1986, a thin AlN buffer layer [65] was employed, reducing the lattice mismatch to 13% and subsequently improving crystalline quality and reducing the electron concentration (n) from 10^{19} to 10^{17} cm^{-3} [66]. The introduction of a low temperature GaN buffer layer in 1991 further reduced n to 4×10^{16} cm^{-3} (300 K) [67]. The insertion of a sapphire nitridation layer (*i.e.* substrate anion exchange with N) before the AlN buffer layer has demonstrated further improvement in material quality by reducing the dislocation density to 4×10^{8} cm^{-2} [68]. The proper preparation of these buffer layers has been shown to suppress the formation of hexagonal facets as well as affect the film polarity [69], which significantly affects subsequent electrical and optical properties.

Alloying of III-Nitrides is dominated by the cohesive energy per bond for substrate temperatures (T_s) below that of significant decomposition [70], demonstrated as 630, 850, and 1040 °C in vacuum for InN, GaN, and AlN respectively [71]. Thus, if only considering contributing atomic species at the growth interface – ignoring hydrocarbon ligand adsorption and desorption, gas phase depletion, and similar considerations of MOCVD and possible MOMBE conditions – the more weakly bound cation is displaced under III-rich growth conditions. For wurtzite AlN, GaN, and InN, the cohesive energy per bond is 2.88, 2.2, and 1.93 eV respectively [72] meaning that Al will preferentially incorporate over Ga and similarly Ga over In.

Stoichiometric AlN powders were first synthesized in 1964 using AlF_3 and NH_3 [73]. The $Al_xGa_{1-x}N$ system exhibits complete solubility at T_s > 600 °C [74], hence the entire composition range has been demonstrated and is typically deposited at T_s ~ 1050-1150 °C for MOCVD [75] and T_s ~ 700-900 °C for MBE.

While InN powders were first synthesized in 1938 using $InF_6(NH_4)_3$ [76], the growth of $In_xGa_{1-x}N$ alloys remains challenging. The equilibrium vapor pressure of N_2 over InN is several orders of magnitude greater than that of AlN and GaN (Fig. 1.13) [77], resulting in indium re-evaporation for $T_s > 540$ °C (vs. 710 °C for Ga) [78]. This necessitates high nitrogen pressure and low T_s to prevent dissociation of the weak In-N bond. However, $T_s < 540$ °C which enables sufficient InN incorporation in the alloy significantly compromises adatom surface diffusion and crystallinity in MOCVD and MOMBE. Moreover, the large interatomic spacing difference between GaN and InN yields a solid phase immiscibility gap resulting in phase separation (spinodal decomposition) [79,80].

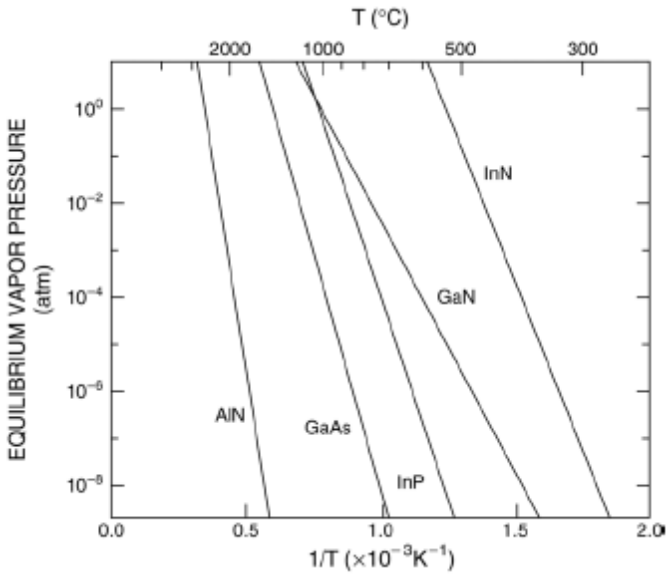

Fig. 1.13. Equilibrium vapor pressure of N_2 over AlN, GaN, and InN as well as the sum of $As_2 + As_4$ over GaAs and $P_2 + P_4$ over InP [77].

Significant challenges in the growth of III-Nitrides yield films with high defect density that subsequently limits device performance. Defects include native isolated

defects (vacancies, interstitials, and antisites), impurities, and combination complexes. Fig. 1.14 shows radiative transitions of various intentional and native GaN defects. A shallow donor level at E_c - 29.5 meV caused by O donors (O_N) is suspected to be the origin of high background n in GaN [81,82]. N vacancies (V_N) have also been suspected as the origin. Si_{Ga} (Ga substitution by Si) introduces a shallow donor at E_c - 20 meV. The comparable sizes of Si and Ga result in a stable substitution. As such, Si_{Ga} is an effective dopant for controlling n-type conductivity in III-Nitrides [81]. Mg_{Ga} (Ga substitution by Mg) is the most successful p-type dopant in GaN, despite a deep acceptor level at E_v + 200 meV. Hole concentration $p \sim 4.5 \times 10^{18}$ cm^{-3} in GaN has been achieved by RF-plasma assisted MBE [83]. Additionally, a broad transition centered at 2.2 eV (yellow) is commonly observed. This yellow luminescence (YL) is suspected to arise from a shallow donor-deep acceptor transition attributed to V_{Ga} [82].

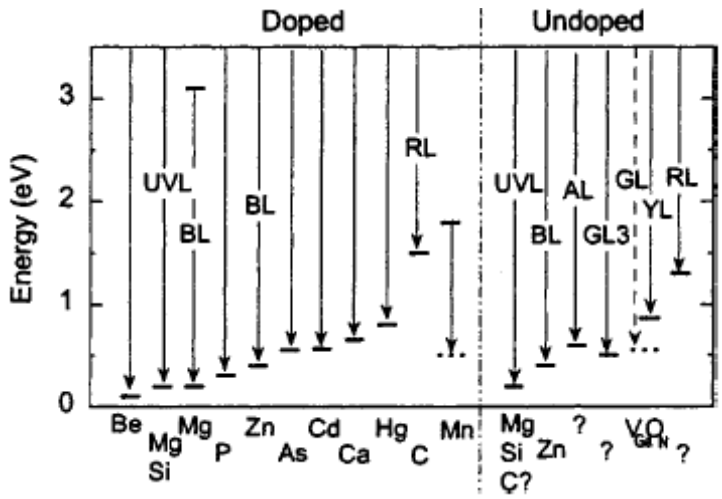

Fig. 1.14. Radiative transitions of various observed GaN defects [84].

Progress in addressing the growth challenges of III-Nitrides and subsequent successes in diverse III-Nitride devices has prompted significant investment in advanced III-Nitride research. Key milestones are summarized in Fig. 1.15.

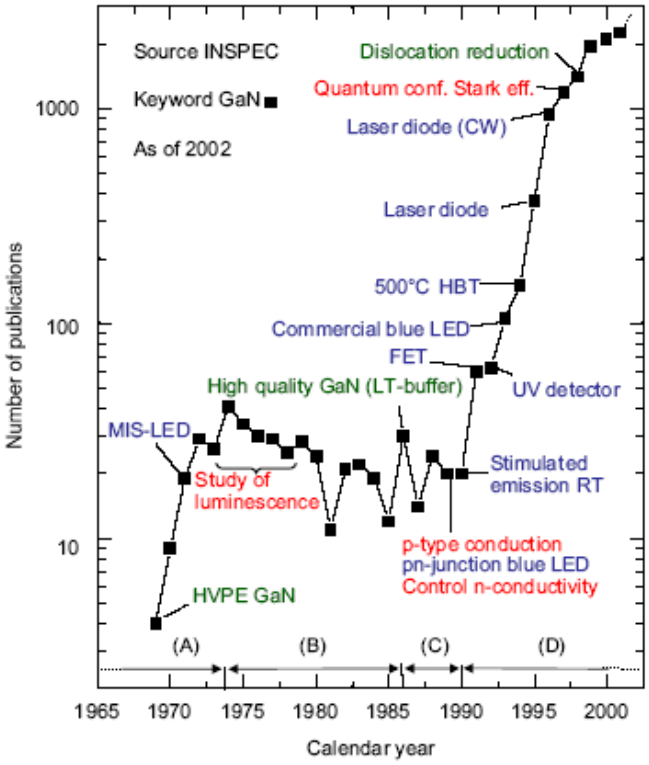

Fig. 1.15. Key III-Nitride publications (indexed by INSPEC) with major crystal growth (green), conductivity control and physics (red), and device (blue) achievements [85].

1.5 Applications and considerations of 3DE

The fundamental vision of 3DE is to free device designs from the constraints imposed by traditional device fabrication techniques – shifting the design paradigm toward "natural" 3D devices (no interface contamination or post-growth process-induced

damage) and "naturally" integrated systems. However, the applications of 3DE that are presented in this section are given solely to clarify the concept of 3DE and to show how 3DE could be leveraged to mitigate traditional fabrication steps.

First, 3DE can be leveraged as a method to define buried sacrificial regions for nano-/micro-electromechanical systems (N/MEMS). An example is for a GaN microfluidic channel shown in Fig. 1.17. In order to form the channel with traditional technology, it is necessary to utilize difficult and problematic masking techniques during photo-electrochemical (PEC) etching or to deposit, pattern, and re-redeposit layers. In this example, the microfluidic channel is formed via dopant selective PEC etching of sacrificial *n*-GaN layers to undercut *p*-GaN layers (Fig. 1.16(d)) [86] (similarly, the structure could be formed using composition/bandgap selective etching of dissimilar bandgap materials such as GaN and InGaN). In standard PEC etching, etching is achieved by irradiating the layer with above bandgap radiation during immersion in an aqueous KOH solution. It is believed that the band-bending at the *n*-GaN/electrolyte interface causes photo-generated holes to be swept toward the surface, chemically dissociating the semiconductor. For GaN, the etching mechanism is postulated to occur through the reaction (1.8):

$$6GaN + 6h^{+} \rightarrow 2Ga^{3+} + N_2 \qquad (1.8)$$

A comprehensive review of PEC and contactless etching can be found in [87]. 3DE could dramatically simplify this fabrication process by dynamically defining the sacrificial regions *during* film deposition. The defined sacrificial regions could then be etched *ex situ* to form the air-gaps/channels.

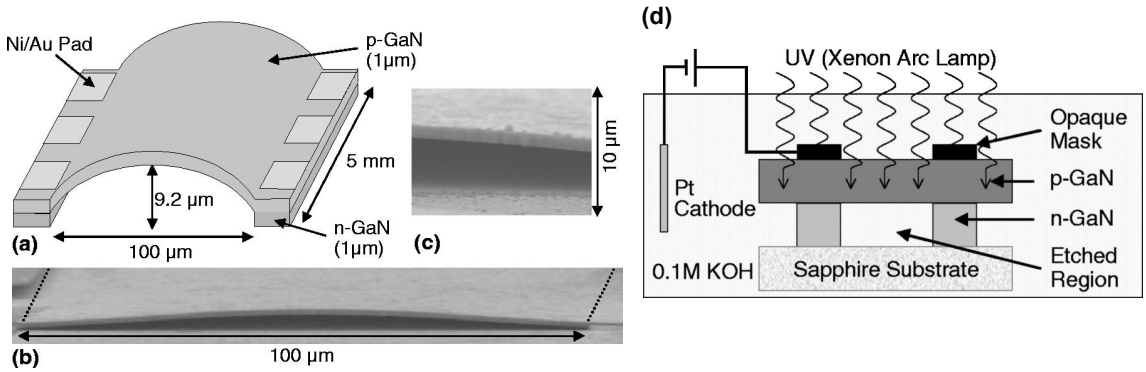

Fig. 1.16. A GaN microfluidic channel. The (a) schematic of device structure and (b) SEM of the side of the bowed and undercut p-GaN membrane. The dashed lines indicate the sidewalls of the channel. (c) is the 1 μm suspended p-type membrane. (d) is the etch process. All from [86].

A fundamental strength of 3DE is its dynamic capability – not only can regions be defined within a layer, but also temporally as growth proceeds. Hence, sacrificial regions are not limited by a patterning via static mask in a single plane, but the regions can be defined in 3D. An application of this capability is for resonator structures (Fig. 1.17). More detail on the theory, fabrication, and application of resonant structures for ultra-fast sensors and actuators and RF filters can be found in [88,89]. As shown in Fig. 1.18, free-standing resonant structures are typically created by a pattern transfer and subsequent etching of sacrificial layers. 3DE would enable a fabrication process that is dramatically more streamlined by defining 3D sacrificial regions and depositing both sacrificial and non-sacrificial materials simultaneously. Specifically in Fig. 1.18, 3DE could merge steps (i) and (ii) into a single step. Here, the advantage of 3DE is leveraging the ability to dynamically define 3D sacrificial regions rather than sacrificial layers (the "alternative techniques/lateral growth" case of Fig. 1.18 could require substrate pre-patterning which is not explicitly counted as a step). Furthermore, 3DE may be the only efficient mechanism to eliminate interface contamination or etching damage if multiple deposition-lithography-processing sequences are necessary. Moreover, the dynamic

patterning capability of 3DE could enable monolithic integration of such devices since the devices could be integrated three-dimensionally (*i.e.* devices could be both adjacent and vertical – both in placement or operation).

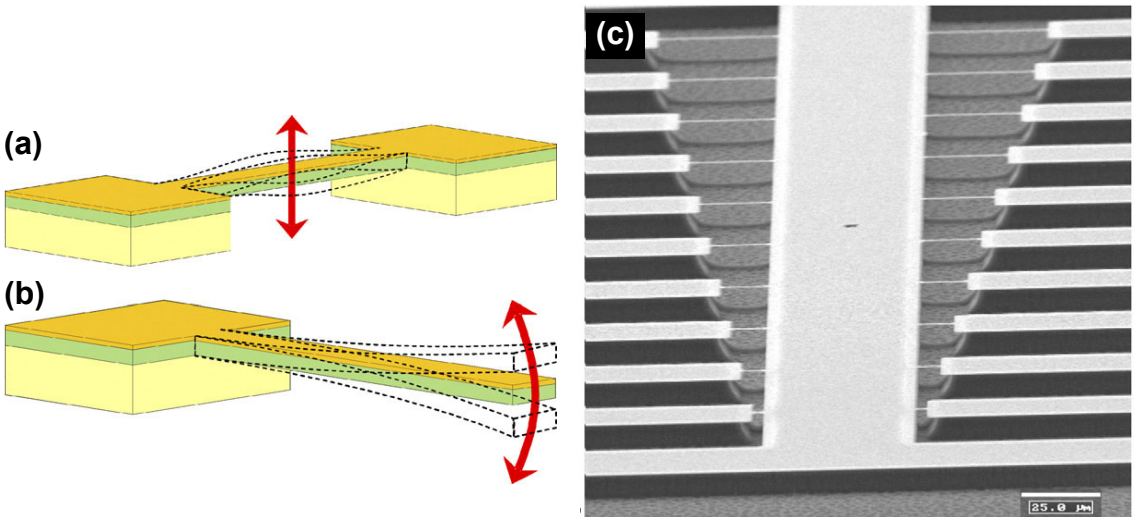

Fig. 1.17. Basic (a) doubly clamped and (b) singly clamped beam configurations of resonant structures. (c) SEM images of resonant beams with 0.5 – 0.8 μm width and 5 – 500 μm length. All from [88].

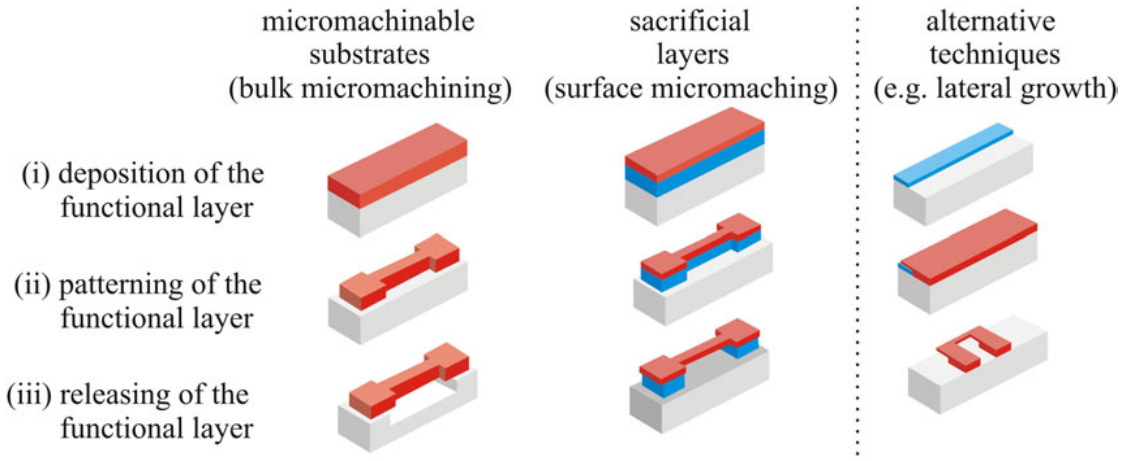

Fig. 1.18. Strategies for the fabrication of free standing resonant beams for N/MEMS applications [89].

Additionally, 3DE could be leveraged to create laterally distributed devices. For example, laterally distributed blue and green MQW LEDs created through traditional techniques have been recently demonstrated for use as phosphor-free white LEDs with stable emission under high injection currents (Fig. 1.19) [90]. Traditional vertically distributed multi-color MQW LEDs suffer from color instability which is believed to arise from non-uniform injection of carriers into the MQWs since the MQWs are connected in series (vertically) [91]. For this application, 3DE could possibly consolidate steps (1) – (5) of Fig. 1.19 such that the laterally distributed MQWs are deposited simultaneously – eliminating the need for mask deposition, patterning, etching, and regrowth. Moreover, 3DE could enable additional colors to be integrated with marginal impact on deposition and processing effort (*i.e.* only software parameters would need to be adjusted for the micromirror-based 3DE approach demonstrated in Chapter 5, affecting the pattern and the modulation duty cycle of the mirrors).

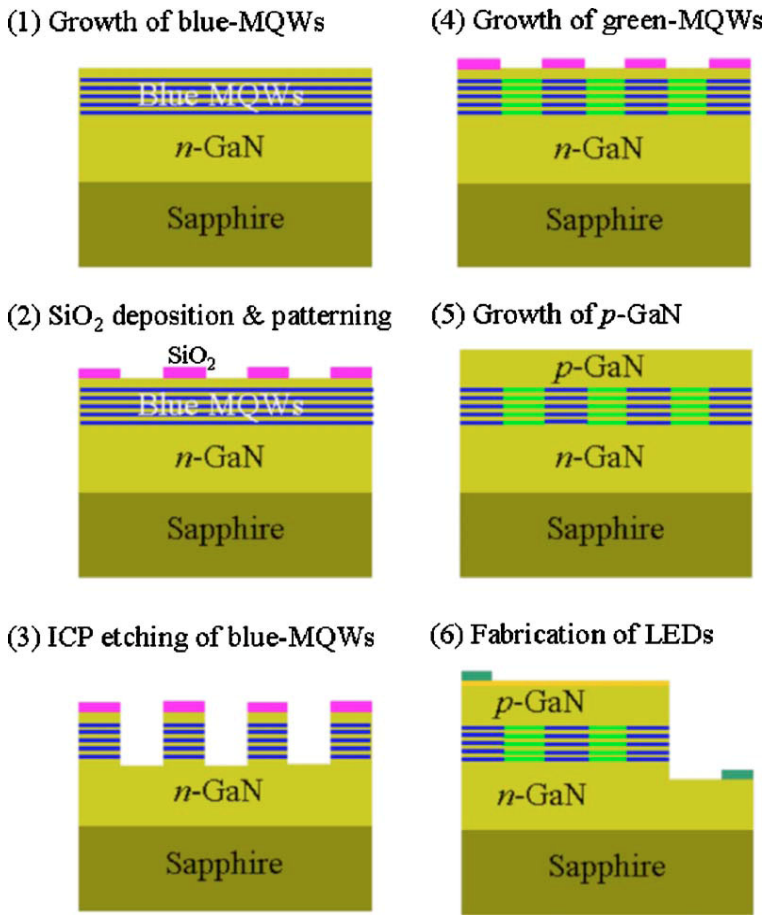

Fig. 1.19. Fabrication flow for dual color, laterally distributed MQW LED [90].

The application of 3DE extends beyond being an alternative to traditional device fabrication processes. ***The complex 3D material property variations that could be patterned by 3DE during growth – such as electronic, optical, and mechanical properties – may usher in a new era of device design in 3D that is no longer constrained by the expensive and time-consuming framework of growth, processing, and regrowth sequences.*** However, 3DE does have fundamental limitations. The novel pathway to 3DE described in this thesis is achieved using UV irradiation during thin film deposition. As such, the ultimate resolution of epitaxial patterns in the growth plane is

diffraction limited (*i.e.* the smallest feature size achievable based on the Rayleigh criterion is on the order of the optical wavelength λ used for patterning – in this work λ = 172, 325, and 365 nm). As such, the pathway for 3DE described herein is better suited for devices which require any small features (feature size < λ) to be along the growth axis. For example, thin HBT base layers and thin MQW layers must be vertically defined by deposition thickness (rather than lateral patterning). However, 3DE could be leveraged to define the size or material composition of such HBT and LED structures. An additional limitation is that simultaneous patterning during growth of both composition and dopant concentration may be mutually exclusive.

1.6 Problem statement

While 3DE is certainly a fascinating concept for enabling future-generation structures and photo-assisted MOMBE is a promising vehicle for enabling 3DE, significant challenges exist in applying these ideas toward a diverse and topical material system, such as the III-Nitrides. The objective of this work is to pioneer NH_3-based MOMBE and leverage novel UV photoexcitation effects during the epitaxy of III-Nitride films in order to realize a pathway toward 3DE. The research presented in this thesis identifies and addresses challenges in the growth of III-Nitrides by NH_3-based MOMBE and details the manipulation of III-Nitride growth using UV photoexcitation. Specifically, this thesis is organized as follows:

- Chapter 2 describes the novel photo-assisted NH_3-based MOMBE growth system that was developed for this work.

- Chapter 3 describes the growth of GaN by NH_3-based MOMBE and the effectiveness of UV photoexcitation for the liberation of hydrocarbon species from the growth interface, subsequently reducing the incorporation of carbon into GaN and providing a mechanism for 3DE of GaN in regards to carbon dopant concentration.

- Chapter 4 describes the growth of InGaN by NH_3-based MOMBE and identifies unique mechanisms which could be locally excited by UV photoexcitation to yield intentional variations in InGaN alloy composition useful for 3DE.

- Chapter 5 describes the lateral compositional pattering of InGaN during NH_3-based MOMBE by digital micromirror patterning of UV photoexcitation, demonstrating the possibility of 3DE of InGaN by UV-assisted MOMBE.

- Chapter 6 describes that the photo-excited In/In-methyl desorption phenomena which enables a pathway toward 3DE of InGaN by UV-assisted MOMBE is dominated by a photochemical mechanism rather than a photothermal mechanism.

- Chapter 7 describes the improvement in GaN and InGaN films grown by NH_3-based MOMBE as a result of an improved understanding of the growth regimes necessary to effectively dope III-Nitride films.

- Chapter 8 describes the growth of Mg-doped GaN by NH_3-based MOMBE and the effect of UV photoexcitation of dramatically increased irradiance (improved focus) on the subsequent GaN dopant concentration and properties.

- Chapter 9 summarizes the accomplishments of this work and presents possible directions and considerations for future work.

CHAPTER 2: CUSTOM UV-ASSISTED, NH_3-BASED MOMBE SYSTEM

2.1 Introduction

III-Nitride films are grown in a custom, two chamber reactor developed specifically to enable novel UV-assisted MOMBE. The two chambers of the reactor and various associated components are shown in Fig. 2.1 and Fig. 2.2. A custom growth system was necessary to allow NH_3-based MOMBE of III-Nitrides and to allow UV radiation to be incident on the sample during growth (for 3DE). The construction of the growth system was completed for this thesis and was highly customized during this work. Once a sample is loaded into the growth chamber of the reactor, a custom growth automation and data collection system controls the entire growth process to maximize growth precision and consistency. This automated control system was designed and developed wholly during this work and is described in Appendix B.

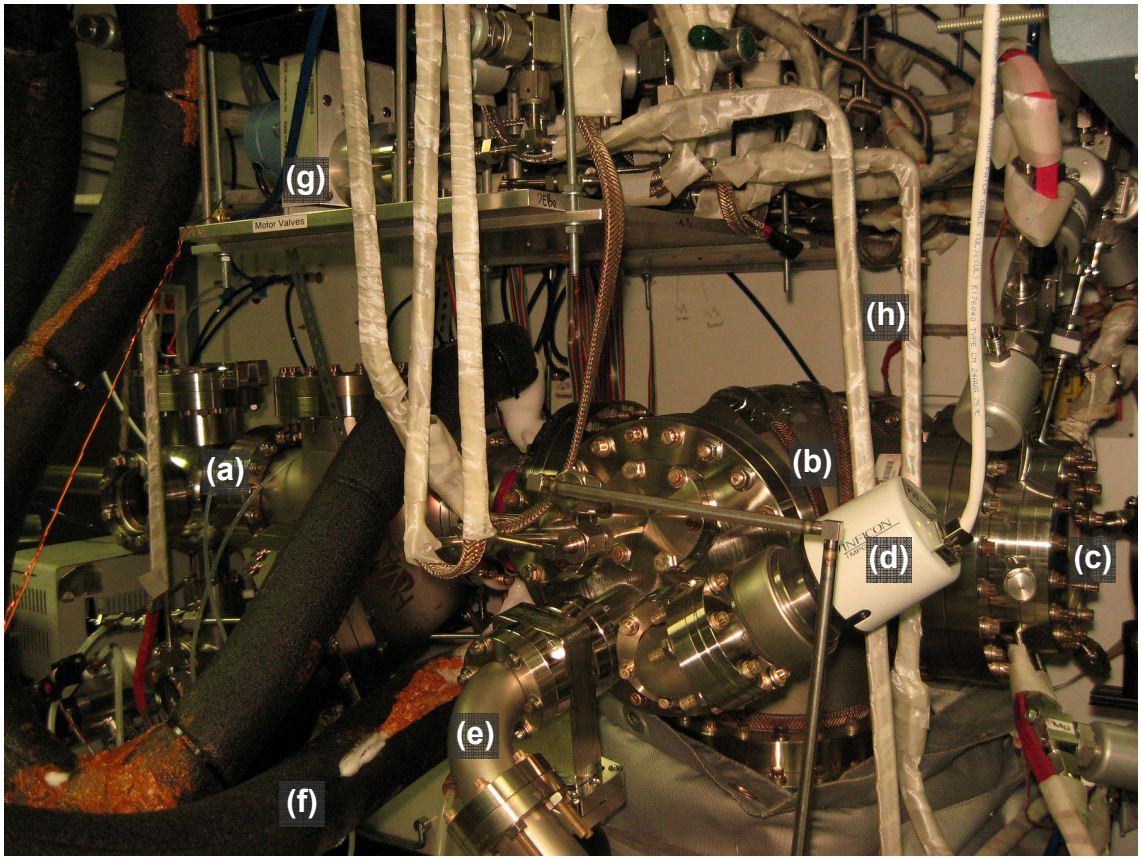

Fig. 2.1. The custom MOMBE reactor. The reactor consists of an (a) introduction chamber and (b) growth chamber. Some other visible components include the (c) growth chamber viewport and showerhead, (d) cold-cathode ion gauge, (e) elbow connecting the RGA, (f) LN_2 cryoshroud supply and return, (g) the motor valve of the custom PCVS for regulating the Be precursor, and (h) the Be and Mg heated precursor lines.

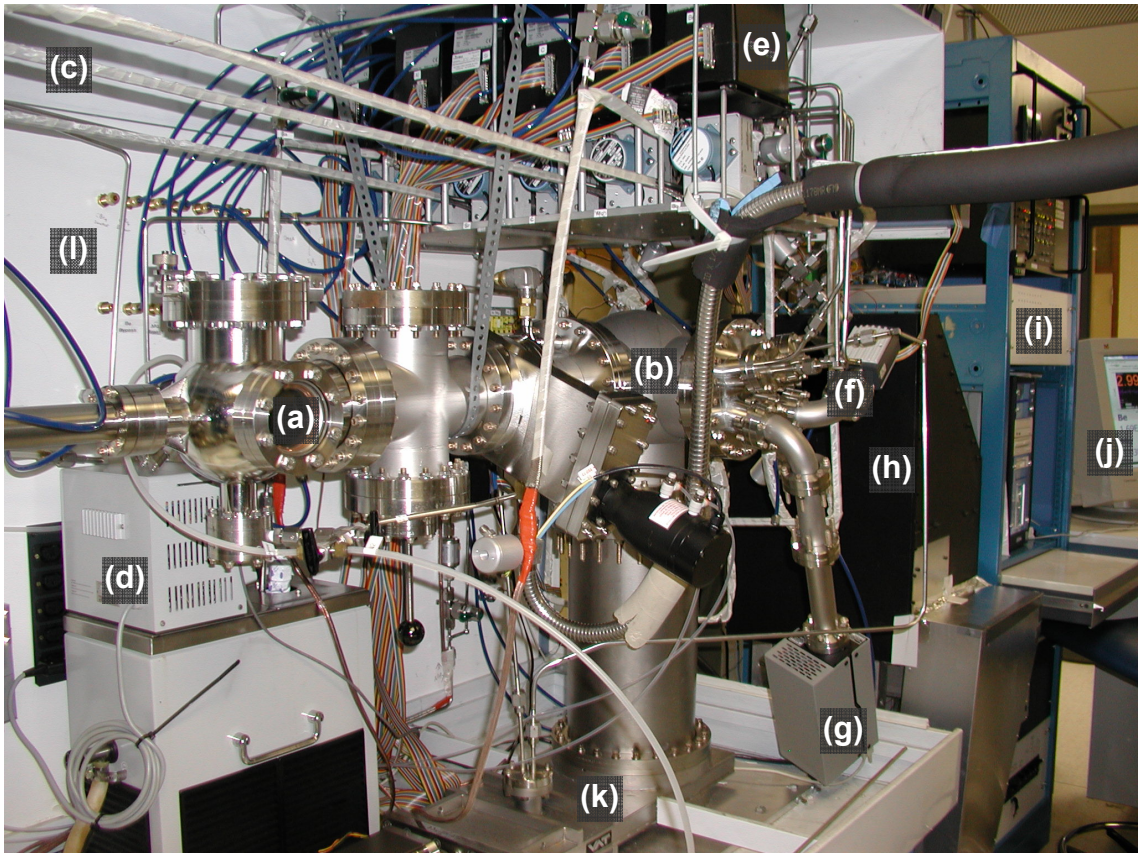

Fig. 2.2. The custom MOMBE reactor near the completion of construction (06/2004). Notable visible components include the (a) introduction chamber viewport, (b) growth chamber, (c) Al, In, and Mg precursor heated delivery tubing, (d) TEGa bubbler bath, (e) PCVS manometers and motor valves, growth chamber (f) ion gauge and (g) RGA, (h) Hg-Xe arc lamp apparatus, (i) instrumentation rack, and (j) control interface. The UHV pump of the growth chamber is below the gate valve (k). Various control pneumatics are also visible (l).

2.2 Novel removable substrate heater

Substrates are loaded and heated in the reactor via a custom, removable substrate heater/block module referred to as the FISH (free idle substrate heater). The FISH is shown in Fig. 2.3 and is constructed mainly of molybdenum and titanium. The FISH integrates a type C thermocouple (TC) positioned at the center of the substrate backside

for T_s measurement. A total of four UHV electrical plugs (MDC Vacuum Products) mechanically support the FISH and provide TC and substrate heater connections for T_s control. The FISH remains stationary during growth (*i.e.* the substrate is "idle" in that it does not rotate so that incident 3DE patterns can be accurately transferred) and allows the growth surface to face towards a 4" UV-transparent viewport (Fig. 2.4) for novel UV-assisted growth.

A Eurotherm 2404 utilizing a proportional-integral-derivative (PID) control loop maintains T_s and mitigates substrate heating induced by the UV radiation sources. The PID controller is configured for automatic gain scheduling so that optimized PID control parameters are utilized for GaN growth (T_s > 550 °C) and InGaN growth (T_s = 430-560 °C).

Substrates are degassed at T_s ~ 150 °C under cryogenic pumping (1×10^{-8} Torr) in the introduction chamber (Fig. 2.5). Electrical connections for degassing samples are made to the rear of the UHV electrical plugs of the FISH while the FISH is loaded into the introduction chamber. Mechanical support of the FISH in the introduction chamber is provided by the transfer arm. The electrical connections for degassing fall from the rear of the FISH as the FISH is loaded into the growth chamber, where the front of the UHV plugs are utilized for electrical connection. This mechanism facilitates a simple technique to degas samples in the introductory chamber while utilizing only one substrate heater in the entire growth system. The mechanism also eliminates difficult transfer of the sample block module and results in no heated elements permanently mounted in vacuum. This latter design advance implies that vacuum would never have to be compromised for maintenance – a major limitation/expense of traditional MBE systems.

The complete loading/unloading process of the FISH is designed to minimize time. For instance, the transfer arm attaches to the FISH "backbone" with a coarse thread (Fig. 2.3(d)). The transfer arm is unscrewed once the FISH is mounted in the growth chamber using the four UHV plugs. If no degassing were performed, a trained operator can completely load and unload the FISH with ease in < 5 min, with no concern about losing expensive sample block modules and substrates in the reactor.

The unique design of the FISH – integrating a substrate heater that is routinely loaded and unloaded from the system with ease and speed – and the absence of in-vacuum sources in the growth system (all source precursor bottles can be replaced without breaking the UHV) allows a near zero system downtime (i.e. low maintenance cost/high throughput) with the exception of pumping and sensor systems maintenance.

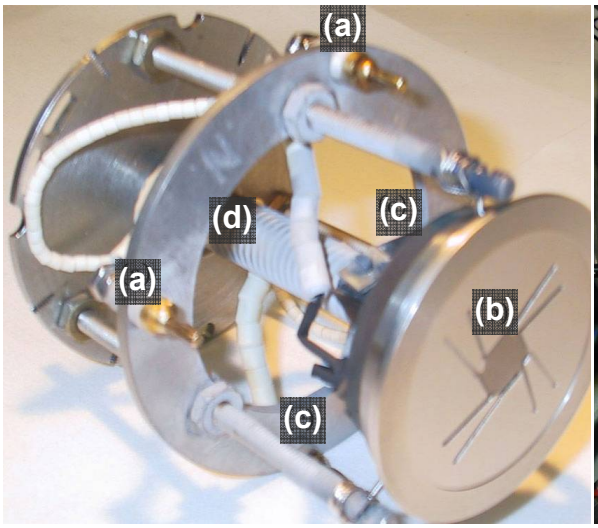

Fig. 2.3. FISH module for sample loading, mounting, and heating. Four UHV plugs mount the FISH, providing (a) TC and (c) substrate heater power. A (b) removable 2" block is mounted directly above the TC and heater. The TC is encapsulated in the FISH (d) "backbone" in order to connect to the UHV plugs from the TC junction positioned at the rear of the substrate.

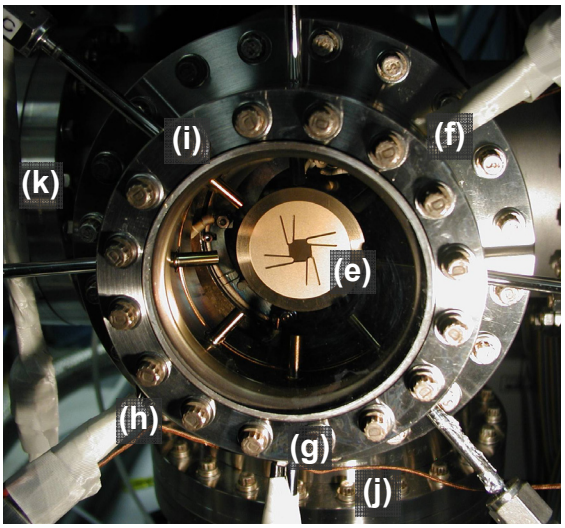

Fig. 2.4. The custom showerhead of the MOMBE growth chamber. The (e) FISH loaded inside the growth chamber faces toward the 4" UV transparent viewport. A LN_2 cryoshroud surrounds the FISH inside the chamber (not visible). Precursors are delivered in heated stainless steal tubing; the showerhead port for each precursor is labeled (f) TEGa, (g) NH_3, (h) Cp_2Mg, and (i) TMIn/TEI. The flanges for the (j) turbomolecular drag pump and (k) RGA and ion gauge.

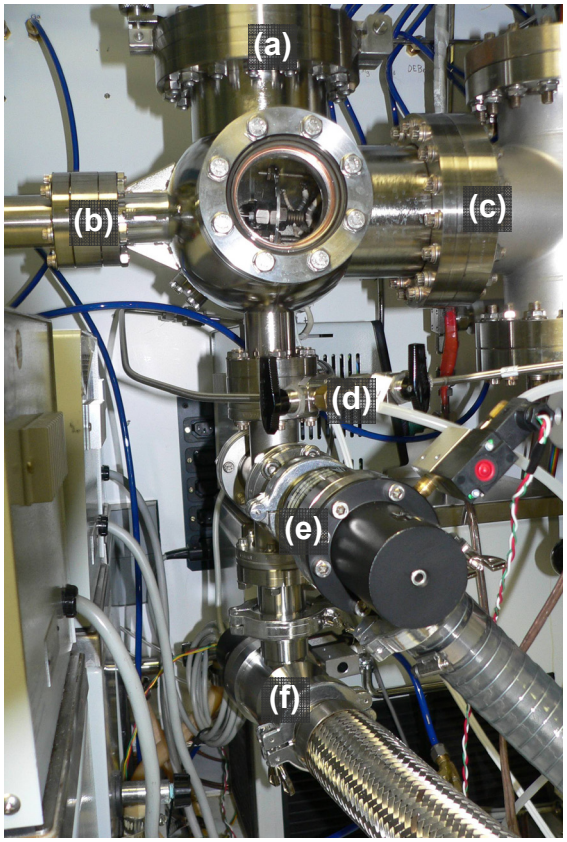

Fig. 2.5. The introduction chamber of the custom UV-assisted MOMBE reactor for loading and unloading of samples. The FISH module is loaded through port (a) and is moved throughout the system using the magnetic transfer arm attached to flange (b). The FISH module is visible through the chamber viewport. After outgassing the samples, the FISH is passed through (c) for loading into the growth chamber. Electrical connections to the FISH substrate heater that are disconnected without breaking vacuum are not visible. Separate valves provide necessary (d) N_2 purging/venting, (e) mechanical rough pumping, and (f) cryogenic pumping capabilities.

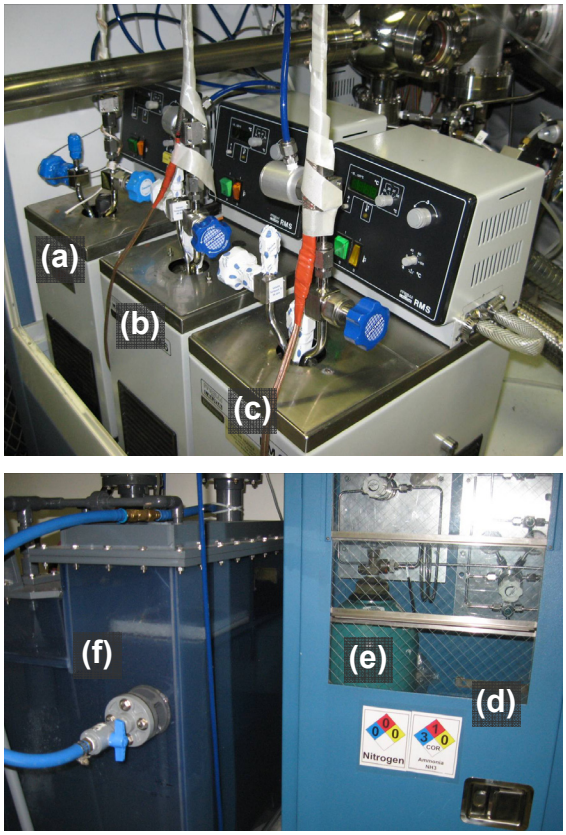

Fig. 2.6. Temperature controlled baths for (a) Al, (b) In, and (c) Mg precursors are located inside a custom fume hood which contains the entire reactor (other baths are not visible). The (d) NH_3 and (e) ultra high purity N_2 purge source are stored in gas cabinets. The exhaust of the vacuum pumps is passed through the (f) scrubber.

2.3 Vacuum system and hazardous gas delivery system

The high vacuum growth chamber is pumped with a magnetic bearing, corrosive-resistant turbomolecular drag pump (Pfeiffer Vacuum TMU1000M backed by an Edwards QDP40 dry pump) and a liquid nitrogen (LN_2) cryoshroud. The base pressure, P_b is ~3×10^{-9} Torr. In Chapter 3, the growth chamber is pumped with a cryogenic pump rather than a turbomolecular drag pump. The typical chamber pressure during III-Nitride growth is $P_{ch} \sim 5 \times 10^{-6} - 5 \times 10^{-5}$ Torr. All gasses exit the system through a dry rotary-vane pump (Edwards QDP40) the exhaust of which is plumbed directly into a hazardous gas scrubber before exhausting to atmosphere (Fig. 2.6(f)). The LN_2 cryoshroud is defrosted every night in order to purge the visible accumulation of condensate on the cryoshroud (P_{ch} may momentarily be greater than 10 Torr during defrosting). Outside of defrosting the LN_2 cryoshroud or performing maintenance, if $P_{ch} > 1 \times 10^{-2}$ Torr, the custom computer control system (Appendix B) assumes a leak to the vacuum system is present and closes all pneumatic valves to prevent a leak of hazardous gases from the system (a fume hood is atop the system). Similarly, if $P_{ch} > 1 \times 10^{-4}$ Torr the computer control system automatically turns off the RGA filament to prevent filament burn-out.

Source precursors are delivered individually into the showerhead via 1/4" stainless steel tubing (Fig. 2.1 and Fig. 2.4). Each metal organic source bubbler is stored in individual temperature-controlled Lauda RMS6 baths (Fig. 2.6) so that their vapor pressure is compatible with the custom pressure controlled vapor source (PCVS) system discussed later. Typical bubbler bath temperatures and corresponding vapor pressures (VP) of TEGa, TMIn, and Cp_2Mg are given in Table 2.1. The vacuum environment

facilitates precursory delivery without carrier gasses. As such, carrier gasses are not used in order to minimize parasitic reactions and maximize growth selectivity. All precursor tubing is heated during growth by self-regulating heater cable (OMEGA SRM/E20-1C) maintained at ~80 °C to prevent precursor condensation during delivery. NH_3 is purified in-line and is regulated by a mass flow controller capable of flux control from 0-1000 sccm (Mykrolis FC2900M).

Table 2.1. Typical bath temperatures of TEGa, TMIn, and Cp_2Mg bubblers and corresponding vapor pressures.

precursor	T_{bath}	**VP(T_{bath})**
TEGa	5	2.03 Torr
TMIn	22	2.03 Torr
Cp_2Mg	23	0.36 Torr

The flow rate J of TEGa, TMIn, DMEAA/TEAl, Si_2H_6, and Cp_2Mg are each independently controlled by a custom PCVS system [92]. The custom system was implemented for each of these sources to maintain precise precursor flow control over a large dynamic range. With this system, each precursor is precisely leaked into the reactor through a dedicated 660 or 40 μm diameter orifice (304 stainless steel VCR blank, laser drilled by Lenox Laser, Glen Arm, MD). Assuming choked flow, J (Torr·L/s) across a circular orifice of conductance C_{eff} (L/s) is directly proportional to the upstream pressure P_{up} (Torr), and is given by (2.1).

$$J = C_{eff} P_{up} \tag{2.1}$$

J of each precursor is regulated by an independent PID control loop which continuously monitors the source line P_{up} (using a MKS Baratron 120 capacitance manometer 18”

upstream from the orifice) and adjusts an upstream motor valve (MKS 245) accordingly to maintain the proper P_{up} for the desired J. C_{eff} for the system is given by (2.2) as the conductance of the stainless steel delivery tube of inner diameter d_i (0.18 in) and length l (18 in) in series with an leak orifice of diameter d.

$$\frac{1}{C_{eff}} = \frac{1}{C_{tube}} + \frac{1}{C_{orifice}} = \frac{1}{12.1\left(\frac{d_i^{\,3}}{l}\right)} + \frac{1}{11.6\pi\left(\frac{d}{2}\right)^2} \tag{2.2}$$

The resultant J in sccm can be converted from Torr·L/s by correcting for cm^3/min at 760 Torr. For the reactor geometry described, the resultant J in sccm is $1.1883P_{up}$ and $0.012P_{up}$ for a P_{up} in Torr behind a 660 and 40 μm leak orifice respectively. For control of J_{TEGa} behind a 660 μm orifice, the PCVS system is capable of accurate and dynamic flux control from ~0.001 – 1 sccm.

2.4 UV irradiation apparatus

UV radiation is incident on the sample during growth through an easily removable 6” ConFlat viewport. The ability to easily remove the viewport is critical because certain growth conditions (empirically, low J_{NH_3}/J_{III} during growth with $J_{NH_3} < 25$ sccm) result in viewport deposition and require removal of the deposition for optical transparency. Two viewports are used in the present work, each with exposure area diameters >3.75” (any smaller of a viewable diameter prevents visibility of the FISH that is necessary to align the UHV plugs for proper sample loading and prevents usage of the LRI system in the described configuration).

A custom calcium fluoride (CaF_2) ConFlat viewport (CeramTec North America) is used for photo-assisted growths at λ = 172 nm since the CaF_2 allows >80% transmission at λ > 172 nm (Fig. 2.7). A 1 μm SiO_2 barrier coating was deposited by Opticorp Inc. (Chelmsford, MA) on the UHV side of the viewport in order to eliminate possible fluorine contamination of growing films as a result of fluorine outgassing from the viewport. As shown in Fig. 2.8, fluorine strongly evolves from the bare (as-is, uncoated) CaF_2 viewport in UHV growth chamber. The thin SiO_2 barrier layer reduces the residual fluorine in the growth chamber by a factor of ~100. The SiO_2 barrier layer thickness was kept thin to prevent mechanical stresses from compromising the viewport or SiO_2 coating and to maintain optical transparency.

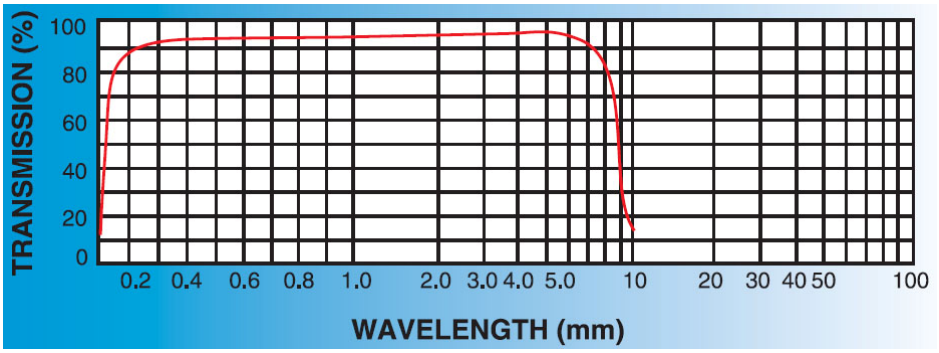

Fig. 2.7. Transmission spectrum of CaF_2 viewports [93].

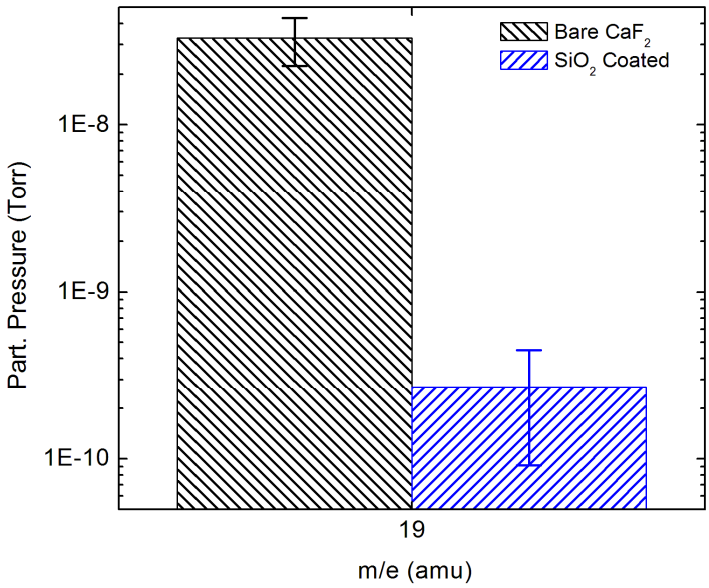

Fig. 2.8. Average partial pressure of m/e = 19 (representative of fluorine) in the growth chamber during outgassing of samples at T_s = 200 °C in the presence of the bare (as manufactured) CaF_2 viewport and the viewport after a 1 μm SiO_2 coating was deposited on the UHV side. Data was collected from 2 different samples for each case.

For photo-assisted growths using radiation at λ = 325 and 365 nm, a quartz fused silica viewport (Kurt J. Lesker VPZL-600Q) allows >90% transparency for λ > 200 nm (Fig. 2.9). The quartz viewport is stocked by various UHV product vendors and cost ~\$1000 – 1/6th the cost of the custom CaF_2 viewport. Hence, the quartz viewport can be easily replaced in the event of deposition or damage (Chapter 8).

Specific UV lamps and specific irradiation configurations are discussed in their respective sections.

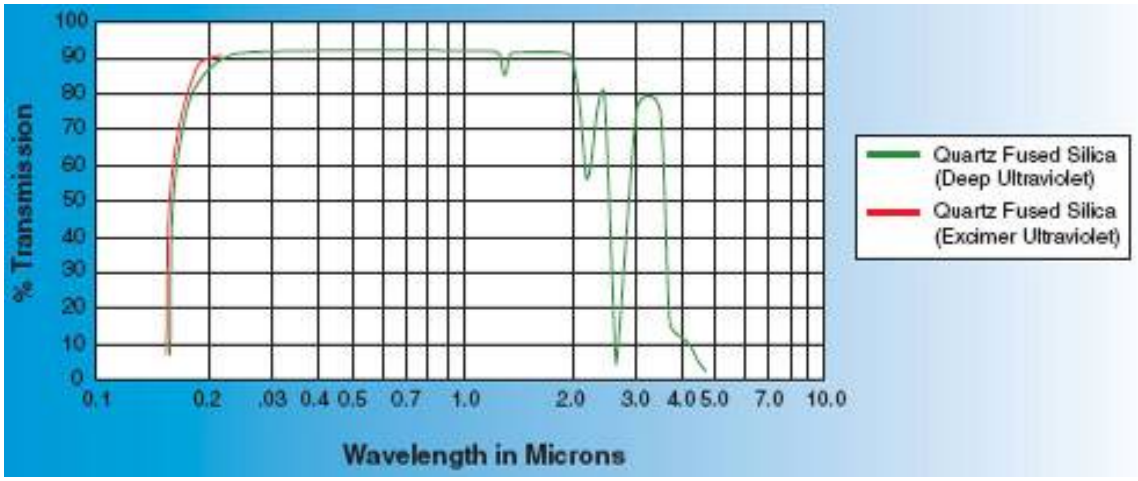

Fig. 2.9. Transmission spectrum of fused silica quartz viewports [93].

2.5 Residual gas analysis

A SRS RGA200 RGA mounted ~30 cm to the side of the growth substrate monitors residual chamber gases during the entire growth process. The RGA is located such that it will measure gases that are not effectively pumped by the LN_2 cryoshroud. Hence, the RGA monitors the relevant *residual byproduct species* in the growth chamber. The mounting configuration of the RGA is shown in Fig. 2.2.

A schematic of the SRS RGA200 is shown in Fig. 2.10. The SRS RGA200 operates by ejecting electrons from oxidation-resistant thoria coated iridium filament. The thermionically emitted electrons are accelerated towards a positively biased anode, ionizing some residual gasses by electron impact. Resulting ions are extracted by a negative biased focus plate and are separated by their mass-to-charge ratio (m/e) using a quadrupole ion filter. An ion detector (faraday cup) measures the ion current at each

mass. The ion currents can be converted to partial pressures by using known calibration/sensitivity factors. Detailed operating principles can be found in [94].

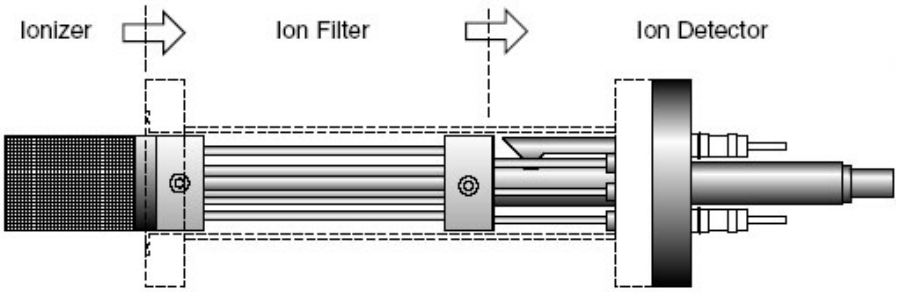

Fig. 2.10. SRS RGA200 probe components.

RGA mass spectra are recorded at 1 amu resolution. Fig. 2.11 shows an example of averaged spectra recorded at 0.1 and 1.0 amu resolution. No additional quantitative data was consistently discerned for spectra recorded at 0.1 amu resolution compared to spectra recorded at 1 amu resolution.

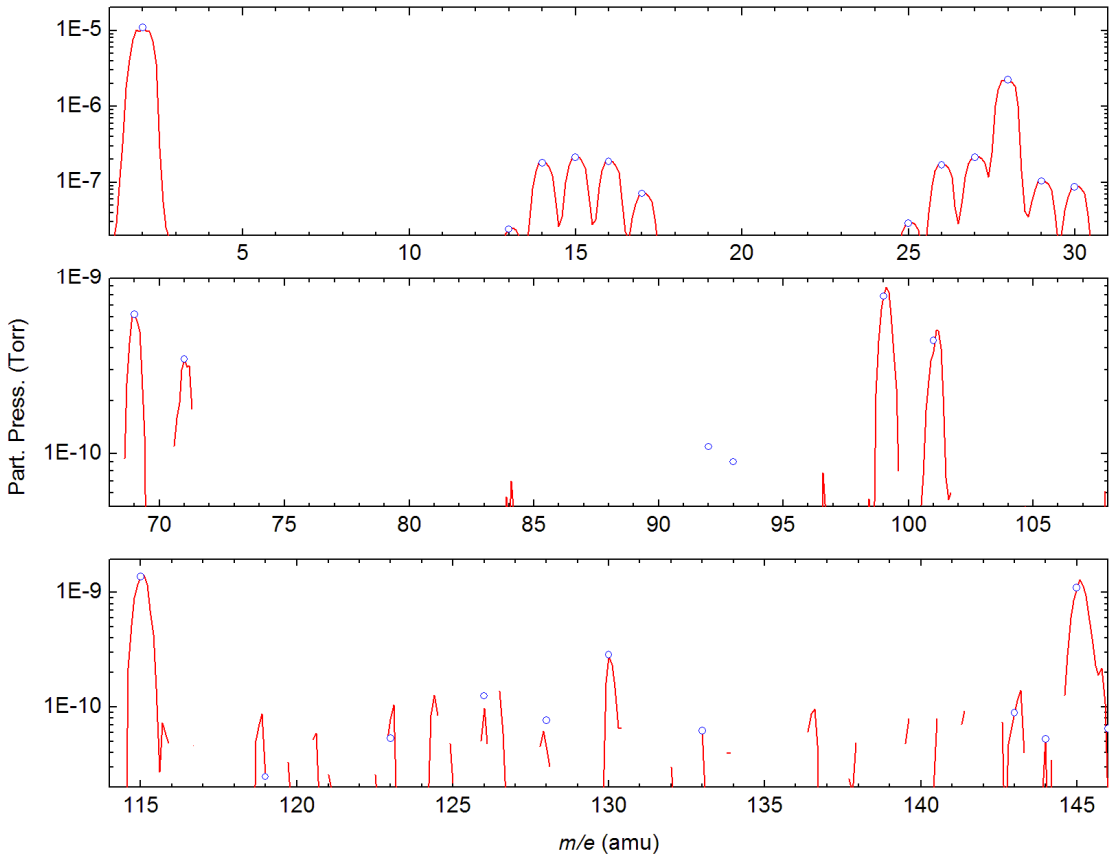

Fig. 2.11. Averaged RGA mass spectra recorded by the SRS RGA200 at 0.1 (red) and 1.0 amu (blue circles). Only *m*/*e* relevant to InGaN growth in the present reactor are shown.

2.6 Laser reflectance interferometry

A custom, in-house designed laser reflectance interferometer (LRI) system enables determination of GR and surface morphology evolution *in situ* [95]. A photograph of the LRI system is shown in Fig. 2.12. A HeNe laser (λ = 632.9 nm, 0.5 mW, Melles Griot) is incident at angle θ_1 = 45° to the surface normal through the 6" viewport of the growth chamber. The reflected light is detected by a Burr-Brown OPT101 photodiode with integrated transimpedance amplifier. The photodiode circuit is

a basic configuration that is powered by a dedicated 10 V linear supply decoupled through a 0.1 μF capacitor. The HeNe beam reflected from the sample is collimated using a 1" diameter collection lens (the substrate-photodiode optical path length is typically >1 ft, meaning the slightest substrate wobble can cause the reflected HeNe beam to miss the 0.09 × 0.09" photodiode in the absence a collection lens). In addition to a collection lens, a HeNe band pass filter directly precedes the photodiode and is necessary to minimize the detection of radiation emitted from the hot substrate or reflected radiation from the UV sources used during photo-assisted growth (the output spectrum of the Hg-Xe lamp includes λ = 632.9 nm, §3.3).

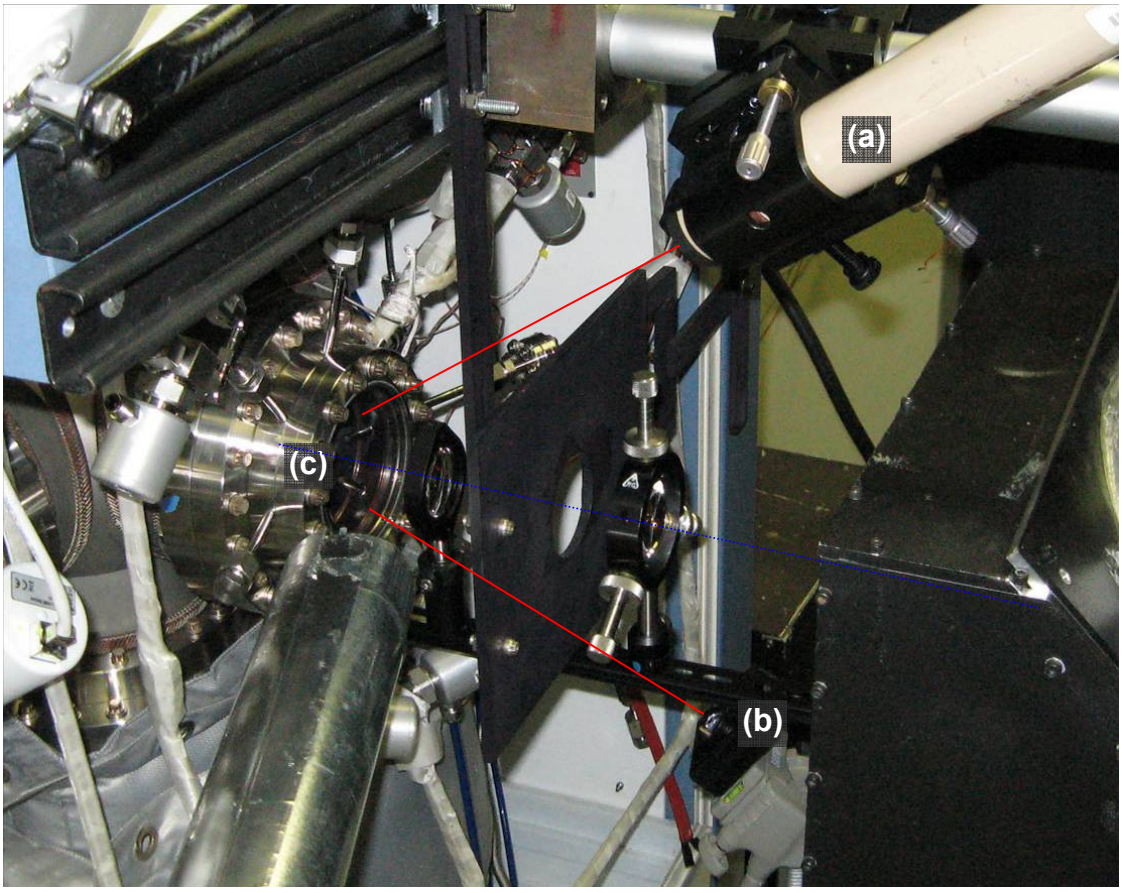

Fig. 2.12. The LRI system (a) HeNe laser and (b) detector circuit. The MOMBE growth chamber viewport is (c). The optical path (red line) and the growth surface normal (blue line) are approximated for reference.

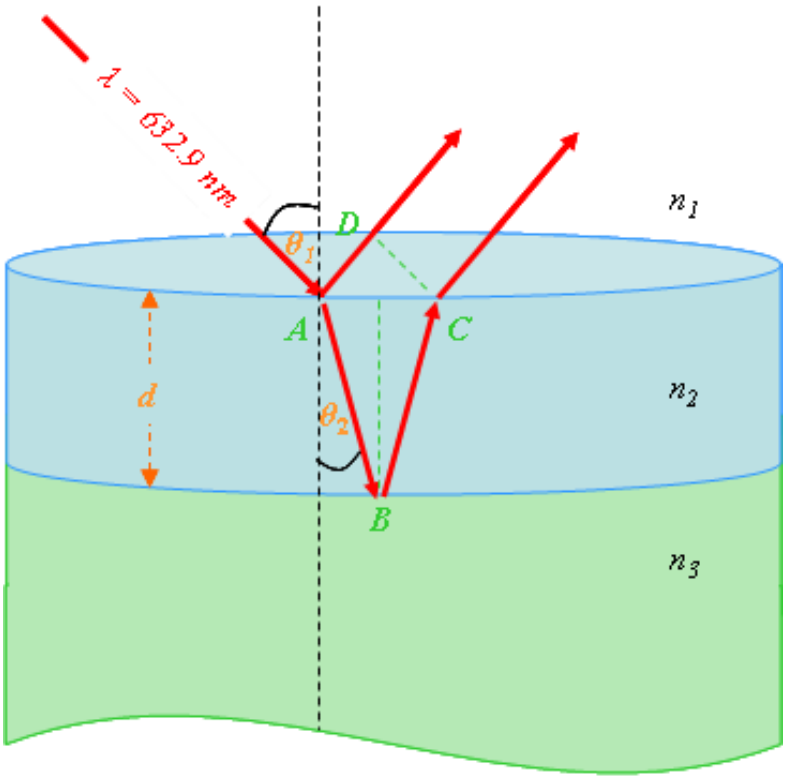

Fig. 2.13. LRI system (λ = 632.9 nm) incident at angle θ_1 to the growing layer normal with refractive index n_2 and thickness d.

Fig. 2.13 summarizes the theory of the LRI system. A growing layer with refractive index n_2 and thickness d induces an optical path length difference Λ in the optical waves reflected from the front surface and back surface of the growing layer. Λ is given by (2.3).

$$\Lambda = n_2(AB + BC) - n_1 AD = 2n_2 d\cos\theta_2 \tag{2.3}$$

θ_2 is given by Snell's law. Multiplying (2.3) by the phase constant $2\pi/\lambda$ yields the resulting phase shift φ between the reflected waves, given by (2.4).

$$\varphi = \frac{4\pi n_2 d}{\lambda}\cos\theta_2 \tag{2.4}$$

The layer thickness that results in a complete reflectivity interference oscillation ($\varphi = 2\pi$) is given by (2.5).

$$d_{\varphi=2\pi} = \frac{\lambda}{2n_2 \cos\theta_2} \tag{2.5}$$

Therefore, each period T of a reflectivity interference oscillation ($T = 1/f$) observed with the LRI system corresponds to 129, 145, and 152 nm of InN, GaN, and AlN growth (or conversely, film removal/decomposition) respectively based on the refractive indices given in Table 1.1.

The interference oscillations observed by the LRI system can be modeled by a standard sinusoidal oscillation, the frequency f of which can be used to accurately determine the GR *in situ*. The basic sinusoidal model is given in (2.6).

$$\frac{R}{R_{\max}} \sin(2\pi f t + \phi) \tag{2.6}$$

Here $R/R_{\max}$ represents the reflectivity normalized to the reflectivity maximum. Normalization mitigates variations in the absolute reflectance intensity which typically arise from differences in the incident laser intensity (viewport deposition) or the input voltage of the LRI photodiode. These absolute intensity variations affect the measurement sensitivity and only marginally affect the GR accuracy (possibly a few nm/hr, the accuracy of which is dependent of the quantity of data).

The surface morphology evolution can be modeled by expanding (2.6) with a damped oscillation containing a dampening coefficient α with a linear term β, given by (2.7).

$$\beta t + e^{-\alpha t}\left(\frac{R}{R_{\max}}\sin(2\pi f t + \phi)\right) \tag{2.7}$$

Qualitatively, α describes the change in the reflectivity oscillation *amplitude* that can result from both bulk attenuation (*e.g.* optical scattering from pits in the bulk, but negligible optical scattering from an atomically smooth surface). β describes the change in *average reflectivity*, which can result from surface roughening [96] or propagating (thickness dependant) defects, such as pits.

CHAPTER 3: NH_3-BASED MOMBE OF GAN AND UV-INDUCED CARBON DOPANT MODULATION

3.1 Introduction

Counter to the usual status of carbon as an unintentional dopant, carbon has attracted significant interest as an intentional dopant for achieving both *p*-type GaN and highly resistive (HR) GaN. N substitution by C (C_N) yields a theoretical GaN acceptor level near $E_v + 0.15\text{-}0.20$ eV [97,98] that has been observed experimentally [99]. While the C_N GaN acceptor level is rather deep – limiting the room temperature hole ionization – *p*-type carbon doping has yielded limited success [100,101]. Hole concentrations up to $p = 6 \times 10^{17}$ cm^{-3} in cubic GaN by plasma-assisted MBE have been achieved. HR GaN produced by the compensation of native GaN donors by carbon acceptors has been more successful [102,103]. HR GaN:C buffers have been employed in HEMTs [104-107], where the HR GaN is necessary for device pinch-off and high f_{max} operation. However, the presence of a trap level associated with C [99] has been suggested as a possible source of current collapse in these HEMT structures [104].

Despite progress in the application of GaN:C, the efficient doping of carbon in GaN has been limited. In MBE, a suitable C source is still in question. CBr_4 has recently has showed some success [108] over alternatives such as CCl_4 and CH_4. In MOCVD, C exists natively from the metal organics but requires a drastic reduction in chamber pressure (P_{ch}) in order to incorporate sufficient C [103,109]. These limitations of MBE

and MOCVD in regards to high carbon incorporation present a unique opportunity for NH_3-based MOMBE if the C doping of GaN can be effectively regulated in the MOMBE environment. Moreover, MOMBE may provide a means of achieving higher-than-before-possible C dopant concentration versus present alternatives.

3.2 Experimental procedure

GaN films were grown in the custom built NH_3-based MOMBE showerhead reactor (Chapter 2) on c-plane (0001) sapphire. The high vacuum chamber is equipped with a cryogenic pump and LN_2 cryoshroud, yielding a P_b ~7×10^{-8} Torr. A ~3 μm molybdenum film was sputtered onto the backside of each substrate to promote efficient heating. Samples were degreased twice by soaking in trichloroethylene, then acetone, then methanol for 30 min each in an ultrasonic cleaner and rinsing with deionized water and drying with N_2 before loading into the reactor.

The GaN growth process consisted of 7 primary steps. Each sapphire wafer was annealed at T_s = 200 and 1000 °C for 20 and 10 min respectively. Next, sapphire nitridation (J_{NH_3} = 100 sccm) was performed at T_s = 1000 °C for 10 min. Next, a GaN buffer layer was deposited at T_s = 540 °C for 5 min (J_{NH_3} = 100 sccm and J_{TEGa} = 0.24 sccm). Next, T_s was ramped at 0.7 °C/s to the growth temperature in order to promote coalescence and prevent buffer layer decomposition. During the ramp, J_{NH_3} = 100 sccm, and for T_s > 680 °C, J_{TEGa} = 0.12 sccm. Following the ramp, the sample was annealed at

the growth temperature for 1.25 min with NH_3 and TEGa still introduced. Afterwards, a GaN layer was grown for 80 min.

The nucleation procedure is far from optimized, resulting in structural quality figures of merit that have much room for improvement compared to MBE and MOCVD GaN films, additional details are in §A.5. Additionally, *ex situ* x-ray diffraction (XRD) and RHEED show evidence of cubic and hexagonal phases, which has been previously demonstrated in the growth of GaN via MOMBE [110,111]. While the inclusion of a cubic phase was evidenced, the relative phase purity has not been considered in the current discussion.

Only the growth conditions in the final GaN layer were varied between the individual experiments. In the growth of the final GaN layer, P_{ch} ranged from ~6×10^{-6} – 2×10^{-5} Torr – well under the 10^{-4} Torr limit for molecular flow [112]. J_{TEGa} was fixed at 0.24 sccm. To examine the effects of growth conditions, T_s was varied from 770-920 °C and J_{NH3} = 50 or 100 sccm. The change in J_{NH3} resulted in variations in P_{ch} averaging 7.67×10^{-7} Torr.

3.3 Custom UV irradiation apparatus

The effects of sample exposure to UV radiation from a parabolically collimated, 5 kW Hg-Xe arc lamp (ORC Advanced Specialty Lighting HVF5000-1C, λ = 365 nm) during GaN growth was also investigated. The arc lamp is housed in a custom apparatus which directs the UV radiation onto the sample. The optical exit of the assembly is

shown in Fig. 3.1. The UV radiation is collected by a custom electroformed parabolic reflector and then turned (Edmund Optics NT43-571 spherical mirror, UV enhanced Al coating for 85% reflectivity from 200-700 nm, *f*/# 10, EFL 125", and 12.5" diameter) onto the sample. The custom assembly is versatile in that the irradiance on the sample can be drastically varied by changing the relative position of the lamp arc with respect to the focal point of the parabolic reflector. Hence, the reflector can maximize irradiance (with slight compromises in image quality) when compared to conventional commercial systems that only use lenses for collection (Fig. 3.2). The arc lamp and mirror are cooled by forced air convection using a 1050 ft^3/min blower (additional lamp cooling will prevent complete Hg evaporation, eliminating UV emission). The exhaust of the fan is introduced through the bottom opening of the parabolic reflector and across the arc lamp envelope.

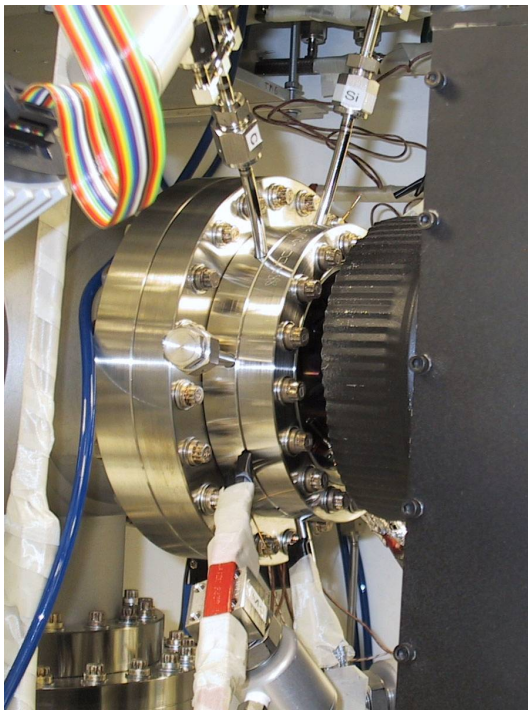

Fig. 3.1. The 5 kW Hg-Xe arc lamp assembly optically aligned to irradiate samples *in situ* through the growth chamber viewport.

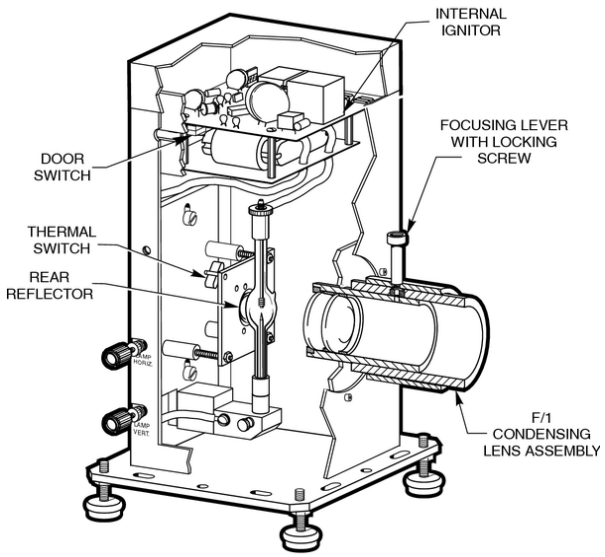

Fig. 3.2. Newport Corporation 250-500 W Oriel Research arc lamp housing [113]. The conventional collection mechanism provides minimal irradiance compared to certain configurations of the aspherical reflector utilized in this work.

The range of the estimated irradiance that is capable of being delivered on the sample by the apparatus is given in Table 3.1. These values are *estimations* of the irradiance. The given range of irradiance is achieved by adjusting the position arc gap of the lamp relative to the focus of the parabolic reflector, resulting in focusing of the incident radiation. This is illustrated by the two optical paths shown in Fig. 3.3 and Fig. 3.4. These optical paths represent the lower and upper limit of the UV power density incident on the samples during the experiments of this chapter. Other chapters utilize different irradiances and the specific optical configurations are discussed in their respective sections. In Fig. 3.3, the lamp arc gap is placed in the focal point of the parabolic reflector, creating a collimated 14" diameter spot. In Fig. 3.4, the lamp arc gap

is positioned so that the parabolic reflector focuses the light to a 6" diameter spot at the substrate. Considering a viewport transmittance of 90% for $\lambda > 200$ nm (Fig. 2.9), 65% [114] of the Hg-Xe arc lamp emission is collected by the parabolic reflector, and neglecting other losses (reflection, etc.), the maximum possible irradiance that is incident on the samples during growth can be calculated. For a spatially uniform irradiation with spot diameter at the substrate of 14" and 6", the corresponding broadband irradiances are 2.95 and 16.03 W/cm^2 respectively. The Hg-Xe arc lamp spectral distribution is given in Fig. 3.5 and Table 3.2. The dependence of the bandgap (E_g) of GaN on temperature T (K) is given by (3.1) [115].

$$E_g(T_s) = 3.486 - \frac{8.32 \times 10^{-4} T^2}{835.6 + T} \text{ eV} \qquad (3.1)$$

For the present growth temperatures T_s = 770 and 920 °C, the E_g for GaN is calculated as 3 and 2.9 eV respectively. Therefore, all radiation shorter than $\lambda < 430$ nm is of sufficient energy to be absorbed by GaN at T_s = 770 – 920 °C, corresponding to ~19.8% of the radiation emitted by the Hg-Xe arc lamp (Table 3.2). Hence, for a spot diameter at the substrate of 14" and 6", corresponding irradiances (maximum) of 0.58 W/cm^2 and 3.17 W/cm^2 can be absorbed by GaN. Assuming that the energy of every photon is 3.4 eV (λ = 365 nm), the corresponding maximum photon fluence incident during the present growths that can be absorbed by GaN is 5.24×10^{19} cm^{-2} s^{-1} respectively.

Table 3.1. Estimated irradiance and photon fluence at the substrate delivered by the Hg-Xe arc lamp apparatus configured to focus differently. The above-bandgap irradiance is calculated by only considering He-Xe arc lamp radiation shorter than $\lambda < 430$ nm.

substrate spot diameter (")	broadband irradiance (W/cm^2)	above-bandgap irradiance (W/cm^2)	above-bandgap photon fluence (10^{18} photons/cm^2·s)
14	2.95	0.58	1.07
12	4.01	0.79	1.46
10	5.77	1.14	2.10
8	9.02	1.79	3.28
6	16.03	3.17	5.82
4	36.08	7.14	13.1
2	144.31	28.6	52.4

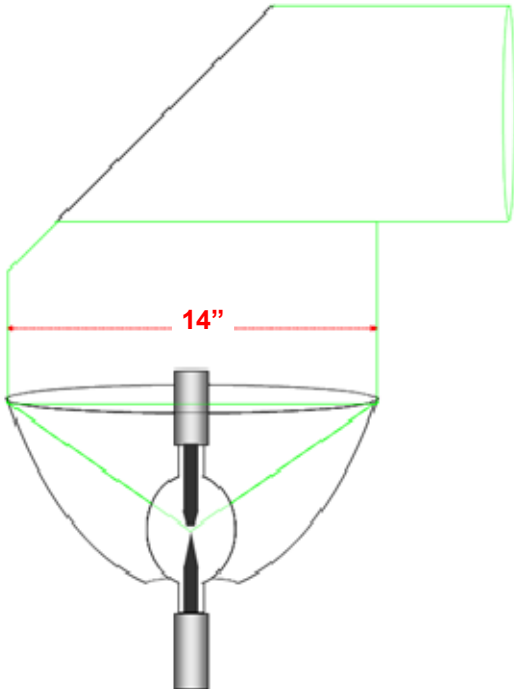

Fig. 3.3. Optical path of custom 5 kW Hg-Xe arc lamp assembly. The parabolic mirror is used to collimate the light in this configuration.

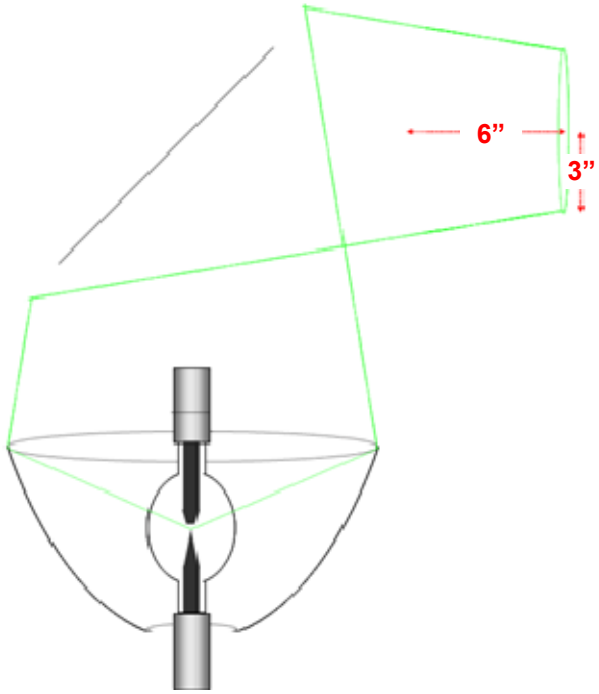

Fig. 3.4. Optical path of custom 5 kW Hg-Xe arc lamp assembly. The parabolic mirror is used to focus the light to a 6” diameter spot on the sample in this configuration. The lamp arc gap to reflector focal point distance is exaggerated.

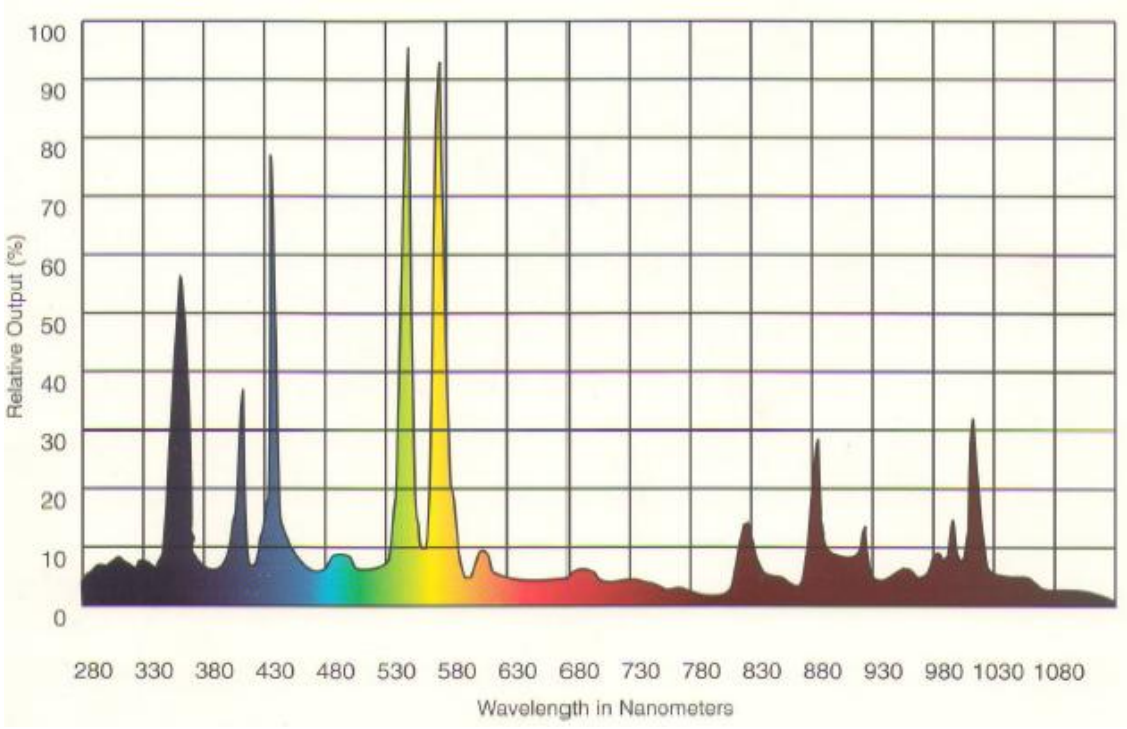

Fig. 3.5. Relative output (%) of the Hg-Xe arc lamp [116].

Table 3.2. Spectral distribution (%) of the Hg-Xe arc lamp [116].

λ (nm)	**output (%)**	**λ (nm)**	**output (%)**
230-280	0.7	780-830	2.9
280-330	2.0	830-880	2.6
330-380	10.0	880-930	5.4
380-430	7.1	930-980	3.1
430-480	7.9	980-1030	7.4
480-530	4.0	1030-1080	7.4
530-580	18.6	1080-1130	1.0
580-630	10.1	1130-1180	1.0
630-680	2.7	1180-1230	0.7
680-730	2.7	1230-1280	0.7
730-780	2.0	1280-2500	7.7

3.4 Crystalline quality and GR dependence on T_s

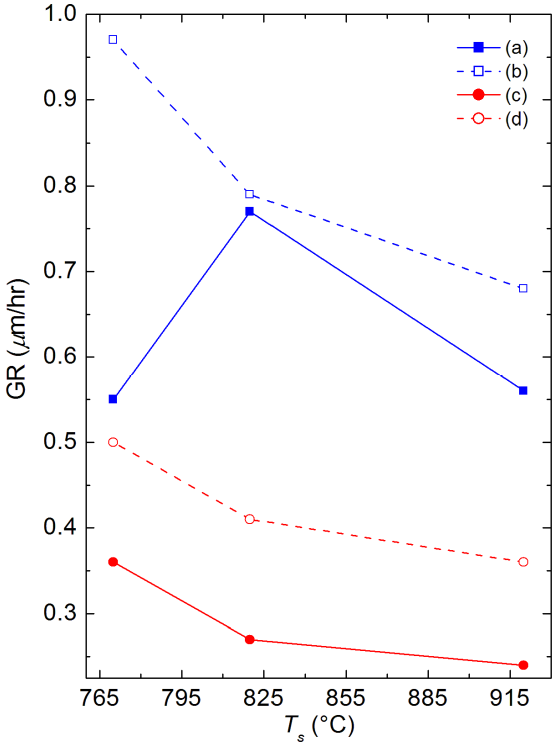

Fig. 3.6. GaN GR versus T_s at fixed J_{TEGa}. (a) and (b) correspond to an J_{NH3} = 50 sccm without and with UV exposure. (c) and (d) correspond to an J_{NH3} = 100 sccm without and with UV exposure.

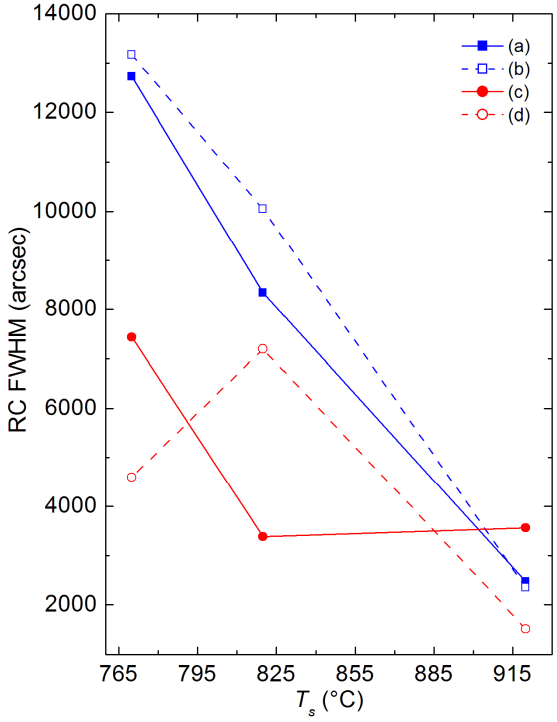

Fig. 3.7. XRD RC FWHM versus T_s at fixed J_{TEGa}. (a) and (b) correspond to an J_{NH3} = 50 sccm without and with UV exposure. (c) and (d) correspond to an J_{NH3} = 100 sccm without and with UV exposure.

Fig. 3.6 plots the GaN GR as a function of T_s. As shown, the GR decreases with increasing T_s, which may be attributed to both GaN decomposition [109] and Ga/DEGa desorption [24,117]. The GR doubles when J_{NH3} is halved, suggesting a local deviation from molecular flow (significant NH_3-TEGa gas-phase interaction) affecting the TEGa diffusion and/or reaction on the substrate surface. This GR trend suggests that growth is N-rich – more details are discussed in Chapter 7. When exposed to intense UV radiation, the GR increases significantly—an average of 48% (J_{NH3} = 100 sccm) and 33% (J_{NH3} = 50 sccm). This photocatalytic effect could be attributed to more efficient cracking of

NH_3; however, this hypothesis is not supported by the RGA analysis presented later. Instead, a more plausible hypothesis to explain the increased GR under intense UV irradiation is that the UV radiation efficiently removes hydrocarbon species that block surface sites.

Fig. 3.7 shows the XRD rocking curve (RC) full width half maximum (FWHM) as a function of T_s. For the J_{NH3} = 50 sccm cases, the FWHM decreased with increasing T_s. This may be attributed to improved species surface migration lengths or increased desorption of hydrocarbon species blocking precursor diffusion to the surface [118]. Additionally, the effects of UV exposure on FWHM are negligible at T_s = 770 and 920 °C. However, for the J_{NH3} = 100 sccm case, an average reduction of 47% in FWHM is observed for the T_s = 770 and 920 °C films grown under UV exposure. At T_s = 820 °C, UV exposure is shown to degrade crystalline quality under both J_{NH3} conditions. In all cases, the FWHM of these initial films is significantly greater than typical from advanced MBE or MOCVD growth, indicating a need for optimization of the buffer growth conditions and perhaps the need for growth at elevated T_s as inferred from the trends indicating improved quality with increasing T_s. However, the RC FWHM of the T_s = 920 °C films is consistent with GaN films grown under similar conditions [35].

3.5 Carbon doping of GaN

Fig. 3.8 plots the carbon depth profiles measured by SIMS for the highest crystalline quality samples (T_s = 920 °C). The differences in sputter depth can be

attributed to GR variations (Fig. 3.7), since all samples were grown with the same duration of 80 min. As shown, doubling J_{NH_3} approximately halved both the C concentration and the GR of the film – an effective factor of 2 decrease in carbon incorporation. More interestingly, C concentration reduced by factors of 4 (J_{NH_3} = 100 sccm) and 2.4 (J_{NH_3} = 50 sccm) in films exposed to the intense UV *in situ*. This effect on C reduction is consistent with GaAs growth under weak UV excitation [119]. As the intense UV exposed films exhibited a faster GR, 58% less integrated carbon content was measured for the films exposed to UV. Over this limited growth regime range (T_s = 920 °C, UV exposure, J_{NH_3} = 50 or 100 sccm) ***a one decade of variation in C concentration is observed. In all cases, the carbon concentration obtained through NH_3-based MOMBE is significantly higher than the upper limits possible via other reported carbon sources*** [100,101,108].

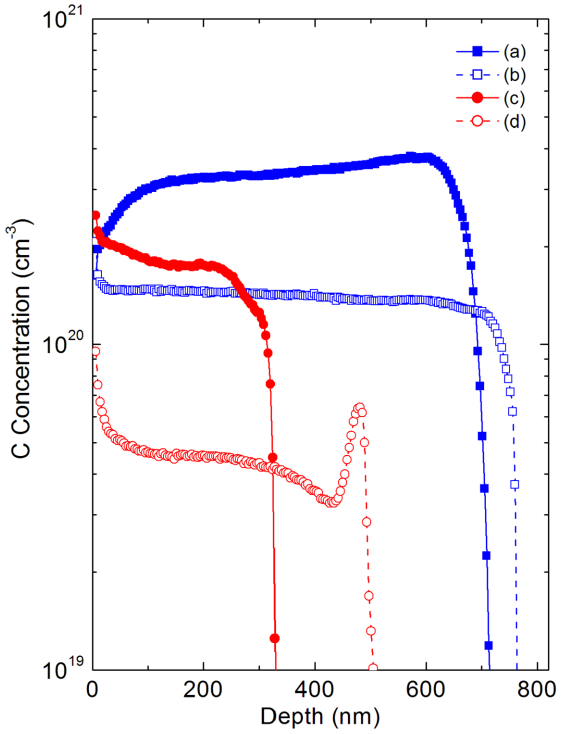

Fig. 3.8. SIMS depth profile indicating carbon reduction for increased J_{NH3} and intense UV exposure as well as improved growth rate for UV exposure. (a) and (b) correspond to an J_{NH3} = 50 sccm without and with UV exposure. (c) and (d) correspond to J_{NH3} = 100 sccm without and with UV exposure.

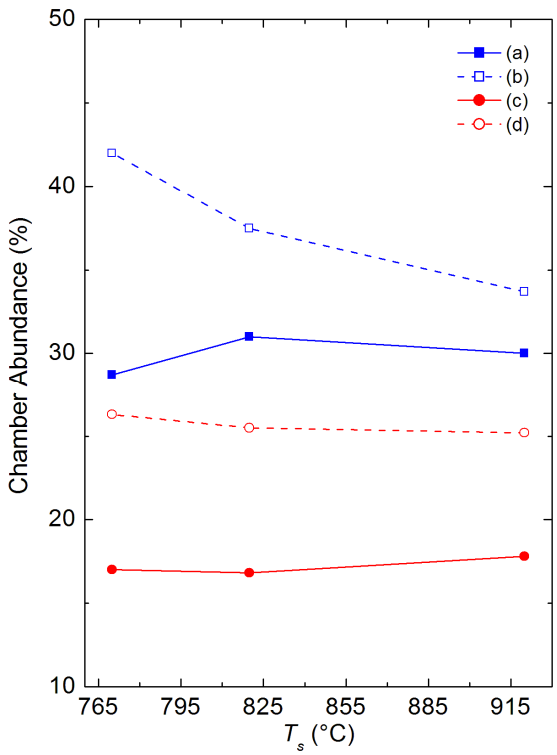

Fig. 3.9. Variation in C_2H_4 chamber content as a function of T_s at fixed J_{TEGa}. (a) and (b) correspond to J_{NH3} = 50 sccm without and with UV exposure. (c) and (d) correspond to an J_{NH3} = 100 sccm without and with UV exposure.

3.6 Quantification of residual surface reaction byproducts

The quantification of surface reaction byproducts from observed RGA mass spectra for each set of growth conditions requires identifying potentially relevant species as well as determining the individual contributions of each species to each mass spectra. Oxygen related byproducts (*e.g.* CO_2 and O_2) were not considered to be dominant factors in the growth chemistry since two outgassing steps were included in the growth procedure and all subsequent RGA spectra contained negligible oxygen related signatures.

As shown in Fig. 3.10, the partial pressure of m/e = 16 (indicative of O, but the signal also consists of contributions from hydrocarbon and NH_x species) after outgassing is 4×10^{-9} Torr. While the subsequent analysis does not identify oxygen related byproducts as dominant species in the growth chemistry, the resultant GaN films are heavily doped with O.

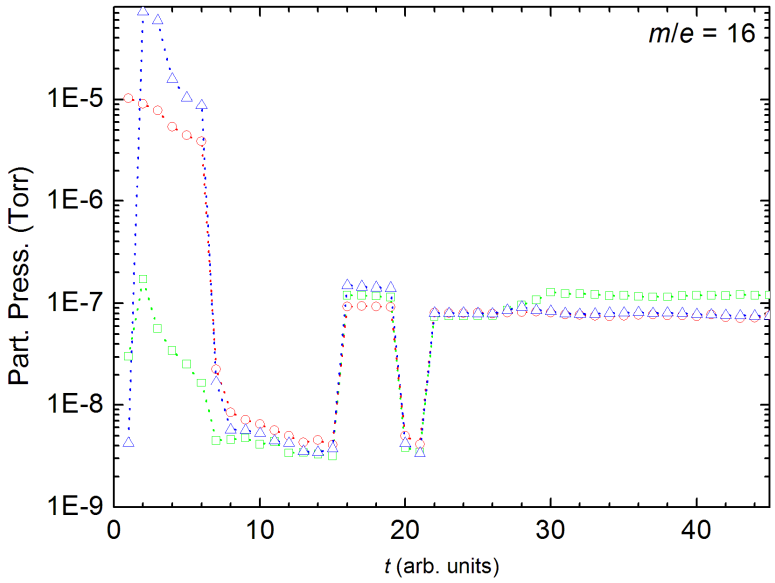

Fig. 3.10. Evolution of RGA m/e = 16 signal for three of the present growths. After degassing at T_s = 1000 °C during t = 12-15, the partial pressure of m/e = 16 is 4×10^{-9} Torr. For t > 15, the signal is dominated by NH_x species. The final GaN layer begins at t = 30.

Statistically significant byproducts are initially identified through Pearson product moment correlation (Table 3.3) of their respective fragment patterns to representative RGA mass spectra for each set of growth conditions. These representative RGA mass spectra were formed from the 5-16 spectra recorded during the 80 min bulk growth period by – for each m/e signal – removing the high and low partial pressures and averaging the remaining partial pressure data points. Each mass spectrum was modeled

through the superposition of scaled fragment patterns for all statistically significant species. The scaling factors necessary to fit each fragment pattern represent the approximate percent abundance of each statistically significant species in the growth chamber for each specific growth condition.

Table 3.3. Average Pearson product moment correlation coefficient (<r>) and average abundance (<%>) over all growth conditions of the most abundant chamber species.

species	***m*/*e***	**<r>**	**<%>**
C_2H_4	28	0.49	27.63
C_2H_6	30	0.51	7.15
CH_4	16	-0.03	0.22
NH_3	17	-0.03	0.72
CO	28	0.50	0.50
H_2	2	0.83	50.29
N_2	28	0.50	13.04

3.7 Model of residual surface reaction byproducts

Table 3.3 lists the average percent abundance – over all of the growth conditions – of the most plentiful species present during the 80 min of bulk GaN growth. Other additional species, such as acetylene (C_2H_2) were evaluated, however, their calculated abundances are considered negligible. As shown in Table 3.3, the low abundance of CO reinforces the suspicion that oxygen related species are not dominant in the growth chemistry. With an average abundance of 50.29%, H_2 is the most abundant residual byproduct during growth. This is not surprising as it is ineffectively pumped by the cryopump or LN_2 cryopanel and it can be a byproduct of NH_3 or TEGa pyrolysis and

subsequent interactions. N_2 averages 13% of the chamber residual gas content. The most abundant residual hydrocarbons, ethylene (C_2H_4) and ethane (C_2H_6), average 27.63% and 7.15% respectively. These four species represent the most measurable residual surface reaction byproducts and consistent variations with growth conditions are observed for each byproduct. Additionally, the identification of ethylene as the primary MOMBE hydrocarbon byproduct when using TEGa is consistent with mass spectrometry studies of GaAs growth [68,106,107].

Fig. 3.9 plots the variation of residual ethylene as a function of T_s. A significant reduction in ethylene is observed when J_{NH_3} is doubled, which can be attributed to an increase in the contribution of NH_3-related species to the chamber gas content. Residual ethylene was relatively constant with T_s for J_{NH_3} = 100 sccm. However, exposure to UV radiation dramatically increases the abundance of ethylene an additional 7.4% (25.2% total) of the chamber gas content.

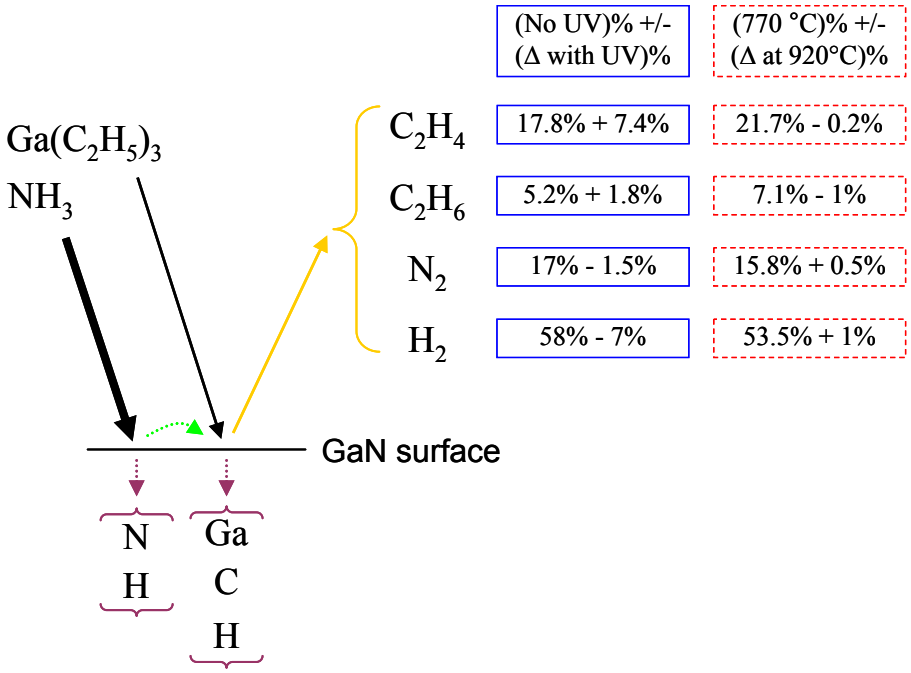

Fig. 3.11. Variation in residual C_2H_4, C_2H_6, N_2, and H_2 during GaN growth using J_{NH3} = 100 sccm as a result of UV exposure at T_s = 920 °C (blue solid boxes) and T_s elevation from 770 to 920 °C (red dotted boxes).

Fig. 3.11 summarizes the variations in byproduct abundances during UV exposure at T_s = 920 °C and T_s increase from 770 to 920 °C for J_{NH3} = 100 sccm. Residual ethane decreases with increase in T_s and ethane is weakly affected by UV irradiation – comprising an additional 1.8% (to 7% total) of the overall chamber content during UV exposure. Significant increases in residual ethylene and ethane result from UV irradiation during growth and are their increase is accommodated by reductions in the residual H_2 and N_2, which decrease in total chamber gas content by 7% (to 51% total) and 1.5% (to 15.5% total) respectively. The reduction in residual H_2 content as a result of UV irradiation suggests that ethylene and ethane may be a product of H_2 consumption reactions. Indeed, while favorable consumption reactions exist, the origin of intermediates is not clear (*e.g.* $2CH_{2(g)} + H_{2(g)} \rightarrow C_2H_{6(g)}$, ΔG = -499 kJ at 900 °C). The

abundance of and H_2 and N_2 increase slightly with increasing T_s. This T_s dependence suggests that the excess N that is present from increased J_{NH_3} and T_s (increased NH_3 cracking efficiency) may reduce the surface lifetime of atomic N through the formation of N_2. This is consistent with the reduced GR observed at elevated T_s. Moreover, this reduction in atomic N available on the surface ($J_{eff,N}$) has previously been observed to have a dependence on J_{TEGa} and adversely affect the film GR [120].

While it is still unknown which reaction pathways are dominant during the NH_3-based MOMBE growth process, the dominant growth byproducts are only weakly affected by variation in T_s over the studied range – perhaps a consequence of subtle differences in NH_3 decomposition efficiency over this T_s range [3,121]. GaN GR and crystalline quality are both dramatically affected by T_s, but are a consequence of factors that are not able to be discerned through the present residual reaction byproduct analysis. However, ***exposure to intense UV radiation during GaN growth strongly affects the TEGa decomposition process or the surface interaction of TEGa with NH_3, yielding a discernable increase in residual ethylene and ethane in the growth chamber, a faster GR, an improved crystalline quality, and a reduction in carbon dopant concentration (at T_s = 920 °C). These benefits are suspected to be a result of an increase in the liberation of site-blocking hydrocarbons from the growth surface in the presence of intense UV irradiation.*** Increases in residual ethylene are indicative of TEGa decomposition through β-elimination [21,122,123] which is the preferred decomposition pathway for low carbon incorporation [124]. Moreover, the subsequent hydrocarbon liberation should uncover N sites, allowing for more efficient GaN bond formation – a plausible mechanism for the improved GR under intense UV irradiation.

3.8 Conclusions

The effect of growth conditions on the GR, crystalline quality, and carbon concentration of GaN during NH_3-based MOMBE has been investigated. An increase in J_{NH3} from 50 to 100 sccm reduces the GR while improving the crystalline quality (except for T_s = 920 °C). The same general trends were observed as T_s is increased from 770 to 920 °C. The GR, crystalline quality, and mitigation of carbon contamination were further enhanced by exposing the growth surface to intense UV radiation during growth. Over the growth conditions examined, ethylene and ethane were identified as the primary residual surface reaction hydrocarbon byproducts. Increases in residual ethylene and ethane, with corresponding reductions in hydrogen and nitrogen, were observed for growth conditions that resulted in films of better crystalline quality and reduced carbon concentration. Moreover, exposure to intense UV radiation during growth encouraged the formation of ethylene and ethane. While the processes responsible for the formation of ethylene and ethane are uncertain, the removal of hydrocarbon species from the growth surface was observed to enhance GaN growth. Therefore, monitoring these species during growth may facilitate an additional means of film optimization or carbon concentration prediction *in situ*.

The results demonstrate that the NH_3-based MOMBE is capable of doping GaN with higher levels of carbon ($>10^{20}$ cm^{-3}) than presently achieved by advanced MBE and MOCVD growth technology. Moreover, UV irradiation is effective in regulating the C dopant concentration – an effect that could be leveraged by 3DE to locally define regions of varying C concentration in GaN. The extremely high carbon doping that is capable by

NH_3-based MOMBE renders all of the present GaN films SI/HR. While the high carbon concentrations achieved in GaN may be a pathway toward C-doped *p*-type GaN, the GaN films presented in this chapter are grown under N-rich/Ga-limited conditions rather than the Ga-rich/N-limited conditions necessary for C incorporation as C_N (*p*-type) (Fig. 3.12) [125]. Hence, it is suspected that most of the carbon incorporates as C_{Ga} or interstitial C (C_I). More details on GaN growth by NH_3-based MOMBE under Ga-rich vs. N-rich growth conditions are presented in Chapter 7.

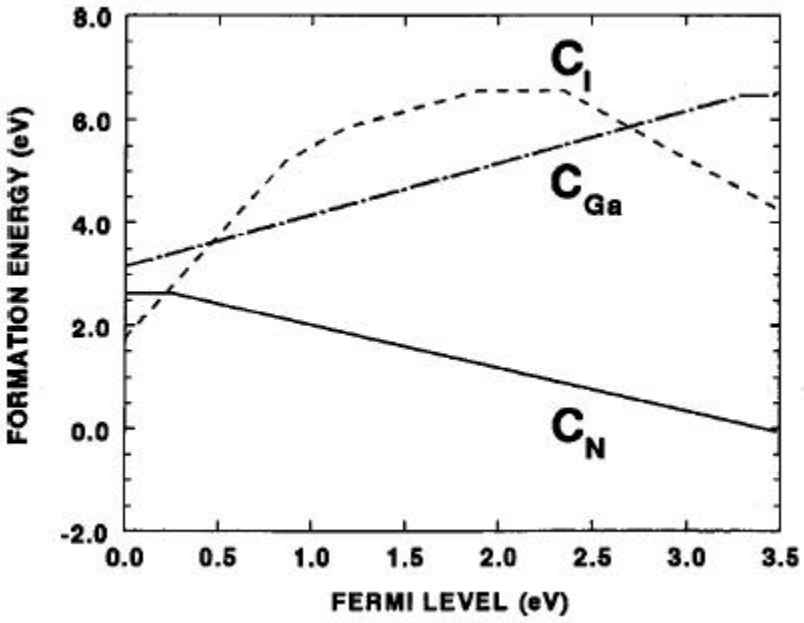

Fig. 3.12. Formation energies of C_I, C_N, and C_{Ga} as a function of Fermi-level position in the GaN bandgap as calculated by density-functional theory for the wurtzite structure under Ga-rich growth conditions [125].

CHAPTER 4: NH_3-BASED MOMBE OF $In_xGa_{1-x}N$

4.1 Introduction

$In_xGa_{1-x}N$ alloys are of significant interest for the development of robust optoelectronic devices from the UV to near infrared IR spectral range. This spectrum tailoring is achieved through variation of the indium mole fraction from pure GaN to InN, resulting in a bandgap energy range from 3.4 to ~0.65 eV [47]. MOCVD has dominated growth of $In_xGa_{1-x}N$-based LEDs and LDs [126] while NH_3-based MBE has only recently demonstrated MQW LDs [127]. However, increasingly complex device structures may require the *in situ* analysis and potentially more abrupt interfaces enabled by the high vacuum environment of MBE. Merging the MOCVD and MBE techniques in NH_3-based MOMBE retains the vacuum nature of MBE while utilizing the MOCVD convenience of all gaseous sources. This eliminates solid-source replacement downtime and consumption driven, slow flux variation of MBE, while drastically reducing the quantity of expensive and toxic precursors consumed in MOCVD. Moreover, MOMBE may be better suited for selective epitaxy which may be necessary for the economical realization of complex device concepts such as lateral bandgap energy modulation [1].

In this chapter, the first NH_3-based MOMBE growth of $In_xGa_{1-x}N$ is reported. The effects of T_s, J_{NH3}, and J_{TEGa}/J_{TMIn} on the GR, alloy composition, and III-alkyl desorption is presented. Indium compositions of up to 19% are reported with significant

growth variations observed as a result of deficient active N, surface In/In-methyl species, and III-alkyl desorption.

4.2 Experimental procedure

$In_xGa_{1-x}N$ films were grown in the custom built NH_3-based MOMBE showerhead reactor (Chapter 2) on c-plane (0001) sapphire using TEGa, TMIn (trimethylindium), and NH_3 precursors. A ~2 μm tantalum film was sputtered onto the backside of each substrate to promote efficient heating. Samples were immersed twice for 10 min each in a 90 °C piranha solution of H_2SO_4:H_2O_2 (4:1) before loading into the reactor, additional details of the etch are in [128].

After annealing for 30 min at T_s = 150 °C in the introductory chamber and T_s = 200 °C in the growth chamber, the sapphire substrate was exposed to J_{NH3} = 100 sccm while heating to T_s = 800 °C for a subsequent 10 min nitridation. A ~30 nm GaN buffer layer was grown for 16 min at T_s = 540 °C with J_{NH3} = 100 sccm and J_{TEGa} = 0.119 sccm. Afterwards, T_s was ramped to 870 °C at 0.5 °C/s with J_{NH3} = 25 sccm. Next, a ~200 nm GaN layer was deposited with J_{NH3} = 25 sccm and J_{TEGa} = 0.38 sccm. Next, T_s was reduced to 400-660 °C with J_{NH3} = 100 sccm for the growth of $In_xGa_{1-x}N$. To rule out the effects of buffer quality, two $In_xGa_{1-x}N$ layers (T_s = 560 and 660 °C) were grown on 3.5 μm Si-doped GaN templates (Lumilog, Vallauris, France). All InGaN layers were grown for 2 h.

4.3 Indium incorporation dependence on growth condition

XRD 2θ-ω scans of $In_xGa_{1-x}N$ films grown from T_s 400-660 °C are shown in Fig. 4.1. J_{NH_3} = 70 sccm and J_{TEGa}/J_{TMIn} = 1 remained fixed during growth of the $In_xGa_{1-x}N$ layer. The $In_xGa_{1-x}N$ layer growth of 2 hr resulted in layer thicknesses of at least 3 times the respective critical thickness as calculated by Holec *et al.* [129]. Therefore, for interpretation of the XRD data, it is assumed that the $In_xGa_{1-x}N$ layer is fully strain relaxed and that Vegard's law applies. At T_s = 400 °C, indium droplets are observed and identified by the XRD peak near 33°. As T_s is increased from 400 to 660 °C, the indium composition reduces from 19 to 2%. This T_s dependence of indium composition is expected to be a result of indium re-evaporation for T_s > 540 °C [78]. The GR variation with T_s is shown in Fig. 4.2(a). As shown, the GR increases with increasing T_s, consistent with N-limited growth (no greater than ~4% NH_3 cracking efficiency [121] is expected in this regime). This suggests that as T_s is increased, growth becomes less III-rich as a result of increased active N.

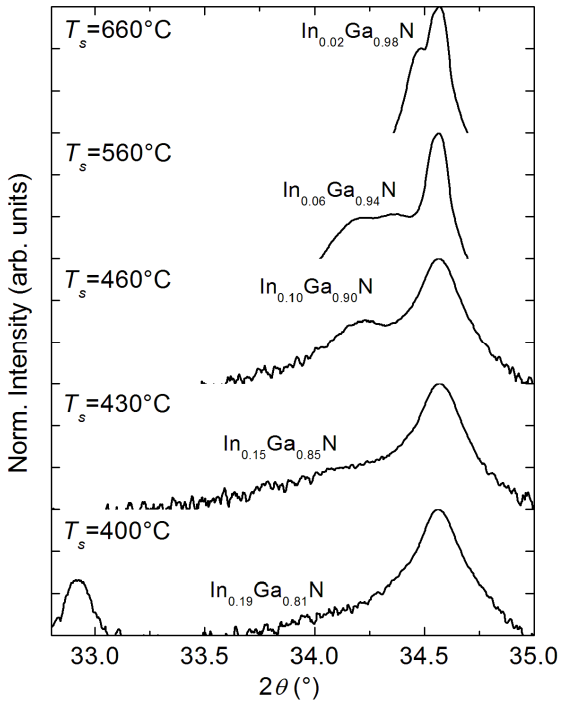

Fig. 4.1. XRD 2θ-ω of $In_xGa_{1-x}N$ films grown from T_s = 400-660 °C, with all other growth parameters constant (J_{NH3} = 70 sccm and J_{TEGa}/J_{TMIn} = 1).

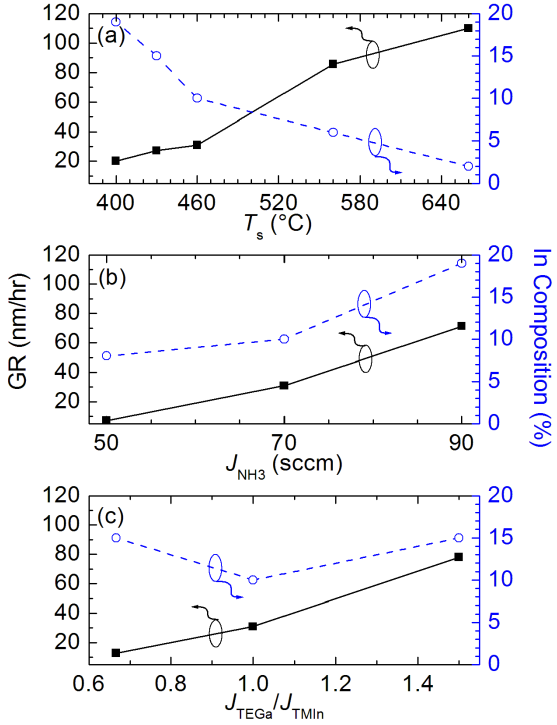

Fig. 4.2. GR and composition variation for $In_xGa_{1-x}N$ grown at (a) T_s = 400-660 °C, (b) J_{NH3} = 50, 70, and 90 sccm, and (c) J_{TEGa}/J_{TMIn} = $^2/_3$, 1, and $^3/_2$. Only the dominant indium composition is shown.

For the T_s = 460 °C case in Fig. 4.1, the effects of J_{NH3} (constant T_s and J_{TEGa}/J_{TMIn}) on indium composition are shown in Fig. 4.3. With J_{NH3} = 50 sccm, the dominant phase contains 8% indium. Increasing J_{NH3} to 70 and 90 sccm increased the indium composition to 10 and 19% respectively. The increases in indium incorporation with 20 sccm increases in J_{NH3} suggests that while in the N-limited regime, excess Ga is present during the J_{NH3} = 50 and 70 sccm cases to significantly limit indium incorporation. Since it is energetically favorable for surface Ga atoms to exchange with underlying In atoms due to more strongly bound Ga atoms and unfavorable strain conditions in the bulk [130], the Ga must be consumed before In atoms will effectively incorporate. This is

reinforced in 4.2(b) as both the GR and indium incorporation increase with increasing J_{NH3}.

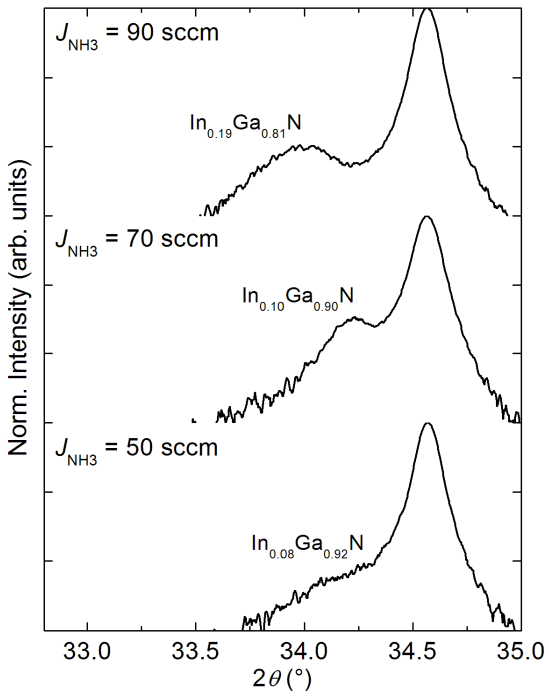

Fig. 4.3. XRD 2θ-ω of $In_xGa_{1-x}N$ films grown with J_{NH3} = 50, 70, and 90 sccm with all other growth parameters constant (T_s = 460 °C and J_{TEGa}/J_{TMIn} = 1).

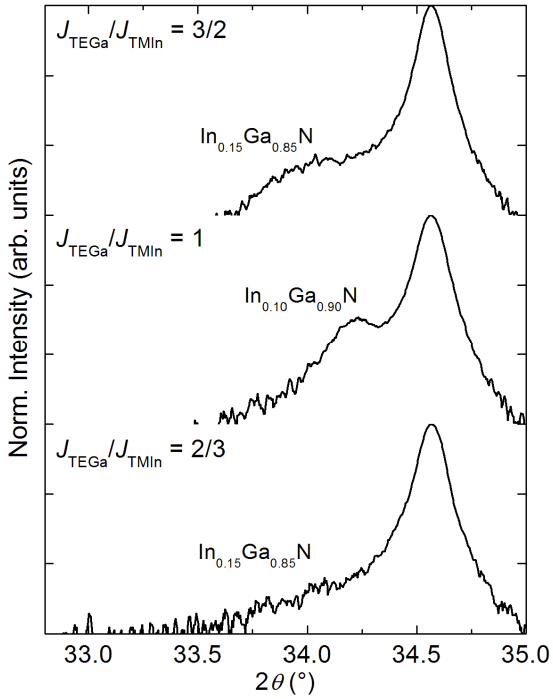

Fig. 4.4. XRD 2θ-ω of $In_xGa_{1-x}N$ films grown with J_{TEGa}/J_{TMIn} = $^2/_3$, 1, and $^3/_2$, with all other growth parameters constant (T_s = 460 °C and J_{NH3} = 70 sccm).

For the T_s = 460 °C and J_{NH3} = 70 sccm case in Fig. 4.3, the effects of J_{TEGa}/J_{TMIn} on indium composition are shown in Fig. 4.4. J_{TEGa}/J_{TMIn} = 1 was maintained with J_{TEGa} = 0.119 sccm and J_{TMIn} = 0.119 sccm. J_{TEGa}/J_{TMIn} = $^2/_3$ was maintained with J_{TEGa} = 0.095 sccm and J_{TMIn} = 0.143 sccm. J_{TEGa}/J_{TMIn} = $^3/_2$ was maintained with J_{TEGa} = 0.143 Torr and J_{TMIn} = 0.095. Increasing J_{TEGa} while reducing J_{TMIn} (J_{TEGa}/J_{TMIn} = $^3/_2$) yielded the highest indium incorporation and the fastest GR (Fig. 4.2(c)), a similar trend to that observed for increasing J_{NH3}. Since growth is already occurring in the III-rich

regime, this trend is clearly not simply a result of supplying more Ga. Since *more* In incorporates despite *less* In – and more Ga – being supplied suggests that GR is inversely related to the J_{TMIn} in this regime, as Ga will preferentially incorporate over In. Hence, ***a physisorbed In/In-methyl surface layer in the case of high J_{TMIn} is suspected to be inhibiting growth.***

4.4 Quantification of III-alkyl desorption

Fig. 4.5 plots RGA mass spectra representative of GaN and $In_xGa_{1-x}N$ growths in the present reactor. As shown, desorbing III-alkyl species ($m/e \geq 69$) are not observed during GaN growth but are significant during $In_xGa_{1-x}N$ growth. The desorbing III-alkyl species are listed in Table 4.1 and Table 4.2. Variations in signals below $m/e = 69$ have been ignored as they are dominated by NH_3 and hydrocarbon byproducts not critical to the present analysis.

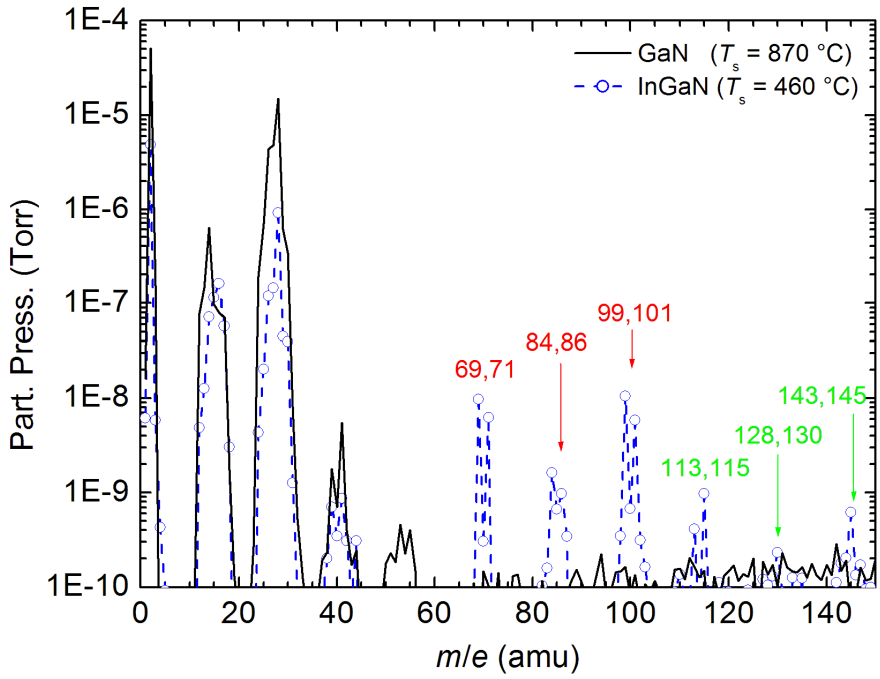

Fig. 4.5. RGA mass spectra representative of typical GaN and InGaN growths in the present reactor.

Desorbing Ga-methyls are identified with the RGA by isotope doublets at *m/e* = 69 and 71, 84 and 86, and 99 and 101, corresponding to $Ga(CH_3)_x$, where x = 0 (Ga), 1 (monomethylgallium – MMGa), or 2 (dimethylgallium – DMGa). ***Since the ethyl-gallium TEGa is used as the Ga precursor – not the methyl-gallium source TMGa – methyl related byproducts, $Ga(CH_3)_x$ species, are suspected to arise from surface reactions (and possibly gas phase reactions in the case of high local pressure) with methyl byproducts from TMIn.*** These species are not suspected as byproducts of RGA ionization, as separate measurements of TEGa cracking in the present reactor show different species at *m/e* = 85 and 87, 114 and 116, and 157 and 159 which are not observed during $In_xGa_{1-x}N$ growth. Moreover, rapid alkyl exchange has been observed in InGaAs with TMIn and TEGa [131,132], AlGaSb with TIBAl and TEGa [133], and infrared laser pyrolysis of gas-phase TEGa and TMGa [134]. In these cases, mixed alkyl

precursors are employed – causing any weakly bonded alkyls (typically ethyl groups) to be rapidly replaced by strongly bonded, less reactive alkyls (typically methyl groups).

Desorbing In-methyls are identified with the RGA by isotope doublets at *m/e* = 113 and 115, 128 and 130, and 143 and 145, corresponding to $In(CH_3)_x$, where $x = 0$ (In), 1 (monomethylindium – MMIn), or 2 (dimethylindium – DMIn). Pearson product-moment coefficients show a strong statistical correlation between all three doublets, however, the lighter isotope within each doublet consistently represented more than 20% of the respective doublet, rather than the 4.3% predicted from the indium natural isotope abundance. The heavier isotope within each $In(CH_3)_x$ doublet was found to be representative of desorbing In-methyls, whereas the lighter isotope within each indium doublet consistently tracked the Ga-methyl species, not the In species. As explained later, when Ga methyl/ethyl combinations exist in the chamber, the lighter mass RGA signal of each doublet is found to be dominated by mixed Ga-*alkyl* ($Ga(CH_3)_x(C_2H_5)_y$) contributions with minimal contribution from the In-methyl RGA signals. Moreover, even though the Ga-alkyls dominate the lighter mass of each *m/e* ≥ 113 doublet, the following detailed statistical analysis shows that ***these higher mass (m/e ≥ 113) RGA signals have negligible contributions from Ga species, allowing only m/e = 69 and 115 to accurately represent the desorption of Ga and In respectively.***

Table 4.1. Calculated mass spectrum of desorbing Ga-alkyls during present $In_xGa_{1-x}N$ growths.

***m*/*e* (amu)**	**Ga species, abundance (%)**	**Ga-alkyl**
69	27.81 ± 1.19	Ga
71	17.86 ± 0.88	
84	04.46 ± 0.11	MMGa, $GaCH_3$
86	02.89 ± 0.17	
99	29.60 ± 0.71	DMGa, $Ga(CH_3)_2$
101	17.64 ± 0.84	
113	00.71 ± 0.22	MMEGa, $Ga(CH_3)(C_2H_5)$
115	00.47 ± 0.15	
128	00.57 ± 0.30	DMEGa, $Ga(CH_3)_2(C_2H_5)$
130	00.38 ± 0.20	
143	00.36 ± 0.16	?
145	00.24 ± 0.11	

Table 4.2. Calculated mass spectrum of desorbing In-methyls during present $In_xGa_{1-x}N$ growths.

***m*/*e* (amu)**	**In species, abundance (%)**	**In-methyl**
113	02.39 ± 0.13	In
115	53.24 ± 2.97	
128	00.32 ± 0.03	MMIn, $InCH_3$
130	07.07 ± 0.63	
143	01.59 ± 0.13	DMIn, $In(CH_3)_2$
145	35.39 ± 2.89	

For quantitative accuracy, the Ga-alkyl contributions among the In-methyl RGA signals were calculated. The Ga-alkyl contributions were determined by the fraction of Ga and In necessary in each doublet to yield the expected gallium and indium natural isotope abundance. For example, considering the *m/e* = 113 and 115 doublet, the partial pressure for *m/e* = 113 (PP_{113}) is given by (4.1):

$$y \cdot [(PP_{113} + PP_{115}) \cdot 0.043] + (1\text{-}y) \cdot [(PP_{113} + PP_{115}) \cdot 0.60] = PP_{113} \qquad (4.1)$$

Here, the first bracketed term represents the signal contribution of *m/e* = 113 due only from In species. The second bracketed term represents the signal contribution of *m/e* = 113 due only from Ga species. Additionally, *y* represents the fraction of the doublet due to In/In-methyls (vs. Ga-alkyls) and 0.043 and 0.6 are the fractional natural isotope abundance for ^{113}In and ^{69}Ga respectively. Note that if no Ga-alkyl contribution were present, *y* would equal 1. By solving each doublets' contributions from Ga-alkyls (1-*y*) and In-methyls (*y*), the mass spectra of the desorbing Ga-alkyls and In-methyls during the present $In_xGa_{1-x}N$ growths were calculated, as listed in Table 4.1 and Table 4.2 respectively. As shown in Table 4.1, no more than 1% of any of the In-methyl dominated signals (*m/e* ≥ 113) is comprised of MMEGa (monomethylethylgallium) or DMEGa (dimethylethylgallium). Therefore, the tendency for the lighter isotope within each doublet with *m/e* ≥ 113 to track Ga-methyls was due to the 60% gallium natural isotope abundance for the lighter isotope versus a significantly smaller 4.3% for that of indium. While not important to the results described herein, this fortuitous weighting of isotope abundances for In and Ga results in a sensitive method to examine mixed ethyl/methyl interactions, as less than 1% mixed ethyl/methyl species can be accurately measured. It

is uncertain what Ga-alkyls may exist with m/e = 143 and 145. However, their very low abundance and high relative standard deviations suggest that that these species are not critical.

4.5 Growth condition dependence on III-alkyl desorption

Fig. 4.6(a) shows the desorption variation of III-alkyls with T_s change from 400-660 °C at a fixed J_{NH_3} = 70 sccm and J_{TEGa}/J_{TMIn} = 1. Only m/e = 69 and 115 are shown since they are considered representative of the desorbing alkyls due to relatively small standard deviations in the mass spectra shown in Table 4.1 and Table 4.2. At T_s = 400 °C, no desorbing III-alkyls are observed above the 10^{-12} Torr noise floor. At T_s = 430 °C, desorbing III-alkyls are noticeable and increase by factors of 19.6 (Ga) and 3.9 (In) as T_s is increased to 460 °C. However, the GR continues to increase while indium incorporation decreases (Fig. 4.2(a)) despite a factor of 5 preferential increase in Ga-alkyl desorption. This suggests that there is a significant population of site blocking Ga-alkyl species present at T_s = 400 °C which are readily desorbed at T_s = 460 °C. However, indium still does not incorporate effectively as enough Ga remains to preferentially incorporate. From T_s = 460-560 °C, In-methyls increase by a factor of 5.4 and Ga-alkyls increase by 1.5, consistent with an increase in indium re-evaporation at elevated T_s. From T_s = 560-660 °C, In-alkyl desorption saturates while Ga-alkyl desorption reduces by 23%. This is most likely a result of reduced TMIn adsorption at T_s = 660 °C, resulting in fewer methyl ligands present on the surface to scavenge Ga.

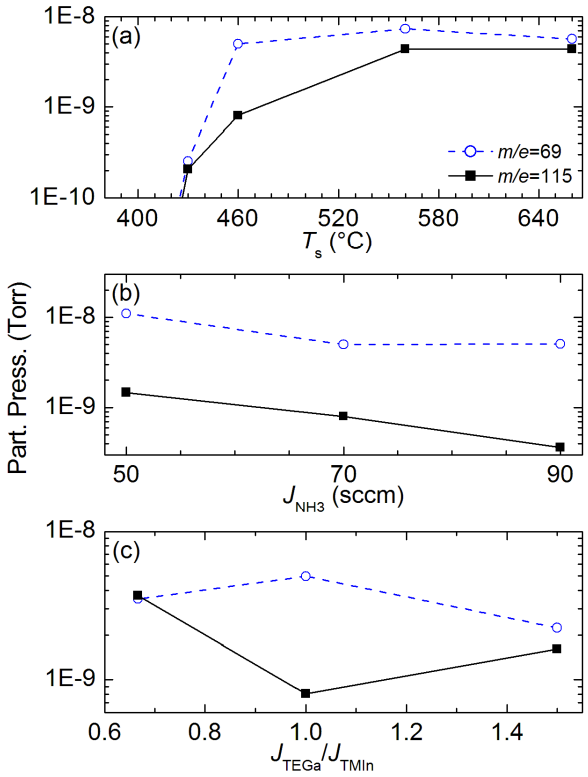

Fig. 4.6. Partial pressures of m/e = 69 and 115 (with Ga-alkyl contributions removed) during $In_xGa_{1-x}N$ growth for (a) T_s = 400-660 °C, (b) J_{NH3} = 50, 70, and 90 sccm, and (c) J_{TEGa}/J_{TMIn} = $^2/_3$, 1, and $^3/_2$.

For the T_s = 460 °C case, the effects of J_{NH3} (constant T_s and J_{TEGa}/J_{TMIn}) on III-alkyl desorption are shown in Fig. 4.6(b). A 40% increase in J_{NH3} from 50 to 70 sccm reduced Ga-alkyl and In-methyl desorption by 45% and 55% respectively, as more active N is available to consume excess Ga and In. Increasing J_{NH3} from 70 to 90 sccm decreased In-methyl desorption by 45% without affecting Ga-alkyl desorption. This demonstrates saturation of Ga-alkyl desorption due to lack of available Ga. Furthermore, the indium residence time is sufficiently long at this reduced T_s, such that the increased active N is able to consume the available In before it can desorb – resulting in the observed increases in GR and indium incorporation (Fig. 1.20b).

For the T_s = 460 °C, J_{NH_3} = 70 sccm case, the desorption variation of III-alkyls with J_{TEGa}/J_{TMIn} change from $^2/_3$ to 1 is shown in the left half of Fig. 4.6(c). A 50% increase in J_{TEGa}/J_{TMIn} ($^2/_3$ to 1) yields a 43% increase in Ga-alkyl desorption. This suggests that despite the 20% reduction in J_{TMIn}, nearly enough surface methyl species exists to scavenge the additional Ga supplied. This is consistent with the observed increases in Ga incorporation and GR (Fig. 4.2(c)). The drastic 78% reduction in In-methyl desorption with only a 20% reduction in J_{TMIn} is consistent with the scavenging of the Ga species. Specifically, as excess Ga species are available to the scavenging methyls, they are removed from the surface through alkyl exchange, resulting in additional In to contribute to the surface physisorbed layer as well as additional Ga-alkyl species.

For the T_s = 460 °C, J_{NH_3} = 70 sccm case, the desorption variation of III-alkyls with J_{TEGa}/J_{TMIn} change from 1 to $^3/_2$ is shown in the right half of Fig. 4.6(c). Increasing J_{TEGa}/J_{TMIn} from 1 to $^3/_2$ reduced Ga-alkyl desorption by 45% while doubling In-methyl desorption. The reduction in Ga-alkyl desorption is consistent with fewer surface methyl groups (reduced J_{TMIn}) available to scavenge Ga species. Similarly, the observed increase in In-methyl desorption is attributed to the reduced Ga-alkyl scavenging by In-methyls (more active N available with higher J_{TEGa}/J_{TMIn}). As discussed in the next section, the additional N available with higher J_{TEGa}/J_{TMIn} in this case promotes indium incorporation and increased GR by uncovering NH_3 adsorption sites.

4.6 Model of indium incorporation

While the results demonstrate that NH_3-based growth of InGaN is possible in the present regime, it is clear that the lack of active N due to low NH_3 cracking drastically limits the indium incorporation and GR. Indium composition and GR increase when active N is more abundant. This is seen explicitly by increasing J_{NH_3} or indirectly by increasing J_{TEGa}/J_{TMIn}, as gallium has been shown to better catalyze NH_3 cracking when compared to indium [135]. However, it is clear that what little increased active N is produced by increasing T_s > 560 °C does not compensate for the drastic increase in indium desorption. These trends are consistent with traditional RF-MBE growth of InGaN in the metal rich regime [130].

This deficiency of active N suggests the presence of a surface riding physisorbed In/In-methyl layer. This is clear by the saturation in In-methyl desorption for $T_s \geq 560$ °C, consistent with InGaAs [136,137] and InGaN MBE studies [137]. ***The ability of the In/In-methyl surface layer to block NH_3 adsorption sites and terminate $In_xGa_{1-x}N$ growth [138] is apparent in cases of low J_{NH_3} and low J_{TEGa}/J_{TMIn}.*** Therefore, the seemingly counterintuitive *increase* in indium composition with *reduced* J_{TMIn} (resulting in reduced In-methyl desorption) is consistent with the reduction of the physisorbed In/In-methyl layer surface coverage. This In/In-methyl induced site blocking issue is exacerbated by the slow GR as a result or active N deficiency, as slower growth would increase In surface segregation. This is observed in Fig. 4.2(b) in the increase in indium composition as GR increases by increasing J_{NH_3}. Furthermore, this

suggests that in NH_3-based growth, it is critical to be near $T_s \sim 540$ °C [78] to achieve both as much active N as possible and to reduce In/In-methyl surface coverage.

Furthermore, ***the high surface In/In-methyl coverage helps facilitate the formation and desorption of Ga-alkyl species by rapid alkyl exchange (ethyl with methyl)*** in a similar manner to that previously observed with the use of mixed alkyl precursors [131-134]. As physisorbed In and In-methyl species ride on the surface, methyl ligands strongly bond to excess Ga atoms made available via facile β-elimination [122,123]. The surface layer has been shown to enhance desorption of Ga-alkyls in the case of In covered GaAs [25] and InGaAs with TMIn [140]. The latter case proposed Ga-ethyl desorption, but no direct evidence identifying Ga-ethyl (vs. Ga-methyl) species was given. As no desorbing Ga-ethyls are presently observed, it is suspected that the exchange with surface methyl ligands occurs rapidly [134], resulting in the observed Ga-alkyl desorption (mostly Ga-methyl as shown in Table 4.1). However, the III-rich conditions and surface methyl ligands inhibit subsequent incorporation of the Ga-methyl species, facilitating their desorption [141]. This is most apparent in the $T_s = 660$ °C case (Fig. 4.6(a)), as In-methyl desorption saturates while Ga-alkyl desorption decreases after monotonic increases with increasing T_s. This suggests that enough surface In-methyl species have been removed as a result of an increase in In/In-methyl desorption at elevated T_s, allowing Ga adsorption. This is also clear in the highest J_{TEGa}/J_{TMIn} case (Fig. 4.6(c)) where Ga-alkyl desorption is reduced (Ga incorporation) while In-methyl desorption increases (reduced In/In-methyl surface layer), resulting in an observed *increase* in indium incorporation. This methyl exchange can be a mechanism for incorporating additional indium by scavenging Ga species (in the present case as the Ga-

methyls originate from the TMIn species exchanging with TEGa) if enough active N is available to consume the physisorbed In/In-methyl layer. ***However, the use of precursors with the same alkyl species, all ethyl- or all isopropyl- for this temperature regime [142], should alleviate mixed alkyl induced scavenging.***

4.7 Conclusions

The growth of $In_xGa_{1-x}N$ by NH_3-based MOMBE and the effects of T_s, J_{NH3}, and J_{TEGa}/J_{TMIn} on the GR and alloy composition have been investigated. N-limited growth from insufficient NH_3 cracking at T_s = 400–660 °C is observed as GR increases with increasing J_{NH3}. A physisorbed In/In-methyl surface layer is shown to further inhibit growth by blocking precursor adsorption in cases of highly deficient active N and high J_{TMIn}. Desorbing III-alkyl species are observed and cracking patterns for the desorbing species are calculated. The observed variations in III-alkyl desorption with changing growth conditions suggest that methyl groups attach to decomposed TEGa species and do not incorporate. Instead, the methyl groups effectively scavenge surface Ga atoms for N-limited growth with high In/In-methyl surface coverage.

The results demonstrate for the first time that NH_3-based MOMBE is capable of $In_xGa_{1-x}N$ growth but active N, indium surface coverage, and mixed alkyl scavenging must be carefully considered. These three interdependent variables set an upper limit to In incorporation but also provide sensitive, exploitable mechanisms to enable 3DE. Hence, these multiple mechanisms governing alloy composition and GR suggest that

NH_3-based MOMBE may be a good candidate to realize 3DE via localized manipulation of these mechanisms, as demonstrated in Chapter 5.

CHAPTER 5: UV-INDUCED $In_xGa_{1-x}N$ ALLOY MODULATION AND PATTERNING

5.1 Introduction

Novel device concepts integrating features such as low-dimensionality and lateral bandgap energy modulation are complicated by expensive lithography, etching, and regrowth sequences. *In situ* patterning via direct write technologies such as focused ion beam (FIB) [143] and laser rastering [144] are demonstrating increasing potential as a pathway toward realizing 3DE. Alternatively, MOMBE may be a better candidate for patterned epitaxy *in situ* because of its sensitive growth mechanism in a high vacuum environment – allowing potentially easier manipulation of growth while maintaining high selectivity. The MOMBE growth mechanism consists of metal organic surface adsorption and reaction with subsequent surface diffusion, lattice incorporation, or desorption of resultant ligands – any of which may be carefully manipulated for selective epitaxy. Despite successful arsenide [31], phosphide [31], and antimonide [32] based structures grown by MOMBE with patterned dielectric masks, NH_3-based MOMBE of nitrides has received little attention.

In this chapter, the effects of UV irradiation during $In_xGa_{1-x}N$ growth are investigated. ***UV radiation during growth is observed to inhibit indium incorporation in InGaN. This effect of UV radiation is leveraged by digital micromirror optical patterning technology to produce the first intentionally compositionally patterned***

InGaN by NH_3-based MOMBE. These results demonstrate that the presented technology is a feasible pathway toward realizing 3DE.

5.2 Experimental procedure

$In_xGa_{1-x}N$ films were grown in a custom NH_3-based MOMBE showerhead reactor (Chapter 2) on c-plane (0001) sapphire using TEGa, TMIn, and NH_3. A ~2 μm tantalum film was sputtered onto the backside of each substrate to promote efficient heating. Samples were immersed twice for 10 min each in a 90 °C piranha solution of H_2SO_4:H_2O_2 (4:1) before loading into the reactor, additional details of the etch are in [128].

InGaN films were grown on a ~200 nm GaN layer. The GaN layer was grown following a NH_3 nitridation of the sapphire substrate and subsequent GaN buffer deposition at T_s = 540 °C described elsewhere [145]. The InGaN was grown at T_s = 460 °C with J_{NH_3} = 70 sccm and $J_{TEGa} = J_{TMIn}$ = 0.119 sccm. To preclude variations from buffer layer quality due to difficult low temperature GaN nucleation using NH_3 [33], the compositionally patterned InGaN samples were grown on 3.5 μm Si-doped GaN templates (Lumilog, Vallauris, France), additional details are in §A.5. Additionally, the patterned samples were grown using slightly higher indium incorporation and GR conditions of J_{NH_3} = 90 sccm and $J_{TEGa} = J_{TMIn}$ = 0.095 sccm [145].

5.3 Inhibition of indium incorporation by UV photoexcitation

XRD 2θ-ω scans of $In_xGa_{1-x}N$ (002) are shown Fig. 5.1. For interpretation of the XRD data, it is assumed that the layer is fully strain relaxed and that Vegard's law applies. The data summarizes four samples – two exposed to UV photoexcitation during InGaN deposition, and two without UV photoexcitation. The only growth condition variation was the presence of UV photoexcitation during the InGaN layer. The UV photoexcitation was introduced by a custom 5 kW Hg-Xe arc lamp assembly such that the spot size on the substrate was ~6" in diameter, corresponding to an estimated maximum above-bandgap irradiance of 3.17 W/cm^2 and above-bandgap photon fluence of 5.82×10^{18} photons/cm^2·s (§3.3). ***$In_{0.10}Ga_{0.90}N$ is grown in the absence of UV photoexcitation at a GR of 31 nm/hr. Exposing the films to UV photoexcitation during growth – with all other conditions constant – increases the GR by a factor of 4 and inhibits indium incorporation, resulting in GaN growth*** (as evidenced by only a single GaN (002) diffraction peak). No consistent variations in surface morphology as discerned as a result of UV photoexcitation.

Fig. 5.2 plots the average partial pressure during InGaN growth of signals characteristic of NH_3 (m/e = 14, 16, 28), hydrocarbon byproducts such as ethane (m/e = 30), argon (m/e = 40), CO_2 (m/e = 44), desorbing Ga/Ga-alkyls (m/e = 69), and desorbing In/In-methyls (m/e = 115). As shown, exposure to UV photoexcitation increased the NH_3, ethane, and Ga-alkyl related partial pressures in the chamber by a factor of ~4, which is slightly greater but comparable to the factor of 2.6 increase in the unrelated argon partial pressure indicating that some photoenhanced desorption occurs – a known effect of UV

irradiation on vacuum systems. However, UV exposure increased the CO_2 and In/In-methyl partial pressures by one-order. The drastic increase in CO_2 is likely a result of effective cleaning of adsorbed hydrocarbon contaminants from the chamber walls by stray UV [146]. ***However, the one-order increase In/In-methyl desorption during growths exposed to UV irradiation and the absence of In in the resultant films suggests that the UV irradiation inhibts indium incorporation via a surface In/In-methyl depletion mechanism.***

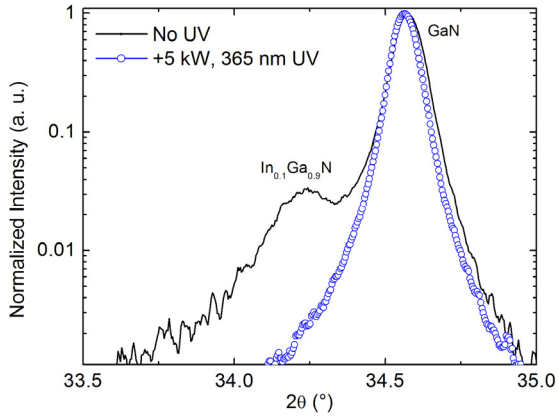

Fig. 5.1. XRD 2θ-ω of $In_{0.1}Ga_{0.9}N$ (002) with and without *in situ* UV photoexcitation.

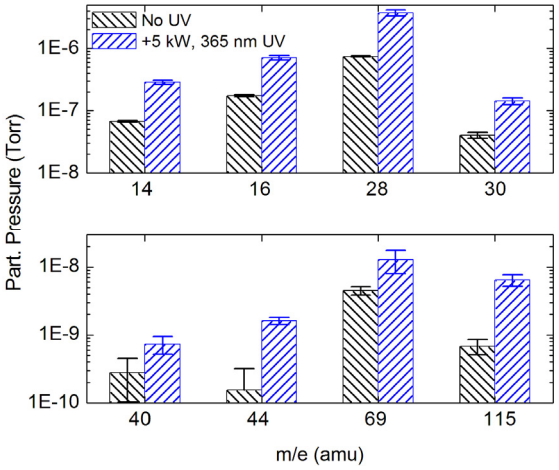

Fig. 5.2. Partial pressure of signals characteristic of NH_3 (*m/e* = 14, 16, 28), hydrocarbon byproducts such as ethane (*m/e* = 30), argon (*m/e* = 40), CO_2 (*m/e* = 44), desorbing Ga-alkyls (*m/e* = 69), and desorbing In-methyls (*m/e* = 115) during InGaN growth with and without *in situ* UV photoexcitation.

5.4 Absence of gas-phase photolysis

TEGa, TMIn, and NH_3 which are used for the growth of InGaN are transparent to radiation with $\lambda \geq 310$ nm. Hence, photolysis of the source precursors is not considered a

mechanism for the inhibition of indium incorporation under UV irradiation (*e.g.* depletion of indium by dissociation of TMIn in the gas phase). TEGa exhibits no absorption for $\lambda \geq 310$ nm, with strong absorption for $\lambda < 213$ nm and a corresponding absorption cross section, $\sigma \sim 7 \times 10^{-18}$ cm^2·molecule^{-1} [119,147,148]. TMIn exhibits no absorption for $\lambda \geq 270$ nm, with strong absorption for $\lambda < 211$ nm and a corresponding $\sigma \sim 3 \times 10^{-17}$ cm^2·molecule^{-1} [149-151]. NH_3 exhibits no absorption for $\lambda \geq 225$ nm, with strong absorption of $\lambda < 208$ nm and a corresponding $\sigma \sim 1 \times 10^{-17}$ cm^2·molecule^{-1} [152].

5.5 Mechanism for inhibition of In incorporation – preliminary observations

The increase in In/In-methyl desorption and the subsequent reduction in indium incorporation and increase in GR is consistent with an increase in $T_s > 560$ °C [145], where In re-evaporation results in a deficiency of indium available to incorporate in the growing film. Compensation of power to the substrate heater by ~25% (23.2 W) by the PID controller is observed when UV irradiation is incident on the sample. The power compensation suggests that significant heating of the surface may be a mechanism reducing the incorporation of indium, as has been observed during the MBE of InGaN using a focused thermal beam [144]. The factor of 4 faster GR observed under UV irradiation is consistent with an increase in active N availability during growth under III-rich/N-limited conditions, which could arise from an increase in NH_3 cracking efficiency with elevated T_s [135] or the decrease in surface indium coverage. However, a detailed treatment given in Chapter 6 shows that the UV-induced preferential desorption of In/In-

methyls occurs predominately through a photochemical mechanism, rather than through significant heating of the surface.

5.6 Dynamic patterning of incident UV for localized indium inhomegeneity

Fig. 5.3 shows a schematic of the apparatus used to irradiate films with patterned UV *in situ*. A Texas Instruments UV-grade DMD (>90% single pass window transmission) is used to pattern radiation from the 5 kW Hg-Xe arc lamp assembly. The UV-grade DMD (Fig. 5.4) consist of a 1024×768 array of mechanical mirrors on a ~13 μm pitch, each capable of being individually and simultaneously deflected across a hinged diagonal. A quartz fused silica lens focuses the DMD patterns onto the sample. A photograph of the optical assembly is shown in Fig. 5.5.

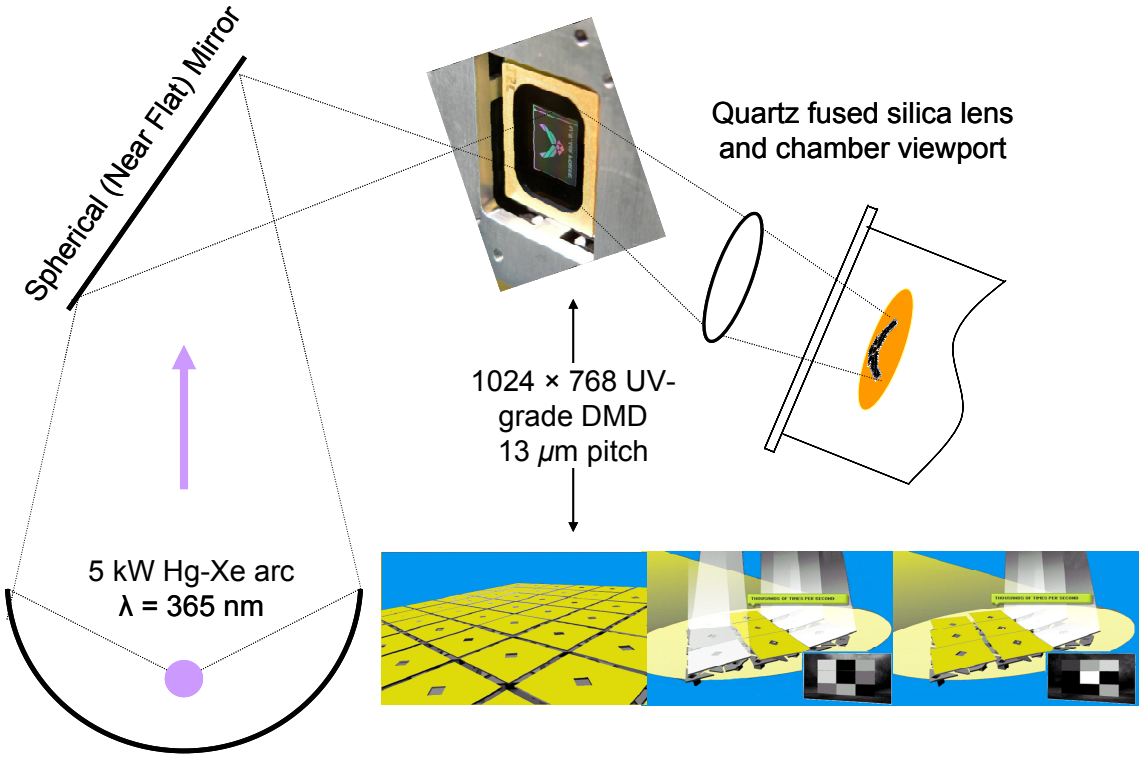

Fig. 5.3. Schematic representation of optical assembly for patterned *in situ* UV photoexcitation. The DMD operation showing grey scale formation is courtesy of Texas Instruments. The schematic is not to scale.

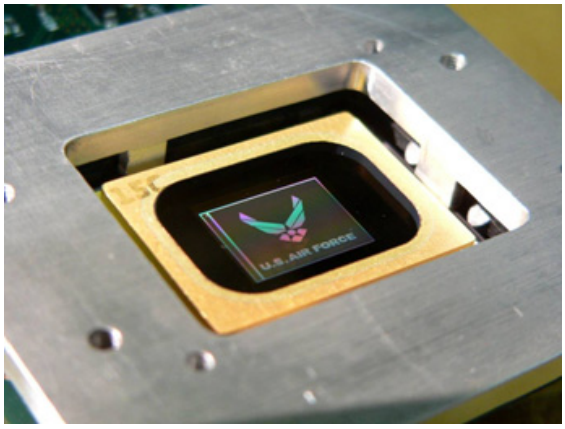

Fig. 5.4. TI UV-grade DMD (UV-DMD) of a DMD Discovery 1100 system displaying the U.S. Air Force logo. The DMD consist of a 1024 × 768 array of mechanical mirrors on a ~13 μm pitch.

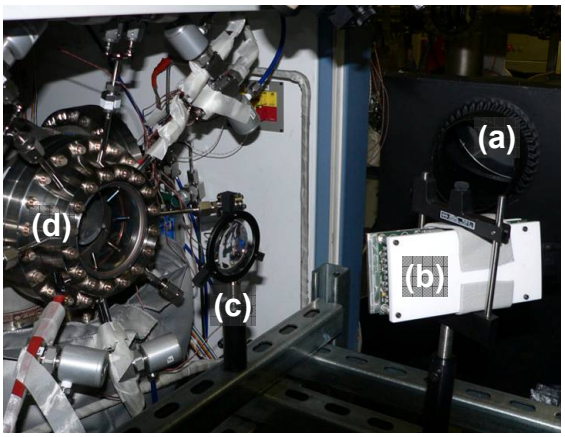

Fig. 5.5. UV patterning assembly using a UV-DMD, with the (a) 5 kW Hg-Xe UV illumination assembly, (b) TI DMD Discovery 1100 system with UV-DMD (only the backside is visible), (c) quartz focusing lens, and (d) MOMBE growth chamber with sample loaded.

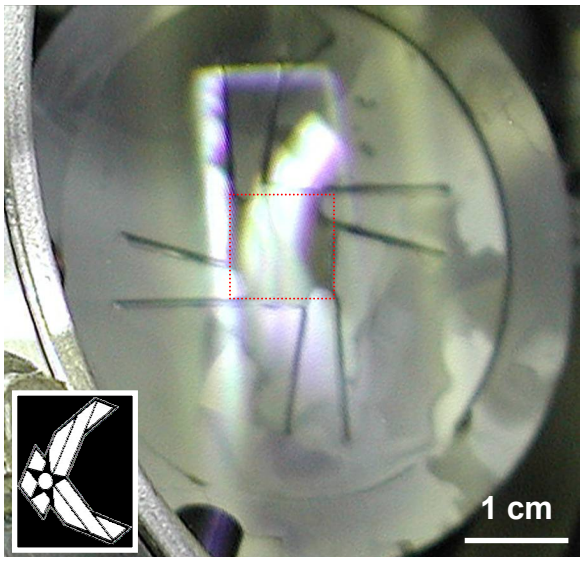

Fig. 5.6. Visible component of the 5 kW Hg-Xe arc lamp radiation patterned by a UV-DMD and incident on the sample (red box). The inset displays the DMD pattern.

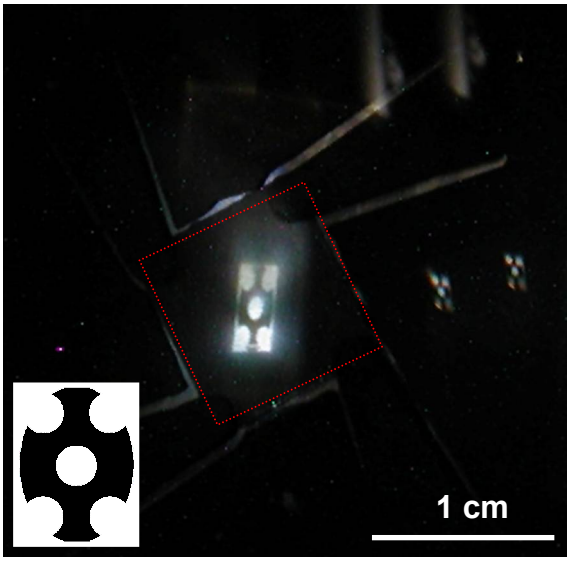

Fig. 5.7. Visible component of the 5 kW Hg-Xe arc lamp radiation patterned by a UV-DMD and incident on the sample (red box). The inset displays the DMD pattern.

Fig. 5.6 shows a photograph of the visible component of the 5 kW Hg-Xe arc lamp radiation patterned by the UV-DMD and incident on a 1×1 cm sample. The corresponding normalized XRD intensity map of the $In_{0.1}Ga_{0.9}N$ (002) peak for the sample grown under the DMD patterned UV irradiation is shown in Fig. 5.8(a), with the patterned UV irradiation overlaid in white. The main region exposed to UV irradiation shows a significant intensity reduction for the 10% indium mole fraction peak. When the same layer is grown without UV irradiation, a radial variation in the intensity of the same peak is observed (as expected) – as shown in Fig. 5.8(b). The detectability limit of XRD and the blurred projected features are expected to contribute to the modest detection of patterned submillimeter features in the XRD intensity map. Fig. 5.7 shows that a significantly improved projection contrast ratio is possible.

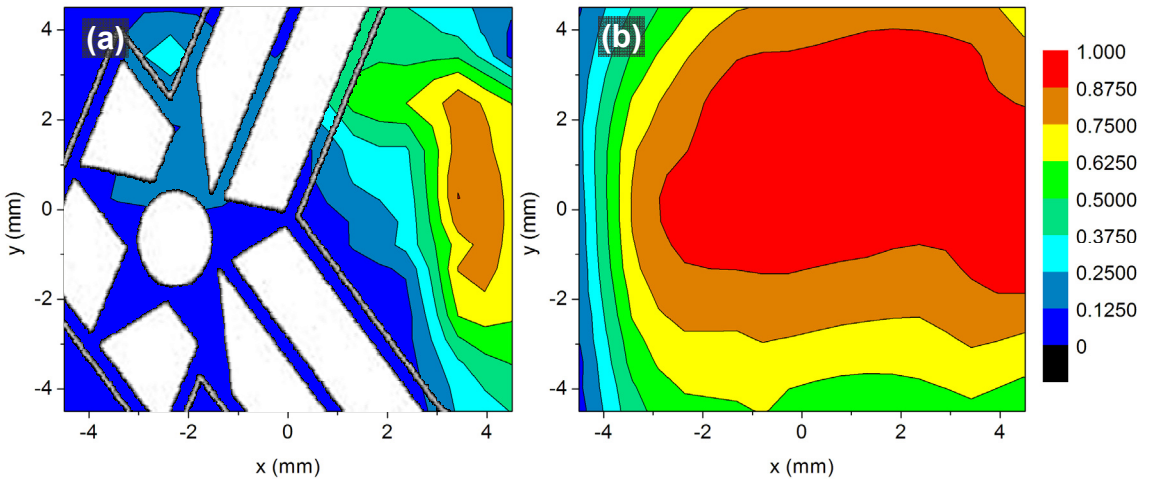

Fig. 5.8. 1 × 1 mm resolution normalized XRD intensity map of $In_{0.1}Ga_{0.9}N$ (002) peak of (a) sample exposed to DMD patterned UV irradiation (white overlay) and (b) sample not exposed to UV irradiation.

5.7 Conclusions

The manipulation of InGaN growth *in situ* by UV photoexcitation during NH_3-based MOMBE has been investigated. UV photoexcitation during growth resulted in a factor of 4 faster GR while inhibiting the incorporation of indium. Analysis of reaction byproducts suggest that the ***UV photoexcitation preferentially desorbs In/In-methyl species during growth, effectively limiting the surface indium available to incorporate into the alloy. Moreover, the first successful in situ compositionally patterned InGaN using digital micromirror patterning of incident UV photoexcitation is reported.*** Coupled with UV photoexcitation effects on GaN carbon doping [38], the technique shows promise for dynamic manipulation during NH_3-based MOMBE which could be used as a pathway toward the realization of complex 3D device structures by 3DE.

CHAPTER 6: IMPROVED UNDERSTANDING OF UV-INDUCED $In_xGa_{1-x}N$ ALLOY MODULATION

6.1 Introduction

UV irradiation during NH_3-based MOMBE has demonstrated significant GaN dopant [38,153] and $In_xGa_{1-x}N$ composition [154] variation. In Chapter 3, UV irradiation during GaN growth increased hydrocarbon liberation from the surface, effectively limiting the C incorporation into the film. Analysis of the residual byproducts during growth showed that the formation and subsequent liberation of stable hydrocarbon species was significantly more dependent on UV irradiation than T_s – suggesting that the photo-induced processes in the studied regime were predominately photochemical rather thermally activated (pyrolytic). In Chapter 5, UV irradiation was found to increase residual In/In-methyl species preferentially during InGaN deposition, effectively limiting the indium species available to incorporate into InGaN. However, In/In-methyl desorption is strongly dependent on T_s (Chapter 4) in the studied regime, making it unclear if the observed photo-desorption is thermally or chemically activated.

In this chapter, the dominant origin of the photo-induced In/In-methyl desorption that has been identified as the mechanism for the reduction in indium incorporation during UV irradiation of InGaN growth is discussed. Thermodynamic analysis suggests that photo-induced heating of the film should be mitigated effectively by the compensation applied to the substrate heater by the PID control loop. Therefore, a

photochemical effect – rather than photothermal effect – is believed to be the dominant origin for the preferential increase in In/In-methyl desorption (and consequently reduction in indium incorporation) during NH_3-based MOMBE of InGaN under UV irradiation, with an estimated above-bandgap irradiance threshold between 102 mW/cm^2 – 3.17 W/cm^2 under the present conditions.

6.2 Mitigation of heating induced by UV irradiation

While the integrated thermocouple (TC) of the FISH module (§2.2) probes the substrate backside temperature, the TC is capable of sensing the GaN surface temperature within ~1 °C in the present configuration. This is supported by considering the largest temperature gradient (ΔT) capable of being sustained across the substrate stack – from the front surface Si-doped GaN template layer, through the sapphire substrate, and to the backside-metalized tantalum layer. The largest ΔT that can be sustained (upper limit) is approximated by using the following assumptions:

1. Heat is input only from the UV irradiated Si-doped GaN template layer, hence it is considered the hottest side of the layer stack in this model (heat input from the substrate heater is neglected to model the largest ΔT).
2. Heat is lost only via radiation from the metalized backside tantalum layer of area $A = 1 \times 10^{-4}$ m^2, hence it is considered the coldest side of the layer stack in this model (radiative loss from the GaN surface and the edges are neglected to model the largest ΔT).

3. The thermal gradients through in the 3.5 μm GaN template layer (thermal conductivity κ = 130 W $m^{-1}K^{-1}$) and the 2 μm tantalum layer are negligible compared to the sapphire substrate (3.3 × 10^{-4} m thick, κ = 15 W m^{-1} K^{-1}). The thermal gradient through a deposited InGaN layer is considered insignificant.
4. Negligible conductive losses occur between the layers.

With these assumptions, the worst case possible ΔT of the substrate layer stack for the present growths can be approximated. For a sample thickness d and thermal conductivity κ, ΔT can be approximated by (6.1) [155].

$$A\varepsilon\sigma T_s^4 = \kappa A\frac{\Delta T}{d} \tag{6.1}$$

The Stefan-Boltzmann constant, σ = 5.6703 × 10^{-8} W m^{-2} K^{-4}. At T_s = 750 K and a tantalum emissivity ε_{Ta} ~ 0.1, a ΔT through the sapphire substrate (effectively the substrate layer stack) of less than 0.1 °C can be sustained. Even assuming black body radiation loss from the cold side, the sustained ΔT is less than 0.4 °C. Therefore, ***the thermal conductivity of the sapphire sufficiently limits an appreciable temperature gradient (ΔT) through the substrate layer stack and that the temperature gradient from the irradiated front side to the metalized backside is insignificant. This negligible ΔT eliminates the possibility that the average temperature of the growth surface could be significantly hotter under UV irradiation compared to the substrate backside being probed by the TC, which could cause the TC to provide insufficient input to the PID control loop.*** Even though the true surface temperature could be in question (the accuracy of the true surface temperature in UHV is ~±40 °C), the TC can sense variations in the average surface temperature accurately for input to the PID control loop.

Additional details supporting that the power compensation to the substrate heater sufficiently mitigates heating of the sample by irradiation from the Hg-Xe arc lamp is given in §A.4.

6.3 Effects of HeCd laser irradiation on InGaN growth

The preceding analysis describes that UV-induced heating is sufficiently mitigated and as such is not believed to be the dominant origin for the increased desorption of In/In-methyl species under UV irradiation. In this section, the effects of irradiating films with a continuous wave (CW) HeCd laser (Omnichrome 3056-M-A03, 18 mW, λ = 325 nm) during InGaN growth is investigated in an attempt to clarify possible photochemical mechanisms resulting in In/In-methyl desorption. Two HeCd laser line dielectric mirrors with $R > 99\%$ at $\lambda = 325$ nm direct the laser beam onto the sample. The laser spot diameter on the surface is 4.5 mm and the laser yields yellow luminescence (YL) from the MOCVD-grown Si-doped GaN template (Fig. 6.1). No significant heating is observed under HeCd laser irradiation, as detailed in §A.4.

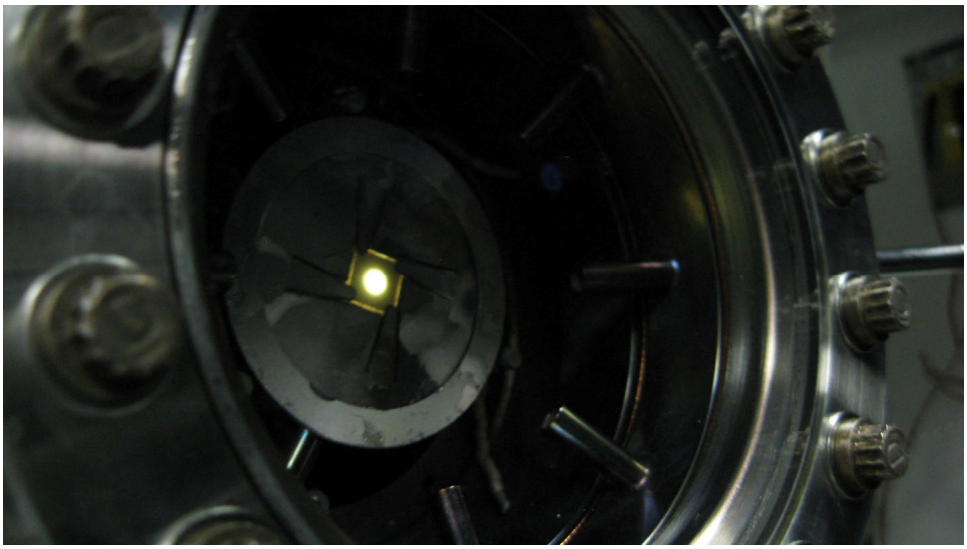

Fig. 6.1. HeCd laser irradiation incident on a 1 × 1 cm GaN template at 300 K before InGaN growth. YL is observed from the Si-doped GaN template.

No dramatic variations in InGaN films are observed as a result of HeCd laser irradiation during growth. Normalized XRD 2θ-ω scans and respective GRs of $In_xGa_{1-x}N$ films grown on Si-doped GaN templates at T_s = 430, 460, and 500 °C are shown in Fig. 6.2. Corresponding surface morphologies and σ_{RMS} are shown in Fig. 6.3. J_{NH_3} = 85 sccm, J_{TMIn} = 0.095 sccm, and J_{TEGa} = 0.143 sccm (J_{TEGa}/J_{TMIn} = $^3/_2$) remained fixed during deposition of each $In_xGa_{1-x}N$ layer (123 min, N-rich conditions). For interpretation of the XRD data, it is assumed that the $In_xGa_{1-x}N$ layer is fully strain relaxed and that Vegard's law applies. With increasing T_s, the resultant indium mole fraction x decreases while the GR increases. Also, the surface morphologies (T_s = 460 and 500 °C) are indicative of N-rich growth with an increasing degree of N-richness with increasing T_s (Chapter 7). These observations are consistent with reduced In/In-methyl site-blocking and increased N availability at increased T_s. $In_xGa_{1-x}N$ films grown with HeCd laser radiation show variations in x, GR, and surface morphology that are within the run-to-run repeatability and uniformity limit of the $In_xGa_{1-x}N$ films grown under the

specified low T_s conditions. Similarly, no variations in residual byproduct species in the growth chamber are observed that are a result of HeCd laser irradiation.

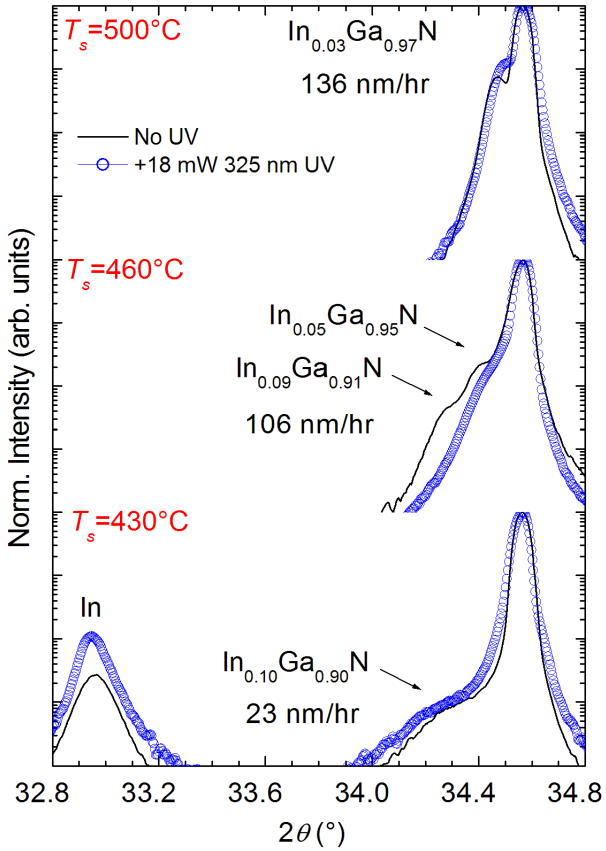

Fig. 6.2. XRD 2θ-ω of $In_xGa_{1-x}N$ (002) grown at T_s = 430, 460, and 500 °C with and without HeCd laser irradiation *in situ*. GR for each T_s are shown and are independent of HeCd laser irradiation.

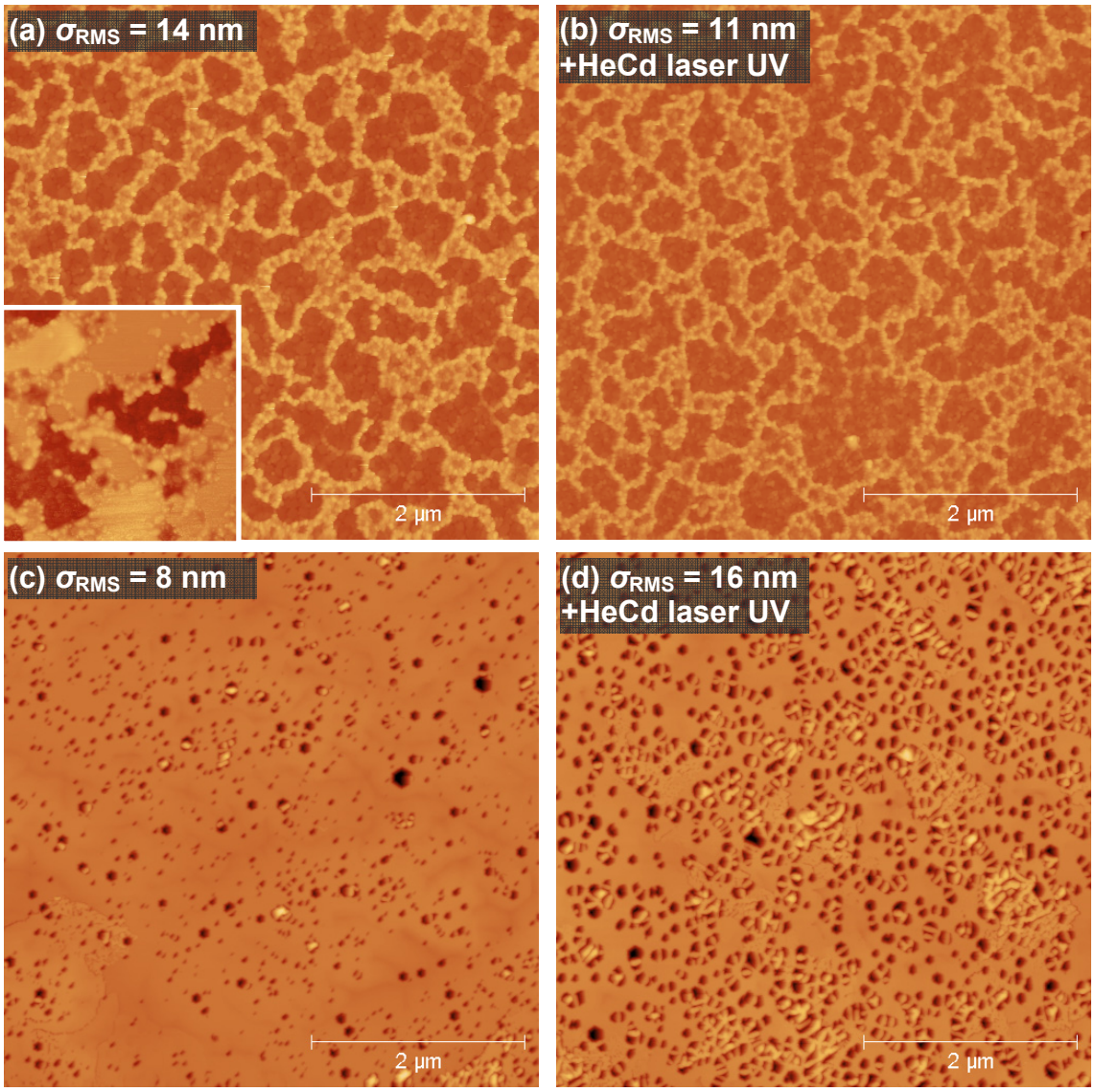
(a) σ_{RMS} = 14 nm
2 µm
(b) σ_{RMS} = 11 nm
+HeCd laser UV
2 µm
(c) σ_{RMS} = 8 nm
2 µm
(d) σ_{RMS} = 16 nm
+HeCd laser UV
2 µm

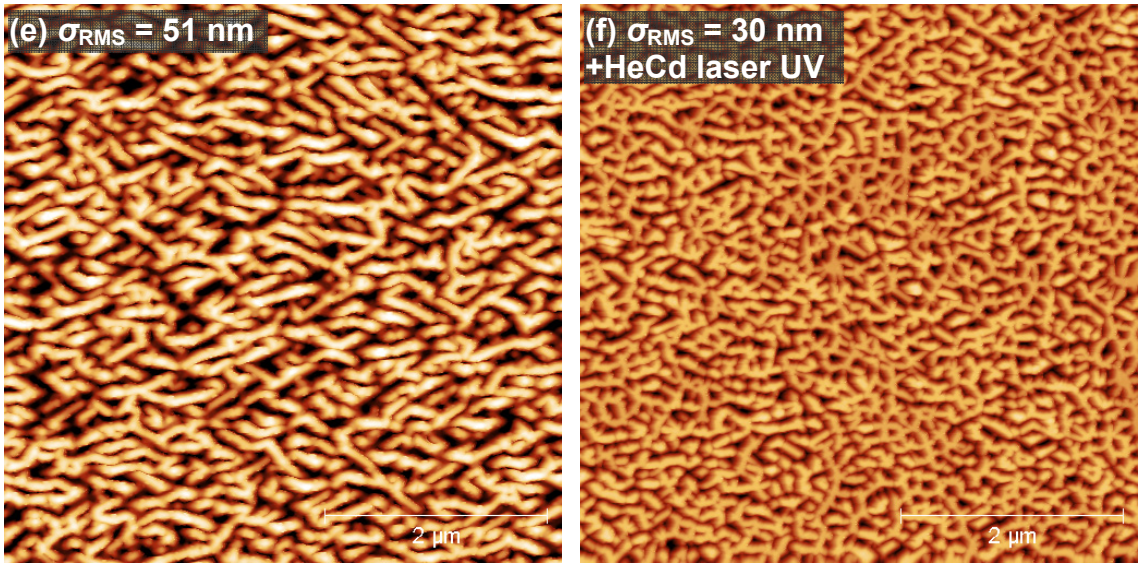

Fig. 6.3. $5 \times 5\ \mu m^2$ AFM surface morphologies and σ_{RMS} of InGaN layers grown at T_s = (a,b) 430, (c,d) 460, and (e,f) 500 °C under the specified HeCd laser irradiation conditions. The height scales are -100 to 100 nm. The inset of (a) is $2 \times 2\ \mu m^2$ morphology of an InGaN layer with III-droplets that are not etched by HCl prior to AFM measurement.

6.4 Irradiance threshold for UV-induced photodesorption

Assuming a spatially uniform HeCd laser beam, an irradiation beam spot diameter of 4.5 mm, and a viewport transmittance of 90% at λ = 325 nm, the maximum above-bandgap irradiance is estimated at 102 mW/cm^2. Assuming that the energy of every photon is 3.82 eV (λ = 325 nm), the corresponding photon fluence incident during growth is 1.66×10^{17} cm^{-2} s^{-1}. Table 6.1 shows the effective number of 3.82 eV photons per GaN surface atom deposited for the present conditions, assuming one ML of GaN (0001) contains 1.14×10^{15} atoms/cm^2 [156] (GaN atomic density of 8.775×10^{22} atoms/cm^3, 1 ML = 5.189/2 Å). For the T_s = 430 °C case, the photons are incident on metallic indium, and as such the case is not considered. Since no dramatic heating occurs in bulk, the lack of a dramatic effect of HeCd laser irradiation *in situ* on the resultant InGaN films

suggests that the incident fluence from the HeCd laser is insufficient to induce significant desorption affecting the indium incorporation or residual In/In-methyl species. In contrast, the above-bandgap irradiance of the Hg-Xe arc lamp focused to a 6" diameter spot is 3.17 W/cm^2 (§3.3), corresponding to an above-bandgap photon fluence of 5.82×10^{18} photons/cm^2·s, which is a factor of ~35 higher than that of the HeCd laser. The effective number of 3.4 eV photons per GaN atom deposited for the observed GRs of Chapter 5 are given in Table 6.2. As described in Chapter 5, these irradiance conditions of the Hg-Xe arc lamp are sufficient to induce a discernable increase in the In/In-methyl residual species, which effectively limits the indium available to incorporate by photo-desorbing these species from the surface. The exact threshold for this effect remains unknown, but it is clear that the HeCd laser is insufficient for inducing a strong effect on indium incorporation. Therefore, the necessary above-bandgap irradiance is estimated at 102 mW/cm^2 – 3.17 W/cm^2.

Table 6.1. The average GRs and corresponding number of 3.82 eV photons per atom during HeCd irradiation of the present $In_xGa_{1-x}N$ growths. The calculations assume all photons are 3.82 eV and are incident on 1.14×10^{15} atoms/cm^2 of GaN.

T_s (°C)	**<GR> (nm/hr)**	**<GR> ML/s**	**<GR> atoms/cm^2·s**	**photons per each atom deposited (1.66×10^{17} photons/cm^2·s)**
430	23	0.0246	2.81×10^{13}	5,925
460	106	0.1135	1.29×10^{14}	1,286
500	137	0.1467	1.67×10^{14}	995
-	1000	1.0706	1.22×10^{15}	136

Table 6.2. The average GRs and corresponding number of 3.4 eV photons per atom during Hg-Xe arc lamp irradiation (6" spot diameter) of the $In_xGa_{1-x}N$ growths in Chapter 5. The calculations assume all photons are 3.4 eV and are incident on 1.14×10^{15} atoms/cm^2 of GaN.

T_s (°C)	**<GR> (nm/hr)**	**<GR> ML/s**	**<GR> atoms/cm^2·s**	**photons per each atom deposited (6" spot diameter, 5.82×10^{18} photons/cm^2·s)**
460	31	0.0332	3.78×10^{13}	153,884
460 (UV)	124	0.1328	1.51×10^{14}	38,471

6.5 Photochemical effects of UV irradiation

Unless multi-photon absorption occurs, the present irradiation does not directly induce photodissociation of bulk/surface atoms. The cohesive energy per each In-N bond is 1.93 eV [157], resulting in a bond strength ~ 4 × 1.93 eV = 7.72 eV (3 × 1.93 eV = 5.79 eV for a surface atom) meaning that incident photons (~3.4 eV) are of insufficient energy to cleave anything but a single bond.

A variety of photochemical processes may be responsible for the observed increase residual In/In-methyl species in the presence of intense UV irradiation. The above-bandgap irradiation can directly excite the adsorbate molecules or indirectly excite carriers in the GaN template that can subsequently diffuse to the surface; either of these cases can stimulate desorption through a variety of processes. These processes are classified under the blanket of desorption induced by electronic transitions (DIET) which is described generally by the Menzel-Gomer-Redhead model in which the absorption of a

photon or electron excites a repulsive state that induces desorption if the lifetime of the excited state is sufficiently long [158,159]. This model suggests a virtually endless variety of scenarios which may be photostimulated, including the enhanced desorption of TMIn or necessary dissociating species (*e.g.* DMIn), the production of intermediates which subsequently desorb, or the enhanced adsorption of TEGa, among others. Unfortunately, the present residual gas data does not elucidate specific reaction pathways that result in the observed increase in residual In/In-methyl species under intense UV irradiation. Further work would be necessary to elucidate specific reactions.

6.6 Conclusions

The origin for the increase in residual In/In-methyl species under intense UV irradiation is considered. Thermodynamic analysis shows the temperature gradient that can be sustained through the substrate layer stack is negligible, meaning that the compensation by the PID control loop should mitigate significant UV-induced heating in the substrate and that the origin of In/In-methyl residual species is through chemical photodesorption. The effects of HeCd laser irradiation *in situ* on the growth of InGaN by NH_3-based MOMBE are studied and the irradiance delivered is observed to be insufficient to induce a strong effect on the resultant InGaN films. The threshold for the above-bandgap irradiance that is necessary to inhibit the incorporation of indium is estimated to be 102 mW/cm^2 – 3.17 W/cm^2 under the present conditions.

CHAPTER 7: IMPROVED UNDERSTANDING OF NH_3-BASED MOMBE

7.1 Introduction

In order to grow high quality GaN, effectively dope impurities into GaN, or effectively alloy InN or AlN with GaN, it is necessary to identify the regime for which GaN is growing and understand the effect of growth parameters on the growth regime. The regime under which GaN growth proceeds has significant effects on the growth process, and consequently affects the composition and characteristics of the resultant film. The growth regimes for GaN have been studied extensively in plasma-assisted MBE, and growth has been modeled in the context of three regimes: N-rich, Ga-rich, and Ga-rich with droplets [160]. However, the availability of reactant adatoms in NH_3-based MOMBE is significantly more complicated than that of plasma-assisted MBE. ***In NH_3-based MOMBE, the adatom densities exhibit complex interdependencies between precursor flux J, reactant surface coverage and residence lifetime, alkyl species, GR, and T_s.*** For example, utilizing on-surface cracking of NH_3 to produce active N means that the active N population is dependent on T_s. The active N population is also dependent on the density of catalysts, such as Al or Ga atoms. But, the effective cation population is dependent on not only the GR (*e.g.* surface segregation) and T_s, but also the presence of alkyls which can effectively getter the cation species (Chapter 4). Such interdependencies significantly complicate the NH_3-based MOMBE growth process. In order to improve the quality of III-Nitride films by NH_3-based MOMBE and to identify

the growth conditions for which dopants should effectively incorporate, the growth regimes and their dependence on growth parameters must be better defined.

In this chapter, the growth regimes during the NH_3-based MOMBE of GaN are studied for the first time. The influence J_{NH3}/J_{III} on the growth regimes and GR are identified for T_s relevant to the doping of GaN with Mg. ***Specific N-rich/Ga-limited growth conditions are identified during NH_3-based MOMBE that result in GaN films exhibiting atomically smooth surfaces.*** Granular surfaces with ~3 nm RMS roughness are observed for certain Ga-rich conditions. The surface morphologies resulting from growth under different regimes are also correlated to reflectivity transients measured during growth, demonstrating that LRI can be a useful technique for growth optimization *in situ*. Moreover, the findings are applied to InGaN growth to yield atomically smooth InGaN at significantly faster GR than that attained in Chapter 4.

7.2 Experimental procedure

Films were grown in a custom NH_3-based MOMBE showerhead reactor (Chapter 2) on 3.5 μm Si-doped GaN templates (Lumilog, Vallauris, France). A ~2 μm tantalum film was sputtered onto the backside of each substrate to promote efficient heating. Samples were immersed twice for 10 min each in a 90 °C piranha solution of H_2SO_4:H_2O_2 (4:1) before loading into the reactor, additional details of the etch are in [128].

Samples were degassed for 30 min at T_s = 150 °C in the introductory chamber. In the growth chamber, samples were annealed for 10 min at T_s = 600 °C with J_{NH_3} = 19 sccm before growth. GaN layers are grown using TEGa and NH_3, while TMIn is also supplied for InGaN growth. Disilane (Si_2H_6) is used as the Si precursor for Si-doping of InGaN (§A.1).

7.3 GaN growth regimes

The variation in GR with J_{TEGa} for GaN grown at T_s = 860, 770, 680, 590, and 500 °C on GaN template layers is shown in Fig. 7.1. The GR is determined using the custom LRI system described in Chapter 2 (some of the *R* curves used to extract these GRs are shown in §7.5). For a fixed J_{NH_3} = 19 sccm, the GR is dependent only on J_{TEGa} within T_s = 590-860 °C. The J_{TEGa} at which the GR saturates at fixed J_{NH_3} and T_s is the abrupt growth regime transition between N-rich/Ga-limited growth and Ga-Rich/N-limited growth [161]. This regime transition is indicative of an effective N/Ga adatom ratio ($J_{eff,N}/J_{eff,Ga}$) = 1 resulting in stoichiometric growth. Three distinct regimes can be identified based on the J_{TEGa} dependence of the GR. These three regimes are shown in Fig. 7.2 for the T_s = 770 °C case of Fig. 7.1:

- At T_s = 770 °C, growth is N-rich/Ga-limited when J_{TEGa} < 0.5 sccm, corresponding to a condition such that $J_{eff,N}/J_{eff,Ga}$ > 1.
- At T_s = 770 °C, growth is Ga-rich/N-limited when 0.5 sccm < J_{TEGa} < 0.54 sccm, corresponding to the condition $J_{eff,N}/J_{eff,Ga}$< 1.

- At $T_s = 770$ °C, growth is excessively Ga-rich/N-limited, resulting in Ga droplets when $J_{TEGa} > 0.55$ sccm, corresponding to a condition such that $J_{eff,N}/J_{eff,Ga} << 1$.

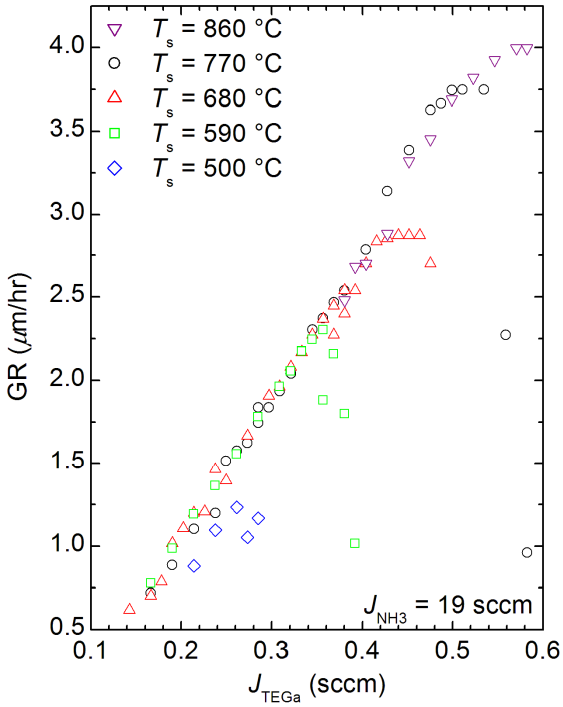

Fig. 7.1. GR vs. J_{TEGa} for GaN grown at T_s = 500, 590, 680, and 770 °C with J_{NH3} = 19 sccm.

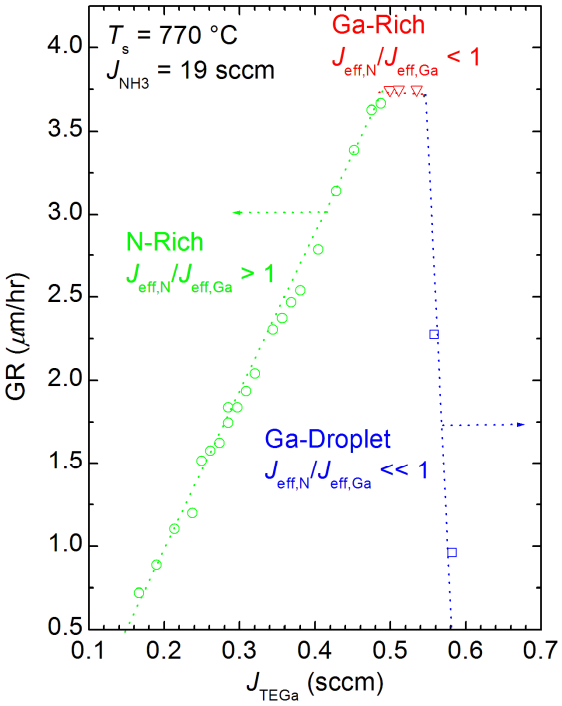

Fig. 7.2. The three growth regimes for GaN grown at T_s = 770 °C with J_{NH3} = 19 sccm: N-rich, Ga-Rich, and Ga-droplet (Ga-rich with Ga droplets).

The NH_3/TEGa flux ratio (J_{NH3}/J_{TEGa}) necessary to achieve stoichiometric growth for each T_s (J_{NH3} = 19 sccm) and the corresponding GR are listed in Table 7.1. ***For each increase in T_s, a higher J_{TEGa} is necessary to achieve stoichiometric growth; however, the GR also increases with each increase in T_s.*** This trend is a result of enhanced NH_3 pyrolysis at higher T_s [3], resulting in additional active N (higher $J_{eff,N}$). For traditional MBE, increasing T_s also increases Ga (and DEGa in the case of MOMBE) desorption and reduces the effective Ga flux $J_{eff,Ga}$ – meaning J_{TEGa} must be increased accordingly. However, in the present case, the observed GRs increase linearly with T_s, from 1.28 ML/s

at T_s = 500 °C to 4.28 ML/s at T_s = 860 °C. The Ga residence lifetime on GaN (0001) during plasma-assisted MBE has been calculated as 5 – 0.6 s for T_s = 685 – 750 °C respectively, with a corresponding activation energy for desorption of 2.2 eV [162]. Recent work by Koblmüller *et al.* [156] suggests that the Ga residence lifetime may be slightly longer (activation energy of 3.2 eV for Ga droplets). Hence, the GR observed in the present study at each T_s is sufficiently fast compared to respective Ga surface lifetime. This suggest that the Ga incorporation rate is near unity for each T_s, meaning $J_{eff,Ga} \sim J_{TEGa}$. Assuming $J_{eff,Ga} = J_{TEGa}$, the NH_3 efficiency (η_{NH3}) for each T_s was calculated using the J_{TEGa} necessary to achieve $J_{eff,N}/J_{eff,Ga}$ = 1. The calculated η_{NH3} is similar to that calculated for MBE of GaN using NH_3 [3].

Table 7.1. J_{NH3}/J_{TEGa} and corresponding η_{NH3}, GR, and σ_{RMS} for GaN grown at T_s = 500, 590, 680, 770, and 860 °C under stoichiometric conditions.

T_s (°C)	J_{NH3}/J_{TEGa}	J_{TEGa} (sccm)	$J_{eff,N}/J_{eff,Ga}$	η_{NH3} (%)	GR (μm/hr)	GR (ML/s)	σ_{RMS} (nm)
500	73	0.26	1	1.38	1.20	1.28	41
590	55	0.34	1	1.81	2.30	2.46	18
680	43	0.44	1	2.31	2.87	3.07	10
770	38	0.50	1	2.63	3.75	4.01	3.9
860	34	0.56	1	2.94	4.00	4.28	3.6

A decrease in J_{NH3}/J_{TEGa} during Ga-rich/N-limited ($J_{eff,N}/J_{eff,Ga} < 1$) growth conditions drastically decreases the GR at each T_s. This trend is apparent in Fig. 7.1 for increasing J_{TEGa} and in Fig. 7.3 for decreasing J_{NH3}. This trend is expected to result from growth under Ga-droplet conditions which results in the accumulation of excess,

physisorbed Ga that blocks surface sites and reduces GR at excess Ga surface coverage (low T_s or low J_{NH_3}/J_{TEGa}) [161,163]. The onset of the excess Ga resulting in Ga droplets has been calculated as 2.7 ML on a GaN (0001) surface [156].

A unique difference of MOMBE compared to MBE is that under N-rich/Ga-limited growth conditions, excess NH_3 inhibits growth. In Fig. 7.3, the GR increases with decreasing J_{NH_3} (until $J_{NH_3} < 28$ sccm) under N-rich/Ga-limited conditions. Similarly, Fig. 7.4 shows the GaN GR using J_{NH_3} = 19, 33, and 93 sccm for a range of J_{TEGa}. For J_{NH_3} = 19 sccm, the GR saturates at J_{TEGa} = 0.26 sccm (indicating stoichiometric growth conditions, further increasing J_{TEGa} at this J_{NH_3} and T_s leads to growth under Ga-rich/N-limited conditions). Increasing J_{NH_3} to 33 and 93 sccm under N-rich/Ga-limited conditions decreases the GR. This is most pronounced with J_{NH_3} = 93 sccm where the fastest GR is only 1/3 of that achieved with J_{NH_3} = 33 sccm under the same J_{TEGa} and T_s. The increase in GR with decreasing J_{NH_3} during growth in the N-rich/Ga-limited regime is consistent with the site-blocking model proposed by Koleske *et al.* [164] and can be understood as an increase in Ga surface accumulation ($J_{eff,Ga}$) with decreasing J_{NH_3} [165]. Subsequently, more Ga is available to form GaN and to catalyze NH_3 dissociation [121,135]. This suggests that the excess NH_3 supplied during growth in the N-rich/Ga-limited regime inhibits growth. These observations are consistent with previous reports of GaN grown in the same reactor under N-rich/Ga-limited conditions [38]. However, J_{TEGa} can be increased to consume the excess N, as observed in Fig. 7.4.

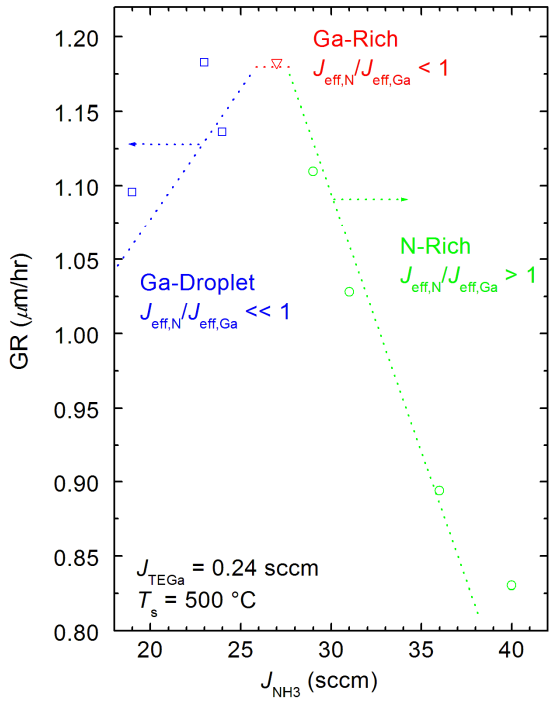

Fig. 7.3. GR vs. J_{NH3} for GaN grown at T_s = 500 °C with J_{TEGa} = 0.24 sccm. The three growth regimes are denoted.

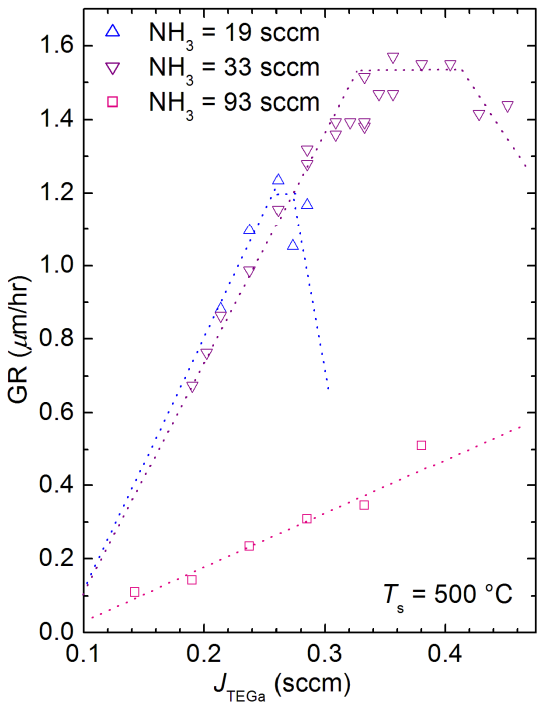

Fig. 7.4. GR vs. J_{TEGa} for GaN grown at T_s = 500 °C with J_{NH3} = 19, 33, and 93 sccm. For J_{NH3} = 93 sccm, the GR does not saturate at the investigated J_{TEGa}.

7.4 Effects of growth regime on GaN surface morphology

Fig. 7.5 shows the surface morphologies of the GaN films listed in Table 7.1 grown under the stoichiometric growth conditions ($J_{eff,N}/J_{eff,Ga}$ = 1). Granular morphologies are observed at each T_s. Similar morphologies have been observed for GaN under slightly N-rich/Ga-limited conditions [166] and $Al_{0.15}Ga_{0.85}N$ grown at under Ga-Rich/N-limited conditions – both grown by plasma-assisted MBE [167]. Increasing planarization of the surface is observed with each increase in T_s, saturating at T_s = 770 – 860 °C as films exhibit σ_{RMS} = 3.9 and 3.6 nm respectively (Table 7.1). For GaN grown in MBE using NH_3, increasing planarization and similar σ_{RMS} was observed by increasing

J_{NH_3}/J_{TEGa} under N-rich/Ga-limited growth conditions [168,169], which is in contrast to plasma-assisted MBE where planarization occurs under Ga-rich/N-limited conditions [166] as a result of efficient lateral diffusion of adatoms through a metal adlayer [170]. Since the $J_{eff,N}/J_{eff,Ga}$ is constant in the present case and assuming that the planarization is independent of GR, the improvement in planarization is suspected to be a result of enhanced adatom surface mobility with increased T_s.

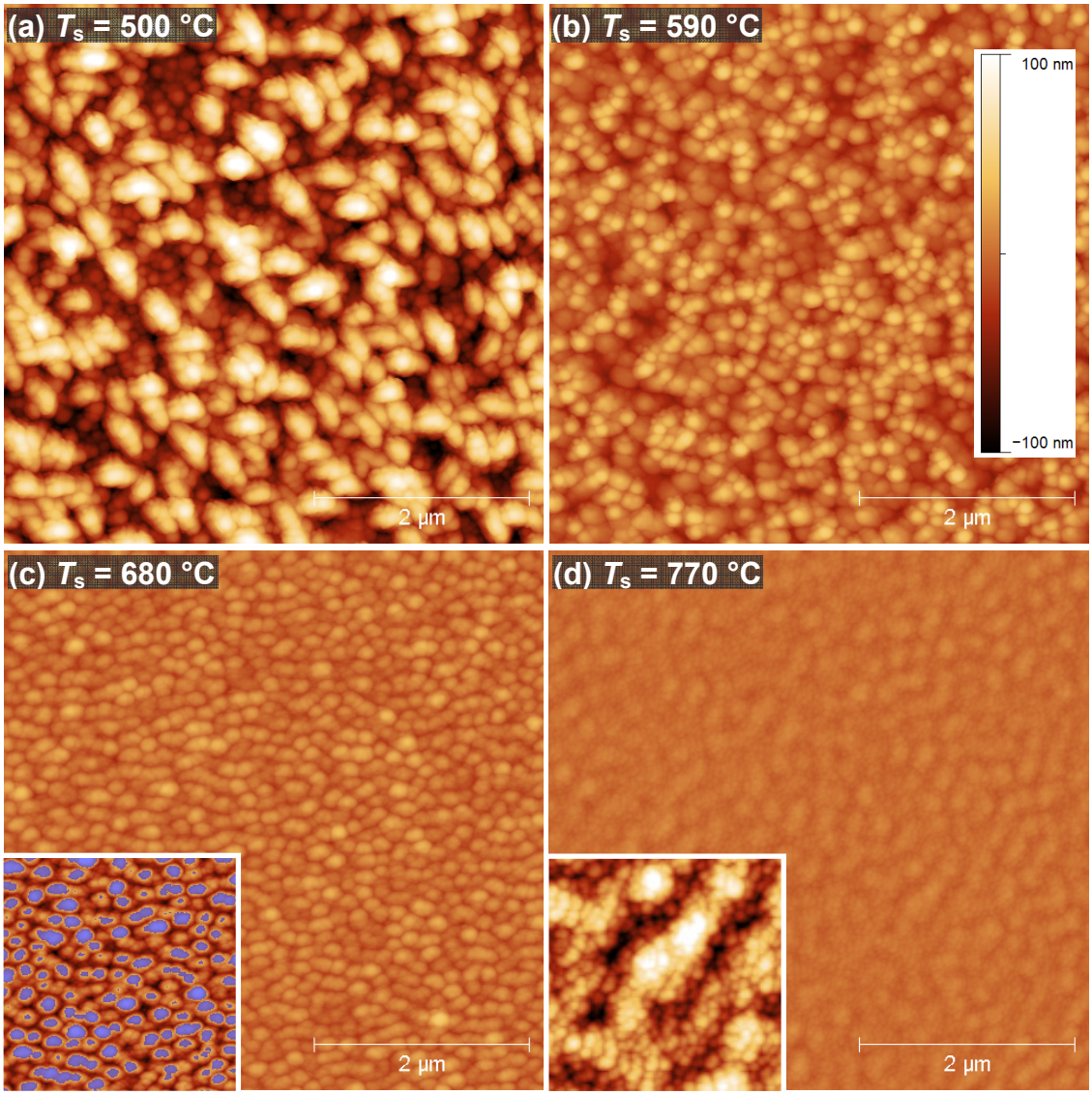

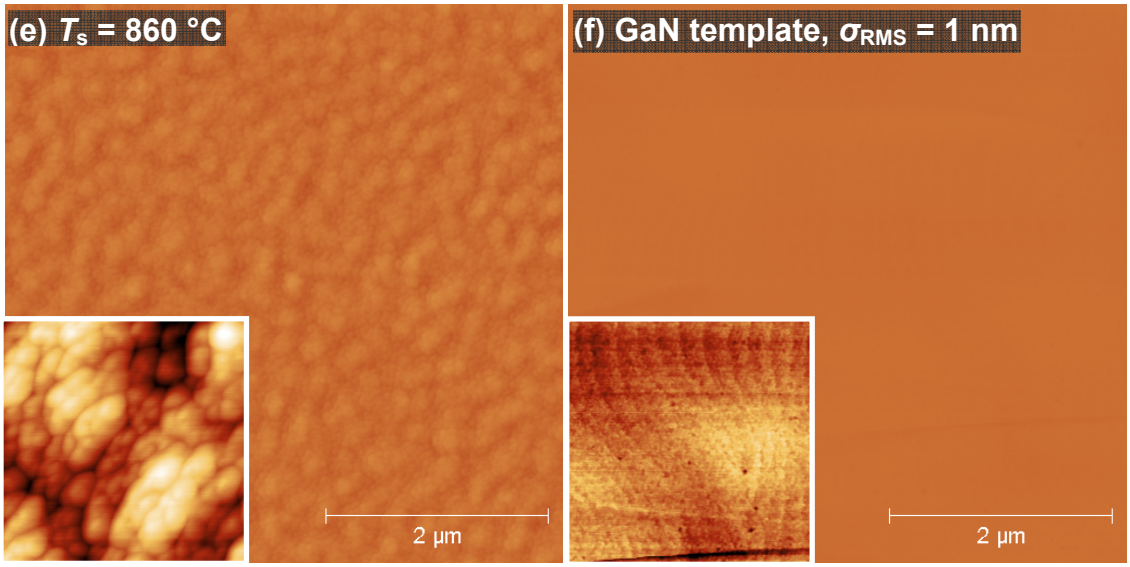

Fig. 7.5. 5 × 5 μm^2 AFM surface morphologies of GaN grown at T_s = (a) 500, (b) 590, (c) 680, (d) 770, and (e) 860 °C under stoichiometric growth conditions. The growth conditions are summarized in Table 7.1. The thickness of each GaN layer is ~0.5 μm. The GaN template virtual substrate is shown in (f). The height scale for (a) – (f) is -100 to 100 nm as shown in inset (b). The inset of (c) is 2 × 2 μm^2 and the height scale is -30 to 30 nm – grains are marked in blue. The inset of (d) is 1 × 1 μm^2 and the height scale is -10 to 10 nm. The inset of (e) is 0.5 × 0.5 μm^2 and the height scale is -8 to 8 nm. The inset of (f) is 2 × 2 μm^2 and the height scale is -2 to 2 nm.

While the films planarize with increasing T_s under stoichiometric growth conditions, the grains shown in Fig. 7.5 become increasingly fine and dense with increasing T_s. Fig. 7.6 quantifies the evolution of mean σ_{RMS}, grains size, and grain density with T_s. Grain analysis was performed by identifying grains using a height threshold of 50% with Gwyddion [171] – one example is shown in the inset of Fig. 7.5(c). The increase in gain density is attributed to the increase in GR with T_s (up to 4.28 ML/s at T_s = 860 °C). The fast GR will dramatically limit the adatom surface diffusion length, resulting in grains on the order of the diffusion length. Additionally, these fast GR conditions (GR > 1.25 μm/hr) result in GaN films which are gold in color and darken with increasing GR (increasing J_{TEGa} in the N-rich/Ga-limited growth regime). The darkening of film color is suspected to be a result of increased C incorporation into the growing GaN layers as the fast GR also limits hydrocarbon liberation from the surface

(this is distinct from an increase in GR as a result of hydrocarbon liberation as discussed in Chapter 3).

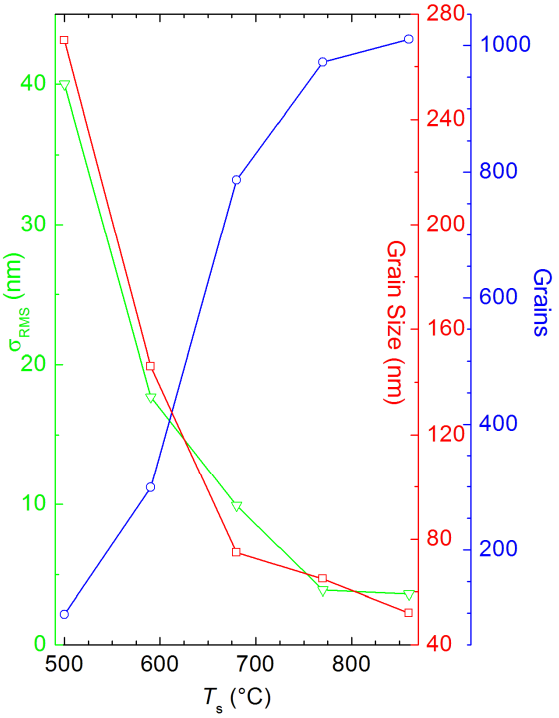

Fig. 7.6. σ_{RMS} (green triangles), grain size (red squares) and number of grains (blue circles) over 5 × 5 μm^2 for GaN grown at T_s = 500, 590, 680, 770, and 860 °C under stoichiometric conditions.

Fig. 7.7 shows the surface morphologies of GaN films grown under Ga-rich/N-limited ($J_{eff,N}/J_{eff,Ga} < 1$) growth conditions. Specific growth conditions are denoted. Using the calculated η_{NH3} (Table 7.1) and assuming $J_{eff,Ga} = J_{TEGa}$ (as justified previously), the given $J_{eff,N}/J_{eff,Ga}$ show that the growths are increasingly Ga-rich from (a) to (c). The morphologies of (a) and (b) are similar to those observed under stoichiometric conditions. However, for $J_{eff,N}/J_{eff,Ga}$ = 0.65 shown in (c), spiral hillocks are observed which increase the σ_{RMS}. Under these Ga-rich conditions, the GR ~ 3.25 μm/hr. The spiral hillocks are expected to originate from dislocation cores of the GaN template possessing a screw

component. Similar features have been observed in NH_3-based MBE under Ga-rich conditions [172].

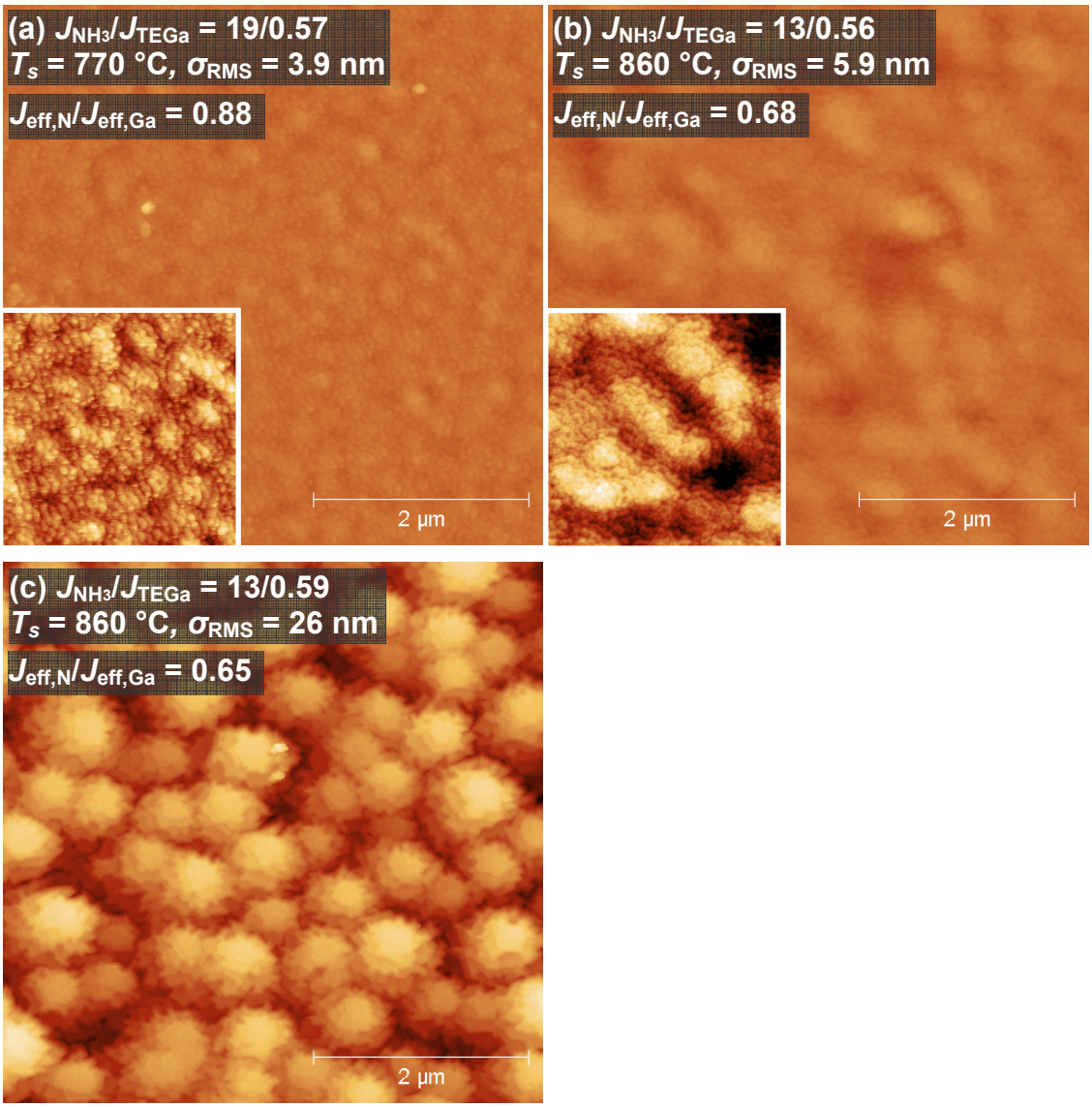

Fig. 7.7. 5 × 5 μm^2 AFM surface morphologies and σ_{RMS} of GaN grown under Ga-rich/N-limited ($J_{eff,N}/J_{eff,Ga} < 1$) growth conditions. All given precursor fluxes are in units of sccm. The thickness of each GaN layer is ~0.5 μm. The height scale for (a) – (c) is -100 to 100 nm. The insets are 2 × 2 μm^2 and the height scale is -15 to 15 nm.

Fig. 7.8 shows the surface morphologies of GaN films grown under the N-rich/Ga-limited growth conditions ($J_{eff,N}/J_{eff,Ga} > 1$). Specific growth conditions are

denoted and are increasingly N-rich from (a) to (d) as determined by the calculated $J_{eff,N}/J_{eff,Ga}$. The morphology grown under $J_{eff,N}/J_{eff,Ga}$ = 1.47 is shown in (a) and is identical to that observed under stoichiometric growth conditions. (b) – (d) exhibit a terraced morphology with 5-10 Å steps. The σ_{RMS} = 1.7 nm observed in (b) is comparable to the GaN template σ_{RMS} and it is the smoothest GaN film grown in this study. Faceted pits are observed which resemble commonly observed V-defects that are believed to originate at screw-type threading dislocations of the GaN template (dislocation density ~5×10^8 cm^{-2}) [160,173].

Fig. 7.9 shows the surface morphologies of GaN films grown under very N-rich/Ga-limited growth conditions ($J_{eff,N}/J_{eff,Ga} >> 1$). The pit defects dominate the morphology with planar pit density for (a) – (c) ~7×10^8, 7.7×10^8, and 1.6×10^9 cm^{-2} respectively. At T_s = 770 °C shown in (a) and (c), the pits extend 30 – 105 nm below the surface; while at T_s = 870 °C shown in (b) the pits extend 30 – 50 nm below the surface. The pits size and σ_{RMS} are reduced at higher T_s, which is consistent with an improvement in adatom surface diffusion.

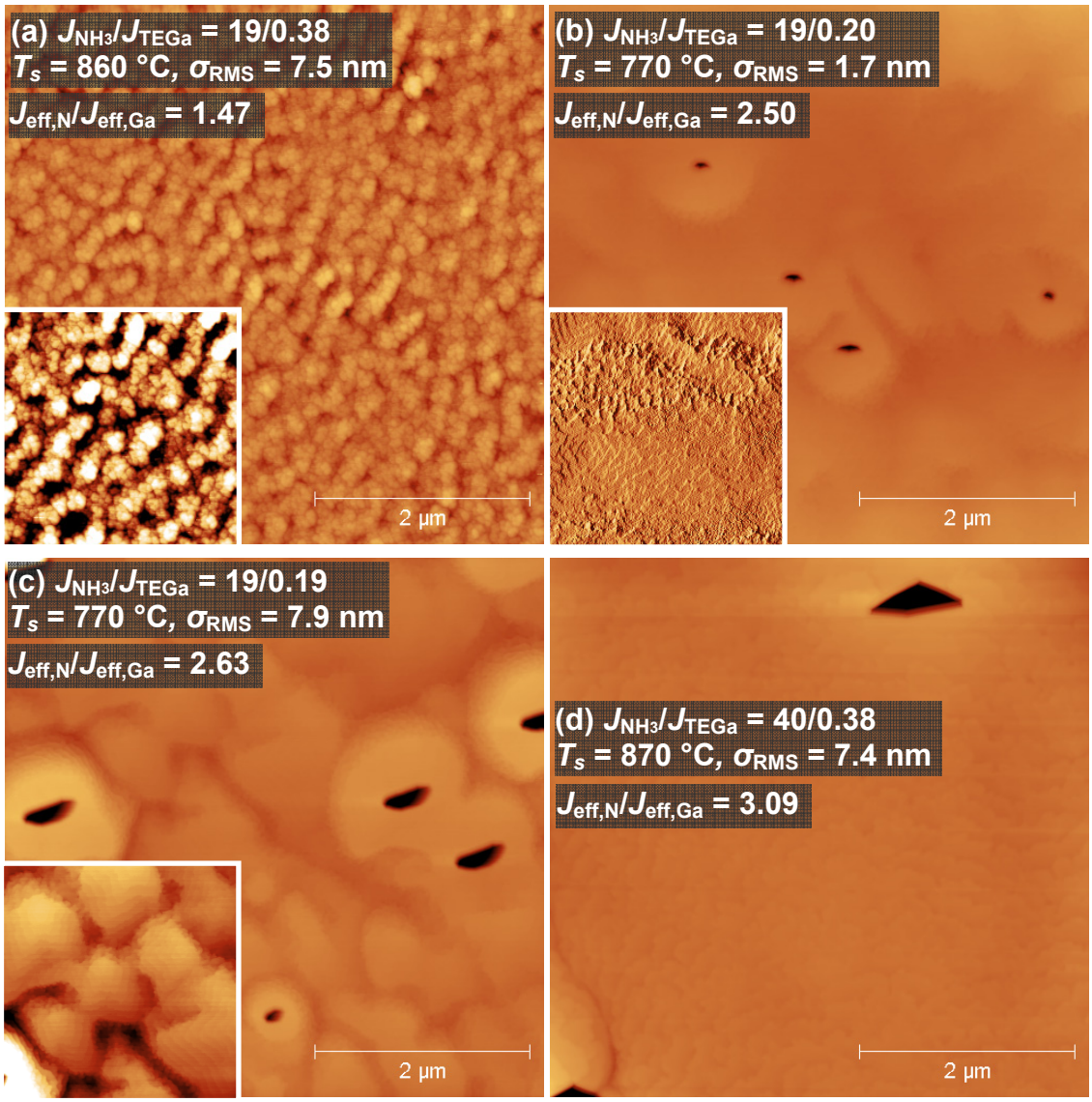

Fig. 7.8. 5 × 5 μm^2 AFM surface morphologies and σ_{RMS} of GaN grown at under N-rich/Ga-limited ($J_{eff,N}/J_{eff,Ga} > 1$) conditions. All given precursor fluxes are in units of sccm. (c) is from [174]. The height scale for (a) – (d) is -50 to 50 nm. The GR are ~2.5, 1, 1, and 2 μm/hr and the thickness of the GaN layers are ~0.5, 0.5, 0.9, and 2 μm for (a) – (d) respectively. The insets of (a) and (c) are 2 × 2 μm^2 and the height scale is -10 to 10 nm. The inset of (b) is 2 × 2 μm^2 amplitude representation.

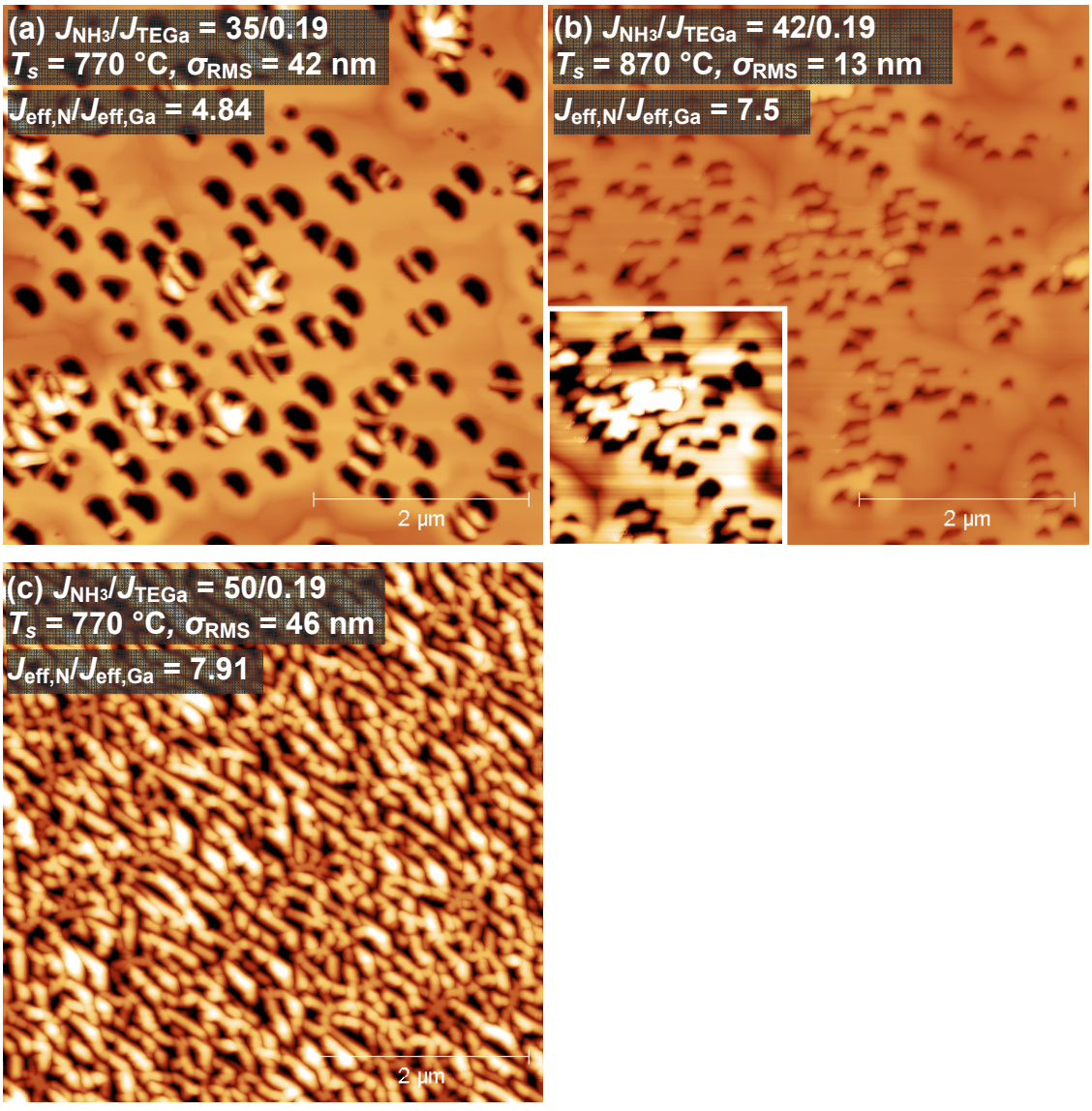

Fig. 7.9. 5×5 μm^2 AFM surface morphologies and σ_{RMS} of GaN grown under very N-rich/Ga-limited ($J_{eff,N}/J_{eff,Ga} >> 1$) conditions. All given precursor fluxes are in units of sccm. (a) and (c) are from [174]**.** The height scale for (a) – (c) is -100 to 100 nm. The GR are 0.61, 0.66, and 0.48 μm/hr, all grown for 1 hr duration. The inset of (b) is 2×2 μm^2 with a height scale is -20 to 20 nm.

7.5 Effects of surface morphology on reflectance

The distinct surface morphologies observed under the aforementioned growth conditions induce significant variations in the reflectance envelope measured by the LRI system. An example of such variations in the reflectance envelope is shown in Fig. 7.10. Here, the reflectivity oscillations during GaN growth under constant J_{NH_3} = 19 sccm and T_s = 590 °C are shown; however, J_{TEG} is varied at specific growth times t (specific J_{TEG} at a given t are defined in the caption) such that as t increases, $J_{eff,N}/J_{eff,Ga}$ decreases (generally). Consequently, the shown reflectivity transient spans the growth of GaN over the range of morphologies described in §7.4. Additional reflectivity transients for GaN growth at T_s = 500, 680, 770, and 860 °C are shown in Fig. 7.11 – 7.14. Salient points A and B are derived for each reflectivity transient. These points A and B represent the $J_{eff,N}/J_{eff,Ga}$ condition for each T_s that corresponds to consistent morphological transitions in the film. The calculated $J_{eff,N}/J_{eff,Ga}$ defining A and B are given in Table 7.2. The following empirical model is offered as a starting point for correlating variations in the reflectivity observed *in situ* to the resultant film morphologies obtained using specific $J_{eff,N}/J_{eff,Ga}$ conditions (it should be noted that while J_{TEG} varies with t in all of the shown reflectivity oscillations, the present model is consistent with reflectivity trends and resultant morphologies observed from the growth of individual layers using constant growth conditions). The model is described as follows using primarily the T_s = 590 °C case shown in Fig. 7.10:

- For $J_{eff,N}/J_{eff,Ga}$ > A, growth is N-rich/Ga-limited (Fig. 7.10, t = 0 – 51.1 min and J_{TEGa} < 0.24 in the inset). The N-rich conditions result in pits which have a density and size that increase with increasing $J_{eff,N}/J_{eff,Ga.}$ Under these conditions, the average reflectivity will decrease and the reflectivity oscillation will dampen with increasing volume of the film that is occupied by pits – which is dependent on the pit density, pit geometry, and film thickness (*i.e.* under constant growth conditions resulting in pits, the average reflectivity will decrease so long as the planar area of the pit continues to increase as the film thickens, simultaneously the reflectivity oscillations dampen due to the increased optical scattering in the bulk resulting from the increasing pit volume).

- For A < $J_{eff,N}/J_{eff,Ga}$ < B, the growth surface is planar (σ_{RMS} < 5 nm). Under these conditions, small pits may be present for $J_{eff,N}/J_{eff,Ga}$ ~ A (slightly N-rich/Ga-limited growth conditions) and fine grains may be present for $J_{eff,N}/J_{eff,Ga}$ ~ B (slightly Ga-rich/N-limited growth conditions). The grain size reduces with increasing GR. The planar surface prevents a dramatic decrease in average reflectivity, but either the pits or the fine grains will induce optical scattering in the bulk, which will result in dampening of the observed reflectivity oscillations. This trend is evident in Fig. 7.10 between t ~ 51.1 – 109.3 min (J_{TEGa} ~ 0.24 – 0.33 sccm). It should be noted that the fine grains may slightly decrease the average reflectivity as a result of their effect on the surface texture; however, small pits can induce a dramatic decrease in average reflectivity as the film thickens (empirically, beyond a few 100 nm of deposition) and increases the planar area of the pit (as mentioned in the N-rich case). This dependence on film thickness is suspected to be the origin for the delay in the decrease of the

average reflectivity, which is observed in a variety of the given reflectivity transients under A < $J_{eff,N}/J_{eff,Ga}$ < B (*e.g.* see t < 30 min in Fig. 7.12(b)).

- For $J_{eff,N}/J_{eff,Ga}$ < B, growth is Ga-rich/N-limited. For $T_s \leq$ 770 °C and very low $J_{eff,N}/J_{eff,Ga}$, Ga or In can accumulate and inhibit growth beyond a critical surface coverage. Consequently, the observed reflectivity oscillations can be quenched (no growth) and/or the average reflectivity can become unstable (increase or decrease depending on the surface coverage). In Fig. 7.10, for J_{TEGa} = 0.37 sccm at t > 133.2 min, the reflectivity initially increases; however, for t > 141 min, the oscillations quench and the reflectivity declines. This instability is perhaps more clearly observed in the inset of Fig. 7.13(b) for t > 69.8 min where J_{TEGa} > 0.51 sccm.

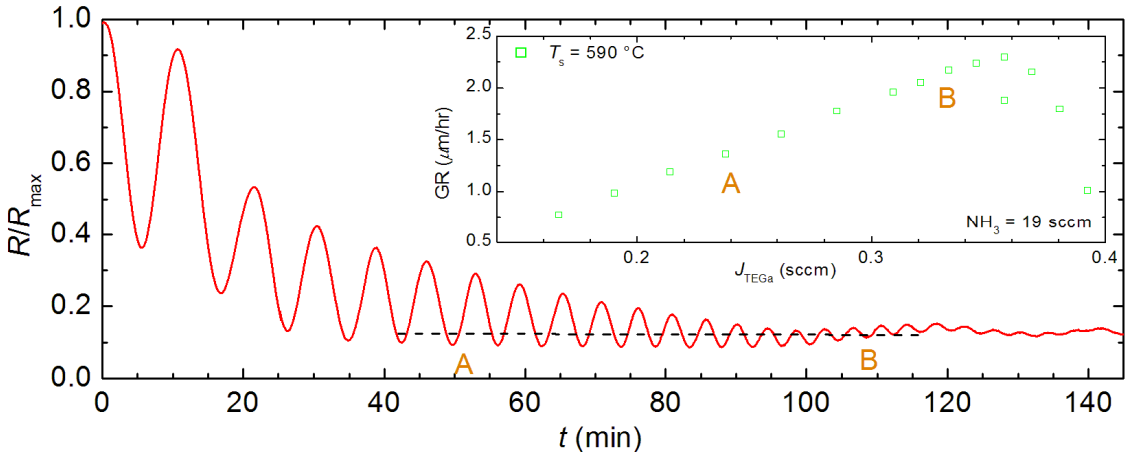

Fig. 7.10. Evolution of reflectivity oscillation during GaN growth with J_{TEGa} = 0.17 – 0.37 sccm at fixed J_{NH3} = 19 sccm and T_s = 590 °C. R is normalized to R_{max}. Salient reflectance transitions are labeled A and B. The inset of shows the corresponding GR vs. J_{TEGa} (at fixed J_{NH3}) and the salient points A and B. J_{TEGa} versus t is defined as J_{TEGa}(t=0-21.3 min) = 0.17 sccm, J_{TEGa}(t=21.3-37.1 min) = 0.19 sccm, J_{TEGa}(t=37.1-51.1 min) = 0.21 sccm, J_{TEGa}(t=51.1-64.5 min) = 0.24 sccm, J_{TEGa}(t=64.5-73.8 min) = 0.26 sccm, J_{TEGa}(t=73.8-85 min) = 0.29 sccm, J_{TEGa}(t=85-95.3 min) = 0.31 sccm, J_{TEGa}(t=95.3-109.3 min) = 0.33 sccm, J_{TEGa}(t=109.3-114.2 min) = 0.36 sccm, J_{TEGa}(t=114.2-126 min) = 0.32 sccm, J_{TEGa}(t=126-133.2 min) = 0.34 sccm, and J_{TEGa}(t=133.2-144.7 min) = 0.37 sccm.

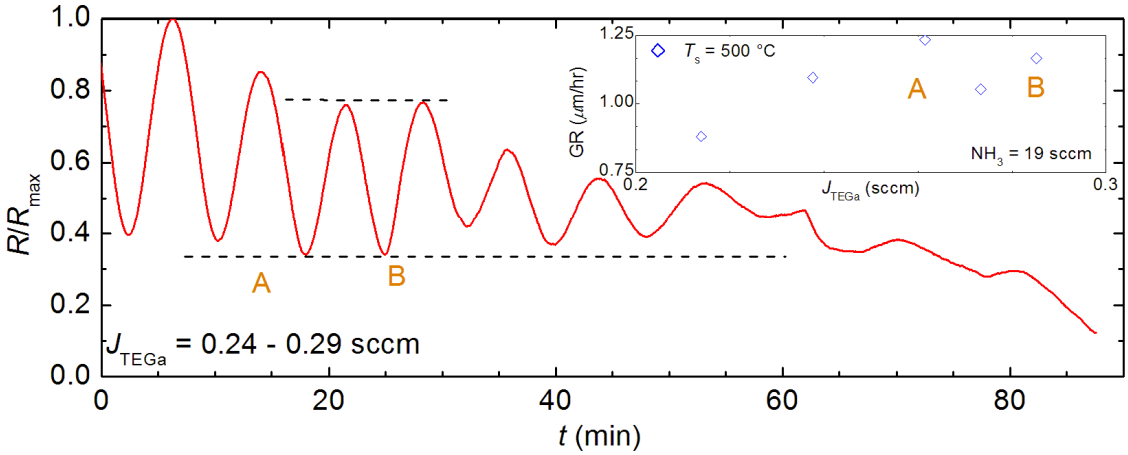

Fig. 7.11. Evolution of reflectivity oscillation during GaN growth with J_{TEGa} = 0.24 – 0.29 sccm at fixed J_{NH3} = 19 sccm and T_s = 500 °C. J_{TEGa} increases with t. R is normalized to R_{max}. Salient reflectance transitions are labeled A and B. The inset of shows the corresponding GR vs. J_{TEGa} (at fixed J_{NH3}) and the salient points A and B. J_{TEGa} versus t is defined as J_{TEGa}(t=0-13.9 min) = 0.24 sccm, J_{TEGa}(t=13.9-25 min) = 0.26 sccm, J_{TEGa}(t=25-36.3 min) = 0.29 sccm, J_{TEGa}(t=36.3-62.6 min) = 0.27 sccm, J_{TEGa}(t=62.6-66.8 min) = 0.21 sccm, J_{TEGa}(t=66.8-77.8 min) = 0.29 sccm, and J_{TEGa}(t=77.9-86.3 min) = 0.26 sccm.

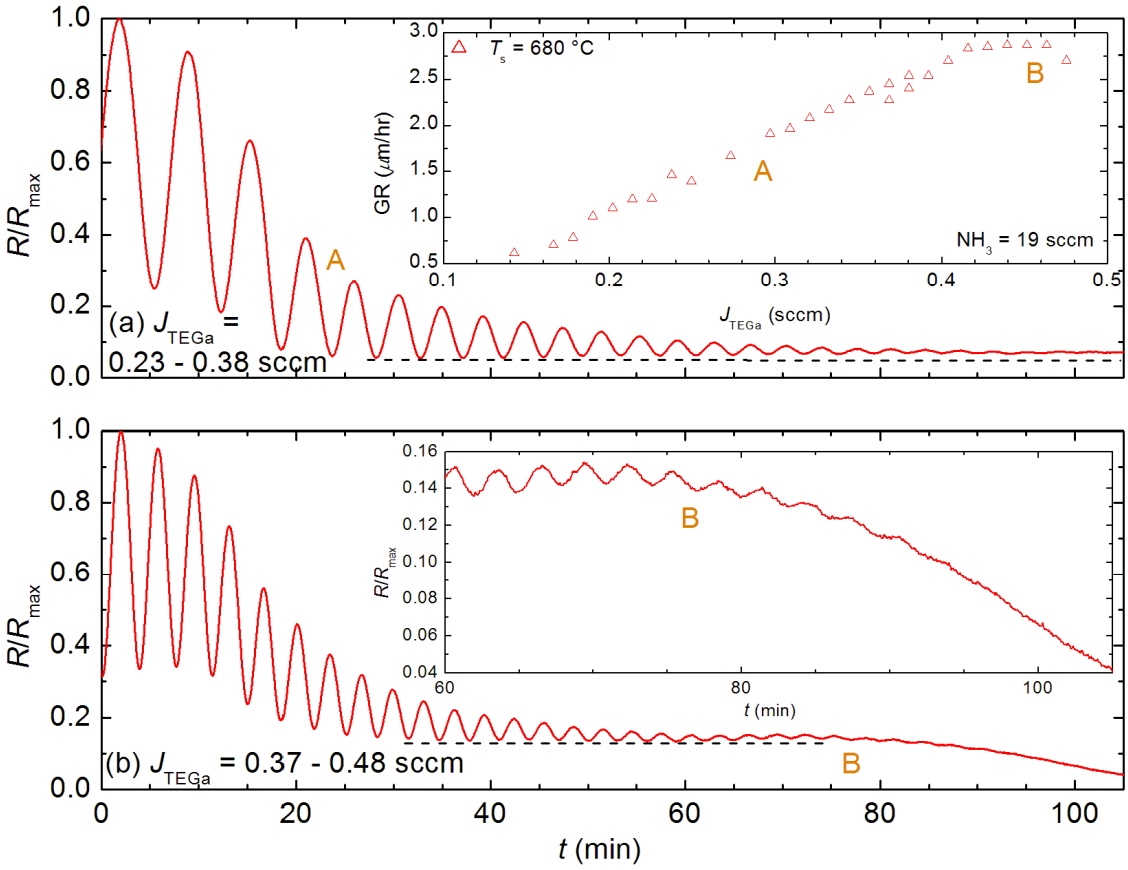

Fig. 7.12. Evolution of reflectivity oscillation during GaN growth with (a) J_{TEGa} = 0.23 – 0.38 sccm and (b) J_{TEGa} = 0.37 – 0.48 sccm at fixed J_{NH3} = 19 sccm and T_s = 680 °C. R is normalized to R_{max}. Salient reflectance transitions are labeled A and B. The inset of (a) shows the corresponding GR vs. J_{TEGa} (at fixed J_{NH3}) and the salient points A and B. J_{TEGa} versus t is defined as follows. For (a), J_{TEGa}(t=0-9.6 min) = 0.23 sccm, J_{TEGa}(t=9.6-17.1 min) = 0.25 sccm, J_{TEGa}(t=17.1-23.4 min) = 0.27 sccm, J_{TEGa}(t=23.4-31.2 min) = 0.30 sccm, J_{TEGa}(t=31.2-37.3 min) = 0.31 sccm, J_{TEGa}(t=37.3-44.3 min) = 0.32 sccm, J_{TEGa}(t=44.3-56.9 min) = 0.33 sccm, J_{TEGa}(t=56.9-65.4 min) = 0.34 sccm, J_{TEGa}(t=65.4-75.2 min) = 0.36 sccm, J_{TEGa}(t=75.2-93 min) = 0.37 sccm, and J_{TEGa}(t=93-104.3 min) = 0.38 sccm. For (b), J_{TEGa}(t=0-9.5 min) = 0.37 sccm, J_{TEGa}(t=9.5-15.6 min) = 0.38 sccm, J_{TEGa}(t=15.6-24.3 min) = 0.39 sccm, J_{TEGa}(t=24.3-36.3 min) = 0.40 sccm, J_{TEGa}(t=36.3-50.2 min) = 0.42 sccm, J_{TEGa}(t=50.2-60.4 min) = 0.43 sccm, J_{TEGa}(t=60.4-77.3 min) = 0.44 sccm, J_{TEGa}(t=77.3-89.8 min) = 0.45 sccm, J_{TEGa}(t=89.8-98.3 min) = 0.46 sccm, and J_{TEGa}(t=98.3-104.8 min) = 0.48 sccm.

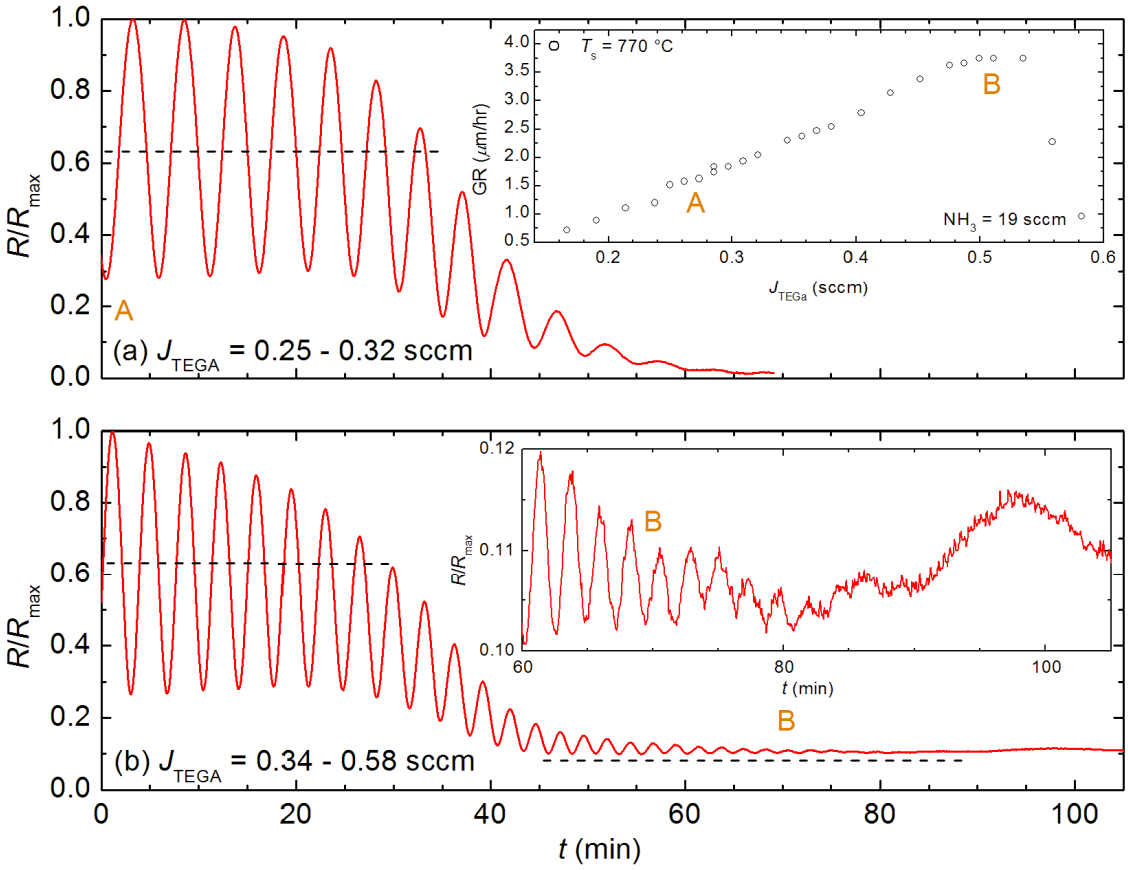

Fig. 7.13. Evolution of reflectivity oscillation during GaN growth with (a) J_{TEGa} = 0.25 – 0.32 sccm and (b) J_{TEGa} = 0.34 – 0.58 sccm at fixed J_{NH3} = 19 sccm and T_s = 770 °C. R is normalized to R_{max}. Salient reflectance transitions are labeled A and B. The inset of (a) shows the corresponding GR vs. J_{TEGa} (at fixed J_{NH3}) and the salient points A and B. J_{TEGa} versus t is defined as follows. For (a), J_{TEGa}(t=0-14.8 min) = 0.27 sccm, J_{TEGa}(t=14.8-21.3 min) = 0.29 sccm, J_{TEGa}(t=21.3-29 min) = 0.30 sccm, J_{TEGa}(t=29-34.4 min) = 0.31 sccm, J_{TEGa}(t=34.4-40.1 min) = 0.32 sccm, J_{TEGa}(t=40.1-51.2 min) = 0.27 sccm, and J_{TEGa}(t=51.2-66 min) = 0.25 sccm. For (b), J_{TEGa}(t=0-8.6 min) = 0.34 sccm, J_{TEGa}(t=8.6-16.6 min) = 0.36 sccm, J_{TEGa}(t=16.6-26.8 min) = 0.37 sccm, J_{TEGa}(t=26.8-32.1 min) = 0.38 sccm, J_{TEGa}(t=32.1-38 min) = 0.40 sccm, J_{TEGa}(t=38-43.1 min) = 0.43 sccm, J_{TEGa}(t=43.1-46.9 min) = 0.45 sccm, J_{TEGa}(t=46.9-54.1 min) = 0.48 sccm, J_{TEGa}(t=54.1-63.1 min) = 0.49 sccm, J_{TEGa}(t=63.1-69.8 min) = 0.50 sccm, J_{TEGa}(t=69.8-81.3 min) = 0.51 sccm, J_{TEGa}(t=81.3-90 min) = 0.53 sccm, J_{TEGa}(t=90-111.3 min) = 0.56 sccm.

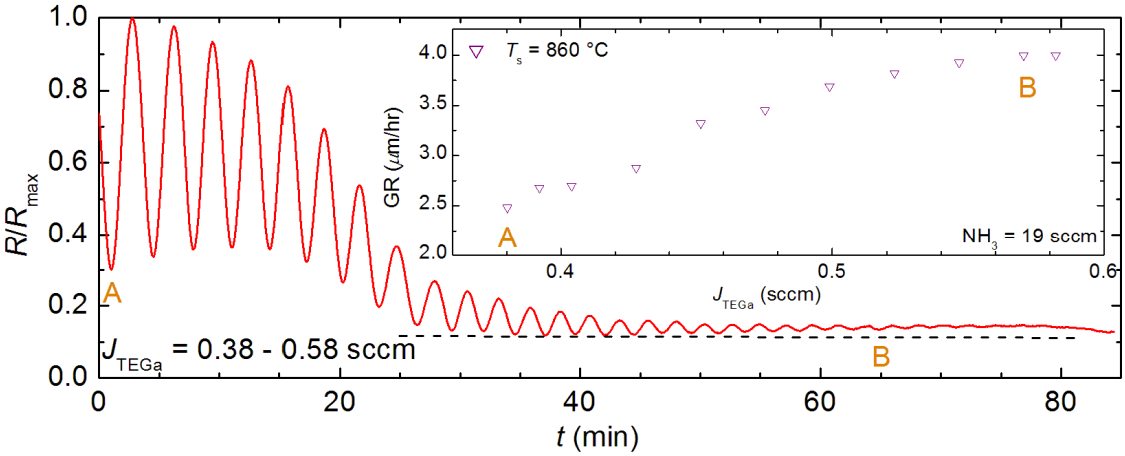

Fig. 7.14. Evolution of reflectivity oscillation during GaN growth with J_{TEGa} = 0.38 – 0.58 sccm at fixed J_{NH3} = 19 sccm and T_s = 860 °C. J_{TEGa} increases with t. R is normalized to R_{max}. Salient reflectance transitions are labeled A and B. The inset shows the corresponding GR vs. J_{TEGa} (at fixed J_{NH3}) and the salient points A and B. J_{TEGa} versus t is defined as J_{TEGa}(t=0-6.7 min) = 0.38 sccm, J_{TEGa}(t=6.7-13.2 min) = 0.40 sccm, J_{TEGa}(t=13.2-22.9 min) = 0.43 sccm, J_{TEGa}(t=22.9-28.6 min) = 0.39 sccm, J_{TEGa}(t=28.6-35.6 min) = 0.45 sccm, J_{TEGa}(t=35.6-43.3 min) = 0.48 sccm, J_{TEGa}(t=43.3-50.6 min) = 0.50 sccm, J_{TEGa}(t=50.6-57.7 min) = 0.52 sccm, J_{TEGa}(t=57.7-65 min) = 0.55 sccm, J_{TEGa}(t=65-72.5 min) = 0.57 sccm, and J_{TEGa}(t=72.5-80 min) = 0.58 sccm.

Table 7.2. $J_{eff,N}/J_{eff,Ga}$ at points A and B for films grown with J_{NH3} = 19 sccm at T_s = 500, 590, 680, 770, and 860 °C.

T_s (°C)	η_{NH3} (%)	J_{NH3} (sccm)	$J_{eff,N}$	$J_{eff,N}/J_{eff,Ga}$ A	$J_{eff,N}/J_{eff,Ga}$ B
500	1.38	19	0.26	1.00	0.92
590	1.81	19	0.34	1.45	1.04
680	2.31	19	0.44	1.42	0.97
770	2.63	19	0.50	1.82	0.98
860	2.94	19	0.56	1.47	0.98

7.6 Implications for InGaN by NH_3-based MOMBE

The fast GRs for GaN demonstrated in §7.3 under N-rich/Ga-limited conditions presents a promising mechanism to increase the indium content in $In_xGa_{1-x}N$ grown by NH_3-based MOMBE. The most effective mechanism presently for incorporating significant indium ($x > 0.05$) has been by the reduction of T_s to < 540 °C. As discussed in Chapter 4 though, T_s < 540 °C results in a drastic deficiency of N and a significant In/In-methyl surface coverage – both of these consequences of T_s compete with $In_xGa_{1-x}N$ growth and indium incorporation. Since GR was less than 120 nm/hr as presented thus far in Chapter 4 a faster GR could be leveraged to incorporate In adatoms before they desorb, which may also facilitate the ability to increase T_s while maintaining a significant In incorporation. An increase in T_s would be useful to limit the surface coverage of the growth-inhibiting In/In-methyl layer, to provide additional N, and to enhance the $In_xGa_{1-x}N$ film quality (*e.g.* reduced surface roughness and reduced [C]).

Fig. 7.15 summarizes the indium composition and GR for InGaN films grown at T_s = 730 and 770 °C. As shown, all T_s are much greater than that used in Chapter 4, but still result in significant indium incorporation. $J_{III} = J_{TEGa} + J_{TMIn} = 0.20$ is maintained to mimic the growth conditions for the atomically smooth GaN shown in Fig. 7.8(b). Specific precursor fluxes are given in Table 7.3. The $In_xGa_{1-x}N$ indium composition is determined by XRD, assuming that the $In_xGa_{1-x}N$ layer is fully strain relaxed and that Vegard's law applies. ***No residual III-alkyl species were observed using the RGA during the present InGaN growths, indicating that the elevated T_s effectively prevents a significant In/In-methyl surface coverage from inhibiting growth. For T_s = 730 °C,***

$In_{0.09}Ga_{0.91}N$ is grown at 355 nm/hr – an increase in GR by one order versus $In_{0.10}Ga_{0.90}N$ films of Chapter 4 and 5. However, the GR of InGaN under these conditions is nearly a factor of 3 lower than that obtained for GaN with the same T_s, J_{III}, and J_{NH_3} – indicative of a lower $J_{eff,III}$ (compared to the GaN case) when TMIn is introduced for the growth of InGaN. The reduction in $J_{eff,III}$ for InGaN (vs. GaN) growth is a result of multiple mechanisms, including indium re-evaporation and mixed-alkyl scavenging of III species.

Fig. 7.16 shows the surface morphologies for the InGaN films grown using the conditions given in Table 7.3. Granular morphologies are observed in (a), (b), (c), and (e) which are similar to that of GaN grown near stoichiometric conditions. The granular InGaN morphologies are indicative of an effective reduction of $J_{eff,N}/J_{eff,III}$ in the presence TMIn (while $J_{eff,III}$ reduces, $J_{eff,N}$ reduces to a greater extent). In NH_3-based MOMBE (and NH_3-based MBE) $J_{eff,N}$ will decline in the presence of TMIn since In is a poorer catalyst of NH_3 decomposition compared to Ga or Al [135]. Quantification of the reduction in $J_{eff,N}$ as a result if TMIn is difficult because the surface coverage of catalytic cation species is dependent on J_{III}, T_s, and GR. Increasing J_{NH_3} to 49 sccm results in the morphology of (d), which exhibits 5-10 Å steps, ~10 nm pits, and a σ_{RMS} comparable to the GaN template – indicative of N-rich/Ga-limited conditions for GaN. However, while J_{NH_3} = 49 sccm compensates for the reduced $J_{eff,N}$ in the presence of TMIn (results in a $J_{eff,N}/J_{eff,III}$ yielding an atomically smooth surface), both the In composition and GR of the InGaN film decrease. Additional studies of Si-doping of InGaN under these conditions show further reductions in In composition and GR with increasing $J_{Si_2H_6}$, as discuss in §A.1.

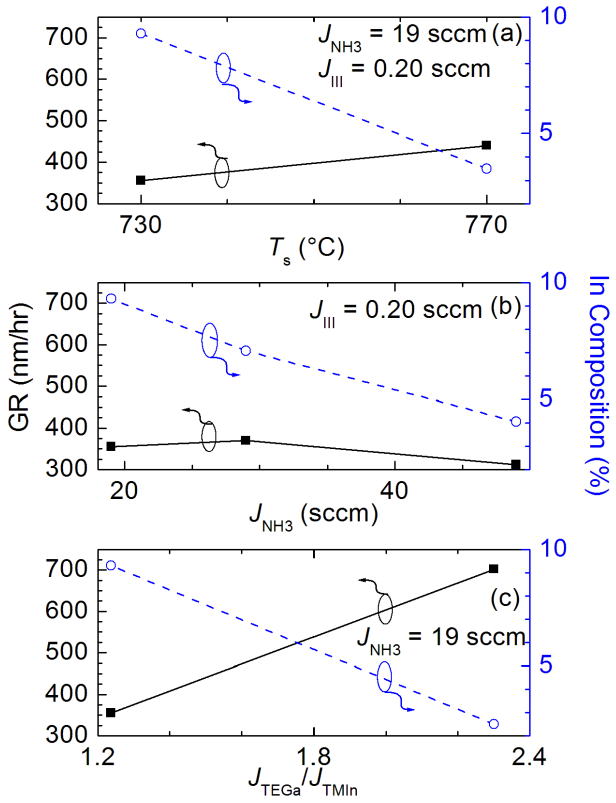

Fig. 7.15. GR and composition variation for $In_xGa_{1-x}N$ grown at (a) T_s = 730 and 770 °C, (b) J_{NH3} = 19, 29, and 49 sccm, and (c) J_{TEGa}/J_{TMIn} = 1.2 and 2.3.

Table 7.3. Specific conditions for InGaN films of Fig. 7.16.

T_s (°C)	J_{NH3} (sccm)	J_{TEGa} (sccm)	J_{TMIn} (sccm)	J_{NH3}/J_{III}	J_{TEGa}/J_{TMIn}	GR (nm/hr)	In (%)	Fig.
770	19	0.11	0.09	95	1.2	441	3.5	7.16(a)
730	19	0.11	0.09	95	1.2	355	9.3	7.16(b)
730	29	0.11	0.09	145	1.2	370	7.1	7.16(c)
730	49	0.11	0.09	245	1.2	312	4.1	7.16(d)
730	19	0.14	0.06	95	2.3	702	2.5	7.16(e)

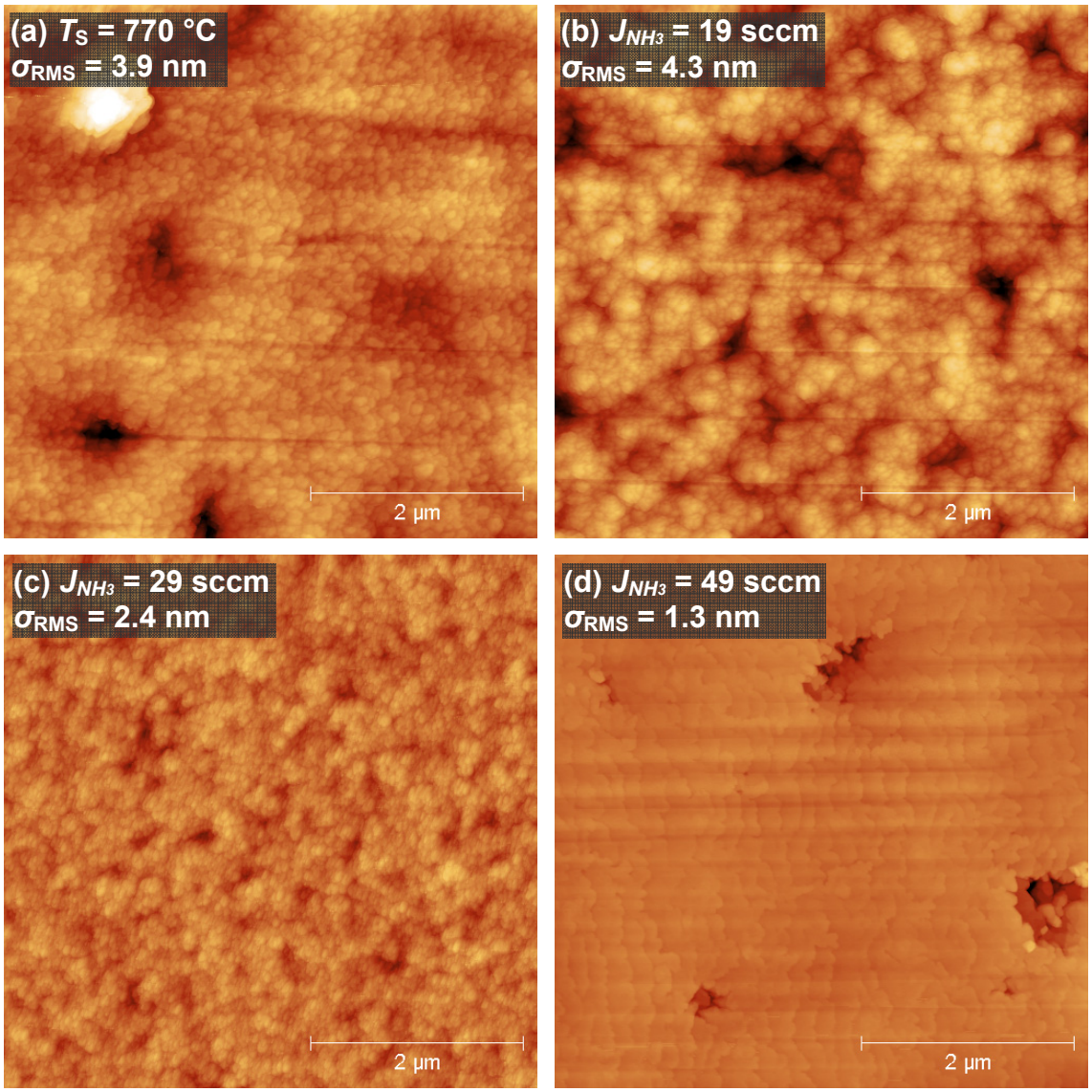
(a) T_S = 770 °C
σ_{RMS} = 3.9 nm
2 µm
(b) J_{NH3} = 19 sccm
σ_{RMS} = 4.3 nm
2 µm
(c) J_{NH3} = 29 sccm
σ_{RMS} = 2.4 nm
2 µm
(d) J_{NH3} = 49 sccm
σ_{RMS} = 1.3 nm
2 µm

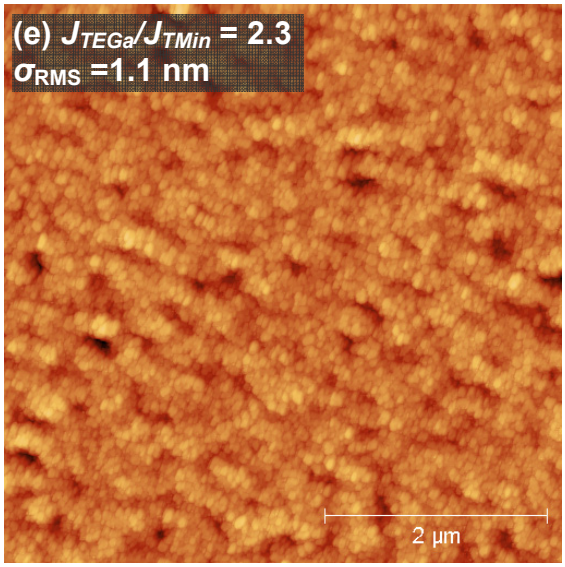

Fig. 7.16. $5 \times 5\ \mu m^2$ AFM surface morphologies and σ_{RMS} of InGaN grown under the conditions given in Table 7.3. The height scale is -20 to 20 nm.

While the present films demonstrate that the improved GR for InGaN can be leveraged to incorporate indium, the window for indium incorporation during NH_3-based MOMBE remains narrow. Consistent with observations of Chapter 4, the highest indium incorporation is obtained under N-limited growth. N-limited growth is identified in Fig. 7.15 by an increase in J_{NH3} from 19 to 29 sccm increasing the GR. Further increasing J_{NH3} to 49 sccm results in growth under N-rich conditions, as identified by the reduction in GR. With the exception of the J_{NH3} = 49 sccm case, the morphologies suggest growth under stoichiometric conditions. The resultant morphologies and GR variations suggest that TMIn reduces both $J_{eff,N}$ and $J_{eff,III}$, reducing the former to a greater extent in the present study. Since Ga incorporation is preferential to In incorporation, the observed indium incorporation under N-limited/III-rich conditions suggests that mixed-alkyl scavenging of Ga adatoms from the growth interface must be a critical mechanism for the incorporation of In during NH_3-based MOMBE of InGaN. Moreover, while sufficient N is necessary to incorporate In, excess N – such that the GR reduces – can inhibit the

incorporation of indium via the N site blocking model discussed in §7.3. To make matters worse, ***excess N is necessary in NH_3-based MOMBE for an atomically smooth surface. Hence, a fundamental difficulty in incorporating indium in NH_3-based MOMBE is that in order for indium to incorporate, N must be present in excess – but in NH_3-based MOMBE, excess N will reduce GR, allowing In to desorb.*** Moreover, indium incorporation and GR are very sensitive to J_{TEGa}/J_{TMIn}. Increasing J_{TEGa}/J_{TMIn} will increase $J_{eff,III}$ and subsequently increase the GR, as shown in Fig. 7.15. However, based on the present model, if an insufficient alkyl population (J_{TMIn}) exists to effectively scavenge $J_{eff,Ga}$, indium will not incorporate and subsequently desorb at the present T_s.

7.7 Conclusions

The growth regimes for GaN growth by NH_3-based MOMBE have been studied for the first time. The influence of J_{NH_3}/J_{TEGa} on the growth regimes and GR of GaN are identified for T_s relevant for the growth of GaN:Mg and InGaN. ***GRs up to ~4 μm/hr are obtained under Ga-rich conditions and atomically smooth GaN is grown at ~1 μm/hr under certain N-rich conditions. Excessively N-rich or excessively Ga-rich conditions are found to inhibit growth.*** The NH_3 efficiency is calculated for each T_s, and effective N/Ga adatom ratios are given that define distinct surface morphology transitions between growth regimes. Moreover, a model is presented which correlates these morphological transitions to reflectivity oscillation trends – providing a fast and simple starting point for optimization of film roughness and identification of growth regime *in situ* using LRI.

The growth conditions resulting in fast growth of GaN are applied to InGaN growth as a means of incorporating increased indium at elevated T_s. ***$In_{0.09}Ga_{0.91}N$ was grown at 355 nm/hr, which is a one-order of magnitude improvement over previous growth conditions used for NH_3-based MOMBE. Atomically smooth $In_{0.04}Ga_{0.96}N$ is demonstrated under N-rich conditions.*** However, consistent with Chapter 4, the highest In incorporation is observed under N-limited growth conditions, suggesting that mixed-alkyl scavenging of Ga species is critical to the incorporation of In during InGaN growth by NH_3-based MOMBE.

CHAPTER 8: NH_3-BASED MOMBE OF MAGNESIUM DOPED GAN AND UV-INDUCED MAGNESIUM DOPANT MODULATION

8.1 Introduction

P-type conductivity in GaN was first achieved in 1989 using bis-cyclopentadienyl magnesium (Cp_2Mg, magnesocene) during atmospheric pressure MOVPE of GaN. *Ex situ* low-energy electron beam irradiation (LEEBI) activated the highly resistive Mg-doped GaN. Hole concentration $p \sim 2 \times 10^{16}$ cm^{-3}, hole mobility $\mu_h \sim 8$ cm^2/V·s, and resistivity $\rho \sim 35$ Ω·cm were achieved [175]. Nakamura *et al.* [176] proposed an acceptor-H neutral complex as the origin of the high resistivity in as-grown Mg-doped GaN in MOVPE. *Ex situ* annealing of highly resistive Mg-doped GaN in N_2 resulted in *p*-type GaN by dissociating neutral Mg-H complexes. Conversely, annealing of Mg-doped GaN in NH_3 resulted in HR GaN by compensating holes via hydrogenation. Mg_{Ga} (Ga substitution by Mg) remains the most successful *p*-type dopant in GaN. However, Mg has a deep acceptor binding (ionization) energy of ~ 200 meV in GaN [84], resulting in only 1% Mg hole activation (doping efficiency) at 300 K. Hence the deep acceptor binding energy of Mg in GaN necessitates an extremely high ~10^{20} cm^{-3} Mg dopant concentration ([Mg]) for a significant concentration of electrically active holes.

Mg-doping of GaN during MBE and MOCVD has been studied extensively. State-of-the-art room temperature $p \sim 3 \times 10^{18}$ cm^{-3}, $\mu_h \sim 9$ cm^2/V·s, and $\rho \sim 0.2$ Ω·cm have been reported for Mg-doped GaN by MOCVD following LEEBI treatment [177].

[Mg] ~ 7×10^{20} cm^{-3} in GaN has been achieved by RF-plasma assisted MBE, resulting in room temperature $p \sim 4.5 \times 10^{18}$ cm^{-3}, $\mu_h \sim 1.1$ $cm^2/V{\cdot}s$, and $\rho \sim 1.3$ $\Omega{\cdot}cm$ [83]. GSMBE (NH_3-MBE) also has produced *p*-type GaN with $p \sim 1 \times 10^{18}$ cm^{-3}, $\mu_h \sim 9$ $cm^2/V{\cdot}s$, and $\rho \sim 0.75$ $\Omega{\cdot}cm$ [178].

Photo-assisted NH_3-based MOMBE is a unique vehicle for the doping of GaN. Drastic C dopant modulation and InGaN alloy modulation have been demonstrated in NH_3-based MOMBE using photoexcitation *in situ* [38,154]. Sun *et al.* [179] has calculated that photoexcitation may reduce the tendency of Mg to segregate at the surface. Hence, photoexcitation may be a mechanism to achieve consistent high [Mg] in GaN or to achieve localized [Mg] inhomogeneity using patterned photoexcitation. Additionally, NH_3-based MOMBE is capable of [C] $>10^{20}$ cm^{-3} [38]. This presents unique C and Mg co-doping scenarios in GaN. Theoretical calculations have predicted that low resistivity *p*-type GaN can be achieved under certain co-doping configurations [180]. *P*-type conductivity has been demonstrated in c-GaN co-doped with O and Be [181], GaN co-doped with Mg and Si, and GaN co-doped with Mg and Zn [182]. However, Mg-doping of GaN by NH_3-based MOMBE has not been reported in the literature. As such, the capabilities of NH_3-based MOMBE for Mg doping and co-doping in GaN as well as the effects of *in situ* photoexcitation during Mg-doping are unknown. ***In this chapter, the first studies of Mg doping of GaN and the effects of photoexcitation during NH_3-based MOMBE of Mg-doped GaN is presented.***

8.2 Complications in the use of Mg for *p*-type GaN

In addition to a deep ~200 meV acceptor binding energy of Mg in GaN, many fundamental complications limit the hole concentration in GaN that results from Mg doping. First, the solubility of Mg in GaN is limited by the competition between incorporation of Mg acceptors and the formation of Mg_3N_2 [183]. Kozodoy *et al.* [184] has observed that Mg incorporation in excess of a critical [Mg] $\sim 3 \times 10^{20}$ cm^{-3} compensates GaN via the formation of such Mg-related complexes (or possibly native donors such as V_N). However, a decrease in Mg acceptor activation energy to 112 meV with increasing [Mg] was observed up to the critical [Mg]. Next, significant surface segregation and accumulation of Mg occur during growth [185]. The inversion of GaN polarity under N-rich growth conditions has been observed for [Mg] $> 2 \times 10^{20}$ cm^{-3} [186]. The polarity inversion of GaN to N-polar consequently reduces the [Mg] as a result of lower Mg incorporation rates for N-polar material [185]. Mg induces Mg-rich pyramidal defects [187], absorbs strongly on growth reactor walls (memory effect) [188], and exhibits an incorporation dependence on ambient O and H [183].

8.3 Experimental procedure

Mg-doped GaN films were grown in the custom built NH_3-based MOMBE showerhead reactor (Chapter 2) on 3.5 μm Si-doped GaN templates (Lumilog, Vallauris, France) using TEGa, Cp_2Mg, and NH_3 precursors. A ~2 μm tantalum film was sputtered

onto the backside of each substrate to promote efficient heating. Samples were immersed twice for 10 min each in a 90 °C piranha solution of H_2SO_4:H_2O_2 (4:1) before loading into the reactor, additional details of the etch are in [128].

Samples were degassed for 30 min at T_s = 150 °C in the introductory chamber. In the growth chamber, samples were annealed for 10 min at T_s = 600 °C with J_{NH_3} = 19 sccm. Afterwards, three GaN layers forming a GaN/GaN:Mg/GaN structure were deposited at T_s = 770 °C with J_{NH_3} = 19 sccm and J_{TEGa} = 0.20 sccm. These conditions are N-rich/Ga-limited and result in an atomically smooth surface (§7.4). First, a 250 nm unintentionally doped (UID) GaN layer is deposited (15 min). Second, a 500 nm Mg-doped GaN layer is deposited (30 min) using one of the following fluxes: J_{Cp_2Mg} = 0.0012, 0.0024, 0.0048, and 0.01 sccm, corresponding to J_{TEGa}/J_{Cp_2Mg} = 170, 85, 42.5, and 20 respectively. Third, a 500 nm UID GaN layer is deposited (30 min). Finally, each sample was cooled at 1 °C/s for 5 min in vacuum ($J_{NH_3} = J_{TEGa} = J_{Cp_2Mg}$ = 0 sccm) in an attempt to activate Mg acceptors. However, Mg-doped GaN films grown by MBE using NH_3 have demonstrated *p*-type conductivity without the post-growth annealing step required for films grown by MOCVD [189].

In order to determine the effects of UV irradiation on the incorporation of Mg into GaN during NH_3-based MOMBE, a second set of GaN/GaN:Mg/GaN structures were grown that were exposed to intense UV radiation during deposition of the 500 nm Mg-doped GaN layer. The Mg-doped GaN layer is the only layer that is exposed to UV irradiation during deposition.

8.4 Custom high irradiance mirror

Chapter 5 demonstrated that intense UV irradiation from a Hg-Xe arc lamp can be patterned with a UV-grade DMD. The patterned UV radiation can then be projected onto a substrate during growth to pattern the composition of the InGaN film that is deposited, such that GaN is deposited in illuminated regions and $In_{0.10}Ga_{0.90}N$ is deposited in dark regions. The feature sizes of the pattern demonstrated were large (millimeter), with only modest contrast ratio. To improve the contrast ratio for patterning, the parabolic reflector of the custom Hg-Xe arc lamp assembly was adjusted to focus the UV radiation to a ~2" diameter spot on the substrate (a maximum broadband irradiance of 144.31 W/cm^2, §3.3), but the commercial turning mirror of the Hg-Xe arc lamp assembly could not withstand the high irradiance. In fact, two turning mirrors were destroyed as a result of focusing the 5 kW Hg-Xe arc lamp radiation. Each mirror cracked after ~40 min of exposure to radiation (Fig. 8.1). Additionally, misalignment of the optical path resulted in the viewport braze being exposed to incident radiation, damaging the flange-quartz braze of one ConFlat quartz viewport. The exposed portion of the viewport braze melted after 95 min of exposure resulting in an instantaneous P_{ch} rise to ~95 mTorr.

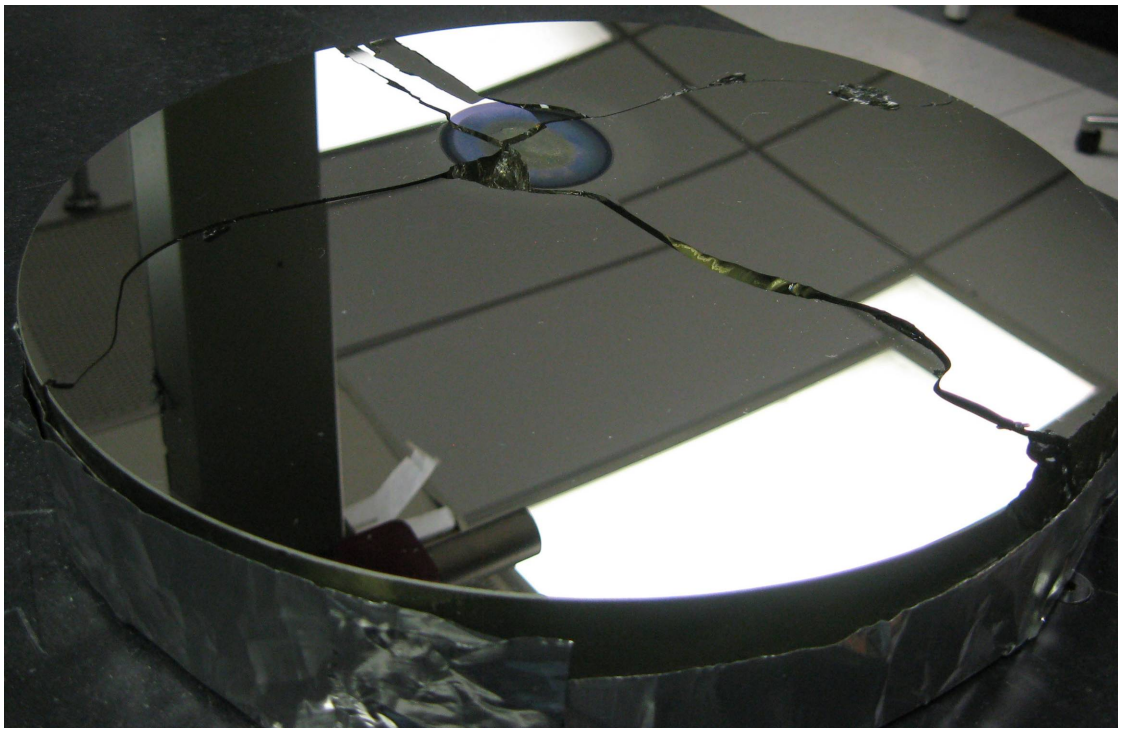

Fig. 8.1. One of two identical UV turning mirror destroyed as a result of ~ 40 min of exposure to 5 kW Hg-Xe arc lamp irradiation. The mirror is 12.5 inches in diameter and 2.13 inches thick.

In order to accommodate the increased irradiance as a result of enhanced focusing of the Hg-Xe arc lamp, a custom high irradiance UV mirror was designed. The custom turning mirror is an all-aluminum, water-cooled design. The mirror was machined in-house from a solid 12.5" diameter rod of 6061-T6511 extruded aluminum. The water channels inside the mirror are shown in Fig. 8.2. Water is injected at 2 gal/min through a ½" NPT fitting at the center of the mirror rear (the water is ~23 °C to prevent condensation on the components). The water is distributed radially through 0.375" wide × 0.5" deep channels and exits the mirror through three ¼" NPT fittings on the side of the mirror. High-temperature tolerant silicone RTV prevents water leakage over channel walls. The sealing flange is recessed into the mirror rear and is sealed with RTV (Fig. 8.5(d)). Additional cooling of the mirror is provided by the 1050 ft^3/min blower which

cools the Hg-Xe arc lamp. An additional 1050 ft^3/min blower cools the viewport components. The rear of the mirror is cool to the touch during operation.

The mirror surface polish and enhanced reflection coating for $\lambda = 365$ nm for the high irradiance UV mirror and was provided by Cabot Microelectronics Polishing Corporation of Addison, Illinois. A photograph of the mirror surface is shown in Fig. 8.3. The flatness of the mirror surface ranges from ~1/4 wave RMS at the center (Fig. 8.4(a)) to ~3/4 wave RMS at the edge (Fig. 8.4(b)). The mirror RMS surface roughness is 25-50 Å (Fig. 8.4(c)-(d)). Cryogenic stress stabilization would be necessary to obtain <1/4 wave RMS flatness (Rayleigh Criterion). Additional polishing of deposited aluminum would be necessary to obtain <20 Å RMS roughness. These two options would have doubled the total mirror cost and were not performed as they were considered unnecessary for the present experiments.

The custom, all-aluminum water-cooled mirror is utilized as the turning mirror in this chapter to expose samples *in situ* to the 5 kW Hg-Xe arc lamp radiation. The radiation is focused to a ~2" diameter spot on the substrate, corresponding to a maximum above-bandgap irradiance of 28.6 W/cm^2 and an above-bandgap photon fluence of 5.2×10^{19} photons/cm^2·s (§3.3). The final Hg-Xe arc lamp assembly is shown in Fig. 8.5. For the present experiments, T_s is automatically controlled by the PID control loop and consistent power compensation to the substrate heater of ~30% (50 W) is observed under UV irradiation (deposition on the viewport in the shape/location of the incident UV is observed under these high irradiance conditions – the power compensation run-to-run is consistent, however, the effect of the deposition on the UV transmission characteristics of the viewport is unknown). Analysis presented in Chapter 6 calculates that the PID

control loop adequately mitigates heating induced by the UV irradiation. As such, the results described in this chapter are not considered a consequence of an increase in T_s resulting from UV irradiation.

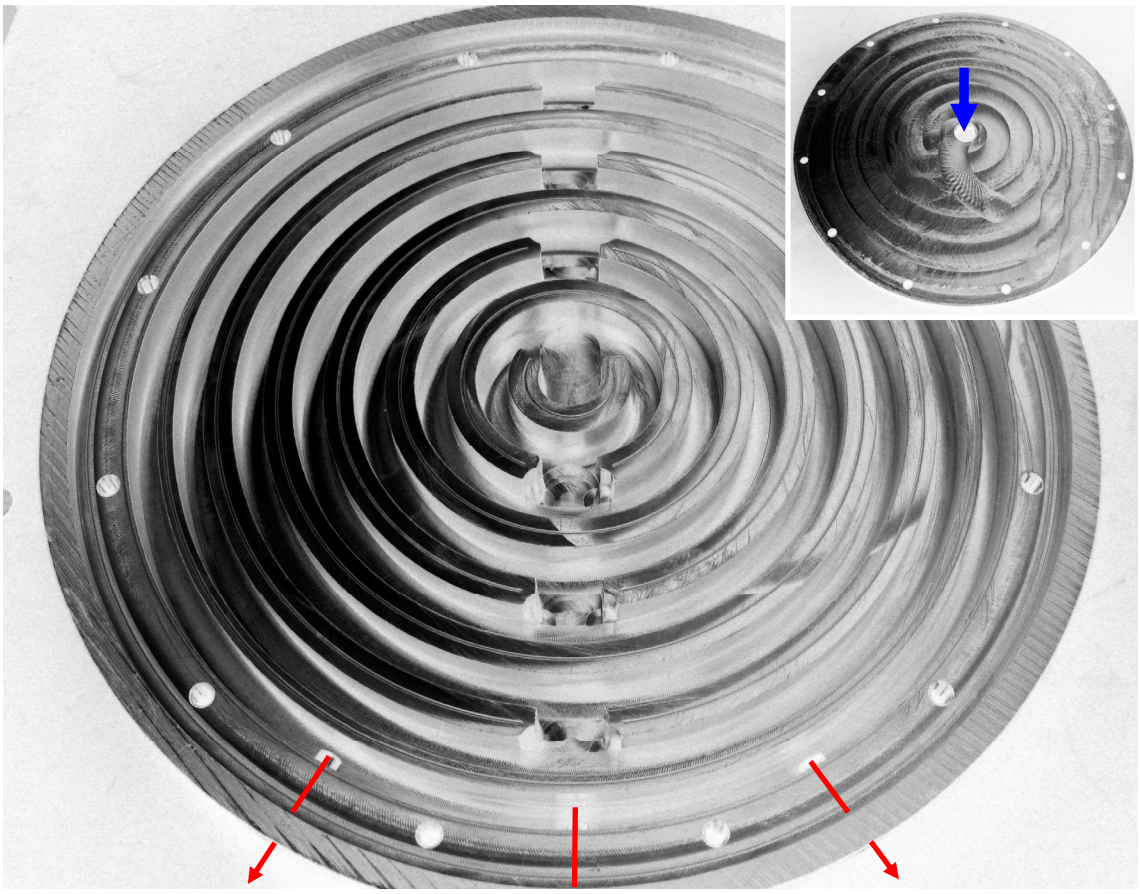

Fig. 8.2. The 0.375” wide × 0.5” deep water-cooling channels of the high irradiance UV mirror (12.5” diameter). The sealing flange (inset) recesses into the rear of the mirror. Water enters the mirror through a ½” NPT fitting in the sealing flange (blue arrow) and exits through three ¼” NPT fittings which penetrate the side of the mirror (red arrows).

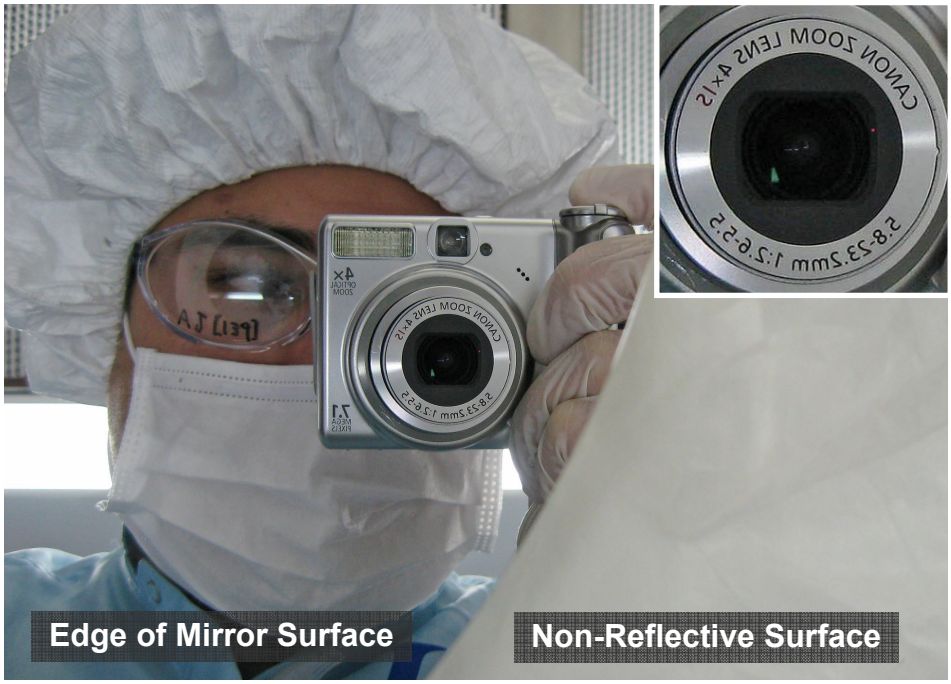

Fig. 8.3. A portion of the mirror surface of the high irradiance UV mirror. The high optical quality of the reflective surface is qualitatively demonstrated by the magnified image shown in the inset.

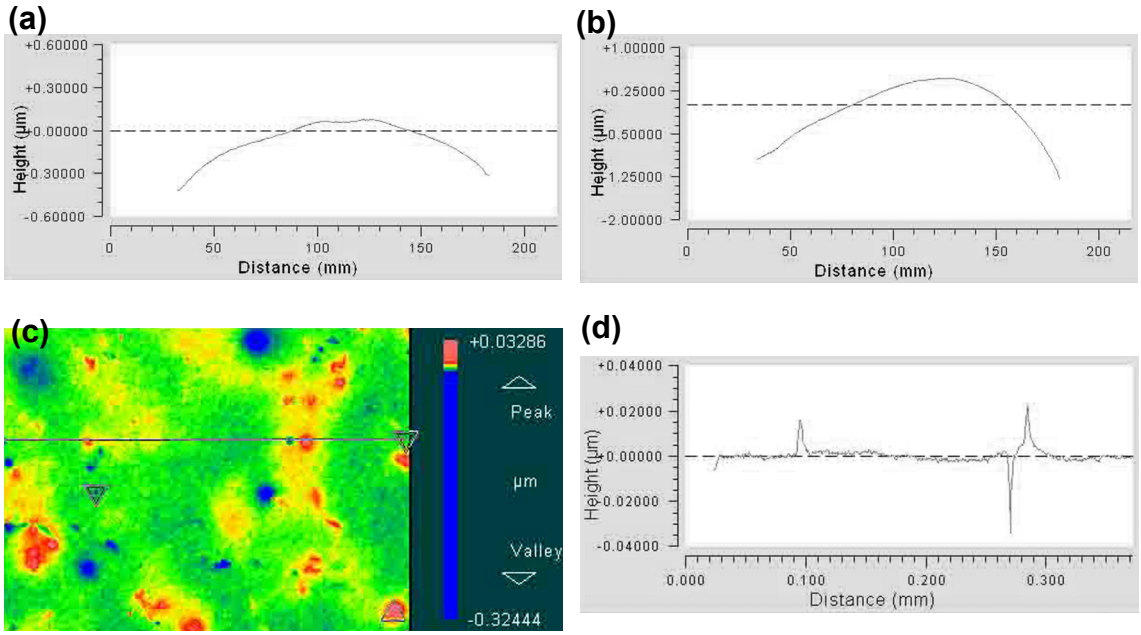

Fig. 8.4. Final surface specifications of UV-enhanced high irradiance mirror. The RMS surface flatness of the mirror is (a) 1/4 wave at the center and (b) 3/4 wave at the edge. A (c) 0.35 × 0.25 mm surface map and (d) associated line profile show $\sigma_{RMS} \sim 30$ Å (other regions show up to $\sigma_{RMS} \sim 50$ Å as a result of localized features). Data courtesy of Cabot Microelectronics Polishing Corporation.

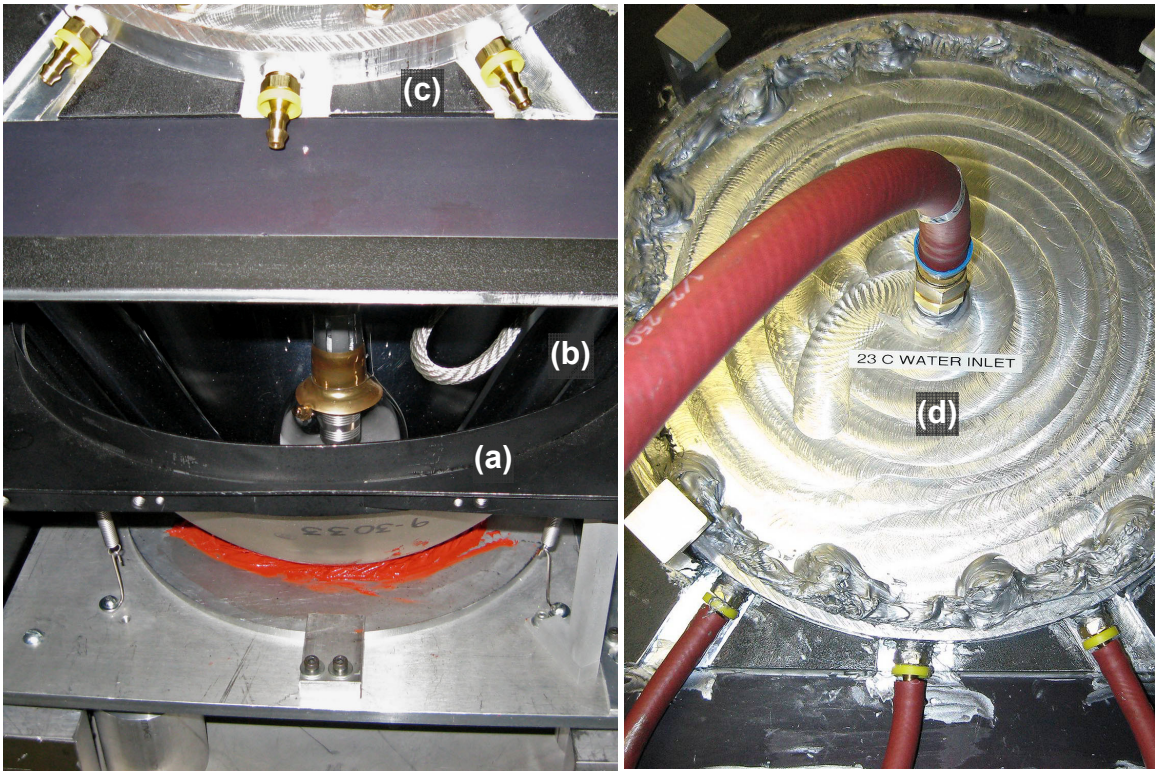

Fig. 8.5. The 5 kW Hg-Xe arc lamp assembly. Part of the assembly housing is removed to show the (a) parabolic reflector and (b) 5 kW Hg-Xe arc lamp. The (c) side and (d) rear of the custom water-cooled, all-aluminum mirror which turns the UV radiation in order to irradiate samples during growth.

8.5 Mg doping of GaN and the effects of UV irradiation

The GR of the GaN layers (Mg doped or UID) that are not exposed to UV radiation during growth is 1.05 μm/hr. The GR is determined via LRI *in situ* and the GR is independent of J_{Cp2Mg} over the studied range. However, for the Mg-doped GaN deposited under UV radiation, the GR is ~0.86 μm/hr. Under UV irradiation, the GR increases slightly with increasing J_{Cp2Mg}, with the GR ranging from 0.85 – 0.88 μm/hr for J_{Cp2Mg} = 0.0012 – 0.01 sccm.

Fig. 8.6 summarizes the effect of J_{Cp2Mg} and UV irradiation during growth on the average [Mg] in GaN. SIMS was performed by Evans Analytical Group (Sunnyvale, CA) and the measured [Mg] depth profiles for each GaN/GaN:Mg/GaN structure are shown in Fig. 8.7 – 8.10. The abruptness of the Mg dopant profile between UID layers and Mg-doped layers (Mg dopant tail-off) is ~2 decade over a thickness of 90 nm (the non-irradiated J_{Cp2Mg} = 0.01 sccm case results in a ~40 nm RMS surface roughness as shown in Fig. 8.13(g), which is expected to lead to the poor [Mg] tail-off in the SIMS depth profile of Fig. 8.10). ***The [Mg] increases with increasing J_{Cp2Mg} over the studied range. A maximum [Mg] ~ 4.1×10^{20} cm^{-3} in GaN is obtained using J_{Cp2Mg} = 0.01 sccm (J_{TEGa}/J_{Cp2Mg} = 20). Exposure to UV radiation during Mg doping of GaN reduces the resultant [Mg] by 21%, 68%, 51%, and 9% for J_{Cp2Mg} = 0.0012, 0.0024, 0.0048, and 0.01 sccm respectively.*** The differences in the percent reduction of [Mg] are believed to be influenced by an accumulation in deposition on the viewport over the course of the present growths, affecting the UV irradiance on the sample (deposition is observed on the viewport during UV irradiation, as described in §8.4). The growths are listed in Table 8.1 in the order they were performed and it is clear that the percent reduction in [Mg] in the GaN:Mg layer decreases as the growths are conducted (*i.e*. deposition accumulates on the viewport under the present extremely high irradiance conditions, affecting the viewport transparency).

Table 8.1. The growth sequence of the present GaN/GaN:Mg/GaN structures and the corresponding J_{Cp2Mg}, J_{TEGa}/J_{Cp2Mg} and UV irradiation conditions during the GaN:Mg layer as well as resultant average [Mg] (<[Mg]>) in the GaN:Mg layer.

Growth ID	J_{TEGa} (sccm)	J_{Cp2Mg} (sccm)	J_{TEGa}/J_{Cp2Mg}	UV during GaN:Mg?	<[Mg]> (cm^{-3})	<Δ[Mg]> with UV
U542	0.20	0.0024	85	Yes	5.0×10^{18}	-68%
U543	0.20	0.0024	85	No	1.6×10^{19}	-
U544	0.20	0.0048	42.5	Yes	7.5×10^{19}	-51%
U545	0.20	0.0048	42.5	No	1.5×10^{20}	-
U546	0.20	0.0012	170	Yes	1.1×10^{19}	-21%
U547	0.20	0.0012	170	No	1.4×10^{19}	-
U548	0.20	0.01	20	Yes	3.7×10^{20}	-9%
U549	0.20	0.01	20	No	4.1×10^{20}	-

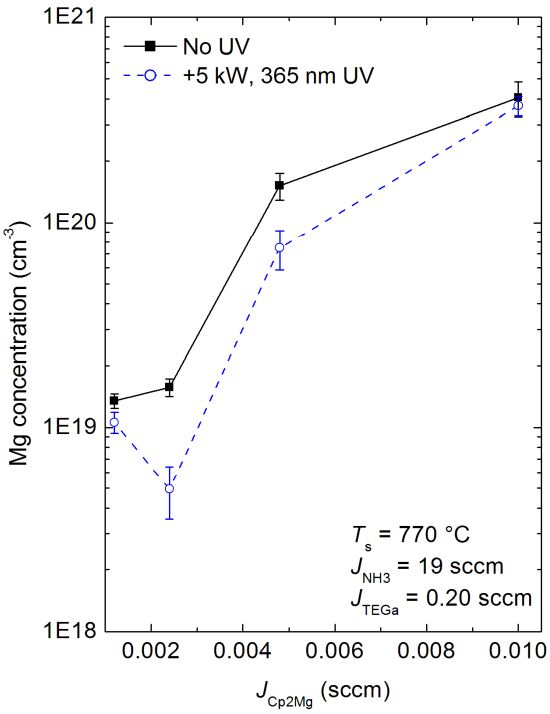

Fig. 8.6. Average Mg concentration in the 500 nm GaN:Mg layer without and with UV irradiation *in situ*. The Mg concentrations are determined using SIMS.

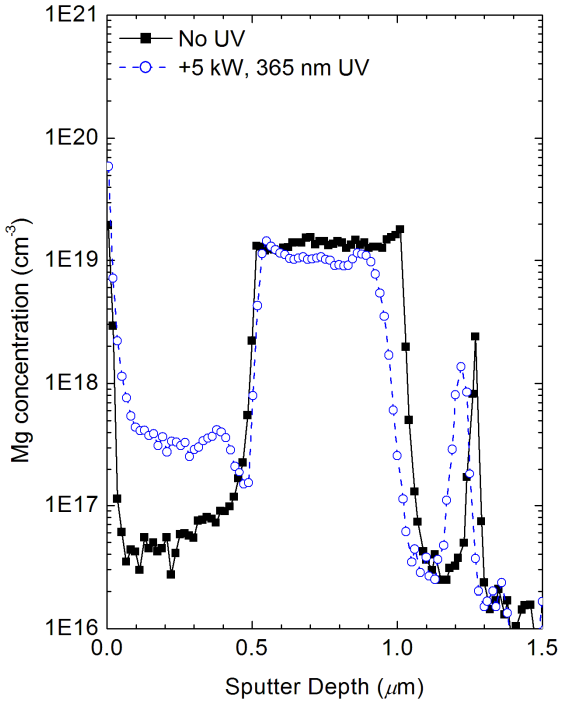

Fig. 8.7. Depth profiles of Mg in GaN/GaN:Mg/GaN (500 nm/500 nm/250 nm) structure without and with UV exposure during Mg doping with J_{Cp2Mg} = 0.0012 sccm (J_{TEGa}/J_{Cp2Mg} = 170). T_s = 770 °C, J_{NH3} = 19 sccm, and J_{TEGa} = 0.20 sccm are constant during the entire deposition.

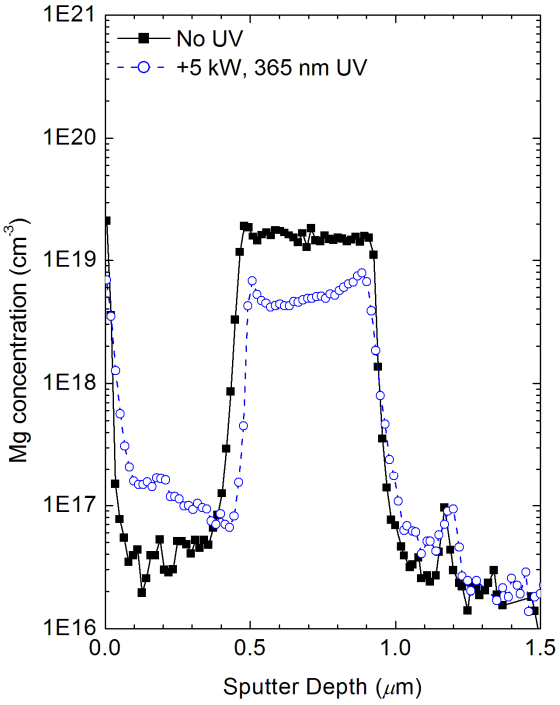

Fig. 8.8. Depth profiles of Mg in GaN/GaN:Mg/GaN (500 nm/500 nm/250 nm) structure without and with UV exposure during Mg doping with J_{Cp2Mg} = 0.0024 sccm (J_{TEGa}/J_{Cp2Mg} = 85). T_s = 770 °C, J_{NH3} = 19 sccm, and J_{TEGa} = 0.20 sccm are constant during the entire deposition.

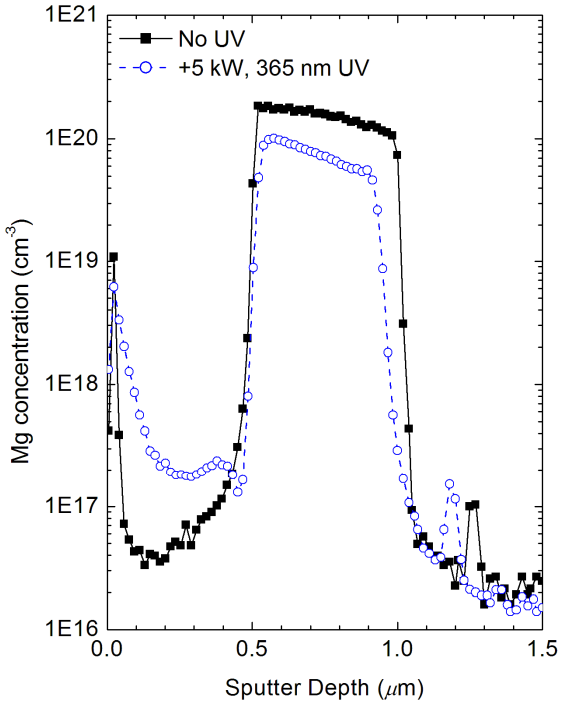

Fig. 8.9. Depth profiles of Mg in GaN/GaN:Mg/GaN (500 nm/500 nm/250 nm) structure without and with UV exposure during Mg doping with J_{Cp2Mg} = 0.0048 sccm (J_{TEGa}/J_{Cp2Mg} = 42.5). T_s = 770 °C, J_{NH3} = 19 sccm, and J_{TEGa} = 0.20 sccm are constant during the entire deposition.

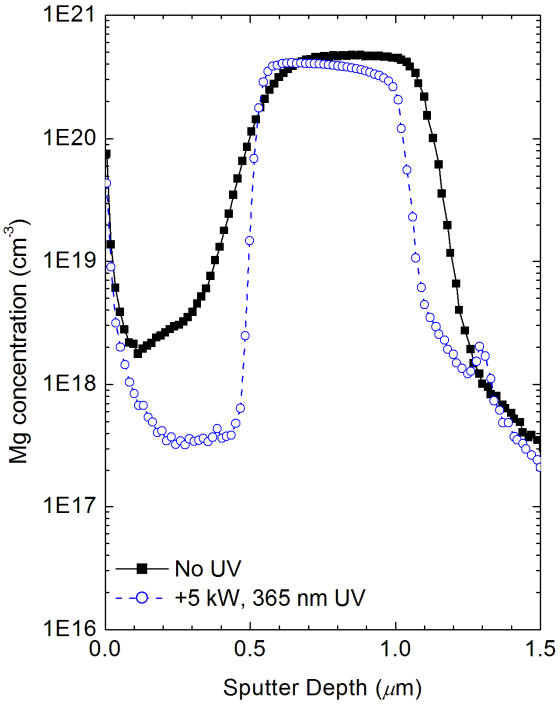

Fig. 8.10. Depth profiles of Mg in GaN/GaN:Mg/GaN (500 nm/500 nm/250 nm) structure without and with UV exposure during Mg doping with J_{Cp2Mg} = 0.01 sccm (J_{TEGa}/J_{Cp2Mg} = 20). T_s = 770 °C, J_{NH3} = 19 sccm, and J_{TEGa} = 0.20 sccm are constant during the entire deposition.

SIMS was performed on the samples employing J_{Cp2Mg} = 0.0048 sccm (J_{TEGa}/J_{Cp2Mg} = 42.5) for Mg-doping in order to determine the effect of Mg incorporation and UV irradiation on the resultant C, O, and H impurity concentrations. The [C], [O], and [H] depth profiles are shown in Fig. 8.11. Since the UV exposed samples have significantly rougher surfaces that might result in higher impurity detection in SIMS, the present analysis only compares the 250 nm UID GaN layer (grown directly on the Si-doped GaN template) with the 500 nm Mg-doped GaN layer (the next grown layer). The Si-doped GaN template is clearly located at >1.25 μm deep in the structure, as evidence

by [Si] ~ 2×10^{18} cm^{-3}. As shown in Fig. 8.11(a), with no UV irradiation during Mg-doping, [C], [O], and [H] increase when compared to UID GaN films. Heavy, unintentional C doping with [C] > 3×10^{20} cm^{-3} is observed, but the increase in [C] as a result of Mg incorporation is modest – a maximum increase by a factor of 1.3. [H] and [O] increase with increasing thickness of the Mg-doped layer, reaching a maximum concentration of ~3×10^{18} cm^{-3}. As shown in Fig. 8.11(b), UV irradiation during Mg doping does not dramatically affect the [H], but reduces the [C] and [O] in the Mg-doped layer by factors of ~1.5 and 2 respectively.

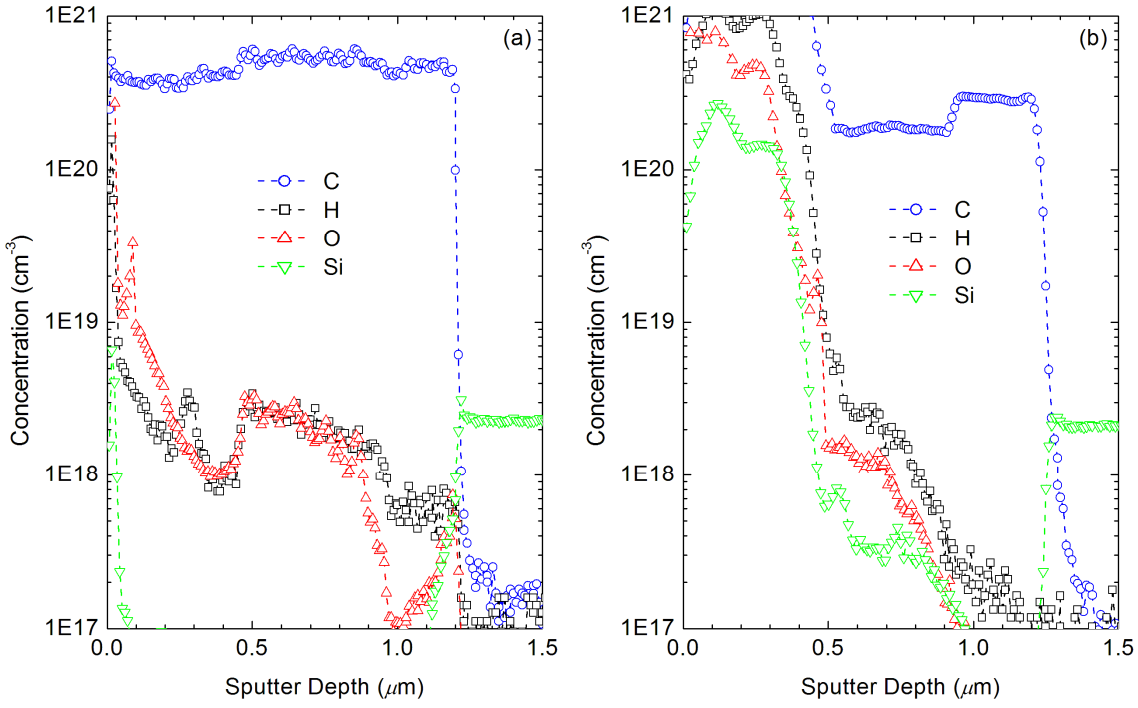

Fig. 8.11. Depth profiles of C, O, H and Si in GaN/GaN:Mg/GaN (500 nm/500 nm/250 nm) structure (a) without and (b) with UV exposure during Mg doping (J_{Cp2Mg} = 0.0048 sccm). T_s = 770 °C, J_{NH3} = 19 sccm, and J_{TEGa} = 0.20 sccm are constant during the entire deposition. Si is shown to identify the Si-doped GaN template.

Fig. 8.12 plots the average partial pressure during GaN and GaN:Mg growth (only the J_{Cp2Mg} = 0.01 sccm case, as justified later) of RGA signals characteristic of NH_3 byproducts (*m/e* = 2, 28), Mg (*m/e* = 24), ethylene (*m*/*e* = 26), ethane (*m*/*e* = 30), argon (*m*/*e* = 40), and O_2/CO_2 (*m*/*e* = 16, 44). In the studied regime, variations in residual gas byproducts as a result of J_{Cp2Mg} are within measurement error. As such, the residual gas byproducts are not considered dependent on J_{Cp2Mg} in this analysis. The only consistent changes in residual byproducts as a result of J_{Cp2Mg} during Mg-doping of GaN are factor of 0.9 reductions in the O_2/CO_2 dominated RGA signals. The decrease in the O_2/CO_2 dominated partial pressures in the chamber is consistent with the observed increase in [O] during Mg-doping. Exposure to UV irradiation during Mg doping of GaN increased the partial pressures of RGA signals related to byproducts of NH_3, Mg, ethylene, and ethane in the chamber by a factor of ~1.5 while increasing the O_2/CO_2 related partial pressures by a factor of 2. These increases in partial pressures from UV appear significant compared to the change in the unrelated argon partial pressure which is within measurement error. The increase in partial pressures of these species indicates that some photo-enhanced desorption occurs, subsequently reducing the incorporation of C, Mg, and O as evidenced by the SIMS data. However, the residual byproducts in the chamber could not be calculated accurately from the measured RGA mass spectra as calculated previously in [38], despite considering additional species that could contribute to the residual gas content of the chamber such as hydrogen cyanide (HCN), propane (C_3H_8), propene (C_3H_6), and methylamine (CH_3NH_2)). Additionally, no desorbing Ga-alkyls (*e.g.* *m*/*e* = 69 and 71) were detected under the present growth conditions, meaning that neither

Cp_2Mg nor related byproducts induce strong scavenging of Ga-alkyls under the present conditions.

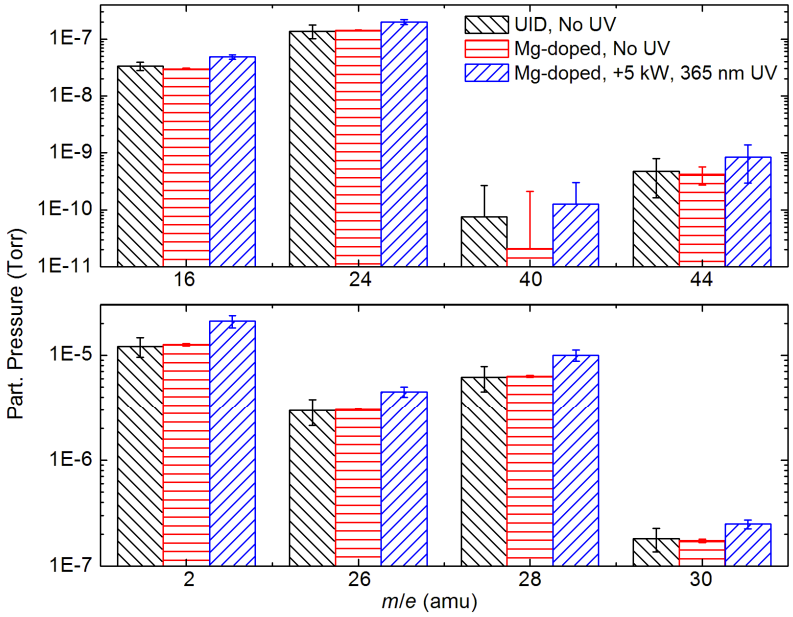

Fig. 8.12. Partial pressure of RGA signals characteristic of NH_3 byproducts (*m/e* = 2, 28), Mg (*m/e* = 24), ethylene (*m/e* = 26), ethane (*m/e* = 30), argon (*m/e* = 40), and O_2/CO_2 (*m/e* = 16, 44) during GaN/GaN:Mg growth with and without *in situ* UV photoexcitation.

Fig. 8.13 shows the surface morphologies for the resultant GaN/GaN:Mg/GaN structures. For structures grown without exposure to UV during deposition of the Mg-doped layer, atomically smooth yet pitted surfaces are observed, as shown in (a), (c), and (e). The reflectivity oscillations measured by the LRI system dampen during these growths, with marginal reduction in average reflectivity (Fig. 8.14(a)) consistent with the observations of Chapter 7. Therefore, under the present conditions, J_{Cp2Mg} does not dramatically affect the surface morphology for $J_{TEGa}/J_{Cp2Mg} > 42.5$ at constant $J_{TEG} = 0.20$ sccm (J_{Cp2Mg} = 0.0048 sccm, σ_{RMS} = 1.4 nm, [Mg] = 1.5×10^{20} cm^{-3}). However,

increasing J_{Cp_2Mg} for $J_{TEGa}/J_{Cp_2Mg} = 20$ ($J_{Cp_2Mg} = 0.01$ sccm) results in a distinctly different surface morphology, as shown in Fig. 8.13(g). The morphology change in this $J_{TEGa}/J_{Cp_2Mg} = 20$ ($J_{Cp_2Mg} = 0.01$ sccm) case is suspected to be a direct consequence of the high [Mg] ~ 4×10^{20} cm^{-3}, as a dramatic decrease in average reflectivity is observed after the introduction of Cp_2Mg (Fig. 8.14(b)).

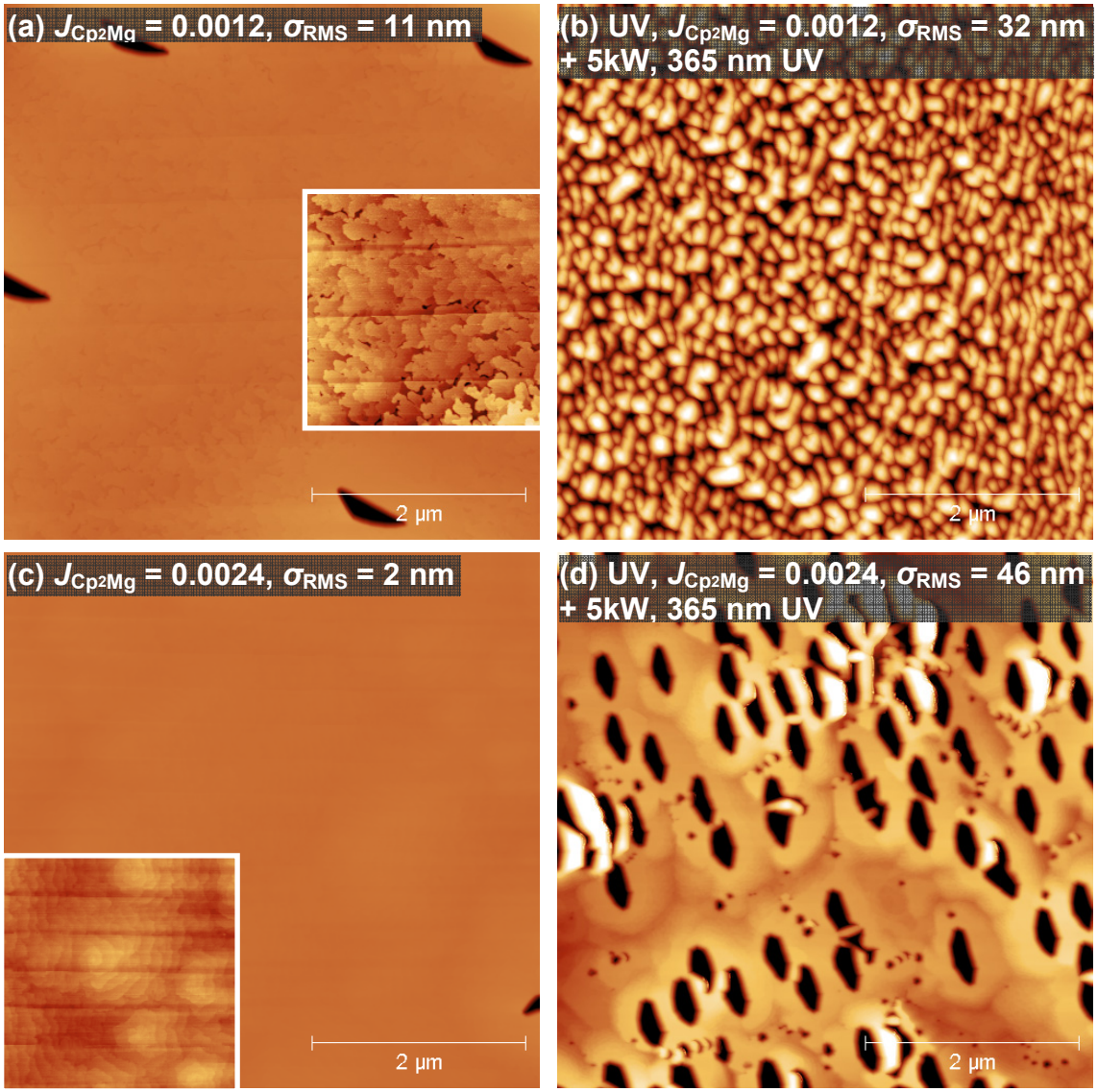

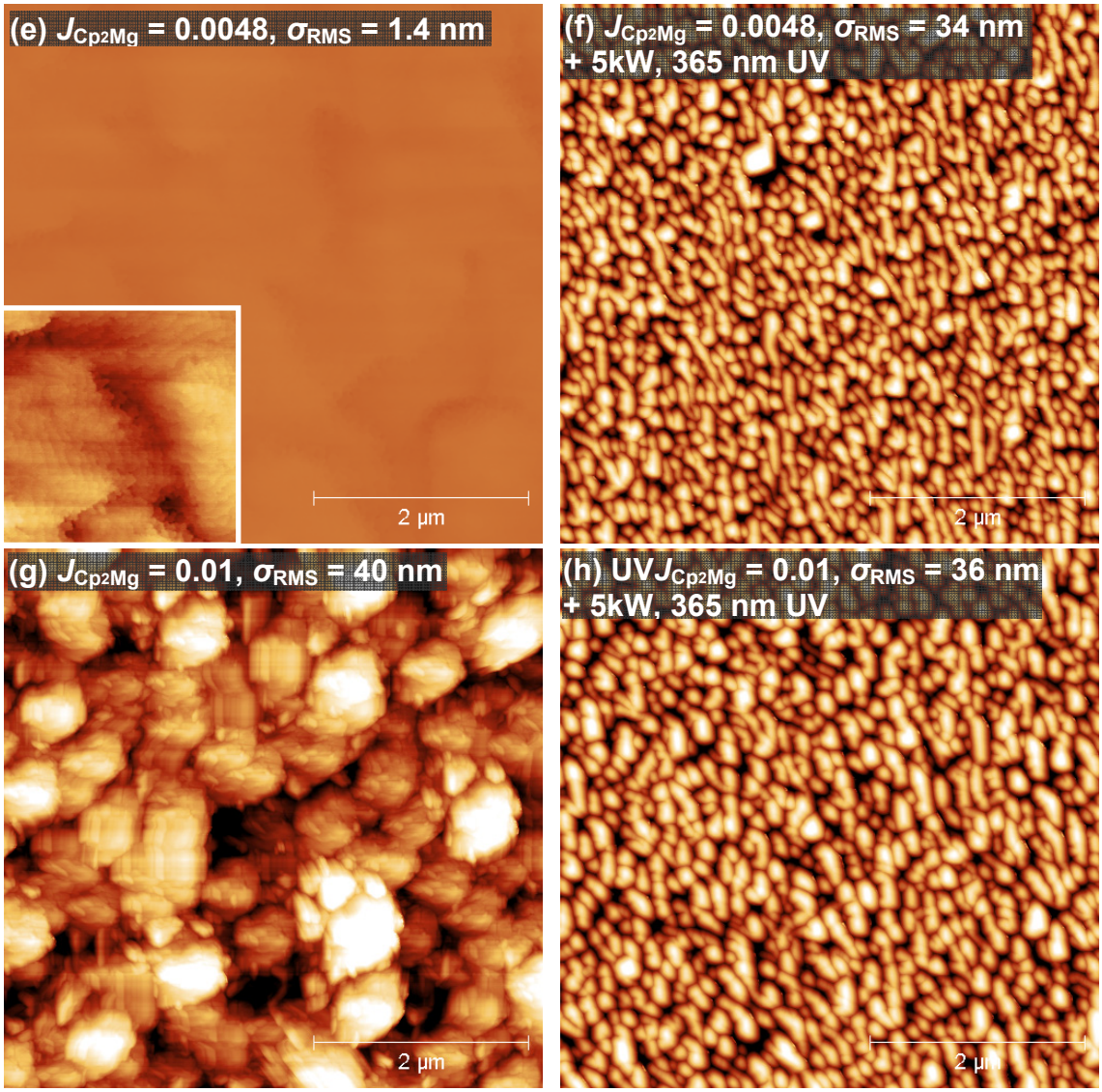

Fig. 8.13. $5 \times 5\ \mu m^2$ AFM surface morphologies and σ_{RMS} of GaN:Mg grown at T_s = 770 °C with J_{NH3} = 19 sccm and J_{TEGa} = 0.2 sccm (N-rich/Ga-limited conditions). J_{Cp2Mg} (sccm) and UV exposure conditions are denoted. The height scale for (a) – (h) is -100 to 100 nm. The inset of (a), (c), and (e) is $2 \times 2\ \mu m^2$ and the height scale is -5 to 5 nm.

Additionally, Fig. 8.13(b), (d), (f) and (h) show that ***all structures exposed to UV radiation during deposition of the Mg-doped GaN layer exhibit ~90 nm deep pits resulting in σ_{RMS} = 32 – 46 nm.*** The rough morphologies are consistent with GaN grown under excessively N-rich/Ga-limited conditions, yielding vertical features as a result of

poor adatom surface diffusion under N-rich conditions (Chapter 7). Excessively N-rich/Ga-limited conditions could be a result of photo-enhanced desorption of Ga and Mg related species. The reductions in GR and [Mg] as a result of exposure to UV radiation, as well as the subsequent increase in residual byproducts, are indicative of photo-enhanced desorption of Ga and Mg species under N-rich growth conditions. Moreover, Fig. 8.14(c) shows that under UV irradiation, the average reflectivity is maintained under the J_{Cp_2Mg} = 0.01 sccm (J_{TEGa}/J_{Cp_2Mg} = 20) conditions – which is suggestive of photo-enhanced desorption of Mg that would otherwise (under no UV irradiation) roughen the surface morphology (Fig. 8.13(g)) and consequently decrease the average reflectivity (Fig. 8.14(b)). Additionally, the average reflectivity during Mg-doping under UV irradiation is maintained (Fig. 8.14(c)), which suggests that the dramatic roughening of the surface does not occur during UV irradiation, but during the growth of the subsequent layer.

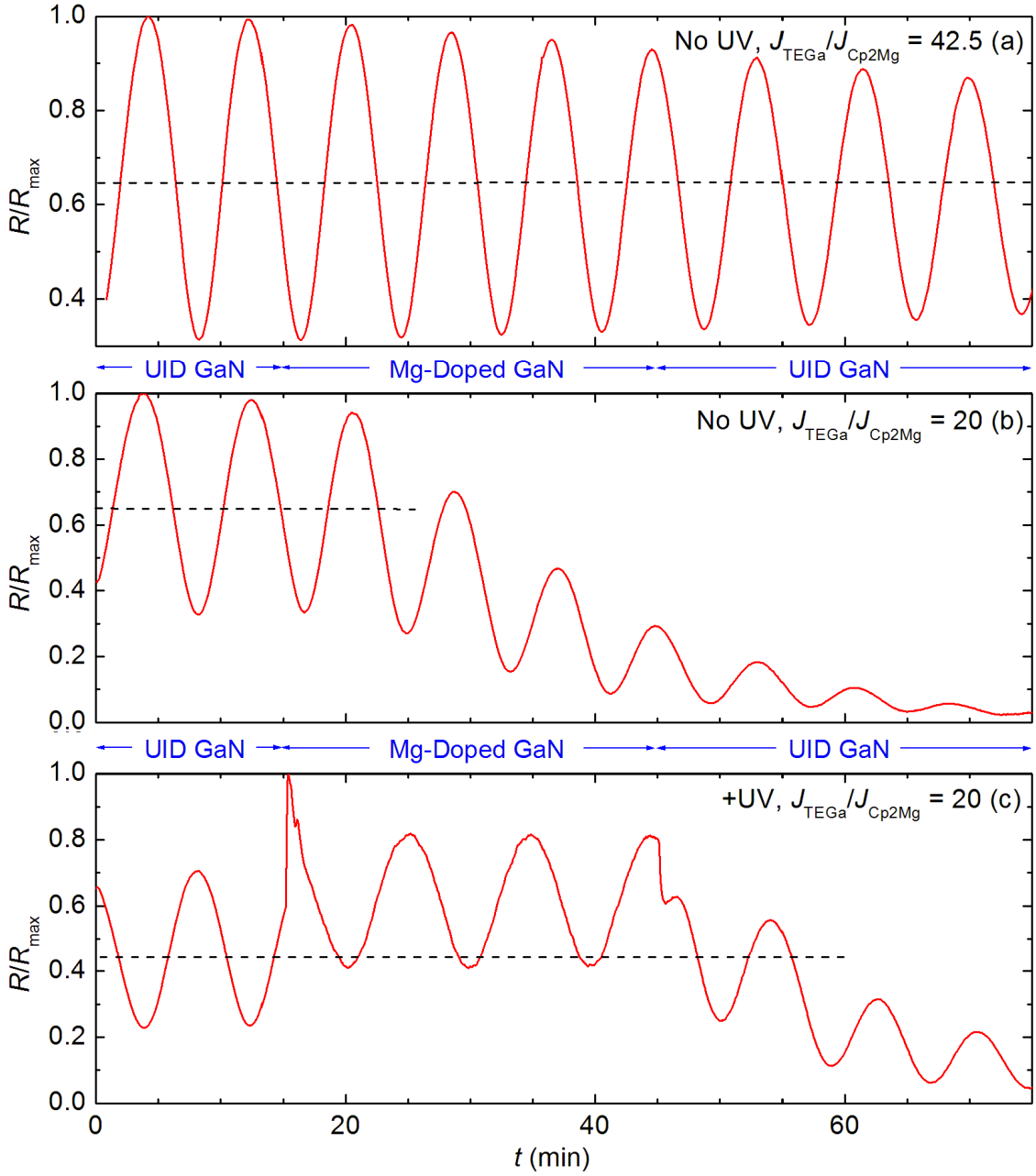

Fig. 8.14. Evolution of reflectivity oscillation during three layer structure consisting of 250 nm GaN, 500 nm GaN:Mg, and 500 nm GaN with (a) no UV and J_{Cp2Mg} = 0.0048 sccm (J_{TEGa}/J_{Cp2Mg} = 42.5) during Mg-doping (representative of J_{TEGa}/J_{Cp2Mg} = 170 and 85), (b) no UV and J_{Cp2Mg} = 0.01 sccm (J_{TEGa}/J_{Cp2Mg} = 20) during Mg-doping, and (c) UV and J_{Cp2Mg} = 0.01 sccm (J_{TEGa}/J_{Cp2Mg} = 20) during Mg-doping. J_{TEGa} = 0.20 sccm, J_{NH3} = 19 sccm, and T_s = 770 °C remained fixed through the entire deposition process. R is normalized to R_{max}. In (c), the change in average reflectivity during UV irradiation is a result of detection of the λ = 632 nm component of the arc lamp emission by the LRI system.

8.6 Electrical characterization

All of the present Mg-doped layers are highly resistive as determined by C-V depth profiling. Separate, individual GaN:Mg layers also exhibit highly resistive behavior in Hall effect characterization. GaN:Mg and $Al_xGa_{1-x}N$:Mg ($0 < x < 0.08$) grown by MBE using NH_3 has demonstrated as-grown *p*-type conductivity in films co-doped with Mg and O at concentrations of ~1.6×10^{20} ($\mu_n \sim 40$ cm^2/V·s) and ~4×10^{18} cm^{-3} ($\mu_n \sim 8$ cm^2/V·s) respectively with acceptor activation of ~1.3% [190]. The co-dopant impurity concentrations are nearly identical to the $J_{Cp_2Mg} = 0.0048$ sccm ($J_{TEGa}/J_{Cp_2Mg} = 42.5$) case of this study ([Mg] ~ 1.5×10^{20} cm^{-3} [O] ~3×10^{18} cm^{-3}, albeit the concentrations are non-uniform). The highly resistive behavior in the present GaN:Mg films is attributed primarily to compensation by heavy carbon doping with [C] > 3×10^{20} cm^{-3}. Sheet resistance ~1×10^8 Ω/□ and resistance > 10^{12} Ω have been measured in unintentionally, yet heavily carbon-doped GaN with [C] ~ 1.5×10^{19} cm^{-3} (achieved using $J_{TEGa} = 0.07$ sccm in order to lower the carbon incorporation) grown by the present reactor.

8.7 Conclusions

Mg-doped GaN films by NH_3-based MOMBE have been demonstrated for the first time. All films are highly resistive with Mg dopant concentrations from 5×10^{18} – 4×10^{20} cm^{-3}. The high resistivity is attributed to compensation by unintentional carbon

doping with [C] > 3×10^{20} cm^{-3}. Mg-doped films that contain [Mg] below the necessary threshold for GaN polarity inversion are atomically smooth. However, films exposed to intense UV radiation during growth exhibit 90 nm deep defects resulting in $\sigma_{RMS} \sim 40$ nm. ***Irradiation by intense UV during Mg-doping of GaN significantly reduces the concentrations of Mg, O, and C in the deposited film. Reductions in GR and [Mg] as a result of exposure to UV radiation, as well as subsequent increases in observed residual byproducts in the growth chamber, suggest that the reductions in [Mg], [O], and [C] are a result of photo-enhanced desorption of Ga and Mg species from the growth interface.*** A maximum reduction in [Mg] from 1.6×10^{19} to 5×10^{18} cm^{-3} (68%) was achieved as a result of intense UV irradiation during growth. Additional results of Mg-doping of GaN by NH_3-based MOMBE are given in §A.2.

CHAPTER 9: CONCLUSIONS AND FUTURE DIRECTIONS

9.1 Conclusions

This work pioneers UV-assisted NH_3-based MOMBE as a particularly selective epitaxy technique to create a pathway toward three-dimensional epitaxy of III-Nitride films. The salient results are:

1. A novel NH_3-based MOMBE system has been developed which enables irradiation of films during deposition with intense UV radiation and dynamically patterned UV radiation.

2. GaN by NH_3-based MOMBE typically contains ~10^{19} – 10^{21} cm^{-3} carbon dopant concentration, rendering films highly resistive. The demonstrated carbon dopant concentration is ~2 orders of magnitude higher than that attainable by advanced MBE and MOCVD growth technology.

3. UV irradiation liberates hydrocarbon species from the growth interface, subsequently reducing the incorporation of carbon into GaN while enhancing the GR. This represents a mechanism for 3DE of GaN in regards to the carbon dopant concentration. Ethylene and ethane are identified as the primary surface

reaction byproducts and can be quantified *in situ* and as a means to predict the resultant carbon concentration.

4. InGaN by NH_3-based MOMBE has been detailed for the first time. Indium incorporation during NH_3-based MOMBE of InGaN is particularly challenging. A maximum indium concentration of 19% is achieved under N-limited conditions. Three interdependent variables are determined to govern indium incorporation: active N, In/In-methyl surface coverage, and III-alkyl desorption.

5. Mixed alkyl metal organic precursors can result in scavenging of cation species from the growth interface. The effect is important for the incorporation of indium into InGaN under the present conditions. Fragment patterns for desorbing III-alkyls during the growth of InGaN are calculated.

6. UV irradiation inhibits the incorporation of indium into InGaN by preferentially photodesorbing In/In-methyl species from the growth interface, effectively limiting the indium available to incorporate into the alloy. The above-bandgap irradiance necessary to inhibit the incorporation of indium into InGaN is estimated to be 102 mW/cm^2 – 3.17 W/cm^2.

7. Lateral compositional patterning of InGaN during NH_3-based MOMBE by digital micromirror patterning of UV photoexcitation is demonstrated for the first time. The novel technique demonstrates a feasible pathway toward the realization 3DE.

8. The growth regimes for GaN growth by NH_3-based MOMBE are studied for the first time. N-rich conditions are necessary for atomically smooth GaN and InGaN films by NH_3-based MOMBE. A model is presented correlating reflectivity transients *in situ* to the surface morphology, enabling film optimization and growth regime identification *in situ*.

9. NH_3-based MOMBE is particularly sensitive to excessively N-rich or excessively III-rich growth conditions, either of which will inhibit growth.

10. NH_3-based MOMBE is capable of GaN growth at fast growth rates (~4 μm/hr). The fast growth rates can be leveraged to retain significant indium incorporation into InGaN at elevated T_s.

11. The doping of GaN by magnesium during NH_3-based MOMBE has been detailed for the first time. Magnesium dopant concentrations of $5 \times 10^{18} - 4 \times 10^{20}$ cm^{-3} in GaN are achieved. All Mg-doped films are highly resistive.

12. UV irradiation decreases the incorporation of magnesium into GaN. A maximum reduction in the magnesium dopant concentration of 68% is observed in the presence of intense UV radiation during growth. The reduction is attributed to photodesorption of Mg and Ga species from the growth interface. This represents a mechanism for 3DE of GaN in regards to the magnesium dopant concentration. However, intense UV irradiation dramatically roughened the resultant films.

9.2 Future directions

While this work has helped establish the foundation for the NH_3-based MOMBE growth process and this work has demonstrated that intense UV irradiation during NH_3-based MOMBE is capable of inducing variations in dopant and alloy concentration (albeit modest in some cases) which may be useful as a pathway for realizing 3DE, this work has also raised practical considerations in the application of MOMBE and 3DE toward the development of devices. Some important considerations are:

1. While MOMBE appears capable of producing III-Nitride films with comparable growth rates, crystalline quality, and smoothness as that of MBE and MOCVD, the challenge which may ultimately decide the fate of NH_3-based MOMBE in the form presented in this work is the ability to sufficiently regulate, passivate, or leverage the carbon concentration in the resultant films, which is clearly dependent on the eventual device application. While the extremely high (state of the art) carbon dopant concentrations detailed in Chapter 3 and Chapter 8 provide HR GaN potentially useful for low leakage III-Nitride transistors, the carbon renders the films grown by NH_3-based MOMBE optically inactive for practical devices (all NH_3-based MOMBE samples grown with the present reactor, including 5-period InGaN/GaN MQW structures that have been characterized by photoluminescence spectroscopy (PL) exhibit weak band-edge emission, but show yellow luminescence emission that is orders of magnitude stronger – typically associated with carbon defect levels). Two thoughts are offered. First,

the carbon dopant source should be decoupled from the cation precursor if it is desired to reduce the carbon dopant concentration toward that of III-Nitrides grown by MBE or MOCVD. If it is important to retain the all gaseous convenience of MOMBE (§1.2 and §2.2), this would require retaining a metal organic precursor as the carbon dopant source, but using a different gallium precursor rather than TEGa or TMGa (it should be noted that the utilization of TEGa in plasma-assisted MBE should enable extremely high carbon dopant concentrations for HR GaN). Second, as discussed in Chapter 3, C_N is a theoretical acceptor in GaN, the formation of which may be encouraged under Ga-rich growth conditions detailed in Chapter 7 (C is amphoteric, and is responsible for a variety of defects states as introduced in §3.1). However, growth under Ga-rich conditions can result in textured, 3D morphologies (vs. atomically smooth GaN under N-rich conditions) which may preclude device operation.

2. The incorporation of indium for InGaN is challenging in NH_3-based MOMBE. As described in Chapter 4, the origin of the problem originates from the compromise of N for In, which is fundamentally rooted in both the substrate temperature and the catalytic nature of NH_3 dissociation. While NH_3 has proven rather suitable for non-indium containing compounds (GaN, GaN:Mg, and AlGaN), NH_3 does not appear well suited for InGaN growth. For $In_xGa_{1-x}N$ with $x > 0.10$ mole fraction, a nitrogen precursor which more readily dissociates at T_s ~500 °C should be utilized. Additionally, such a source may enable buffer layer

nucleation on sapphire by MOMBE, which as described in §A.5, has remained far from optimized using NH_3 through the course of this work.

3. The maximum indium composition able to be modulated by UV (Chapter 5) has been limited by the indium composition consistently attainable in the alloy. As described in §A.3, the whole AlGaN composition range by NH_3-based MOMBE has been achieved recently using the present reactor. Hence, AlGaN may be a better alloy to discern the effects of intense UV irradiation during growth since the whole composition range is available to be manipulated by UV irradiation *in situ*. Additionally, UV irradiation of AlGaN may help elucidate a fundamental UV irradiance threshold. Specifically, the intense irradiances used in this work (especially in Chapter 8) compromise the apparatus (*e.g.* the DMD, incident viewport, flanges, electronics, etc). A lower power (~ 500 W) Hg-Xe arc lamp may be sufficient to induce photodesorption during NH_3-based MOMBE. Moreover, AlGaN is necessary to leverage the HR GaN:C of Chapter 3 for AlGaN/GaN:C HEMT devices by NH_3-based MOMBE, as described in §A.3.

4. While 3DE is certainly a fascinating concept for the creation of devices *in situ*, there are important considerations in implementing the approach detailed in this thesis towards the creation of devices as introduced in §1.1. First, the components which facilitate the irradiation of samples *in situ* (*e.g.* viewport, lenses, DMD, etc.) must be carefully designed such that the patterns can be projected accurately and consistently onto samples. Important considerations include the failure of

optical components (§8.4, extreme cooling of individual components may be necessary; it should be noted that the DMD is believed to be unable to withstand the irradiance used in Chapter 8), deposition on optical components under certain irradiance conditions (§8.5) and growth conditions (§2.4) which can affect run-to-run irradiance, possible film contamination/parasitic reactions as a result outgassing of the viewport (§2.4), and vibration of the optical assembly (the millimeter features demonstrated in §5.6 were not noticeably affected by vibration). Second, the feature size necessary for a particular device must be considered. As described in §1.5, while 3DE may facilitate "natural" devices, the ultimate patterning resolution *within the growth plane* is diffraction limited. However, in practical implementation, the patterning resolution within the growth plane is limited also by the size of individual micromirrors (13.68 μm × 13.68 μm, the DMD is a 1024 × 768 array of micromirrors) and the optical exposure system. Moreover, the formation of structures during deposition means that the vertical acuity (*i.e.* the acuity of the interface *between* light and dark regions during the patterning process; the layer thickness can be controlled to monolayer precision) may be affected by the adatom diffusion length (*i.e.* growth conditions, as discussed in Chapter 7) if diffusion were to dominate over photodesorption during patterning by 3DE (*e.g.* if the photodesorption of indium species is strong, the diffusion of indium adatoms from light to dark patterned regions may be ignored). Finally, the selectivity of patterning may be problematic. As shown in Chapter 8, UV irradiation (of extremely high irradiance) during the Mg doping of GaN affects not only the concentration of *multiple* dopants, but also the surface

morphology. Such complications may preclude the formation of devices by, for example, using patterned UV during deposition to grow a film that may be patterned accurately in terms of dopant concentration, but also patterned morphologically (which could be useful for certain applications).

APPENDIX A: SUPPLEMENTAL DATA

A.1 Si-doping of InGaN

Si is the common dopant for controlling n-type conductivity in III-Nitrides. However, effective Si-doping of III-Nitrides has not been reported using NH_3-based MOMBE. Si-doping during InGaN growth at T_s = 730 °C with J_{NH_3} = 49 sccm, J_{TEGa} = 0.11 sccm, and J_{TMIn} = 0.09 sccm was attempted using disilane (Si_2H_6). The effects of $J_{Si_2H_6}$ on the In composition and GR of InGaN are shown in Fig. A.1. Both In composition and GR decrease with increasing $J_{Si_2H_6}$, such that no discernable indium incorporates (as measured by XRD) for the case of $J_{Si_2H_6}$ = 0.012. Also, at $J_{Si_2H_6}$ = 0.012, the surface morphology is dramatically different as shown in Fig. A.2, with σ_{RMS} = 25 nm compared to $\sigma_{RMS} \leq 1.4$ nm for $J_{Si_2H_6} \leq 0.0048$ sccm.

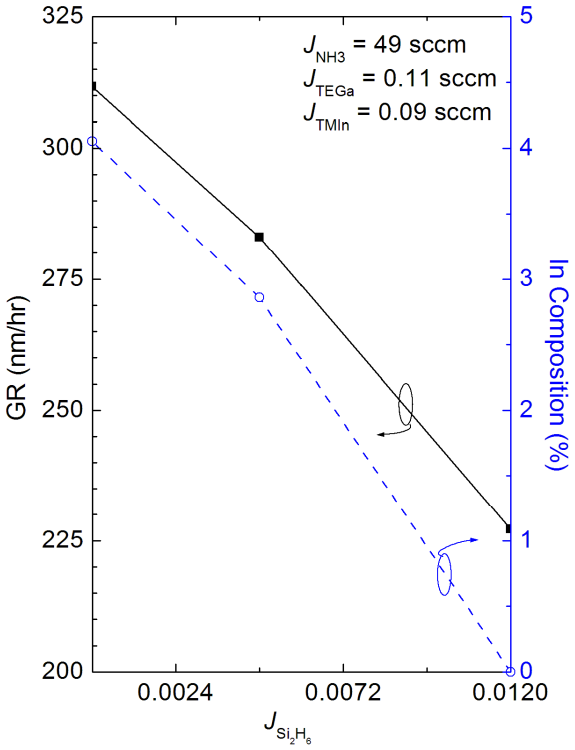

Fig. A.1. GR and composition variation with J_{Si2H6} for InGaN grown at T_s = 730 °C under J_{NH3} = 49 sccm, J_{TEGa} = 0.11 sccm, and J_{TMIn} = 0.09 sccm.

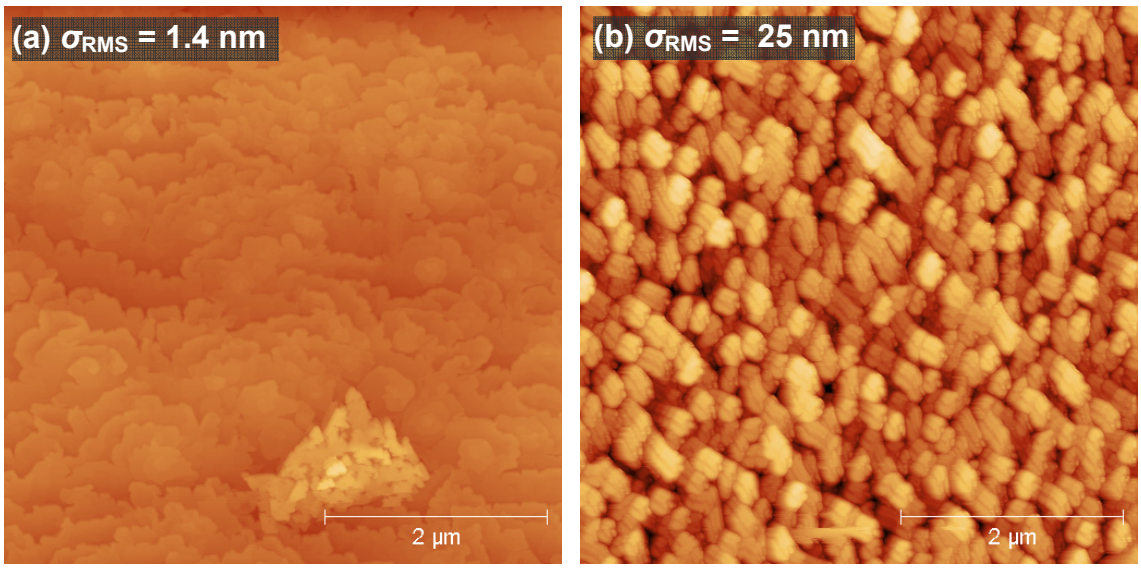

Fig. A.2. 5 × 5 μm^2 AFM surface morphologies and σ_{RMS} of InGaN grown at T_s = 730 °C under J_{NH3} = 49 sccm, J_{TEGa} = 0.11 sccm, and J_{TMIn} = 0.09 sccm with J_{Si2H6} = (a) 0.0048 and (b) 0.012 sccm. The height scale of (a) is -20 to 20 nm. The height scale of (b) is -100 to 100 nm.

A.2 Dependence of T_s on Mg-doping of GaN

Alternating layers of UID GaN and GaN:Mg were grown in a single structure on a Si-doped GaN template at T_s = 870, 840, 810, and 780 °C with J_{NH_3} = 35 sccm, J_{TEGa} = 0.17 sccm, and J_{Cp_2Mg} = 0.024 sccm (J_{TEGa}/J_{Cp_2Mg} = 7). The growth conditions yield N-rich growth (the degree of N-richness decreases with each reduction in T_s). The effect of T_s on [Mg] in GaN is shown in Fig. A.3. [Mg] was determined by SIMS in-house using an Atomika Instruments Ion Microprobe A-DIDA 3000-30 and a calibrated Mg standard. A 2-order increase in [Mg] is observed by decreasing T_s from 870 to 780 °C, resulting in a maximum [Mg] ~ 2.7×10^{20} cm^{-3}. This trend is consistent with strong Mg and Cp_2Mg desorption at T_s ~ 870 °C which precludes significant Mg incorporation. Additionally, the observed increase in GR with reduced T_s is consistent with a reduction in Ga and DEGa desorption during growth in N-rich growth regime.

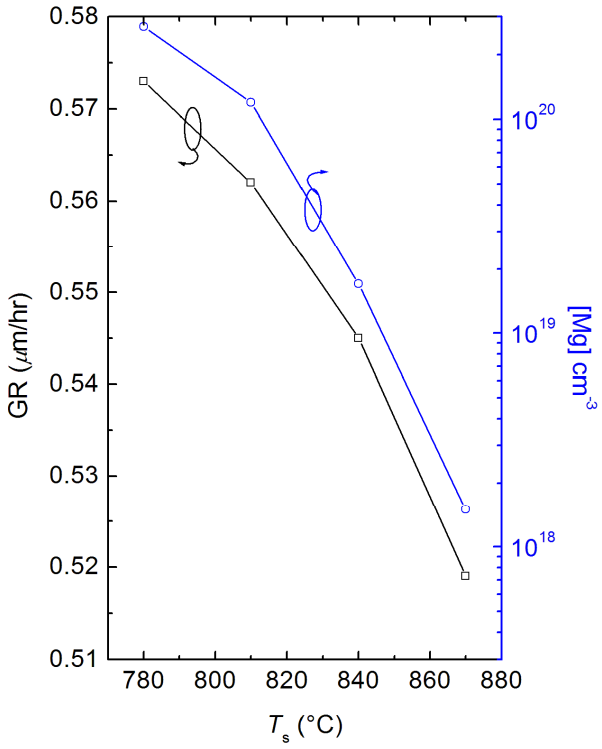

Fig. A.3. GR and Mg concentration for GaN grown at T_s = 780, 810, 840, and 870 °C with all other growth parameters constant.

A.3 AlGaN by NH_3-based MOMBE

Presently, no reports of AlGaN by NH_3-based MOMBE exist in the literature. Initial investigations of AlGaN growth by NH_3-based MOMBE in the present reactor employed TEGa, dimethylethylamine alane (DMEAA), and NH_3. DMEAA is an attractive precursor because AlGaAs by MOMBE has demonstrated reduced C and O impurity concentrations using DMEAA [191]. $Al_xGa_{1-x}N$ with Al mole fraction x up to 1 (AlN) was obtained using DMEAA in the present reactor. However, it was difficult to consistently reproduce x because the vapor pressure from the DMEAA bubbler was

erratic (even after pump down of the delivery line). This anomaly is consistent with the high volatility of DMEAA [192] such that the reproducibility issues were a result of constant decomposition of DMEAA, meaning that an unknown species of high vapor pressure was being introduced in place of DMEAA (or diluting DMEAA) and subsequently affecting the growth of AlGaN.

DMEAA was replaced by triethylaluminum (TEAl) to improve the stability of the Al precursor and to prevent mixed alkyl scavenging from complicating the $Al_xGa_{1-x}N$ alloy composition [145]. Epitaxial $Al_xGa_{1-x}N$ films spanning the entire composition range have been grown at T_s = 870 °C under N-rich conditions by NH_3-based MOMBE using TEAl and have reported for the first time [193]. The crystalline quality of the films mimics the GaN template and atomically smooth surfaces with pits are observed under certain conditions. However, films with $x \geq 0.15$ exhibit microcracks along $<11\bar{2}0>$ and films with $x \geq 0.90$ exhibit a degraded crystal quality and surface morphology [193]. Additional studies are optimizing these AlN and $Al_xGa_{1-x}N$ films grown by NH_3-based MOMBE for use in $Al_{0.3}Ga_{0.7}N$/GaN:C HEMTs [194]. An example of such a HEMT structure is shown in Fig. A.4.

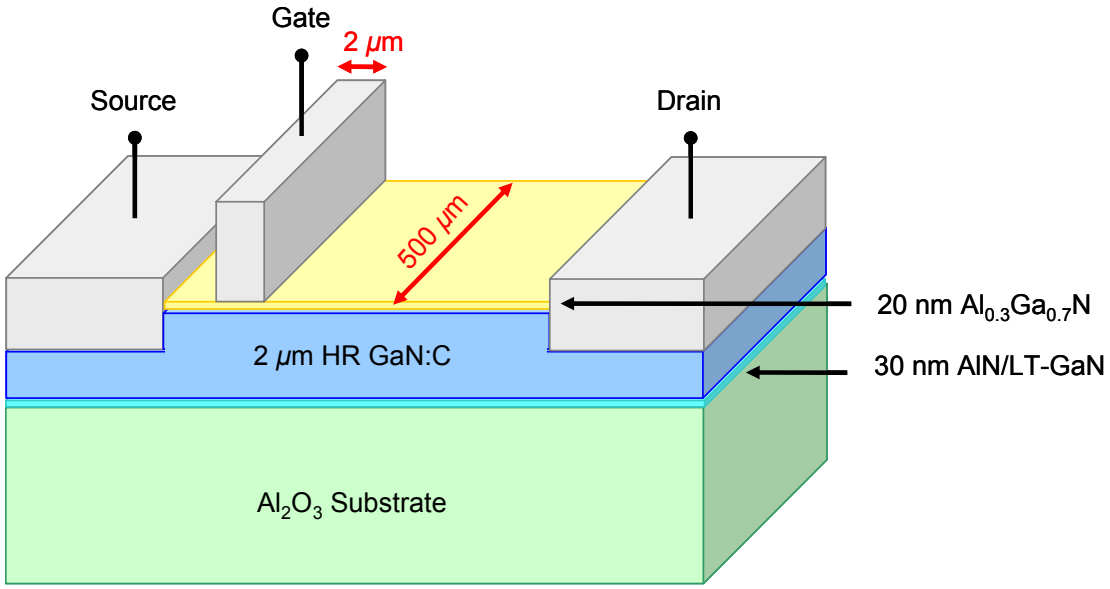

Fig. A.4. Low leakage, high breakdown voltage HEMT structure based on HR GaN:C layer.

A.4 Mitigation of heating induced by UV irradiation – additional details

Under UV irradiation, the PID control loop automatically reduces the power supplied to the substrate heater to maintain constant T_s, effectively reducing the radiation incident on the sample backside from substrate heater. This reduction in the rate of radiation from the substrate heater, $\Delta \dot{q}_{rad,heater}$, can be estimated by (A.1).

$$\Delta \dot{q}_{rad,heater} = \frac{P_{NoUV} - P_{UV}}{A_{heater}} \left(\frac{A_{sample}}{A_{heater}} \right) \tag{A.1}$$

Here, $A_{\text{heater}} = 1.83 \times 10^{-3}$ m, $A_{\text{sample}} = 1 \times 10^{-4}$ m, and $P_{\text{No UV}}$ and P_{UV} are the power applied to the substrate heater to maintain T_s under no UV irradiation and UV irradiation respectively. The reduction in the power applied to the substrate heater is a result of the

TC sensing an increase in radiation emitted from the metalized backside of the substrate layer stack under UV irradiation. This increase in the rate of radiation from the backside of the substrate, $\Delta \dot{q}_{rad,back\text{-}UV}$ can be estimated by (A.2)

$$\Delta \dot{q}_{rad,back-UV} = \varepsilon_{eff} \sigma T_s^4 \qquad \text{(A.2)}$$

Here, ε_{eff} is an effective emissivity approximated as 0.2 (this approximation is only concerned with the rear surface facing the TC, negligible ΔT through the substrate layer stack as determined in Chapter 6 is assumed and the temperature and wavelength dependence of ε are neglected). Assuming steady-state conditions, neglecting conduction or convection in vacuum, and assuming that the TC only senses radiation from the substrate heater and the backside of the substrate, the condition for which the compensation in power to the substrate heater effectively mitigates the heating in the bulk induced by UV is when A.1 and A.2 are equivalent.

Quantitatively for Chapter 8, $\Delta \dot{q}_{rad,heater}$ was calculated using (A.1) as 0.15 W/cm^2 based on an observed compensation in substrate heater power of 50 W under UV irradiation (190 W reduced to 140 W). This $\Delta \dot{q}_{rad,heater}$ would be equivalent to a radiation rate from the substrate backside at T_s = 329 °C using (A.2). This agrees well with an observed steady state T_s = 365 °C resulting from UV irradiation under conditions of constant substrate heater power (with no UV irradiation, constant heater power was applied in order to maintain T_s = 30 °C, the PID control loop was disabled so as to maintain a constant radiative contribution from the substrate heater). Even neglecting the constant contribution of the substrate heater, the differences in the T_s calculated based on observed compensation in substrate heater power verses the observed T_s induced by the

UV irradiation is well within the absolute accuracy of T_s in UHV and the error in ε_{eff} – quantitatively demonstrating that the observed compensation in substrate heater power by the PID control loop sufficiently mitigates UV-induced heating in the substrate bulk.

The observed steady state T_s for a Si-doped GaN template resulting from UV irradiation under constant substrate heater power was also measured for two additional incident irradiance conditions. Fig. A.5 shows the change in R/R_0, $T_s/T_{s,0}$, and $P_{ch}/P_{ch,0}$ as a result of HeCd laser irradiation. R_0, $T_{s,0}$, and $P_{ch,0}$ are the respective reflectivity, substrate temperature, and chamber pressure preceding irradiation. The linear decrease in $T_s/T_{s,0}$ indicates that the substrate is cooling (*i.e.* the constant power applied to the substrate heater is not sufficient to maintain the initial $T_{s,0}$). The cooling of the substrate induces a contraction of the 3.5 μm GaN template which causes the observed increase in R/R_0. The salient feature of Fig. A.5 is that the slopes of both $T_s/T_{s,0}$ and R/R_0 remain constant, even during sample exposure to HeCd laser irradiation (Fig. A.5(b)). Therefore, while the sample is cooling, there is no discernable heating in the bulk ($\Delta T_s = T_s - T_{s,0} \sim$ 0 °C) induced solely as a result of HeCd laser irradiation. In contrast, irradiation with the He-Xe arc lamp (Fig. A.6(b)) clearly increases the T_s when the substrate power is not automatically controlled (*e.g.* using a PID control loop). The high irradiance destroyed the commercial turning mirror during this experiment (as described in Chapter 8) at a TC indicated $T_s \sim$ 143 °C.

Additionally, $\Delta R/R_0$ (such as shown in Fig. A.5 and A.6) could be used as a corroborating measure of ΔT_s, by interpreting $\Delta R/R_0$ as resulting from interferoic dilatometry [195]: if no film deposition/etching is occurring, ΔR would be a result of thermal expansion/contraction of the GaN template by Δd (GaN linear *c*-axis thermal

expansion coefficient of $\langle\alpha_c\rangle \sim 5.0 \times 10^{-6}$ K^{-1} in the relevant T_s regime [196]). Hence, the interpretation of §2.6 is modified only by the origin of Δd. Additionally, the broad spectral output of the Hg-Xe arc lamp contributes to the measured R in the present case (the noise in R/R_0 of Fig. A.6), requiring additional calibration to determine ΔT_s from $\Delta R/R_0$. The use of a modulated laser and lock-in detection should solve this limitation.

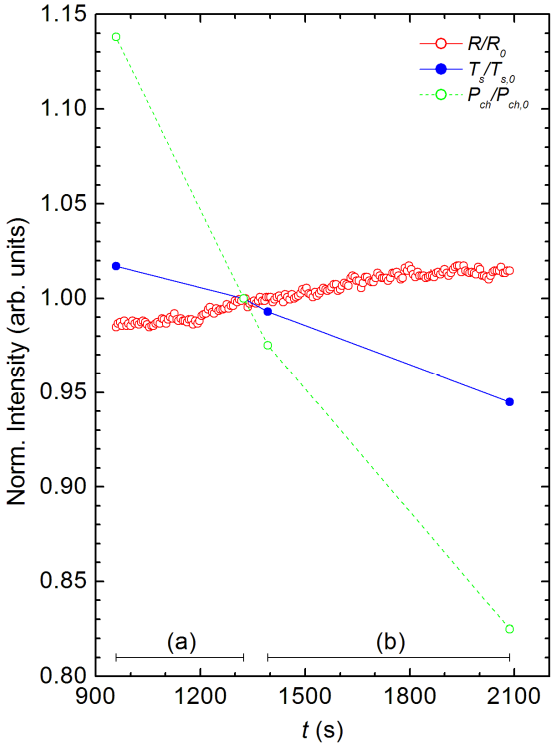

Fig. A.5. Evolution of R/R_0, $T_s/T_{s,0}$, and $P_{ch}/P_{ch,0}$ (a) without and (b) with HeCd laser irradiation (R_0 = 1.505, $T_{s,0}$ = 29.1 °C, and $P_{ch,0}$ = 8.0 × 10^{-9} Torr). The power applied to the substrate heater remains constant over the entire duration.

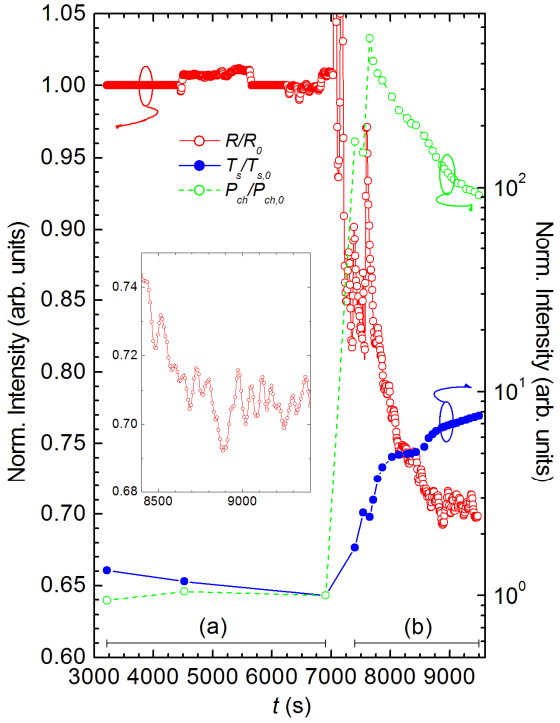

Fig. A.6. Evolution of R/R_0, $T_s/T_{s,0}$, and $P_{ch}/P_{ch,0}$ (a) without and (b) with Hg-Xe lamp irradiation (R_0 = 1.86, $T_{s,0}$ = 18.7 °C, and $P_{ch,0}$ = 5.1 × 10^{-9} Torr). The power applied to the substrate heater remains constant over the entire duration. The noise in R/R_0 at $t \sim 5000$ s is a result of adjustments to the LRI system optics which are of no consequence to the present analysis.

A.5 Crystalline quality of GaN by NH_3-based MOMBE

As described in Chapter 3, buffer nucleation during NH_3-based MOMBE remains challenging, resulting in GaN films with crystalline quality figures of merit significantly worse than advanced MBE and MOCVD growth technology. Commercial 3.5 μm Si-doped GaN templates (Lumilog, Vallauris, France) were utilized in Chapter 5 and afterwards in order to alleviate difficulties in buffer nucleation with NH_3. Fig. A.7 shows the XRD rocking curve of GaN(002) for GaN grown on NH_3-based MOMBE buffer layers (deposited on sapphire) as well as GaN and InGaN grown on commercial GaN templates. The FWHM for the films deposited directly on the GaN templates are similar to that of the GaN template, indicating that the crystalline quality is maintained. Therefore, NH_3-based MOMBE does not inherently result in films of poor crystalline quality, but instead the non-optimal nucleation layers are to blame.

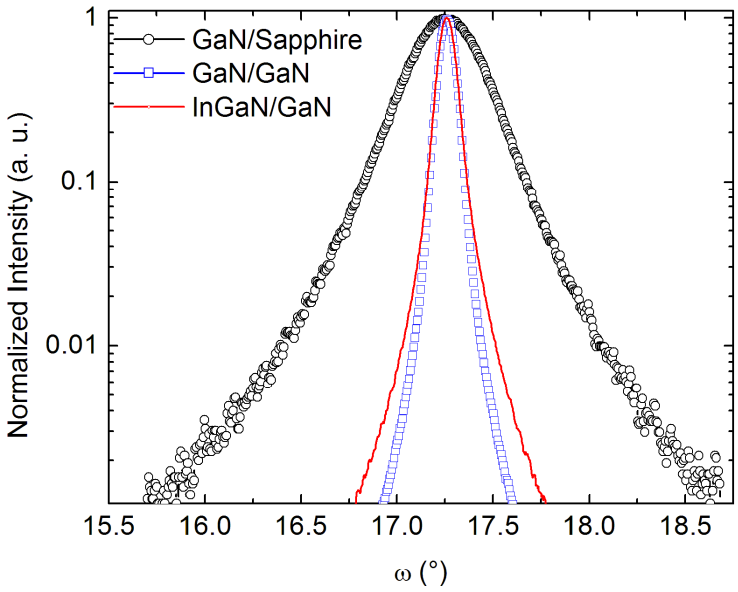

Fig. A.7. XRD 2θ-ω of $In_xGa_{1-x}N$ (002) grown on sapphire with NH_3-based MOMBE buffer layers (FWHM ~ 900 arcsec) and GaN templates (Lumilog, FWHM ~ 340 arcsec).

APPENDIX B: CUSTOM GROWTH AUTOMATION AND MONITORING

During this work, the computer control interface of the NH_3-based MOMBE system that was designed and developed wholly in-house using National Instruments LabView was not only thoroughly debugged but also expanded dramatically. Three salient systems were developed wholly during this work to improve the overall throughput, operation and film consistency, and usability: the growth automation system, parameter monitoring system, and online management system.

B.1 Growth automation system

Precise growth control (*i.e.* immediate and accurate variations in T_s and precursor fluxes) and precise logging of growth data (*e.g.* growth parameters, LRI, RGA, etc.) can only be consistently achieved via computer execution. The automatic execution and logging of growths were implemented to improve the consistency and repeatability of growths. The described growth automation system has effectively executed and managed over 600 III-Nitride growths of the present reactor.

The growth automation system is driven by custom scripts containing low-level instructions. The scripts are standard text files formatted with one instruction per line. Scripts are selected and executed via the Automation Control panel on the Valve Control screen of the LabView interface. The low-level instructions are in the format

command: p_1, <p_2>, <p_3>, <p_4>

<> denote optional parameters (the <> should not be included in the instruction declaration). The supported low-level instructions are described in Table B.1:

Table B.1. Low-level commands of the growth automation system.

instruction	function
log: 'p_1'	Logs data to mySQL database with specified comment p_1. The mySQL primary key field (run_det) must be defined in the LabView interface in order to properly retrieve the data. See §B.3 section for specifics regarding the mySQL database and online data extraction. Example: log: 'GaN Started'
wait: p_1	Waits specified time p_1 in s (integer). Example: wait: 120
temp: p_1, p_2	Sets substrate temperature p_1 (°C) and ramp rate p_2 (°C/s). Both floating point. Example: temp: 560, 2
mfc: p_1	Sets ammonia MFC to specified flow p_1 (sccm, floating point). Example: mfc: 10
mfc_h: p_1	Sets hydrogen MFC to specified flow p_1 (sccm, floating point). Example: mfc_h: 2
valve: p_1, p2	Performs specified action p_2 to specified valve p_1 (Table B.2). p_2 can be 0 (close) or 1 (open). Example: valve: 37, 1

`m_valve: p1, p2`

Moves specified motor valve p_1 (Table B.3) to specified "position" p_2, where:

if $0 < p_2 < 1$, the PCVS will maintain the source flux at pressure p_3 behind the source orifice. If $p_2 < 0.1$, then the remote range turndown is enabled for the Si, Ga, Al, and C capacitance manometers (if $p_2 < 0.01$ for Mg and Be, for improved control accuracy). See Chapter 2.

if $p_2 > 1$ or $p_2 = 0$ the motor valve is set to valve turn position p_2. Remote range turn down of specific capacitance manometer turned off.

if $p_2 = -1$, the motor valve closes completely. Remote range turn down of specific capacitance manometer turned off.

Example: `m_valve: 95, 2500`

`g_valve: p1, p2`

Performs specified action p_2 to specified valve p_1 (Table B.4). p_2 can be `0` (close) or `1` (open).

Example: `g_valve: 53, 1`

`cycle: p1, p2, p3, p4`

Cycles the head and source valves of the specified source p_1 (Table B.5) by specified on time p_3 and specified off time p_4 (integer). P_2 can be `0` (cycling off) or `1` (cycling on). p_1 is defined in Table B.3. NOTE: The final state of the cycled valves is unknown, hence the valves must be commanded to a final state after the cycling is complete (cycling is complete within 1 second of disabling). Other sources can be synchronized to the cycle using 'synch'. The final state of the synched sources is also unknown.

Example: `cycle: 60, 1, 16, 18`

`synch: p1, p2`

Performs specified action p_2 of source p_1 (Table B.6) to the synchronization of the specified source to that of the cycle command.

Example: `synch: 101, 1`

`prompt: p1`

Displays message p_1. Further execution of the script will be suspended until acknowledgement.

Example: `prompt: Continue?`

`alert:` p_1, p_2 — Displays message p_2 on computer with hostname p_1. The computer being sent the message must have the Windows Messenger service running and must be accessible. The script will continue execution regardless of acknowledgement.

Example: `alert: uvmombe, growth starting!`

`beep:` p_1 — Beeps audibly p_1 number of times. p_1 will be coerced between 1 and 5 to prevent long stalls of the VI.

Example: `beep: 3`

`rga:` p_1 — Writes the RGA spectrum to two ASCII files. The files are named: `date—time-(initial` *m*`/`*e*`-final` *m*`/`*e*`)-`p_1 and saved in the RGA and RGA2 directory (corresponding to 1 and 0.1 amu resolution data respectively). The 1 amu file is tab delimited, whereas the 0.1 amu file is carriage return/line feed delimited (excel does not support importing of >256 columns, hence the data points must be in rows for this large of a file). The RGA must already be enabled (see soft command) with the correct *m*/*e* range.

Example: `rga: spectrum_1.txt`

`soft:` p_1, p_2 — Performs specified action p_2 to specified software control p_1. p_2 can be `0` (disable) or `1` (enable).

Example: `soft: 72, 1`

`comment:` p_1 — An arbitrary comment p_1, which is ignored.

Example: `comment:  anneal code`

`status:` p_1 — Displays status p_1 in the status field of the LabView interface (available on if web display and autoscroll are enabled) (25 chars max).

Example: `status: DEFROSTING`

`monitor:` p_1 — Sets monitoring string p_1 for the automatic growth parameter monitor. p_1 is comma delimited and is case and whitespace insensitive. See §B.2.

Example: `monitor: p,t,n,ga`

Table B.2. Parameter p_1 specifying pneumatic valves for the `valve:` command. Cp_2Be is not installed, but the delivery line is available.

source	bubbler valve	bypass valve	head (low) valve	head (high) valve
Si_2H_6	10	20	30	31
Cp_2Be	11	21	32	-
Cp_2Mg	12	22	33	-
C (TMIn)	13	23	34	35
DMEAA/TEAl	14	24	35	-
TEGa	15	25	37	-
NH_3	-	-	38	-

Table B.3. Parameter p_1 specifying PCVS motor valves for the `m_valve:` command. Cp_2Be is not installed, but the delivery line is available.

source	p_1
Si_2H_6	90
Cp_2Be	91
Cp_2Mg	92
C (TMIn)	93
DMEAA/TEAl	94
TEGa	95

Table B.4. Parameter p_1 specifying gate valves for the `g_valve:` command.

valve	p_1
growth chamber to turbo pump	50
turbo pump to rough pump	51
introduction chamber to growth chamber	52
introduction chamber to cryogenic pump	53
RGA to growth chamber	54

Table B.5. Parameter p_1 specifying source of the `cycle:` command.

source	p_1
TEGa	60

Table B.6. Parameter p_1 specifying sources to synchronize to cycled (modulated) source for the `synch:` command.

source	p_1
C (TMIn)	101
Cp_2Mg	102

Table B.7. Parameter p_1 of the `soft:` command.

control	p_1	description
general enable	70	Enables/disables computer control of all pneumatic valves of all source delivery lines.
head enable	71	Enables/disables computer control of all head (at the growth reactor inlet) pneumatic valves of all source delivery lines.
source enable	72	Enables/disables computer control of all source (at each precursor bubbler) pneumatic valves of all source delivery lines.
bypass enable	73	Enables/disables computer control of all bypass (at the bypass manifold) pneumatic valves of all source delivery lines.
RGA enable	74	Enables/disable the RGA.
autoscroll	75	Enables/disable the automatic tab scrolling of the LabView interface.
web display	76	Enables/disables the automatic update the of the LabView interface to the online management system (autoscroll must be enabled). See §B.3.
automation stop	77	Queues the automation for stop. The automation will stop immediately after execution of the current command.
pressure protect	78	Enables/disables the automatic safety interlocks. See Chapter 2.
LRI enable	79	Enables/disables the LRI system (LRI data logging enabled/disabled automatically).
ion gauge	80	Enables/disables the ion gauge.
clear latched alarms	81	Clears latched alarms triggered by the parameter monitoring system. See §B.2.
monitor enable	82	Enables/disables the automatic parameter monitoring system. See §B.2.
lock monitor parameters	83	Resets the target parameters of the automatic parameter monitoring system to the present parameters. See §B.2.

A custom high-level language was designed and developed to drastically simplify the creation of the low-level instruction scripts. The high-level language uses easy-to-read parameters (*e.g.* sources are referred to by their elemental names and total growth step durations can be specified rather than declaring redundant `wait:`, `log:`, and `rga:` sequences) that are translated by a custom TCL program (*summary_to_recipe.tcl*) into sequences of the low-level scripts for use by the LabView system. The high-level language consists of two instructions, the primary instruction is declared:

`macro: (<a>|<b>|<c>|<d>)`

<> denote optional parameters (the <> should not be included in the instruction statement). The `macro:` instruction summarizes the automation script sequence of setting pneumatic valves sources then waiting a defined duration while logging and recording data. The command is highly flexible, as described in Table B.8.

Table B.8. Parameter definition of the `macro:` instruction of the growth automation system high-level language.

parameter	function
<a>	Specifies the logging title. This will populate `comment:` instructions that will bound the resulting script. The initial `log:` instruction (if applicable) will include this title. Also, the `rga:` instructions will specify the filename as this title with '`_x.txt`' appended, where `x` increments for each file.
<b>	Specifies the total wait time in seconds for this step. If <b> is < 1, no logging will occur.
<c>	Specifies the number of times to log during the total wait time, hence logging occurs every interval of <b>/<c> (logging here refers to the `rga:` and `log:` instructions, LRI data is logged on frequency input into the LabView interface). <c> must be > 0 for logging to occur.

Specifies the valve actions. Valve actions are performed first (*i.e.* before any subsequent `wait:`/`log:`/`rga:` sequences that will be output by the *summary_to_recipe.tcl* program for the particular `macro:` instruction. If this is `?`, no action will be performed for any valves. Otherwise, a comma delimited list can be specified as follows:

```
[source]:[flux (pressure behind orifice) or motor valve
position]:[1/0/?]-[s/b/h]_... , ... , ...
```

An example follows:

```
Ga:0.20:0-b_1-sh,Mg:-1:0-sh_1-b,N:19:1-h
```

The list can include *any number of sources in any order*, with the specified order being retained during translation to the low-level language. This given example affects three sources:

- The Ga flux set to 0.20 Torr behind the leak orifice while the Ga bypass valve is closed and the Ga source and head valve are opened (introducing TEGa for growth).
- The Mg motor valve is closed (no Cp_2Mg flux), and the Mg source and head valves are closed while the bypass valve is opened (pump down the Cp_2Mg delivery line).

<d>

- The N flux is set to 19 sccm while opening the N head valve (introducing NH_3 for growth).

`[sources]` defined as

`Si, Be, Mg, C, Al, Ga, and N.`

`[flux (pressure behind orifice) or motor valve position]` defined as

The PCVS regulated pressure behind the orifice or specific motor valve position, `?` can be specified (*e.g.* if only pneumatic valves are to be adjusted for a particular source, with no change in flux/motor valve position).

[`1/0/?`] defined as

The corresponding action [open/close/nothing] to performed to the valves specified after the '-', `s` (source), `b` (bypass), or `h` (head) for this particular source. Any combination of `s`, `b`, and `h`, can be used, so as they are available (*e.g.* N does not have a pneumatic source valve). Declarations such as `1-sbhshbh` are legitimate. Additional valve actions can be declared as delimited by a '_'. Additionally, this section can be specified as `?` so that no pneumatic valves are adjusted.

The other instruction of the high-level language is the `setup:` instruction declared as `setup: (begin)` or `setup: (end)`. The `begin` and `end` calls insert growth startup or shutdown script sequences respectively into the final script output.

For example, the following high-level instructions

```
comment: 500 nm Mg GaN
macro: (GaN_Mg|1800|10|Mg:0.004:1-hs)
```

are translated by the *summary_to_recipe.tcl* program into the following low-level instructions (the low-level instructions are necessary to execute the growth automation in the LabView interface).

```
comment: 500 nm Mg GaN
comment: GaN_Mg BEGIN
m_valve: 92, 0.004
beep: 2
valve: 33, 1
valve: 12, 1
alert: uvmombe, GaN_Mg Starting (30.00 mins)
log: 'GaN_Mg Started'
rga: GaN_Mg_1.txt
wait: 180
log: ' - 3.00 mins'
monitor: p,t,man,mg
soft: 82, 1
soft: 83, 1
soft: 81, 1
rga: GaN_Mg_2.txt
wait: 180
log: ' - 7.00 mins'
rga: GaN_Mg_3.txt
wait: 180
log: ' - 9.00 mins'
rga: GaN_Mg_4.txt
wait: 180
log: ' - 12.00 mins'
rga: GaN_Mg_5.txt
wait: 180
log: ' - 15.00 mins'
rga: GaN_Mg_7.txt
wait: 180
log: ' - 18.00 mins'
rga: GaN_Mg_7.txt
wait: 180
```

```
log: ' - 21.00 mins'
rga: GaN_Mg_8.txt
wait: 180
log: ' - 24.00 mins'
rga: GaN_Mg_9.txt
wait: 180
log: ' - 27.00 mins'
rga: GaN_Mg_10.txt
wait: 180
log: ' - 30.00 mins'
rga: GaN_Mg_11.txt
soft: 82, 0
comment: GaN_Mg END
```

Additionally, the high-level language supports the low-level instructions, such that the low-level instructions are inserted into the final low-level automation script output from the *summary_to_recipe.tcl* program in the order that they appear.

An example of a complete growth script written in the high level language follows. The script performs the growth of a GaN/GaN:Mg/GaN structure as described in Chapter 8.

```
comment: U544 - UV Effect on Mg at 0.004
setup:   (begin)
macro:   Close_Valves|0|0|Si:?:0-sbh,Be:?:0-sbh,Mg:?:0-sbh,C:?:0-
         sbh,Al:?:0-sbh,Ga:?:0-sbh,N:?:0-h)
prompt:  CLOSE N2 Purge.  OPEN LN2 source and return.
temp:    300, 1
prompt:  Wait for motor valves to fully close.
macro:   (Ramp_1|10|1|Ga:599:1-sb_0-h,Mg:599:1-sb_0-h,N:0:1-h)
prompt:  Wait for 300 C and LN2/pressure to normalize
prompt:  Open NH3 to MFC
temp:    600, 2
macro:   (NH3_Ramp_1|200|5|N:10:1-h)
macro:   (Outgas_1|600|4|?)
macro:   (Close_Valves_2|10|1|Ga:-1:0-sb,Mg:-1:0-sb)
prompt:  Wait for motor valves to close
alert:   uvmombe, Verify that TEGa Cp2Mg bottles are OPEN

temp:    770, 2
macro:   (NH3_Ramp_2|180|3|Ga:630:0-sb,Mg:0:0-sb)
comment: Ga is 650 for 0.17 Torr behind orifice
comment: 1 um per hour
```

```
comment: 250 nm UID GaN
macro:   (GaN_UID|900|6|Ga:0.17:1-hs,N:10:?)
alert:   uvmombe, UV ON if necessary

comment: 500 nm Mg GaN
macro:   (GaN_Mg|1800|10|Mg:0.004:1-hs)

comment: 500 nm UID GaN Cap
macro:   (GaN_Cap|1800|10|Mg:-1:0-sh)

temp:    0, 1.0
alert:   uvmombe, close Ga N Mg bottles
comment: close NH3 during ramp down so H does not passivate Mg
macro: (NH3_Ramp_3|300|3|Ga:499:0-sh_1-b,Mg:299:0-sh_1-b,N:0:0-h)
setup:   (end)
```

B.2 Parameter monitoring system

The parameter monitoring system alerts operators visually and audibly that specified growth parameters are not within specified tolerances. Specifically, the system alerts operators within 250 ms if a parameter of the "monitor string" deviates from its respective "locked" parameter by the specified (and dynamically adjustable) tolerance (Fig. B.1). The "locked" parameters are the parameter values considered "correct" (*e.g.* if T_s should remain fixed at 770 °C, T_s can be "locked" at 770 °C and the system will alarm if $T_s >$ (770 °C + tolerance) or $T_s <$ (770 °C - tolerance)). The "locked" parameters (Fig. B.2) can be set at any time from the current parameter values (*i.e.* for each growth step, once parameters are stable they can be "locked"). The system monitors all specified parameters continuously, as long as the system is enabled. Any alarms that occur are latched in that they persist until the alarm is manually cleared by an operator. The parameters which can be monitored are P_{ch}, T_s, J_{NH_3}, J_{H_2} (for a custom filament H_2 cracker), J_{Cp_2Mg}, J_{TMIn}, $J_{Si_2H_6}$, J_{TEAl}, J_{TEGa} (an error condition for all of the capacitance

manometers of the PCVS system is monitored without explicit declaration). Examples of visual alerts by the system are shown in Fig. B.3. Additionally, low-level automation instructions are automatically inserted by the *summary_to_recipe.tcl* program for any high-level automation `macro:` instruction that is greater than 30 min in duration (parameters will be "locked" and the monitoring system will be enabled after a 3 min stabilization period of the growth step).

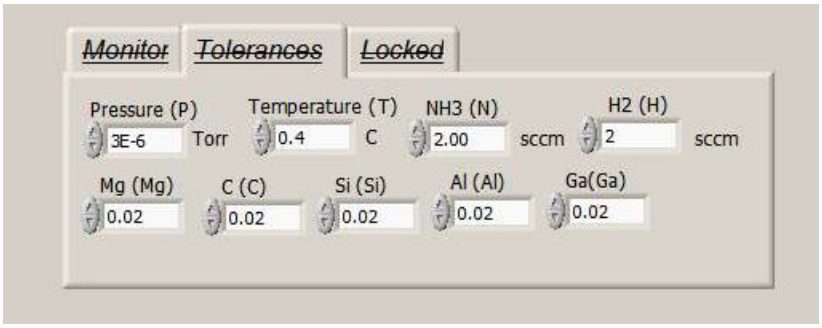

Fig. B.1. Parameter monitoring system tolerance configuration on the 'Options' tab of the MOMBE growth system LabView interface. All tolerances can be dynamically adjusted

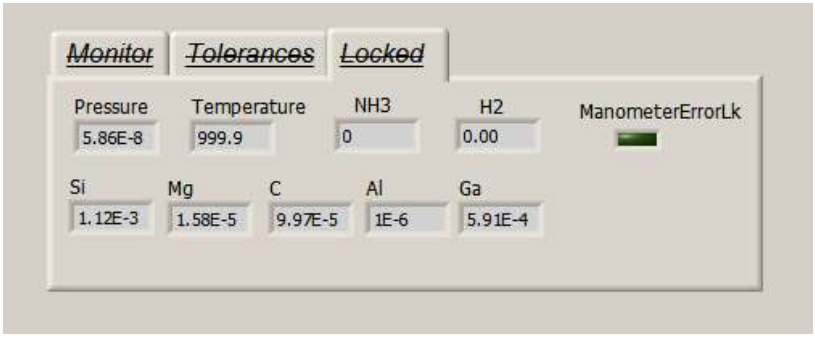

Fig. B.2. Parameter monitoring system display of "locked" parameters on the 'Options' tab of the MOMBE growth system LabView interface. Locked parameters are set using parameter values at the time of being "locked", and can be "re-locked" at any time by an operator or an automation instruction.

Fig. B.3. 'Options' tab of the MOMBE growth system LabView interface. In this example, the parameter monitoring system is actively monitoring P_{ch}, T_s, J_{TEGa}, J_{TMIn}, J_{NH3}, and J_{Cp2Mg}. The system is reporting alarms for J_{Cp2Mg}, J_{TMIn}, and J_{TEGa}. TMIn is referred to as C on the LabView interface.

B.3 Online management system

The online management system is a custom secure online portal to manage the events of the MOMBE system (growths, maintenance, etc.), retrieve all growth data (growth parameters and characterization data from RGA, LRI, XRD, AFM, Hall effect, SEM, photographs, etc.), manage system maintenance tasks, and monitor and control the MOMBE system *remotely*. The entire site is written in PHP and interfaces with a

mySQL database (mostly populated by the `log:` command of the automation system) and associated files and directories.

The home page is shown in Fig. B.4. Before execution of a growth, a MOMBE user adds the growth via the homepage using the `[add run]` link. The submitted information will create an entry into the mySQL database (an entry into the event log is also added into the database automatically to log the growth event) with the primary key *run_det* (*run_det* is unique and automatically generated; it is independent of the growth ID number). The *run_det* value must be input into the Automation Control of the LabView interface in order for the `log:` instructions of the growth automation system to insert data into the mySQL database and for that data to be associated with the particular growth of the online management system (RGA, LRI, and other data is stored in growth-specific directories for access by the online management system, as shown in Fig. B.5) – the online interface to view logged growth parameters is shown in Fig. B.6. The growth automation system can be set via the WebLog option of the LabView interface (Fig. B.7) so that data is not logged into the mySQL database during growth, but rather into an ASCII file (SQL format). In addition to automatic logging by the growth automation system, manually logging is supported via online forms.

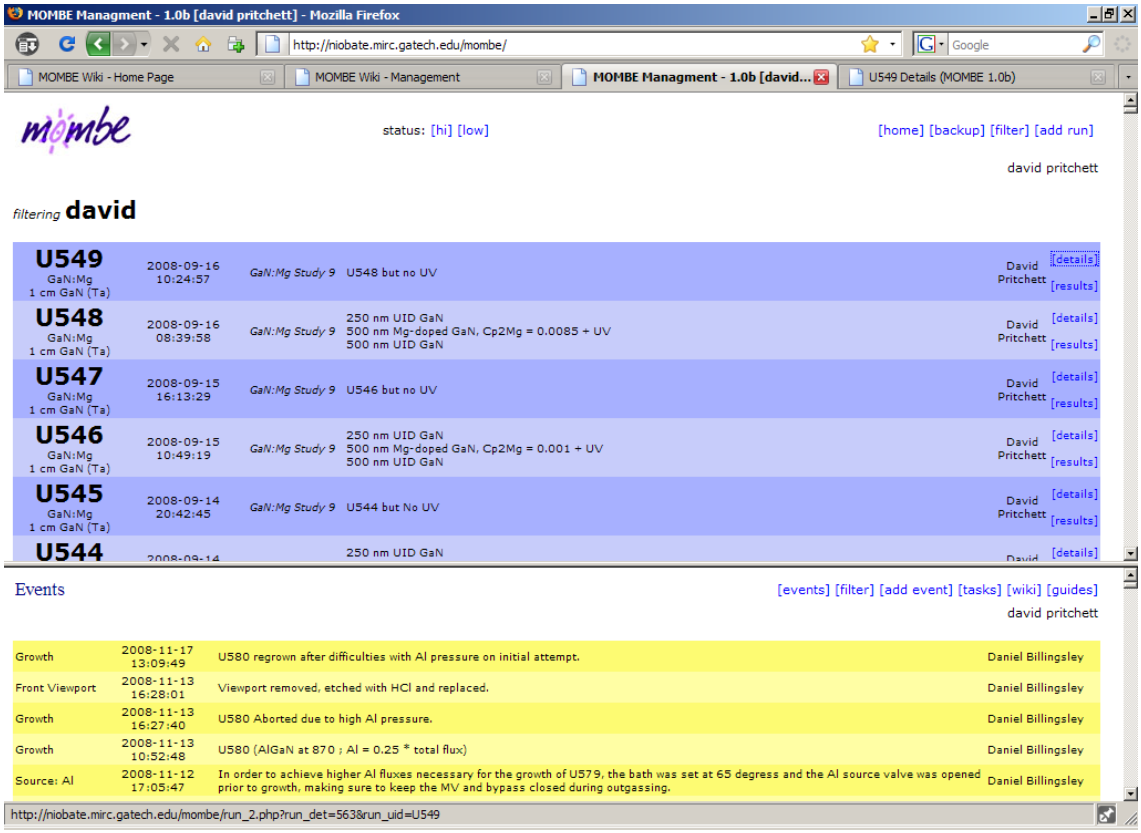

Fig. B.4. The homepage of the MOMBE online management system. Growths are displayed in the top frame and events are displayed in the bottom frame.

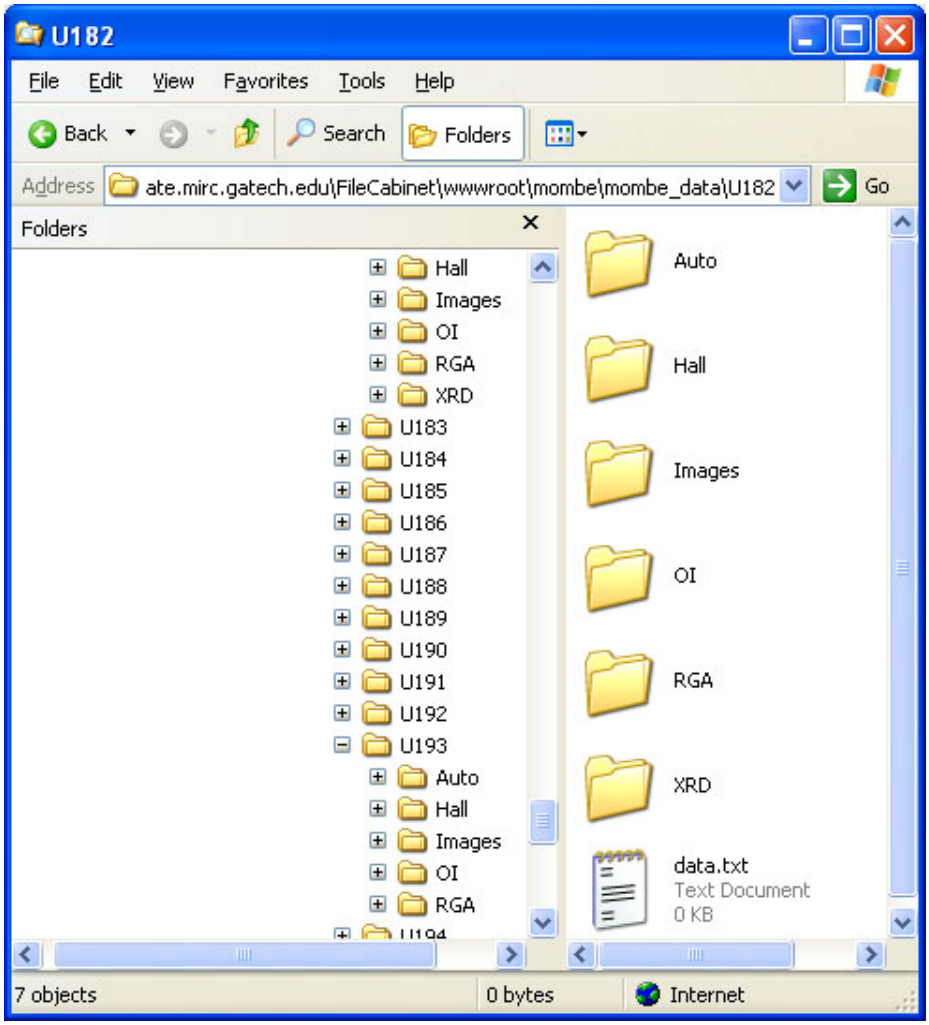

Fig. B.5. File structure of characterization/miscellaneous data of growths for the MOMBE online management system.

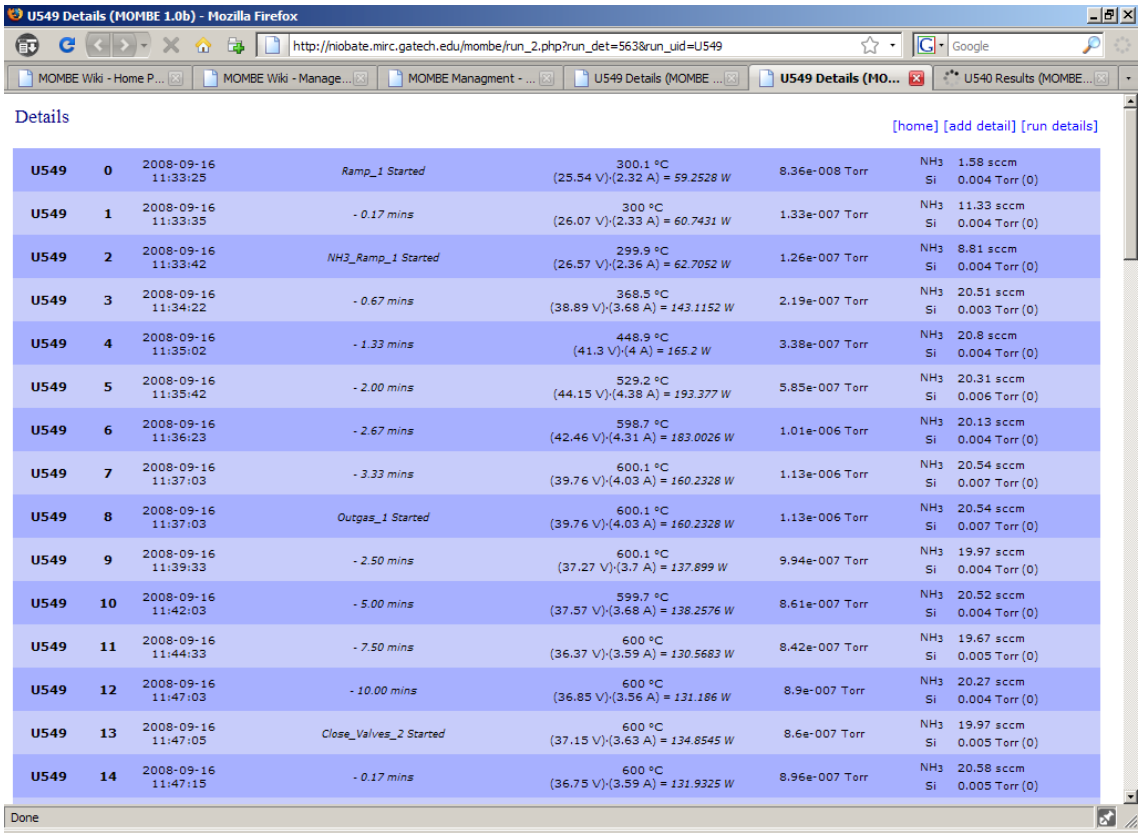

Fig. B.6. 'Run details' page of growth U549 of the MOMBE online management system.

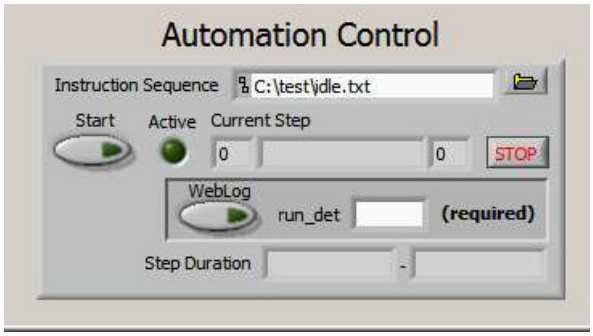

Fig. B.7. Growth automation control on the 'Main' tab of the MOMBE growth system LabView interface.

The online management system also provides the capability to manage tasks assigned to individual users. This capability is accessed through the [task] link in the 'Events' frame. Tasks can be assigned to individuals and a priority can be specified (Fig. B.8). Additionally, email reminders can be sent using the [email reminder] link on the bottom of the Task Frame.

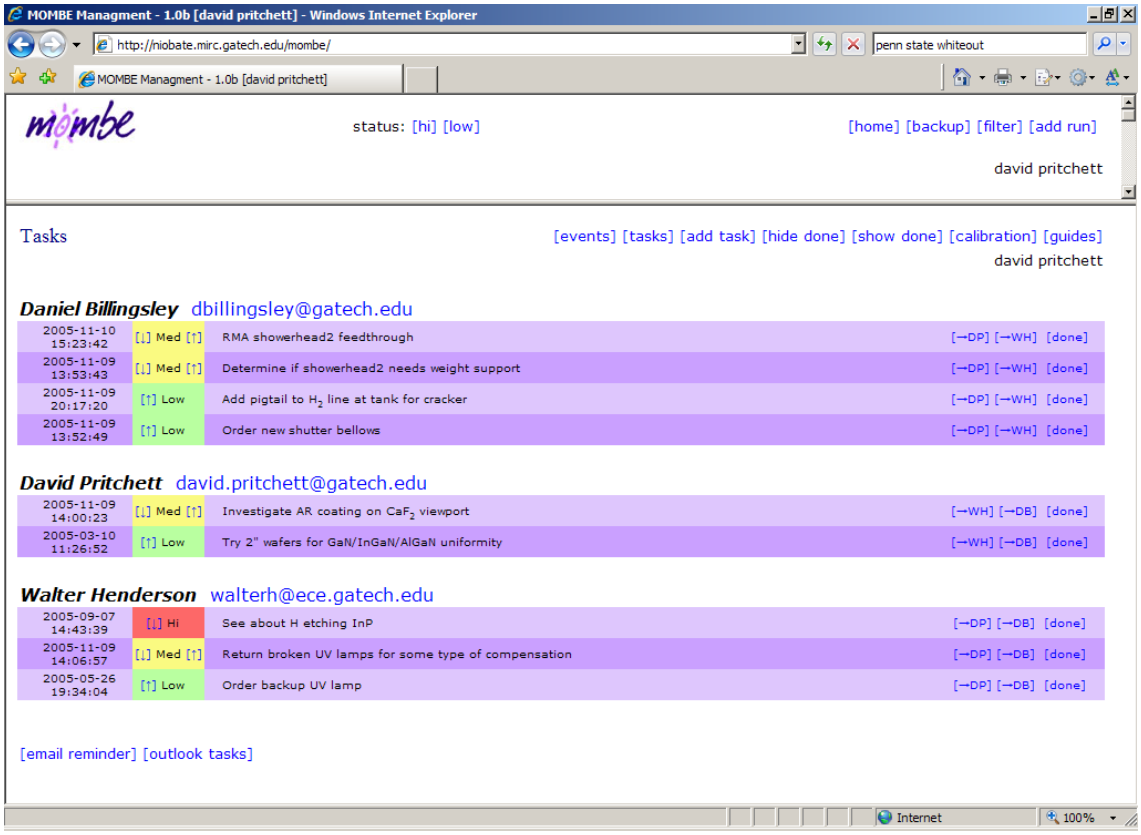

Fig. B.8. 'Tasks' control of the MOMBE online management system.

The online management system also provides the capability to monitor and control the MOMBE system remotely. The status: [hi] [low] links on the top of the home page (Fig. B.4) provide access to delayed system status information. The [hi] link shows full resolution screen captures of LabView control interface. The [low] link

provides a low-bandwidth (mobile optimized) MOMBE system status information (Fig. B.9) that is automatically updated every 8 s and automatically highlights system parameters that are not typical of an idle system state. Automation scripts can be executed remotely via SFTP if the 'Remote Script Enable' option is enabled on the MOMBE LabView interface ('Options' tab). In order to trigger a script remotely, the filename of the script to be executed (*e.g.* close_valves.txt) must be entered into a specific file that is continuously monitored by the MOMBE computer control system. Only one filename may be entered at a time. Once the filename is entered and the specific file has been saved, the LabView interface will execute the specified script and replace the specific file with a blank file (*i.e.* to execute another script if desired). Additionally, the MOMBE computer control system will visually and audibly notify local system users before remotely executing automation scripts.

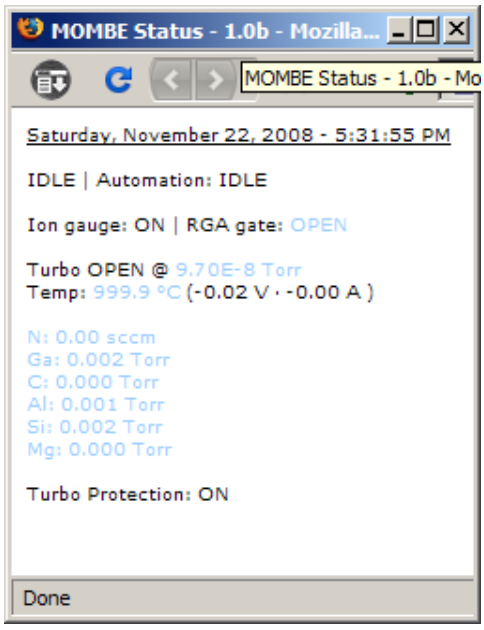

Fig. B.9. The low-bandwidth MOMBE system status accessible via the MOMBE online management system.

REFERENCES

[1] E. Veuhoff, "Exploitation of surface selective growth in metalorganic growth technologies for device applications" *J. Cryst. Growth* **195,** 444 (1998).

[2] J. E. Davey, and T. Pankey, "Epitaxial GaAs films deposited by vacuum evaporation" *J. Appl. Phys.* **39,** 1941 (1968).

[3] M. Mesrine, N. Grandjean, and J. Massies, "Efficiency of NH_3 as nitrogen source for GaN molecular beam epitaxy" *Appl. Phys. Lett.* **72,** 350 (1998).

[4] J. S. Foord, G. J. Davies, and W. T. Tsang, *Chemical beam epitaxy and related techniques* (Wiley, New York, 1997).

[5] H. M. Manasevit, and W. I. Simpson, "The use of metal-organics in the preparation of semiconductor materials I. Epitaxial gallium-V compounds" *J. Electrochem. Soc* **116,** 1725 (1969).

[6] R. D. Dupuis, and P. D. Dapkus, "Room temperature operation of $Ga_{1-x}Al_xAs$/GaAs double-heterostructure lasers grown by metalorganic chemical vapor deposition" *Appl. Phys. Lett.* **31,** 466 (1977).

[7] M. Mizuta, S. Fujieda, Y. Matsumoto, and T. Kawamura, "Low Temperature Growth of GaN and AlN on GaAs Utilizing Metalorganics and Hydrazine" *Jap. J. Appl. Phys.* **25,** L945 (1986).

[8] C. R. Kingsley, T. J. Whitaker, A. T. S. Wee, R. B. Jackman, and J. S. Foord, "Development of chemical beam epitaxy for the deposition of gallium nitride" *Mat. Sci. Eng. B* **29,** 78 (1995).

[9] J. D. Mackenzie, C. R. Abernathy, J. D. Stewart, and G. T. Muhr, "Growth of Group III nitrides by chemical beam epitaxy" *J. Cryst. Growth* **164,** 143 (1996).

[10] R. P. Campion, T. Li, C. T. Foxon, and I. Harrison, "The Growth of GaN Using Plasma Assisted Metalorganic Vapour Phase Epitaxy" *Phys. Stat. Sol. A* **188,** 663 (2001).

[11] A. Thon, and T. F. Kuech, "High temperature adduct formation of trimethylgallium and ammonia" *Appl. Phys. Lett.* **69,** 55 (1996).

[12] A. Koukitu, N. Takahashi, and H. Seki, "Thermodynamic Study on Metalorganic Vapor-Phase Epitaxial Growth of Group III Nitrides" *Jap. J. Appl. Phys.* **36,** L1136 (1997).

[13] J. R. Creighton, G. T. Wang, and M. E. Coltrin, "Fundamental chemistry and modeling of group-III nitride MOVPE" *J. Cryst. Growth* **298,** 2 (2007).

[14] E. Veuhoff, W. Pletschen, P. Balk, and H. Lüth, "Metalorganic CVD of GaAs in a molecular beam system" *J. Cryst. Growth* **55,** 30 (1981).

[15] N. Vodjdani, A. Lemarchand, and H. Paradan, "Parametric studies of GaAs growth by metalorganic molecular beam epitaxy" *J. Phys. (Paris)* **43,** 339 (1982).

[16] E. Tokumitsu, Y. Kudou, M. Konagai, and K. Takahashi, "Molecular beam epitaxial growth of GaAs using trimethylgallium as a Ga source" *J. Appl. Phys.* **55,** 3163 (1984).

[17] A. Robertson, T. H. Chiu, W. T. Tsang, and J. E. Cunningham, "A model for the surface chemical kinetics of GaAs deposition by chemical-beam epitaxy" *J. Appl. Phys.* **64,** 877 (1988).

[18] V. M. Donnelly, and A. Robertson, "Kinetic Modelling of GaAs chemical beam epitaxy" *Surf. Sci.* **293,** 93 (1993).

[19] J. S. Foord, C. L. French, C. L. Levoguer, and G. J. Davies, "Reaction models for the epitaxy growth of III-V semiconductors by chemical beam epitaxy" *Phil. Trans. R. Soc. Lond. A* **344,** 507 (1993).

[20] T. Martin, R. W. Freer, C. R. Whitehouse, and P. A. Lane, "Advances in the understanding of chemical beam epitaxy growth mechanisms" *J. Cryst. Growth* **136,** 69 (1994).

[21] V. M. Donnelly, and J. A. McCaulley, "Products of thermal decomposition of triethylgallium and trimethylgallium adsorbed on Ga-stabilized GaAs(100)" *Surf. Sci.* **238,** 34 (1990).

[22] M. Suzuki, and M. Sato, "Diffusivity and Thermal Cracking Rate of Metalorganic Gases by Chromatography" *J. Electrochem. Soc* **132,** 1684 (1985).

[23] Z. Mahmood, I. Hussain, R. E. Linney, and D. K. Russell, "Comparative infrared laser-powered homogeneous pyrolysis studies of triethylgallane, trimethylgallane, triisopropylgallane, triisobutylgallane, and tri-tert-butylgallane" *J. Anal. Appl. Pyrolysis* **44,** 29 (1997).

[24] T. Martin, and C. R. Whitehouse, "Modulated-beam mass spectrometry studies of the MOMBE growth of (100) GaAs and $In_{0.1}Ga_{0.9}As$" *J. Cryst. Growth* **105,** 57 (1990).

[25] E. T. FitzGerald, C. L. French, and J. S. Foord, "Surface chemical studies of the influence of In and Al on the decomposition of TEG on GaAs(100)" *J. Cryst. Growth* **120,** 57 (1992).

[26] J. R. Creighton, B. A. Bansenauer, T. Huett, J. M. White, "Mechanism of carbon incorporation during GaAs epitaxy" *J. Vac. Sci. Technol. A* **11,** 876 (1993).

[27] C.R. Abernathy, S. J. Pearton, R. Caruso, F. Ren, and J. Kovalchik, "Ultrahigh doping of GaAs by carbon during metalorganic molecular beam epitaxy" *Appl. Phys. Lett.* **55,** 1750 (1989).

[28] F. Ren, C. R. Abernathy, S. J. Pearton, T. R. Fullowan, J. R. Lothian, P. W. Wisk, Y. K. Chen, W. S. Hobson, and P. R. Smith, "Carbon and tin doped *npn* and *pnp* AlGaAs/GaAs HBTs grown by MOMBE" *Electron. Lett.* **27,** 2391 (1991).

[29] G. P. Brivio, and T. B. Grimley, "Dynamics of adsorption/desorption at solid surfaces" *Surf. Sci. Reports* **17,** 1 (1993).

[30] T. Vondrak, and X.-Y. Zhu, "Dissociation of a surface bond by direct optical excitation: H-Si(100)" *Phys. Rev. Lett.* **82,** 1976 (1999).

[31] H. Heinecke, A. Milde, B. Baur, and R. Matz, "Selective-area growth of III/V semiconductors in chemical beam epitaxy" *Semicond. Sci. Technol* **8,** 1029 (1993).

[32] X. F. Liu, H. Asahi, Y. Okuno, D. Marx, K. Inoue, and S. Gonda, "Selective area epitaxy of GaSb and AlGaSb by metalorganic molecular beam epitaxy" *J. Cryst. Growth* **136,** 250 (1994).

[33] E. Kim, I. Berishev, A. Bensaoula, S. Lee, S. S. Perry, K. Waters, and J. A. Schultz, "Nucleation and growth of chemical beam epitaxy gallium nitride thin films" *Appl. Phys. Lett.* **71,** 3072 (1997).

[34] E. Kim, I. Berishev, A. Bensaoula, S. Lee, S. S. Perry, K. Waters, and J. A. Schultz, "Surface composition and morphology of chemical beam epitaxy grown GaN thin films" *J. Vac. Sci. Technol. B* **16,** 1270 (1998).

[35] M. Kappers, J.-L. Guyaux, J. Olivier, R. Bisaro, C. Grattepain, J.-C. Garcia, "Chemical beam epitaxy of GaN on (0001) sapphire substrate" *Mater. Sci. Eng. B* **59,** 52 (1999).

[36] E. Kim, I. Rusakova, I. Berishev, A. Tempez, and A. Bensaoula, "GaN thin film growth on GaAs (0 0 1) by CBE and plasma-assisted MBE" *J. Cryst. Growth* **243,** 456 (2002).

[37] T. Honda, and H. Kawanishi, "Reflection high-energy electron diffraction pattern of GaN grown on 6H–SiC by metalorganic molecular beam epitaxy using AlGaN template" *J. Vac. Sci. Technol., B* **21,** 1822 (2003).

[38] D. Pritchett, W. Henderson, S. D. Burnham, and W. A. Doolittle, "Influence of growth conditions and surface reaction byproducts on GaN grown via metal organic molecular beam epitaxy: toward an understanding of surface reaction chemistry" *J. Electron. Mater.* **35,** 562 (2006).

[39] I. Vurgaftman, and J. R. Meyer, "Band parameters for nitrogen-containing semiconductors" *J. Appl. Phys.* **94,** 3675 (2003).

[40] J. Wu, W. Walukiewicz, K. M. Yu, J. W. Ager, E. E. Haller, Hai Lu, and W. J. Schaff, "Small band gap bowing in $In_{1-x}Ga_xN$ alloys" *Appl. Phys. Lett.* **80,** 4741 (2002).

[41] W. Shan, J. W. Ager III, K. M. Yu, W. Walukiewicz, E. E. Haller, M. C. Martin, W. R. McKinney, and W. Yang, "Dependence of the fundamental band gap of $Al_xGa_{1-x}N$ on alloy composition and pressure" *J. Appl. Phys.* **85,** 8505 (1999).

[42] J. Edmond, A. Abare, M. Bergman, J. Bharathan, K. L. Bunker, D. Emerson, K. Haberern, J. Ibbetson, M. Leung, P. Russel, D. Slater, "High efficiency GaN-based LEDs and lasers on SiC" *J. Cryst. Growth* **272,** 242 (2004).

[43] S. Sumiya, Y. Zhu, J. Zhang, K. Kosaka, M. Miyoshi, T. Shibata, M. Tanaka, and T. Egawa, "AlGaN-based deep ultraviolet light-emitting diodes grown on epitaxial AlN/sapphire templates" *Jap. J. Appl. Phys.* **47,** 43 (2008).

[44] Y. Taniyasu, M. Kasu, and T. Makimoto, "An aluminum nitride light-emitting diode with wavelength of 210 nanometres" *Nature* **441,** 325 (2006).

[45] S. Nagahama, N. Iwasa, M. Senoh, T. Matsushita, Y. Sugimoto, H. Kiyoku, T. Kozaki, M. Sano, H. Matsumura, H. Umemoto, K. Chocho, and T. Mukai, "High-Power and Long-Lifetime InGaN Multi-Quantum-Well Laser Diodes Grown on Low-Dislocation-Density GaN Substrates " *Jap. J. Appl. Phys.* **39,** L647 (2000).

[46] E. F. Schubert, *http://www.lightemittingdiodes.org,* Accessed 2007.

[47] K. M. Yu, Z. Liliental-Weber, W. Walukiewicz, W. Schan, J. W. Ager III, S. X. Li, R. E. Jones, E. E. Haller, H. Lu, and W. J. Schaff, "On the crystalline structure, stoichiometry and band gap of InN thin films" *Appl. Phys. Lett.* **86,** 71910 (2005).

[48] T. Sasaki, and S. Zembutsu, "Substrate-orientation dependence of GaN single-crystal films grown by MOVPE" *J. Appl. Phys.* **61,** 2533 (1997).

[49] C. J. Sun, P. Kung, A. Saxler, H. Ohsato, E. Bigan, M. Razeghi, D. K. Gaskill, "Thermal stability of GaN thin films grown on (0001) Al_2O_3, (01-12) Al_2O_3 and $(0001)_{Si}$ 6H-SiC substrates" *J. Appl. Phys.* **76,** 236 (1994).

[50] O. Ambacher, "Growth and applications of Group III-nitrides" *J. Phys. D* **31,** 2653 (1998).

[51] M. Stutzmann, O. Ambacher, M. Eickhoff, U. Karrer, A. Lima Pimenta, R. Neuberger, J. Schalwig, R. Dimitrov, P. J. Schuck, and R. D. Grober, "Playing with polarity" *Phys. Stat. Sol. B* **228,** 505 (2001).

[52] H. Morkoç, R. Cingolani, W. Lambrecht, B. Gil, H. X. Jiang, J. Lin, D. Pavlidis, and K. Shenai, "Material properties of GaN in the context of electron devices" *MRS Internet J. Nitride Semicond. Res.* **4S1,** G1.2 (1999).

[53] O. Ambacher, J. Majewski, C. Miskys, A. Link, M. Hermann, E. Eickhoff, M. Stutzmann, F. Bernardini, V. Fiorentini, V. Tilak, B. Schaff, and L. F. Eastman, "Pyroelectric properties of Al(In)GaN/GaN hetero- and quantum well structures" *J. Phys.: Condens. Matter* **14,** 3399 (2002).

[54] U. K. Mishra, P. Parikh, and Y.-F. Wu, "AlGaN/GaN HEMTs-An Overview of Device Operation and Applications" *Proc. IEEE* **90,** 1022 (2002).

[55] Y.-F. Wu, A. Saxler, M. Moore, R. P. Smith, S. Sheppard, P. M. Chavarkar, T. Wisleder, U. K. Mishra, and P. Parikh, "30-W/mm GaN HEMTs by Field Plate Optimization" *IEEE Electron Dev. Lett.* **25,** 117 (2004).

[56] T. Inoue, Y. Ando, H. Miyamoto, T. Nakayama, Y. Okamoto, K. Hataya, and M. Kuzuhara, "30-GHz-Band Over 5-W Power Performance of Short-Channel AlGaN/GaN Heterojunction FETs" *IEEE Trans. Microwave Theory Tech* **53,** 74 (2005).

[57] H. Okumura, "Present Status and Future Prospect of Widegap Semiconductor High-Power Devices" *Jap. J. Appl. Phys.* **45,** 7565 (2006).

[58] O. Madelung, 3 ed. (Berlin: Springer-Verlag, 2004), p. 16-25, 88-91, 103-109, 117-128, 137-139.

[59] S. Krukowski, A. Witek, J. Adamczyk, J. Jun, M. Bockowski, I. Grzegory, B. Lucznik, G. Nowak, M. Wróblewski, A. Presz, S. Gierlotka, S. Stelmach, B. Palosz, S. Porowski, P. Zinn, "Thermal properties of indium nitride" *J. Phys. Chem. Sol.* **59,** 289 (1998).

[60] T. P. Chow, "High-voltage SiC and GaN power devices" *Microelectron. Eng.* **83,** 112 (2006).

[61] F. Chen, A. N. Cartwright, H. Lu, and W. J. Schaff, "Hole transport and carrier lifetime in InN epilayers" *Appl. Phys. Lett.* **87,** 212104 (2005).

[62] H. Nakayama, P. Hacke, M. R. H. Khan, T. Detchprohm, K. Hiramatsu, and N. Sawaki, "Electrical transport properties of p-GaN" *Jap. J. Appl. Phys.* **35,** L282 (1996).

[63] W. C. Johnson, J. B. Parsons, and M. C. Crew, "Nitrogen compounds of gallium III. Gallic Nitride" *J. Phys. Chem* **36,** 2651 (1932).

[64] O. Briot, J. P. Alexis, M. Tchounkeu, R. L. Aulombard, "Optimization of the MOVPE growth of GaN on sapphire" *Mat. Sci. Eng. B* **43,** 147 (1997).

[65] H. Amano, N. Sawaki, I. Akasaki, and Y. Toyoda, "Metalorganic vapor phase epitaxial growth of a high quality GaN film using an AlN buffer layer" *Appl. Phys. Lett.* **48,** 353 (1986).

[66] I. Akasaki, H. Amano, Y. Koide, K. Hiramatsu, and N. Sawaki, "Effects of AlN buffer layer on crystallographic structure and on electrical and optical properties of GaN and $Ga_{1-x}Al_xN$ ($0<x<0.4$ films grown on sapphire substrate by MOVPE" *J. Cryst. Growth* **98,** 209 (1989).

[67] S. Nakamura, "GaN growth using GaN buffer layer" *Jap. J. Appl. Phys.* **30,** L1705 (1991).

[68] S. Keller, B. P. Keller, Y.-F. Wu, B. Heying, D. Kapolnek, J. S. Speck, U. K. Mishra, and S. P. DenBaars, "Influence of sapphire nitridation on properties of gallium nitride grown by metalorganic chemical vapor deposition" *Appl. Phys. Lett.* **68,** 1525 (1996).

[69] D. Huang, P. Visconti, K. M. Jones, M. A. Reshchikov, F. Yun, A. A. Baski, T. King, and H. Morkoç, "Dependence of GaN polarity on the parameters of the buffer layer grown by molecular beam epitaxy" *Appl. Phys. Lett.* **78,** 4145 (2001).

[70] R. Averbeck, and H. Riechert, "Quantitative Model for the MBE-Growth of Ternary Nitrides" *Phys. Stat. Sol. A* **176,** 301 (1999).

[71] O. Ambacher, M. S. Brandt, R. Dimitrov, T. Metzger, M. Stutzmann, R. A. Fischer, A. Miehr, A. Bergmaier, and G. Dollinger, "Thermal stability and desorption of Group III nitrides prepared by metal organic chemical vapor deposition" *J. Vac. Sci. Technol. B* **14,** 3532 (1996).

[72] W. A. Harrison, *Electronic structure and the properties of solids: the physics of the chemical bond* (W. H. Freeman, San Francisco, 1980).

[73] H. Funk, and H. Böhland, "Zur Darstellung von Metallnitriden aus Ammoniumfluorometallaten und Ammoniak" *Z. Anorg. Allgem. Chem.* **334,** 115 (1964).

[74] E. A. Albanesi, W. R. L. Lambrecht, and B. Segall, "Electronic structure and equilibrium properties of $Ga_xAl_{1-x}N$ alloys" *Phys. Rev. B* **48,** 17841 (1993).

[75] M. D. Bremser, W. G. Perry, T. Zheleva, N. V. Edwards, O. H. Nam, N. Parikh, D. E. Aspnes, and R. F. Davis, "Growth, Doping, and Characterization of $Al_xGa_{1-x}N$ Thin Film Alloys on 6H-SiC(0001) Substrates" *MRS Internet J. Nitride Semicond. Res.* **1,** 8 (1996).

[76] R. Juza, and H. Hahn, "Crystal structures of Cu_3N, GaN and InN - Metallic amides and metallic nitrides V Announcement " *Z. Anorg. Allgem. Chem* **239,** 282 (1938).

[77] T. Matsuoka, "Progress in nitride semiconductors from GaN to InN-MOVPE growth and characteristics" *Superlatt. Microstruc.* **37,** 19 (2005).

[78] C.R. Abernathy, "Compound semiconductor growth by metalorganic molecular beam epitaxy (MOMBE)" *Mater. Sci. Eng. Rep.* **R14,** 203 (1995).

[79] K. Osamura, S. Naka, and Y. Murakami, "Preparation and optical properties of $Ga_{1-x}In_xN$ thin films" *J. Appl. Phys.* **46,** 3432 (1975).

[80] I. Ho, and G.B. Stringfellow, "Solid phase immiscibility in GaInN" *Appl. Phys. Lett.* **69,** 2701 (1996).

[81] C. Wetzel, T. Suski, J. W. Ager III, E. R. Weber, E. E. Haller, S. Fischer, B. K. Meyer, R. J. Molnar, P. Perlin, "Pressure Induced Deep Gap State of Oxygen in GaN" *Phys. Rev. Lett.* **78,** 3923 (1997).

[82] C. G. Van de Walle, and J. Neugebauer, "First-principles calculations for defects and impurities: Applications to III-nitrides" *J. Appl. Phys.* **95,** 3851 (2004).

[83] S. D. Burnham, G. Namkoong, D. C. Look, B. Clafin, and W. A. Doolittle, "Reproducible increased Mg incorporation and large hole concentration in GaN using metal modulated epitaxy" *J. Appl. Phys.* **104,** 024902 (2008).

[84] M. A. Reshchikov, and H. Morkoç, "Luminescence properties of defects in GaN" *J. Appl. Phys.* **97,** 061301 (2005).

[85] I. Akasaki, "Key inventions in the history of nitride-based blue LED and LD" *J. Cryst. Growth* **300,** 2 (2007).

[86] R. P. Strittmatter, R. A. Beach, and T. C. McGill, "Fabrication of GaN suspended microstructures" *App. Phys. Lett.* **78,** 3226 (2001).

[87] D. Zhuang, and J. H. Edgar, "Wet etching of GaN, AlN, and SiC: a review" *Mater. Sci. and Eng. R* **48,** 1 (2005).

[88] V. Cimalla, F. Niebelschütz, K. Tonisch, Ch. Foerster, K. Brueckner, I. Cimalla, T. Friedrich, J. Pezoldt, R. Stephan, M. Hein, and O. Ambacher, "Nanoelectromechanical devices for sensing applications" *Sens. and Act. B* **126,** 24 (2007).

[89] V. Cimalla, J. Pezoldt, and O. Ambacher, "Group III nitride and SiC based MEMS and NEMS: material properties, technology and applications" *J. Phys. D: App. Phys* **40,** 6386 (2007).

[90] J.-Y. Kim Park. I.-K., M.-K. Kwon, C.-Y. Cho. J.-H. Lim, and S.-J. Park, "Phosphor-free white light-emitting diode with laterally distributed multiple quantum wells" *App. Phys. Lett.* **92,** 091110 (2008).

[91] C. H. Chen, S. J. Chang, Y. K. Su, J. K. Sheu, J. F. Chen, Ch. H. Kuo, and Y. C. Lin, "Nitride-based cascade near white light-emitting diodes" *IEEE Photonics Technol. Lett.* **14,** 908 (2002).

[92] D. Rajavel, Thesis, Georgia Institute of Technology, 1991.

[93] Kurt J Lesker Company, "Viewports" *Product Catalog***,** 145 (2008).

[94] Stanford Research Systems, *Operating Manual and Program Reference, Models RGA100, RGA200, and RGA300 Residual Gas Analyzer, Rev. 1.6* (2005).

[95] S. Nakamura, "In situ monitoring of GaN growth using interference effects" *Jap. J. Appl. Phys.* **30,** 1620 (1991).

[96] C. D. Zuiker, D. M. Gruen, and A. R. Krauss, "*In situ* reflectance interferometry measurement of diamond film growth" *J. Appl. Phys.* **79,** 3541 (1996).

[97] H. Wang, and A.-B. Chen, "Calculations of acceptor ionization energies in GaN" *Phys. Rev. B* **63,** 125212 (2001).

[98] A. F. Wright, "Substitutional and interstitial carbon in wurtzite GaN" *J. Appl. Phys.* **92,** 2575 (2002).

[99] A. Armstrong, A. R. Arehart, B. Moran, S. P. DenBaars, U. K. Mishra, J. S. Speck, and S. A. Ringel, "Impact of carbon on trap states in n-type GaN grown by metalorganic chemical vapor deposition" *Appl. Phys. Lett.* **84,** 374 (2004).

[100] C. R. Abernathy, J. D. MacKenzie, S. J. Pearton, and W. S. Hobson, "CCl_4 doping of GaN grown by metalorganic molecular beam epitaxy" *Appl. Phys. Lett.* **66,** 1969 (1995).

[101] D. J. As, U. Köhler, M. Lübbers, J. Mimkes, and K. Lischka, "p-Type Doping of Cubic GaN by Carbon" *Phys. Stat. Sol. A* **188,** 699 (2001).

[102] H. Tang, J. B. Webb, J. A. Bardwell, S. Raymond, J. Salzman, and C. Uzan-Saguy, "Properties of carbon-doped GaN" *Appl. Phys. Lett.* **78,** 757 (2001).

[103] A. E. Wickenden, D. D. Koleske, R. L. Henry, M. E. Twigg, and M. Fatemi, "Resistivity control in unintentionally doped GaN films grown by MOCVD" *J. Cryst. Growth* **260,** 54 (2004).

[104] P. B. Klein, S. C. Binari, K. Ikossi, A. E. Wickenden, D. D. Koleske, and R. L. Henry, "Current collapse and the role of carbon in AlGaN/GaN high electron mobility transistors grown by metalorganic vapor-phase epitaxy" *Appl. Phys. Lett.* **79,** 3527 (2001).

[105] C. Poblenz, P. Waltereit, S. Rajan, S. Heikman, U. K. Mishra, and J. S. Speck, "Effect of carbon doping on buffer leakage in AlGaN/GaN high electron mobility transistors" *J. Vac. Sci. Technol. B* **22,** 1145 (2004).

[106] S. Haffouz, H. Tang, J. A. Bardwell, E. M. Hsu, J. B. Webb, and S. Rolfe, "AlGaN/GaN field effect transistors with C-doped GaN buffer layer as an electrical isolation template grown by molecular beam epitaxy" *Solid-State Electron.* **49,** 802 (2005).

[107] Y. C. Choi, M. Pophristic, B. Peres, H.-Y. Cha, M. G. Spencer, and L. F. Eastman, "High breakdown voltage C-doped GaN-on-sapphire HFETs with a low specific on-resistance" *Semicond. Sci. Technol* **22,** 517 (2007).

[108] D. S. Green, U. K. Mishra, and J. S. Speck, "Carbon doping of GaN with CBr_4 in radio-frequency plasma-assisted molecular beam epitaxy" *J. Appl. Phys.* **95,** 8456 (2004).

[109] D. D. Koleske, A. E. Wickenden, R. L. Henry, and M. E. Twigg, "Influence of MOVPE growth conditions on carbon and silicon concentrations in GaN" *J. Cryst. Growth* **242,** 55 (2002).

[110] T. Kurobe, Y Sekiguchi, J. Suda, M. Yoshimoto, and H. Matsunami, "Preferential growth of cubic GaN on sapphire (0001) substrates by metal organic molecular beam epitaxy" *Appl. Phys. Lett.* **73,** 2305 (1998).

[111] J. Suda, T. Kurobe, H. Matsunami, "Growth evolution of cubic-GaN on sapphire (0001) substrate by metalorganic molecular beam epitaxy" *J. Cryst. Growth* **201-202,** 437 (1999).

[112] J. Saito, T. Maeda, K. Ono, and K. Kondo, "Background pressure dependence on GaAs and AlGaAs growth rates in gas-source molecular beam epitaxy" *J. Cryst. Growth* **111,** 544 (1991).

[113] Newport Corporation, "Arc Sources" *Product Catalog***,** 112 (2008).

[114] Photon Technology International, "The effects of reflector design and lamp orientation" *http://www.pti-nj.com/UVvis/TechNotes/LampReflectorDesign.pdf***,** Accessed 2008.

[115] W. Shan, T. Schmidet, X. H. Yang, J. J. Song, and B. Goldenberg, "Optical properties of wurtzite GaN grown by low-pressure metalorganic chemical-vapor deposition" *J. Appl. Phys.* **79,** 3691 (1996).

[116] ORC Lighting Products, "Short Arc Mercury Xenon Lamps" *Datasheet*.

[117] R. Held, D. E. Crawford, A. M. Johnston, A. M. Dabiran, and P. I. Cohen, "N-limited versus Ga-limited growth on GaN(000-1) by MBE using NH_3" *Surf. Rev. Lett.* **5,** 913 (1998).

[118] M. Pristovsek, M. Zorn, and M. Weyers, "In situ study of GaAs growth mechanisms using tri-methyl gallium and tri-ethyl gallium precursors in metal-organic vapour phase epitaxy" *J. Cryst. Growth* **262,** 78 (2004).

[119] F. Maury, K. Bouabid, N. Fazouan, A. M. Gué, and D. Estève, "GaAs growth by photon-assisted metalorganic molecular beam epitaxy using ethyl derivatives by gallium and arsenic" *Appl. Surf. Sci.* **86,** 447 (1995).

[120] T. Li, R. P. Campion, C. T. Foxon, S. A. Rushworth, and L. M. Smith, "MOMBE growth studies of GaN using metalorganic sources and nitrogen" *J. Cryst. Growth* **251,** 499 (2003).

[121] S.S. Liu, and D. A. Stevenson, "Growth kinetics and catalytic effects in the vapor phase epitaxy of gallium nitride" *J. Electrochem. Soc.* **125,** 1161 (1978).

[122] N. Pütz, H. Heinecke, M. Heyen, P. Balk, M. Weyers, and H. Lüth, "A comparative study of $Ga(CH_3)_3$ and $Ga(C_2H_5)_3$ in the MOMBE of GaAs" *J. Cryst. Growth* **74,** 292 (1986).

[123] P. W. Lee, T. R. Omstead, D. R. McKenna, and K. F. Jensen, "In situ mass spectroscopy and thermogravimetric studies of GaAs MOCVD gas phase and surface reactions" *J. Cryst. Growth* **85,** 165 (1987).

[124] G. B. Stringfellow, (San Diego: Academic Press, 1999), p. 399-400.

[125] C. H. Seager, A. F. Wright, J. Yu, and W. Götz, "Role of carbon in GaN" *J. Appl. Phys.* **92,** 6553 (2002).

[126] S. Nakamura, M. Senoh, S. Nagahama, N. Iwasa, T. Yamada, T. Matsushita, H. Kiyoku, and Y. Sugimoto, "InGaN-Based Multi-Quantum-Well-Structure Laser Diodes" *Jap. J. Appl. Phys.* **35,** L74 (1996).

[127] S. E. Hooper, M. Kauer, V. Bousquet, K. Johnson, J. M. Barnes, and J. Heffernan, "InGaN multiple quantum well laser diodes grown by molecular beam epitaxy" *Electron. Lett.* **40,** 33 (2004).

[128] S. D. Burnham, Thesis, Georgia Institute of Technology, 2007.

[129] D. Holec, P. M. F. J. Costa, M. J. Kappers, and C. J. Humphreys, "Critical thickness calculations for InGaN/GaN" *J. Cryst. Growth* **303,** 314 (2007).

[130] H. Chen, R. M. Feenstra, J. Northrup, J. Neugebauer, and D. W. Greve, "Indium incorporation and surface segregation during InGaN growth by molecular beam epitaxy: experiment and theory" *MRS Internet J. Nitride Semicond. Res.* **6,** 11 (2001).

[131] V. M. Donnelly, and J. A. McCaulley, "Methyl exchange reaction of trimethylindium on GaAs(100) and the preferential etching of gallium" *Surf. Sci.* **235,** L333 (1990).

[132] M. J. Kappers, M. L. Warddrip, and R. F. Hicks, "Ligand exchange reactions in InGaAs metalorganic vapor-phase epitaxy" *J. Cryst. Growth* **191,** 332 (1998).

[133] H. Asahi, T. Kaneko, Y. Okuno, Y. Itani, K. Asami, and S. Gonda, "MOMBE growth characteristics of antimonide compounds" *J. Cryst. Growth* **120,** 252 (1992).

[134] A. S. Grady, R. E. Linney, R. D. Markwell, and D. K. Russell, "Exchange and Pyrolysis in Mixed Trialkylgallanes" *J. Mater. Chem.* **3,** 483 (1993).

[135] G. W. Wicks, and M. W. Koch, and J. R. Pedrazzani, "Studies of ammonia dissociation during the gas source molecular-beam epitaxial growth of III nitrides" *J. Vac. Sci. Technol. B* **23,** 1186 (2005).

[136] F. Fournier, R. A. Metzger, A. Doolittle, A. S. Brown, C. Carter-Coman, N. M. Jokerst, and R. Bicknell-Tassius, "Growth dynamics of InGaAs/GaAs by MBE" *J. Cryst. Growth* **175/176,** 203 (1997).

[137] I. Stanley, G. Coleiny, and R. Venkat, "Theoretical study of In desorption and segregation kinetics in MBE growth of InGaAs and InGaN" *J. Cryst. Growth* **251,** 23 (2003).

[138] S. Yu. Karpov, R. A. Talalaev, E. V. Yakovlev, and Y. N. Makarov, "Surface segregation and composition fluctuations in ammonia MBE and MOVPE of InGaN" *Mat. Res. Soc. Symp. Proc.* **639,** G3.18 (2001).

[139] A. L. Jackson, *Private Communication*.

[140] N. Kobayashi, J. L. Benchimol, F. Alexandre, and Y. Gao, "Substrate temperature dependence of GaAs, GaInAs, and GaAlAs growth rates in metalorganic molecular beam epitaxy" *Appl. Phys. Lett.* **51,** 1907 (1987).

[141] J. R. Creighton, K. R. Lykke, V. A. Shamamian, and B. D. Kay, "Decomposition of trimethylgallium on the gallium-rich GaAs (100) surface: implications for atomic layer epitaxy" *Appl. Phys. Lett.* **57,** 279 (1990).

[142] R. W. Freer, P. A. Lane, T. Martin, C. R. Whitehouse, T. J. Whitaker, G. M. Williams, A. G. Cullis, P. D. J. Calcott, K. D. Nash, H. Buchannan, A. C. Jones, and S. Rushworth, "Chemical-beam-epitaxy growth of indium-containing III–V compounds using triisopropylindium" *J. Appl. Phys.* **79,** 917 (1996).

[143] D. H. Cho, M. Tanaka, and K. Pak, "Maskless selective epitaxy of InGaN by an InGa low energy focused ion beam and dimethylhydrazine" *J. Cryst. Growth* **227,** 476 (2001).

[144] X. Chen, W. J. Schaff, and L. F. Eastman, "Direct-write composition patterning of InGaN by focused thermal beam during molecular-beam epitaxy" *J. Vac. Sci. Technol. B* **25,** 974 (2007).

[145] D. Pritchett, W. Henderson, D. Billingsley, and W. A. Doolittle, "Mixed alkyl exchange and exploitable surface interactions in InGaN by NH_3-based metal organic molecular beam epitaxy" *J. Cryst. Growth* **310**, 5297 (2008).

[146] R. R. Sowell, R. E. Cuthrell, D. M. Mattox, and R. D. Bland, "Surface cleaning by ultraviolet radiation" *J. Vac. Sci. Technol. A* **11,** 474 (1974).

[147] V. R. McCrary, and V. M. Donnelly, "The ultraviolet absorption spectra of selected organometallic compounds used in the chemical vapor deposition of gallium arsenide" *J. Cryst. Growth* **84,** 253 (1987).

[148] H. Okabe, M. K. Emadi-Babaki, and V. R. McCrary, "Temperature-dependent ultraviolet absorption spectra of group IIIb and Vb compounds used in photo-assisted chemical vapor deposition" *J. Appl. Phys.* **69,** 1730 (1991).

[149] H. H. Gilgen, C. J. Chen, R. Krchnavek, and R. M. Osgood Jr., edited by D. Bäuerle (Berlin: Springer-Verlag, 1984), p. 225.

[150] G. A. Hebner, K. P. Killeen, and R. M. Biefeld, "In situ measurement of the metalorganic and hydride partial pressures in a MOCVD reactor using ultraviolet absorption spectroscopy" *J. Cryst. Growth* **98,** 293 (1989).

[151] T. Ibuki, A. Hiraya, K. Shobatake, Y. Matsumi, and M. Kawasaki, "He(I) photoelectron spectra and VUV absorption cross sections of $Ga(CH_3)_3$ and $In(CH_3)_3$" *Chem. Phys. Lett.* **160,** 152 (1989).

[152] F. Z. Chen, D. L. Judge, C. Y. Robert Wu, and J. Caldwell, "Low and room temperature photoabsorption cross sections of NH_3 in the UV region" *Planet. Space Sci.* **47,** 261 (1999).

[153] D. Pritchett, W. Henderson, D. Billingsley, W. Alan Doolittle, "Mg doped GaN and intentional Mg dopant modulation *in situ* by NH_3-based metal organic molecular beam epitaxy" *J. Cryst. Growth* (in preparation).

[154] D. Pritchett, W. Henderson, D. Billingsley, and W. A. Doolittle, "InGaN compositional patterning by ultraviolet photoexcitation during NH_3-based MOMBE - A pathway to 3D epitaxy" *Phys. Stat. Sol. C* **5,** 1726 (2007).

[155] McD. Robinson, D. J. Lischner, and G. K. Celler, "Large area recrystallization of polysilicon with tungsten-halogen lamps" *J. Cryst. Growth* **63,** 484 (1983).

[156] G. Koblmüller, R. Averbeck, H. Riechert, and P. Pongratz, "Direct observation of different equilibrium Ga adlayer coverages and their desorption kinetics on GaN (0001) and (000-1) surfaces" *Phys. Rev. B* **69,** 035325 (2004).

[157] *This value is from ref 72 which cites an InN bandgap of 1.9 eV. Newer data based on the 0.65 eV value for InN is unavailable.*

[158] P. Avouris, and R. E. Walkup, "Fundamental mechanisms of desorption and fragmentation induced by electronic transitions at surfaces" *Annu. Rev. Phys. Chem.* **40,** 173 (1989).

[159] F. M Zimmerman, and W. Ho, in *Surface Photochemistry*; *Vol. 1*, edited by M. Anpo (Chichester: Wiley, 1996), p. 19-63.

[160] B. Heying, R. Averbeck, L. F. Chen, E. Haus, H. Riechert, and J. S. Speck, "Control of GaN surface morphologies using plasma-assisted molecular beam epitaxy" *J. Appl. Phys.* **88,** 1855 (2000).

[161] R. Held, D. E. Crawford, A. M. Johnston, A. M. Dabiran, and P. I. Cohen, "In situ control of GaN growth by molecular beam epitaxy " *J. Electron. Mater.* **26,** 272 (1997).

[162] S. Guha, N. A. Bojarczuk, and D. W. Kisker, "Surface lifetimes of Ga and growth behavior on GaN (0001) surfaces during molecular beam epitaxy" *App. Phys. Lett.* **69,** 2879 (1996).

[163] D. E. Crawford, R. Held, A. M. Johnston, A. M. Dabiran, and P. Cohen, "Growth rate reduction of GaN due to Ga surface accumulation" *MRS Internet J. Nitride* **1,** 12 (1996).

[164] D. D. Koleske, A. E. Wickenden, R. L. Henry, W. J. DeSisto, and R. J. Gorman, "Growth model for GaN with comparison to structural, optical, and electrical properties" *J. Appl. Phys.* **84,** 1998 (1998).

[165] K. R. Evans, T. Lei, and C. R. Jones, "Gallium incorporation kinetics during gas source molecular beam epitaxy growth of GaN" *Solid-State Electron.* **41,** 339 (1997).

[166] E. J. Tarsa, B. Heying, X. H. Wu, P. Fini, S. P. DenBaars, and J. S. Speck, "Homoepitaxial growth of GaN under Ga-stable and N-stable conditions by plasma-assisted molecular beam epitaxy." *J. Appl. Phys.* **82,** 5472 (1997).

[167] C. R. Elsass, C. Poblenz, B. Heying, P. Fini, P. M. Petroff, S. P. DenBaars, U. K. Mishra, and J. S. Speck, "Influence of Ga flux on the growth and electron transport properties of AlGaN/GaN heterostructures grown by plasma-assisted molecular beam epitaxy" *J. Cryst. Growth* **233,** 709 (2001).

[168] N. Grandjean, M. Leroux, J. Massies, M. Mesrine, and M. Laügt, "Molecular beam epitaxy of GaN under N-rich conditions using NH_3" *Jap. J. Appl. Phys.* **38,** 618 (1999).

[169] T. Koida, Y. Uchinuma, J. Kikuchi, K. R. Wang, M. Terazaki, T. Onuma, J. F. Keading, R. Sharma, S. Nakamura, and S. F. Chichibu, "Improved surface morphology in GaN homoepitaxy by NH_3-source molecular-beam epitaxy" *J. Vac. Sci. Technol. B* **22,** 2158 (2004).

[170] J. Neugebauer, T. K. Zywietz, M. Scheffler, J. E. Northrup, H. Chen, and R. M. Feenstra, "Adatom kinetics on and below the surface: the existence of a new diffusion channel" *Phys. Rev. Lett.* **90,** 056101-1 (2003).

[171] D. Nečas, and P. Klapetek, *http://gwyddion.net/documentation/user-guide/grain-analysis.html,* Accessed 2008.

[172] A. Parkhomovsky, A. M. Dabiran, B. Benjaminsson, and P. I. Cohen, "Hexagonal growth spirals on GaN grown by molecular-beam epitaxy: Kinetics versus thermodynamics" *Appl. Phys. Lett.* **78,** 2315 (2001).

[173] P. Q. Miraglia, E. A. Preble, A. M. Roskowski, S. Einfeldt, and R. F. Davis, "Helical-type surface defects in GaN thin films epitaxially grown on GaN templates at reduced temperatures" *J. Cryst. Growth* **253,** 16 (2003).

[174] D. Billingsley, Thesis, Georgia Institute of Technology, 2010.

[175] H. Amano, M. Kito, K. Hiramatsu, and I. Akasaki, "P-Type Conduction in Mg-Doped GaN Treated with Low-Energy Electron Beam Irradiation (LEEBI)" *Jap. J. Appl. Phys.* **28,** L2112 (1989).

[176] S. Nakamura, N. Iwasa, M. Senoh, and T. Mukai, "Hole Compensation Mechanism of P-Type GaN Films" *Jap. J. Appl. Phys.* **31,** 1258 (1992).

[177] S. Nakamura, M. Senoh, T. Mukai, "Highly p-typed Mg-doped GaN films grown with GaN buffer layers" *Jap. J. Appl. Phys.* **30,** L1708 (1991).

[178] A. Dussaigne, B. Damilano, J. Brault, J. Massies, E. Feltin, and N. Grandjean, "High doping level in Mg-doped GaN layers grown at low temperature" *J. Appl. Phys.* **103,** 013110 (2008).

[179] Q. Sun, A. Selloni, T. H. Myers, and W. A. Doolittle, "Energetics of Mg incorporation at GaN(001) and GaN(000-1) surfaces" *Phys. Rev. B* **73,** 155337 (2006).

[180] T. Yamamoto, and H. Katayama-Yoshida, "Materials design for the fabrication of low-resistivity p-type GaN using a codoping method" *Jpn. J. Appl. Phys.* **36,** L180 (1997).

[181] O. Brandt, H. Yang, H. Kostial, and K. H. Ploog, "High p-type conductivity in cubic GaN/GaAs(113)A by using Be as the acceptor and O as the codopant" *App. Phys. Lett.* **69,** 2707 (1996).

[182] K. S. Kim, C. S. Oh, M. S. Han, C. S. Kim, G. M. Yang, J. W. Yang, C.-H. Hong, C. J. Youn, K. Y. Lim, and H. J. Lee, "Co-doping characteristics of Si and Zn with Mg in P-type GaN" *MRS Internet J. Nitride* **5S1,** W3.84 (2000).

[183] C. G. Van de Walle, C. Stampfl, and J. Neugebauer, "Theory of doping and defects in III-V nitrides" *J. Cryst. Growth* **189/190,** 505 (1998).

[184] P. Kozodoy, H. Xing, S. P. DenBaars, U. K. Mishra, A. Saxler, R. Perrin, S. Elhamri, and W. C. Mitchel, "Heavy doping effects in Mg-doped GaN" *J. Appl. Phys.* **87,** 1832 (2000).

[185] A. J. Ptak, T. H. Myers, L. T. Romano, C. G. Van de Walle, and J. E. Northrup, "Magnesium incorporation in GaN grown by molecular-beam epitaxy " *App. Phys. Lett.* **78,** 285 (2001).

[186] D. S. Green, E. Haus, F. Wu, L. Chen, U. K. Mishra, and J. S. Speck, "Polarity control during molecular beam epitaxy growth of Mg-doped GaN" *J. Vac. Sci. Technol. B* **21,** 1804 (2003).

[187] P. Vennéguès, M. Benaissa, B. Beaumont, E. Feltin, P. De Mierry, S. Dalmasso, M. Leroux, and P. Gibart, "Pyramidal defects in metalorganic vapor phase epitaxial Mg doped GaN" *App. Phys. Lett.* **77,** 880 (2000).

[188] Y. Ohba, and A. Hatano, "A study on strong memory effects for Mg doping in GaN metalorganic chemical vapor deposition" *J. Cryst. Growth* **145,** 214 (1994).

[189] W. Kim, A. Slavador, A. E. Botchkarev, O. Aktas, S. N. Mohammad, and H. Morcoç, "Mg-doped *p*-type GaN grown by reactive molecular beam epitaxy" *App. Phys. Lett.* **69,** 559 (1996).

[190] G. Kipshidze, V. Kuryatkov, B. Borisov, Yu. Kudryavtsev, R. Asomoza, S. Nikishin, and H. Temkin, "Mg and O codoping in *p*-type GaN and $Al_xGa_{1-x}N$ ($0<x<0.08$)" *App. Phys. Lett.* **80,** 2910 (2002).

[191] W. T. Moore, P. Mandeville, R. W. Streater, and C. J. Miner, "Device quality AlGaAs grown by chemical beam epitaxy" *J. Cryst. Growth* **164,** 485 (1996).

[192] H. C.-H. Lee Matsuhashi, T. Nishimura, K. Masu, and K. Tsubouchi, "Superiority of DMAH to DMEAA for al CVD technology" *Mater. Sci. Semi. Proc.* **2,** 303 (1999).

[193] D. Billingsley, W. Henderson, D. Pritchett, and W. Alan Doolittle, "Growth and characterization of $Al_xGa_{1-x}N$ via ammonia-based metal organic molecular beam epitaxy" *J. Cryst. Growth*, *in press* (2009).

[194] D. Billingsley, W. Henderson, D. Pritchett, and W. Alan Doolittle, "Improved Understanding of the Growth of AlGaN Grown by Ammonia-Based Metal Organic Molecular Beam Epitaxy" *in preparation* (2009).

[195] S. J. Bennett, "An absolute interferometric dilatometer" *J. Phys. E: Sci. Instr.* **10,** 525 (1977).

[196] C. Roder, S. Einfeldt, S. Figge, and D. Hommel, "Temperature dependence of the thermal expansion of GaN" *Phys. Rev. B* **72,** 085218 (2005).

VITA

David Pritchett is a native of Atlanta Georgia, USA. He has been awarded degrees in Computer Engineering (B.S. 2002) and Electrical and Computer Engineering (M.S. 2005, Ph.D. 2009) from the Georgia Institute of Technology.

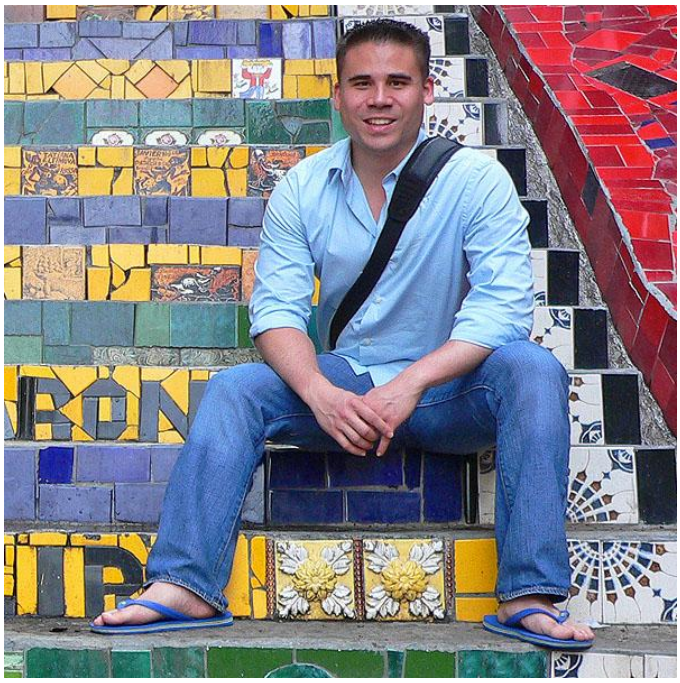

http://www.dpritchett.info

Publications and presentations resulting from this work:

D. Billingsley, W. Henderson, D. Pritchett, W. A. Doolittle, 'Optimization of GaN Surface Morphology Grown by Ammonia-Based Metal Organic Molecular Beam Epitaxy," in preparation.

D. Billingsley, W. Henderson, D. Pritchett, and W. A. Doolittle, "Improved Understanding of the Growth of AlGaN Grown by Ammonia-Based Metal Organic Molecular Beam Epitaxy," in preparation.

D. Pritchett, W. Henderson, D. Billingsley, W. Alan Doolittle, "Mg doped GaN and Intentional Mg Dopant Modulation *in situ* by NH_3-based Metal Organic Molecular Beam Epitaxy," in preparation.

D. Pritchett, D. Billingsley, W. Henderson, W. A. Doolittle, "Growth Regimes of GaN during NH_3-based Metal Organic Molecular Beam Epitaxy," in preparation.

D. Billingsley, W. Henderson, D. Pritchett, and W. Alan Doolittle, "Growth and Characterization of $Al_xGa_{1-x}N$ via Ammonia-based Metal Organic Molecular Beam Epitaxy," *Journal of Crystal Growth* accepted 2009.

D. Pritchett, W. Henderson, D. Billingsley, and W. A. Doolittle, "Mixed Alkyl Exchange and Exploitable Surface Interactions in InGaN by NH_3-based Metal Organic Molecular Beam Epitaxy," *Journal of Crystal Growth* 310, 5297 (2008).

D. Billingsley, D. Pritchett, W. Henderson, A. G. Carver, S. D. Burnham, and W. A. Doolittle, "Investigation into the use of Molecular Hydrogen on the Growth of Gallium Nitride via Metal-organic Molecular Beam Epitaxy," *Physica Status Solidi* C 5, 1723 (2008).

D. Pritchett, W. Henderson, D. Billingsley, and W. A. Doolittle, "InGaN Compositional Patterning by Ultraviolet Photoexcitation during NH_3-based MOMBE - A Pathway to 3D Epitaxy," *Physica Status Solidi C* 5, 1726 (2008).

D. Pritchett, W. Henderson, S. D. Burnham, and W. A. Doolittle, "Influence of Growth Conditions and Surface Reaction Byproducts on GaN Grown via Metal Organic Molecular Beam Epitaxy: Toward an Understanding of Surface Reaction Chemistry," *Journal of Electronic Materials* 35, 562 (2006).

W. A. Doolittle, D. Pritchett, and W. Henderson, "Maskless and Dynamic AllnGaN Compositional and Doping Patterning for Three Dimensional Epitaxy," *U.S. Patent Pending*, February 19, 2007.

D. Pritchett, D. Billingsley, W. Henderson, and W. A. Doolittle, "Toward Engineered 3-Dimensional Epitaxy using Micro-mirror Patterned Photo-assisted Epitaxy," *2008 Electronic Materials Conference*, June 27, 2008

D. Pritchett, W. Henderson, D. Billingsley, and W. A. Doolittle, "InGaN Compositional Control by Ultraviolet Photoexcitation during NH_3-based MOMBE - A Pathway to 3D Epitaxy," *7th International Conference of Nitride Semiconductors*, September 18, 2007.

D. Billingsley, D. Pritchett, S. D. Burnham, W. Henderson, and W. A. Doolittle, "Investigation into the Use of Molecular Hydrogen on the Growth of Gallium Nitride via Metal-Organic Molecular Beam Epitaxy," *7th International Conference of Nitride Semiconductors*, September 18, 2007.

D. Pritchett, D. Billingsley, W. Henderson, and W. A. Doolittle, "Influence of Ultraviolet Photoexcitation on the Growth of InGaN via NH_3-based MOMBE," *2007 Workshop on Compound Semiconductor Materials and Devices*, February 19, 2007.

D. Billingsley, D. Pritchett, W. Henderson, E. Trybus, K.K. Lee, and W. A. Doolittle, "Influence of Surface Nitridation on Gallium Nitride Grown via Ammonia based Metal Organic Molecular Beam Epitaxy," *2006 North American Molecular Beam Epitaxy Conference*, October 9, 2006.

D. Pritchett, W. Henderson, S. D. Burnham, and W. A. Doolittle, "Influence of Intense Ultraviolet Photoexcitation on Surface Reactions during Gallium Nitride Growth via Metal Organic Molecular Beam Epitaxy," *33rd Physics and Chemistry of Semiconductor Interfaces Conference*, January 17, 2006.

D. Pritchett, S. D. Burnham, W. Henderson, and W. A. Doolittle, "Metalorganic Molecular Beam Epitaxy (MOMBE) of GaN: Towards an Understanding of Surface Reaction Chemistry," *2005 Electronic Materials Conference*, June 23, 2005.